Optimized Operational Control for an Electric Power System on More Electric Aircraft

by Xin WANG, MEng

Thesis submitted to The University of Nottingham

for the degree of Doctor of Philosophy, July 2022



Abstract

On more electric aircraft (MEA), reducing fuel consumption and guaranteeing flight safety are pursued by efficient operational management of the electrical power system (EPS). It is essential to design a system-level operational control to coordinate the power and energy among different subsystems, ensuring the flight mission and reducing the operation costs while guaranteeing the safety requirements. This thesis presents an operational control design which adopts different techniques for a novel modular converter-based aircraft EPS architecture, providing an efficient, reliable, and robust operating strategy in both normal and faulty conditions.

Four main issues are integrated into the operational control for the modular converter-based EPS architecture: intelligent load shedding; power allocation and scheduling (PAS); EPS (re)configuration; and energy storage management (ESM). Firstly, this thesis studies the mathematical formulation and optimization methods for the studied EPS and the control targets. The optimal PAS and EPS (re)configuration are studied for a modular converter power distribution system, demonstrating mixed-integer linear programming (MILP) and linearization techniques for mathematical modeling with operation constraints, including the power balancing and limitations, contactor switching logic, the transmission losses of cables, and the nonlinear characteristics of converter efficiencies. The results are compared when two different objective functions are applied for power loss and generator sizing reduction.

Secondly, the aforementioned MILP formulation techniques are applied for decisions on load shedding and ESM for the system in study. With the aim of avoiding worst-case scenarios during the flight, for both cost reduction and safety improvement, a MILP-based model predictive control (MPC) operational control is proposed based on future predictions. The proposed MILP-MPC method aims to achieve multiple control targets, including maintaining energy storage (ES) and prolonging the battery life cycle, minimizing load shedding, and reducing switching activities to improve a device's lifetime and avoid unnecessary transients. To achieve these control targets, three different objective functions are proposed. The importance of the different objective functions and prediction horizons are compared by the proposed evaluation framework.

Thirdly, this thesis proposes an intelligent two-level hierarchical supervisory control method for the entire EPS, achieving all of the multiple control targets in various faulty scenarios. The control targets here include the reduction of total power losses and generator sizing, intelligent ESM and load shedding, and reducing switching activities. The MILP-MPC-

based high level (HL) controller improves the long-term (i.e., the entire flight stages) EPS performance of these control targets with future predictions utilizing a slow clock, to reduce the computation burden. In addition, a rule-based lower level (LL) controller is designed with a faster clock to provide quick responses to load changes and faults which occur over a short timeframe within one of the HL sample intervals. Hence, the proposed hierarchical control provides optimized performances while maintaining quick responses to EPS changes. In addition, the LL controller is designed with the consideration of handling the situation when the HL is in a faulty condition, which improves the reliability of the hierarchical control.

Finally, uncertainties of fluctuating load demands are considered for the aforementioned MILP-MPC operational control of the entire EPS, aiming to avoid poor performance due to imprecise load predictions. To improve the robustness of the control strategy, a chance-constrained stochastic MPC (CC-SMPC) method is proposed to improve both the system operation in terms of the system's objectives as well as the ability to cope with uncertainties due to fluctuating load demands. Both normal and faulty operating conditions are investigated with multi-failure cases, resulting in different uncertainty propagation paths. To verify the effectiveness of the proposed strategy, a comprehensive comparison study is conducted to compare the performance of the proposed CC-SMPC and deterministic MPC (DMPC) techniques.

In summary, this thesis provides the design engineer with different aspects and techniques for designing an optimized operational controller for an aircraft EPS. The practical techniques, performances, and benefits of the proposed methods are presented and discussed, inspiring further studies in the target area with different EPS architectures, requirements, and control targets.

Acknowledgement

Getting the chance to work towards this degree at the Power Electronics, Machines and Control (PEMC) Group, the University of Nottingham, is a great gift for me. During this journey, countless people have offered me a help, inspired and challenged me to become a better scholar. I do want to take this opportunity to thank all of them, also to mention a few in particular.

First and foremost, I am extremely grateful to my supervisors, Prof. Serhiy Bozhko and Dr. Jason Atkin for their invaluable advice, continuous support, and patience during my PhD study. Their immense knowledge and plentiful experience have encouraged me in all the time of my academic research. I am also thankful to Dr. Sharmila Sumsurooah and Dr. Christopher I. Hill for their kind supervision during my PhD programme, and for offering help whenever I needed it.

Special thanks to both Marie Skłodowska-Curie Actions and the University of Nottingham for sponsoring this PhD programme. It has been a great honour to be a Marie Curie Early Stage Researcher, and I have enjoyed complete academic freedom in this research.

I would also like to thank everyone in Marie-Curie INNOVATIVE programme, Institute for Aerospace Technology (IAT), and PEMC group. In particular, I want to thank Dr. Cosimo Spagnolo, Dr. Mahmoud Elkazaz, and Dr. Hossein Balaghi Enalou for their technical guidance during my research.

Furthermore, I am grateful to everyone I've collaborated with externally. I would like to express my deep gratitude to Prof. Josep M. Guerrero and Dr. Najmeh Bazmohammadi for the exciting collaboration with the world-leading research group in Aalborg University. Special thanks also go to Dr. Wing Chun Chan in Newcastle University for his friendship and valuable discussions. I also want to thank Dr. Javier Palacio from dSPACE Ltd. for this technical support during my experiment.

Last but not least, I am always thankful to my family, especially Mum and Dad who have always believed in me and supported my pursuit of education. Without their tremendous understanding and encouragement in the past few years, it would be impossible for me to complete my study. Special thanks to my boyfriend, Yuan Gao, for his love, understanding, being so supportive and helping me every step of the way.

Contents

Abstract III

Acknowledgement V

Contents VII

List of Publications XII

List of Abbreviations and Acronyms XIV

Chapter 1 Introduction 1

1.1 Background and motivation 1

1.1.1 Evolution of electrical power system of MEA 1

1.1.2 Overview of operation control of MEA EPS 7

1.1.3 Novel MEA EPS architecture based on modular converters 10

1.1.4 Operational control problems with the novel MEA EPS 12

1.2 Research aims and objectives 16

1.3 Summary of research contributions 17

1.4 Thesis outline 18

Chapter 2 State of the Art: Operational controller design techniques 21

2.1 Control design techniques 21

2.2 Techniques for mathematical formulations 22

2.2.1 Rule-based methods 23

2.2.2 Optimization-based methods 25

2.3 Model predictive control for future status considerations 29

2.4 Hierarchical control for various dynamics 31

2.5 Techniques for uncertainty considerations 32

2.5.1 Stochastic methods 32

2.5.2 Comparison with robust methods 33
2.6 Chapter summary 34
Chapter 3 Optimal power allocation and scheduling by MILP in the distribution system 35
3.1 Introduction 35
3.1.1 Modular converter-based distribution architecture 35
3.1.2 Targets of optimal PAS with EPS reconfiguration 36
3.1.3 Contributions 37
3.1.4 MILP model 38
3.2 Optimal PAS for minimizing power losses in different flight stages 38
3.2.1 Model formulation 38
3.2.2 Objective functions 41
3.2.3 Constraints 41
3.2.4 Case study 49
3.3 Optimal PAS for generator sizing 52
3.3.1 Model formulation 52
3.3.2 PAS during flight stages with different objectives 53
3.4 Chapter summary 56
Chapter 4 Model predictive control-based ESS and load management system 57
4.1 Introduction 57
4.1.1 Main source-energy storage-load subsystem architecture 57
4.1.2 Energy storage and load management 58
4.1.3 Contributions 58
4.2 System description and MILP-MPC control 60
4.2.1 Nomenclature 60
4.2.2 System description 62
4.2.3 MILP-MPC controller framework 63
4.3 Formulation of objectives and constraints in MPC 65
4.3.1 Designing the Objective Functions 66

4.3.2 System constraints 68
4.4 Evaluation for various objectives 70
4.4.1 Model parameters 70
4.4.2 Load shedding index 71
4.4.3 Contactor status change index 72
4.4.4 Battery energy storage level index 73
4.4.5 Battery power change index 74
4.4.6 SOC target range index 75
4.4.7 Index for multi-objective problem 76
4.4.8 Discussions 77
4.5 Real-time experiment 78
4.5.1 Computational time analysis 78
4.5.2 Real-time test 80
4.6 Chapter summary 84
Chapter 5 Fault-tolerant hierarchical operational control 85
5.1 Introduction 85
5.1.1 Modular converter-based EPS architecture 85
5.1.2 Control functions 86
5.1.3 Contributions 87
5.2 EPS description and assumptions 89
5.2.1 EPS description 89
5.2.2 Assumptions 90
5.2.3 Nomenclature 91
5.3 Hierarchical framework 94
5.3.1 When online MPC is available 96
5.3.2 When online MPC is unavailable 97
5.4 HL controller design 97
5.4.1 Objective functions 97
5.4.2 Constraints 99

5.5 LL controller design 105
5.5.1 LL Mode 1: collaboration mode in EPS normal scenarios 105
5.5.2 LL Mode 2: collaboration mode in EPS faulty scenarios 107
5.5.3 LL Mode 3: independent mode in EPS normal scenarios 112
5.5.4 LL Mode 4: independent mode in EPS faulty scenarios 114
5.6 Evaluation framework design 117
5.6.1 Operation costs 117
5.6.2 Constraint violation costs 119
5.7 Case studies 120
5.7.1 Parameters 120
5.7.2 Case 1: EPS normal scenario without load fluctuations 123
5.7.3 Case 2: EPS normal scenario with load fluctuations 129
5.7.4 Case 3: EPS faulty scenario 135
5.7.5 Conclusions for the case study 145
5.8 Chapter summary 145
Chapter 6 Improved operational control with uncertainty considerations 146
6.1 Introduction 146
6.1.1 Control functions 146
6.1.2 Contributions 147
6.2 CC-SMPC framework 148
6.3 CC-SMPC formulation based on the DMPC which was proposed in Chapter 5. 149
6.3.1 Objective functions 149
6.3.2 Constraints 150
6.4 Evaluation design 154
6.5 Case studies 156
6.5.1 Simulation results for Case 1 158
6.5.2 Simulation results for Case 2 162
6.5.3 Simulation results for Case 3 168

6.6 Chapter summary 177
Chapter 7 Conclusion and Future Work 179
Appendix A : Load profiles in Section 3.3.2 184
Appendix B : Algorithms in the LL Mode 2 in Chapter 5 185
B.1 Algorithm II-A in Algorithm II in the LL Mode 2 185
B.2 Algorithm II-B in Algorithm II in the LL Mode 2 187
B.3 Algorithm II-C in Algorithm II in the LL Mode 2 188
B.4 Algorithm II-D in Algorithm II in the LL Mode 2 189
References 190

List of Publications

The findings of this thesis have been partly published in the publications listed as follows:

1. **X. Wang**, N. Bazmohammadi, J. Atkin, S. Bozhko, J. M. Guerrero, “Chance-constrained model predictive control-based operation management of more-electric aircraft using energy storage systems under uncertainty,” *J. Energy Storage*, vol. 55, p. 105629, 2022, doi: 10.1016/j.est.2022.105629
2. **X. Wang**, J. Atkin, N. Bazmohammadi, S. Bozhko, and J. M. Guerrero. "Optimal Load and Energy Management of Aircraft Microgrids Using Multi-Objective Model Predictive Control". *Sustainability*, 2021, 13, no.24, 13907, https://doi.org/10.3390/su132413907.
3. **X. Wang**, N. Bazmohammadi, J. Atkin, S. Bozhko, J. C. Vasquez, J. M. Guerrero, “Operation Management of More-Electric Aircraft Using Two-stage Stochastic Model Predictive Control,” in *Interdisciplinary Conference on Mechanics, Computers and Electrics* (*ICMECE)*, 2022.
4. **X. Wang**, Y. Gao, J. Atkin and S. Bozhko, "Neural Network based Weighting Factor Selection of MPC for Optimal Battery and Load Management in MEA," *2020 23rd International Conference on Electrical Machines and Systems (ICEMS)*, 2020, pp. 1763-1768, doi: 10.23919/ICEMS50442.2020.9290968.
5. **X. Wang**, J. Atkin, S. Bozhko and C. I. Hill, "Optimal Power Flow Based Architecture Design for Electrical Power System in More-Electric Aircraft," *IECON 2019 - 45th Annual Conference of the IEEE Industrial Electronics Society*, 2019, pp. 5814-5819, doi: 10.1109/IECON.2019.8926777.
6. **X. Wang**, J. Atkin, S. Bozhko and C. Hill, "Application of a MILP-based Algorithm for Power Flow Optimisation within More-Electric Aircraft Electrical Power Systems," *2019 21st European Conference on Power Electronics and Applications (EPE '19 ECCE Europe)*, 2019, pp. P.1-P.8, doi: 10.23919/EPE.2019.8915388.
7. **X. Wang**, J. Atkin, C. Hill and S. Bozhko, "Power Allocation and Generator Sizing Optimisation of More-Electric Aircraft On-board Electrical Power during Different Flight Stages," *2019 AIAA/IEEE Electric Aircraft Technologies Symposium (EATS)*, 2019, pp. 1-10, doi: 10.2514/6.2019-4485.

List of Abbreviations and Acronyms

AC	Alternating Current
ADT	Accessory Drive Train
APU	Auxiliary Power Unit
APUB	Auxiliary Power Unit Bus
CC	Chance-Constrained
CSD	Constant Speed Device
DC	Direct Current
DMPC	Deterministic Model Predictive Control
ECS	Environmental Control System
EPS	Electrical Power System
ESM	Energy Storage Management
ESS	Energy Storage System
FC	Fuel Cell
FSM	Finite State Machine
HL	High Level
HV	High Voltage
HVB	High Voltage Bus
HVL	High Voltage Load
LL	Low Level
LM	Load Management
LP	Linear Programming
LS	Load Shedding
LV	Low Voltage
LVB	Low Voltage Bus
LVL	Low Voltage Load

MEA	More-Electric Aircraft
MILP	Mixed-Integer Linear Programming
MINLP	Mixed-Integer Nonlinear Programming
MIQP	Mixed-Integer Quadratic Programming
MPC	Model Predictive Control
NLP	Nonlinear Programming
PAS	Power Allocation and Scheduling
PDF	Probability Distribution Function
QP	Quadratic Programming
SC/UC	Super/Ultra Capacitor
SD	Standard Deviation
SMPC	Stochastic Model Predictive Control
SOC	State of Charge
WF	Weighting Factor
WIPS	Wing Ice-Protection System

e.g.	Example given
i.e.	id est (latin, ‘that is’)

Chapter 1 Introduction

1.1 Background and motivation

Environmental issues have been the main focus in the development of all transportation systems in recent years. Among all the transportation sectors, the aircraft industry has developed the most rapidly to provide fast, safe, and most far-reaching travel in a little more than a century [1]. However, this also increases the environmental problems: the aviation industry is responsible for approximately 2.5% of global human-induced CO2 emissions. Therefore, the aircraft industry is required to develop more environmentally friendly solutions to meet the CO2 emission targets. For example, Airbus targets a 50% reduction in net aviation carbon emissions of 2005 levels by 2050 [2]. To meet these requirements, the concept of more electric aircraft (MEA) has been put forward as the main development tendency for future aircraft to make air travel more efficient and environmentally friendly.

1.1.1 Evolution of electrical power system of MEA

1.1.1.1 Development of MEA

The environmental impacts of aircraft depend on how we use energy onboard. In conventional aircraft, the power systems are composed of hydraulic, pneumatic, electrical and mechanical subsystems. These four types of power sources support different tasks during the aircraft flight, and they all derive power from the main engines in different ways. For example, the mechanical power, extracted from the engine shaft through the accessory drive train (ADT), is consumed for the accessories, such as generator, fuel and oil pumping. The pneumatic power, obtained by bleeding the compressor, is used to drive motors for the wing ice-protection systems (WIPSs) and environmental control systems (ECSs). The electrical power, generated by the main generators connected to the shaft of the engines, is used to supply avionics systems, lighting, galleys, and in-flight entertainment, while the hydraulic power drives actuators for flight-control actuators, landing gear, and auxiliary systems [3],[4]. This power integration architecture in aircraft is illustrated in Figure 1.1.

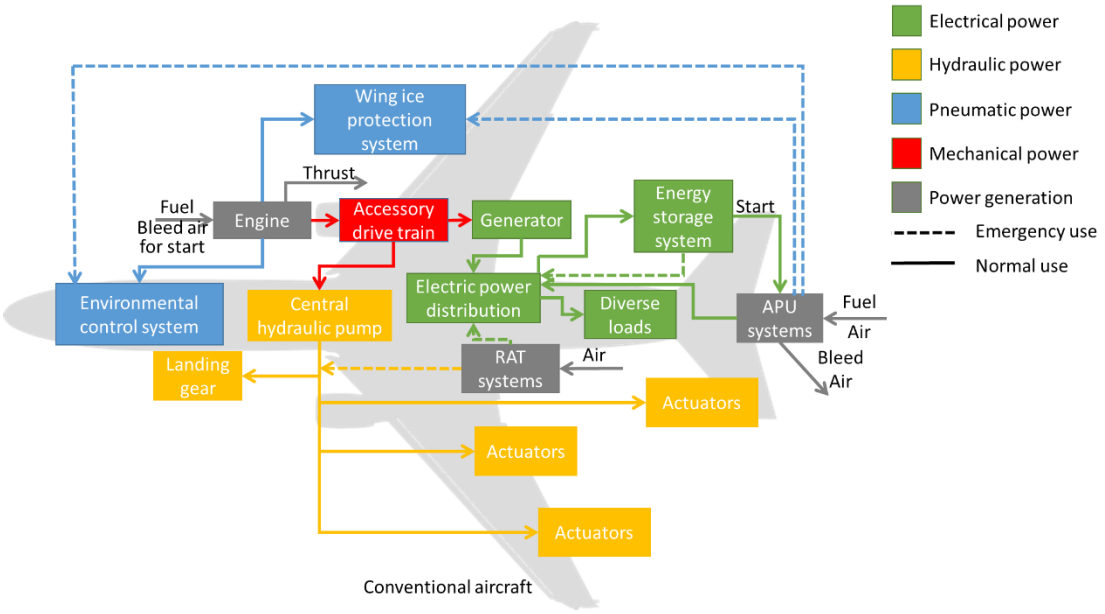


Figure 1.1 Power systems in conventional aircraft

The complicated multiple-source architecture in conventional aircraft is a design that has evolved overtime, however, when the aircraft is considered as a whole, the power system architecture causes the following drawbacks.

1) Compared to using just one power source onboard, e.g. electrical power, conventional aircraft with four power systems have less possibilities to gain better fuel efficiency and weight reductions. For example, bleed air from engines is used to supply the ECS and WIPS, while the air bled from the engine will reduce the operating efficiency of the engine. In addition, without power conversion from mechanical power to other types of power sources, the ADT could be removed from engines to other onboard accessories to reduce the aircraft overall weight.
2) Having four separate power systems on an aircraft, each subsystem is designed to be suitable for its dedicated loads and is irreplaceable in case of failure by any of the other systems. The failure of any kind of power source will affect the aircraft's operation. For example, if a leak occurs in the pneumatic or hydraulic subsystems, the flight has to be interrupted and delayed by grounding the aircraft. Moreover, it is usually difficult and time-consuming to locate and handle the pneumatic or hydraulic leak. Thus, it will be more efficient and reliable if only one type of power source is used for all subsystems, but this should be able to support all functions, providing flexibility as well as being easy to maintain.

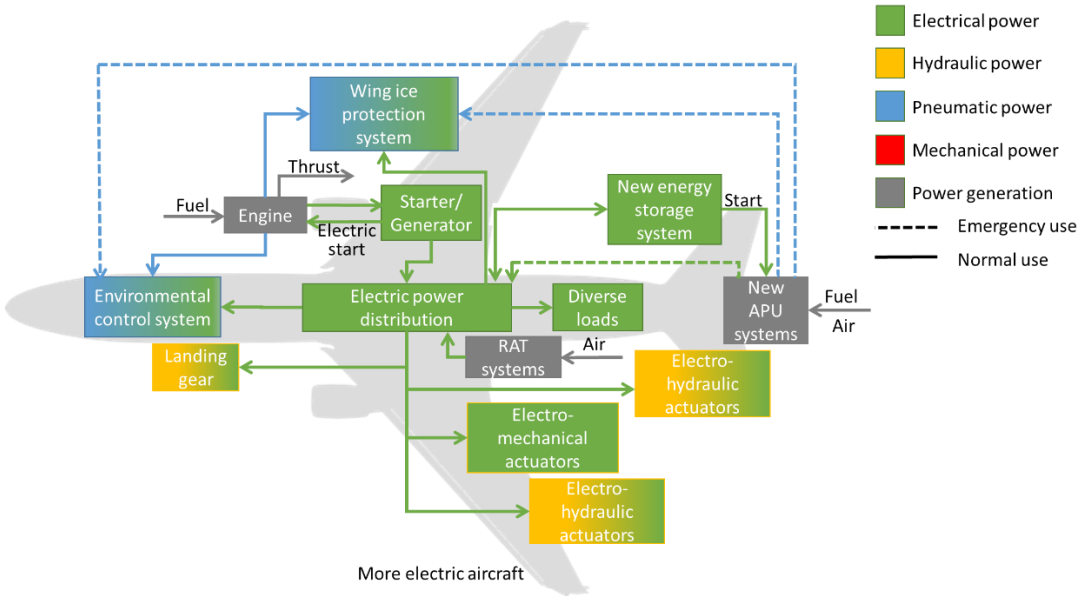


Figure 1.2 Power systems in MEA

Electrical power is the best candidate in terms of functionality, flexibility and reliability [5]. The replacement of other power subsystems by an electrical system leads to the MEA concept. In recent years, the breakthroughs in power electronics, fault-tolerant electrical machines, electro-hydrostatic/electro-mechanical actuators, and motor-drive systems, have dramatically increased the capacity of electric power with more compact volume compared to other power sources. It provides good opportunities for the development of MEA. Therefore, this concept has become a main trend for aviation [6]. Following illustrates the power systems on MEA. Compared to conventional aircraft presented in Figure 1.1, the adoption of MEA in future aircraft has tremendous benefits, such as:

1) The fuel consumption, and the environmental impact of future air travel can be reduced. For instance, the bleed air system can be removed together with the pneumatic system, which will significantly increase the engine efficiency. It is also possible to reduce the overall weight by removing the mechanical and hydraulic systems, because MEA relies on electrical power distribution, avoiding conversion to other types of power sources.
2) The flight costs include both the direct costs (fuel consumption, flight tariff, etc.) and the indirect costs linked to maintenance and availability. For example, 75% of late flights are due to system faults. The electrical system could increase the availability because it can isolate a subsystem in case of failure, and has far more flexibility for reconfigurability [7]. In contrast, a hydraulic leakage in a device leads to the isolation of the entire circuit, which provokes a “No Go” fault [8].
3) The electrical system provides the possibility of prognostics and diagnostics through the health-monitoring capacity. For example, by monitoring the equipment usage and

environmental conditions, and profiles of its failure mechanisms, the service life can be predicted so that preventative maintenance based on usage can be accomplished. In addition, the fault detection and location become easier and more accurate. For instance, reflectometry devices are able to detect and localize cabling faults within 1m of accuracy.

1.1.1.2 Development of MEA EPS

The introduction of MEA brings significant changes to the design of the overall EPS architecture, including the subsystems for power consumption, generation, distribution, and energy storage (ES). The following discusses the four main changes of the EPS, comparing MEA in Following to conventional aircraft in Figure 1.1.

1) As presented in Following, more electrical loads are used in MEA to replace the pneumatic and hydraulic loads. For example, the hydraulically powered flight control actuators are partially replaced by electrical actuators in the Airbus A380 [9], while the ECS and WIPS is driven by the electrical power rather than the pneumatic one in Boeing 787 [10]. Therefore, more electrical power is required on MEA. In addition, with different rated power and voltage, the loads are allocated to different buses. To supply the loads, the EPS requires power supply and distribution with high availability, reliability, and quality to improve flight safety and performance.
2) In MEA, the main generators driven by the engine (during the flight) and auxiliary generator (AG) driven by the auxiliary power unit (APU) (when landing on the airport) are the two main power generation units. In addition, the APU is essential to supply the EPS during emergencies. To improve the fuel efficiency at the generation side, the bleed air is removed from the turbine by replacing the bleed-air extraction system with variable frequency starter generators, which start engines electrically, such as B787. To reduce the overall weight, the constant speed device (CSD) is removed by connecting generators directly to the engine shaft, causing a variable generator output frequency decided by the speed of turbine. If constant frequency AC voltage and DC voltage is required, power converters can be applied in this configuration, such as AC/AC converters and DC link (by means of an AC/DC rectifier and a DC/AC inverter).
3) To supply distributed electrical loads with different rated voltages and frequencies, power conversions based on power electronics are increasingly applied as the development of MEA EPS. In the meantime, conventional breakers are replaced by high performance switches for high reliability, fast response time, and low maintenance, such as solid state power contactors (SSPCs) [11]. Benefited from the aforementioned power conversion and distribution techniques, novel power

distribution designs are exploited in MEA, such as novel topologies for higher reliability and less weight, novel voltage standard to reduce transmission losses, etc.

4) In conventional aircraft, energy storage systems (ESSs) play an essential role in APU start-up and powering up the necessary avionic equipment in case of emergency. As the development of ES technologies, ESSs are increasingly used in all flight stages, in addition to the aforementioned function, such as supplying peak power, maintaining constant bus voltage under dynamic conditions [12]. Among all technologies, the development of batteries, super/ultra-capacitors (SCs/UCs), and fuel cells (FCs) have attracted the most attention for aircraft applications. For example, Li-ion batteries are fast growing in terms of new research and development to replace Pb-acid and Ni-Cd batteries, because they have high energy density, no memory effect, low self-discharge and low maintenance.

1.1.1.3 Typical EPS architectures

Following the aforementioned ESP development tendency and novel technologies and devices, there are four typical EPS architectures applicable for the MEA [6], [13], [14], [15], [16], and [17]:

1) Constant frequency AC EPS (115V/400Hz AC): As presented in Figure 1.3, it consists of 115V/400Hz AC and 28V DC buses. The CSD, connecting the engine shaft and generator, is used to maintain a constant generator rotation speed, thus the frequency of power is constant 400Hz. Generally, transformer rectifier unit (TRU) is adopted to convert the AC power to 28V DC power. The high-power loads, such as galleys, fuel pumps, fans, equip cooling are directly powered by the AC bus, while the 28V DC bus powers avionics and other low power loads. In this system, batteries are only used as emergency power sources and they can power AC loads via DC/AC inverters if necessary. However, the application of CSD causes some disadvantages to the onboard EPS, such as additional weight and power loss for the mechanical power transmission. In addition, the CSD can be expensive to purchase and maintain [4].

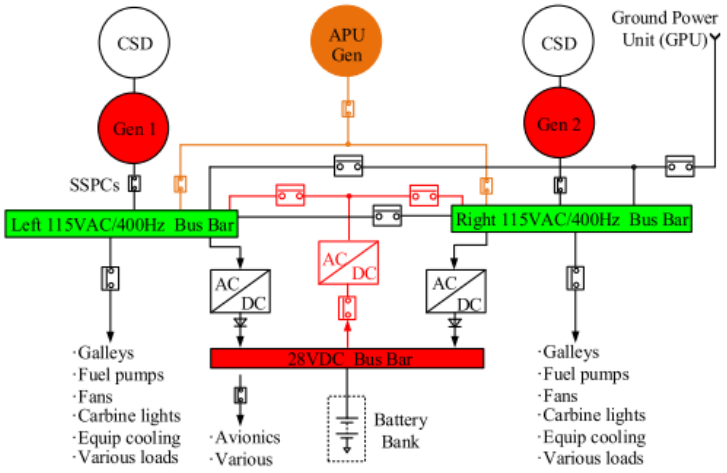


Figure 1.3 Architecture of constant frequency AC EPS [6]

2) Hybrid AC/DC EPS (115V/360-800Hz AC and 270V DC): In the architecture presented in Figure 1.4, the heavy and inefficient CSD is removed, and the generators are connected directly to the engine. The AC power frequency at the primary AC bus varies between 360Hz and 800Hz following the engine speed. The constant 400Hz AC power is obtained via AC/AC converters from primary AC buses, hence, legacy AC loads can be supplied. The 270V high-voltage DC (HVDC) is typically obtained directly by rectifying 115V AC power via an auto-TRU (ATRU). In addition, HVDC leads to the benefit of electrical system weight reduction. This architecture has been adopted in the Airbus A380.

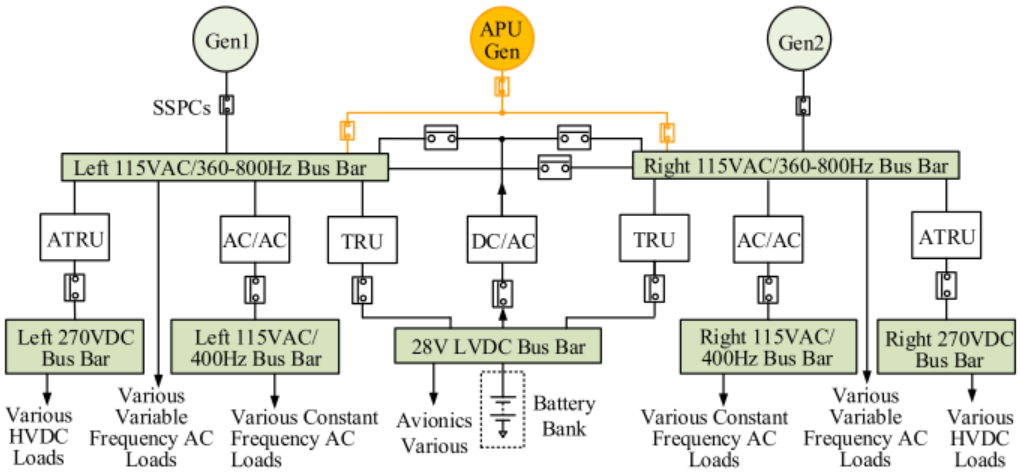


Figure 1.4 Architecture of hybrid AC/DC EPS [6]

3) Hybrid HVAC and HVDC EPS (230V/360-800Hz AC and 270V DC): this architecture is similar to the previous one, while the voltage level of the primary AC bus is higher.

The voltage level of the primary AC bus is increase to 230V. This architecture has been used in the Boeing B787.

4) HVDC EPS (±270V DC): As presented in Figure 1.5, this architecture consists of the ±270V HVDC and the 28V LVDC buses, and DC/DC converters connecting the buses are used to interface them. The 270V HVDC is popular because of less power transmission losses compared to AC system, as well as the potential weight saving by reducing the number of conductors [18]. The HVDC architecture is promising for future MEAs and has been intensively studied in major research programs such as the MOET EU project [6], the CleanSky project [19]. This study is also based on the HVDC EPS architecture.

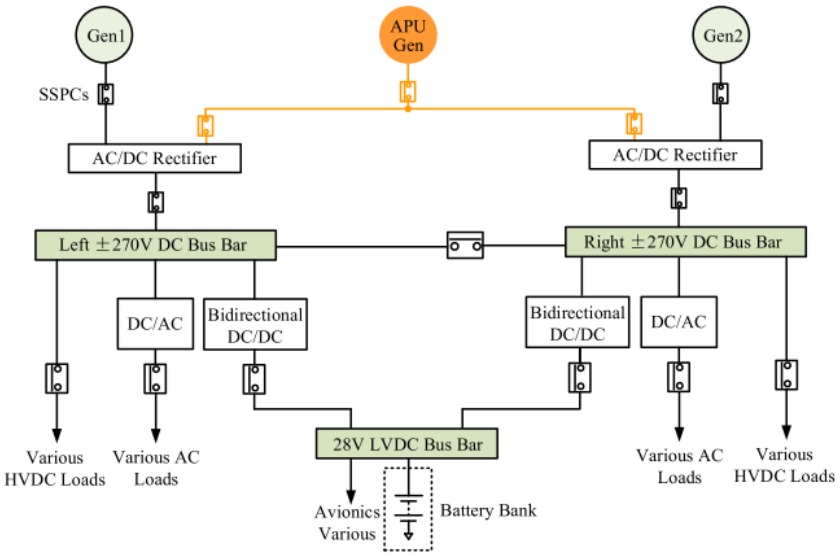


Figure 1.5 Architecture of HVDC EPS [6]

1.1.2 Overview of operation control of MEA EPS

As described in Section 1.1.1, the onboard EPS architectures becomes more complex, integrating generators, high-voltage (HV) and low-voltage (LV) buses, multiple power electronic converters, and switches for flexible power transmission, as well as energy storage systems and different types of loads with higher electrical power demands [20],[5]. In addition, the overall power onboard is significantly increased. To address the consequent environmental concerns, it is especially important to control/manage power and energy onboard in an efficient manner. To coordinate the power/energy of different subsystems and devices to complete the flight mission following the EPS real-time load, safety, efficiency, and EPS operating requirements, a system-level control based on power/energy calculations is needed, which is known as operational control.

An optimized operation control can achieve three main flight objectives. Firstly, the flight mission should be completed by supplying the loads required in different flight stages, including ground, take off, climb, cruise, descent, loiter, and landing [21]. For instance, flight actuators are supplied to control the aircraft positions in all flight stages, while landing gear is used when the aircraft is on the ground. In addition, power is needed to raise and lower the landing gear for takeoff and landing. Hence, the operational control configures the EPS and allocates power for each power source and transmission branch to provide sufficient power to the loads. When completing the flight mission, the operational control supervises the EPS to follow the safety and operating requirements, such as avoiding overload, ensuring critical loads in normal/faulty condition, higher fault tolerance, and avoiding transient issues. Finally, the operational control can provide optimized strategies to the EPS to reduce the flight cost for good EPS performances, including fuel consumptions and component wear and tear, such as energy storage systems (ESSs).

As indicated in the aforementioned flight objectives, the operational control integrates the issues of power consumption, distribution, generation and energy storage (ES) in EPS. Correspondingly, four main functions are achieved when the operational control is applied in different subsystems, as presented in Figure 1.6. When the operational control is studied for demand side, the load management (LM) problems, such as load shedding (LS), power reduction, and regenerative loads, are considered. To distribute power from sources to demand side (consumers), the operational control provides connection strategies to the contactors in both normal and faulty conditions, hence available power sources and transmission branches are adopted to maintain the power availability. In addition, power allocation and scheduling (PAS) is conducted in operational control to decide power of each power supply and transmission branch as the load power changes in all flight stages. Moreover, when ES devices are applied as power sources, the operational control for their configuration and PAS are considered as one specific problem, named energy storage management (ESM).

This section gives a brief introduction to each function and its sub-functions. The detailed introduction to the problems highly focused in this study are marked with yellow background in Figure 1.6, which are presented in the Section 1.1.4.

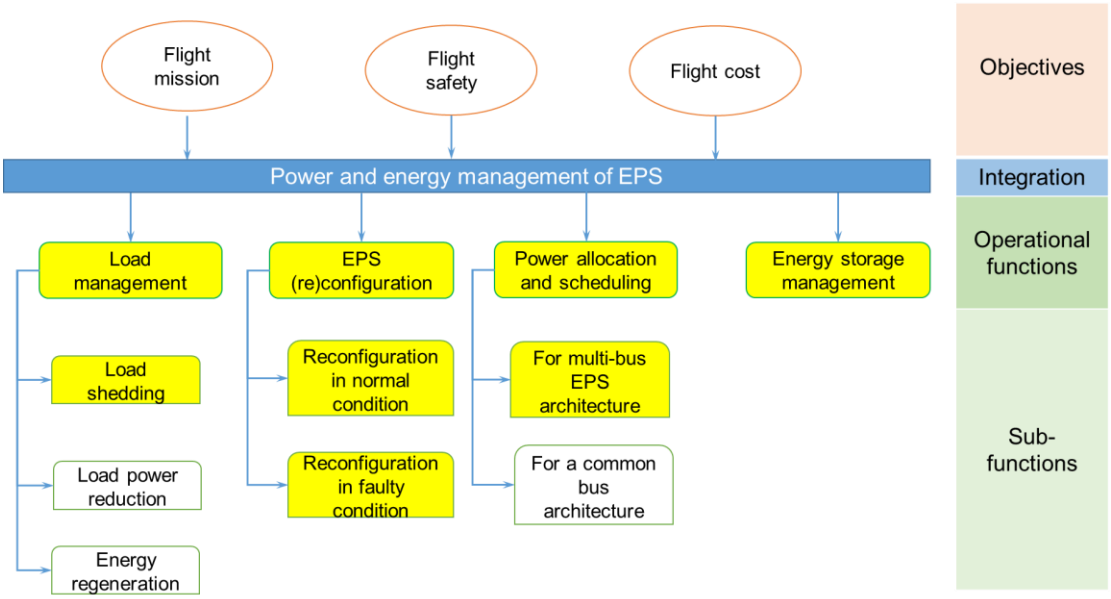


Figure 1.6 Operational control objectives and functions in EPS

1) Load management (LM)

In practice, the generated power needs to match the demanded power at every time instant to avoid grid instability, undesired high voltage fluctuations, and possible failures [22]. LM, also known as demand-side management, is therefore required to balance the supply of electricity in the grid by adjusting/controlling the power consumption rather than the power supply, aiming to reduce the total system peak load, increase load factor, and improve utilization of sources. To reduce load demands, the controller can either disconnect loads or control load power by voltage chopping, which are known as load shedding [23] and load power reduction [22], respectively. When regenerative loads are applied in MEA, such as regenerative braking [24], the EPS requires controller to manage the power/energy from these loads. The mechanism to harvest energy from loads is named energy regeneration. Although this study focuses on LS, the method proposed is applicable to other LM problems.

2) EPS (re)configuration

The EPS configuration is defined by decisions as for status of power sources (generators, APU) and connections provided by the power distribution (transmission lines, switches, interfacing converters). EPS reconfiguration is a process of changing from one configuration to another according to load demand changes or emerged failures, aiming to transfer power from the power supply to the loads [25]. In EPS normal condition, the EPS reconfiguration is required to satisfy all the loads requirements in all flight stages. While in EPS faulty condition, the EPS reconfiguration is required to ensure the flight safety related loads to guarantee the

flight safety, considering component failures such as generators, transmissions, and energy storage system (ESS).

3) Power allocation and scheduling (PAS)

Targeting reducing the EPS operation costs related to power flow, such as power losses and device efficiency, PAS is logistical planning of power flow for deciding power generation and distributing the total available power in the transmission grid to satisfy the load power demands [26], [27]. In addition to power balance and power capacity limitations, PAS is intrinsically decided by the EPS architecture and the configurations, because only the connected components can be applied in power generation/transmission. Hence, according to the EPS architecture, two types of studies are explored for the PAS problem. In [28] and [29], a common bus with parallel energy sources is studied for load sharing to improve EPS efficiency, which is one topic for PAS. In [19] and [30], PAS is studied for a EPS architecture with multiple buses, which are connected with distributed power sources and loads. In these studies, EPS (re)configuration is integrated with PAS problem, which is also the focus of this work. Although the integration of EPS (re)configuration and PAS is common, there are slight differences between these two problems. In system reconfiguration problems, the system configuration requirements and connection availability are more focused, while PAS decides power allocated in each power sources and transmission branch.

4) Energy storage management (ESM)

Electrical ESSs, based on batteries, SCs/UCs, and FCs, play an important role in improving the reliability, stability, and quality of aerospace electrical networks. In conventional aircraft EPS, batteries are commonly used as ESS, while hybrid ESSs with SCs and FSs are increasingly studied for recent MEA studies [31]. In conventional aircraft, batteries are always charged during the flight except engine starting-up stage and emergency conditions. However, with the advances of the energy storage (ES) techniques and the development of MEA architectures [32], scheduling ESSs with other power sources intelligently in all flight conditions is required to be explored for lower operation cost while guaranteeing safety.

1.1.3 Novel MEA EPS architecture based on modular converters

According to Section 1.1.2, considering the components and subsystems adopted in a studied EPS architecture, the specific operational control issues for LM, reconfiguration, PAS, and EMS are required to be discussed. In this work, a novel modular-converter-based EPS architecture is studied as shown in Figure 1.7. It consists of a 270V HVDC network and a 28V LVDC network, which are connected by multiple DC/DC power converters potentially linking any HV and LV buses by the switches. Two main generators are connected to the corresponding

HVDC buses through the rectifiers to supply the HV loads when the generators are available. In addition, there is one auxiliary power unit (APU) that can support EPS load demand with bus interconnections when any of the main generators is out of service. Modular DC/DC converter consisting of a number of cells transfer power between HV and LV sides,. On LV side, each bus is connected to an ESS comprised of one lithium-ion battery and one bidirectional DC/DC power converter, as well as several LV loads.

The benefits of this modular converter-based EPS architecture are discussed in [20]. Firstly, this benefits the aircraft with transmission redundancy, which avoids power interruption in case of cell faults. Consequently, the EPS architecture provides increased level of power availability to the loads and improved safety. Secondly, significant weight and volume benefits can be achieved since each cell is a small and modular line replaceable unit (LRU)-type unit. In addition, by intelligently utilizing the power sources and cells, such as improving their utilization ratio and EPS power efficiency, the number of cell units and the aircraft fuel consumption can be reduced. To achieve the aforementioned advantages, an optimized operational control, as introduced in Section 1.1.2, is required for EPS management to supply loads in all flight stages and normal/faulty conditions, while reducing a variety of operation costs and guaranteeing flight safety. In the following Section 1.1.4, the main control problems in literature with regards to each function are presented.

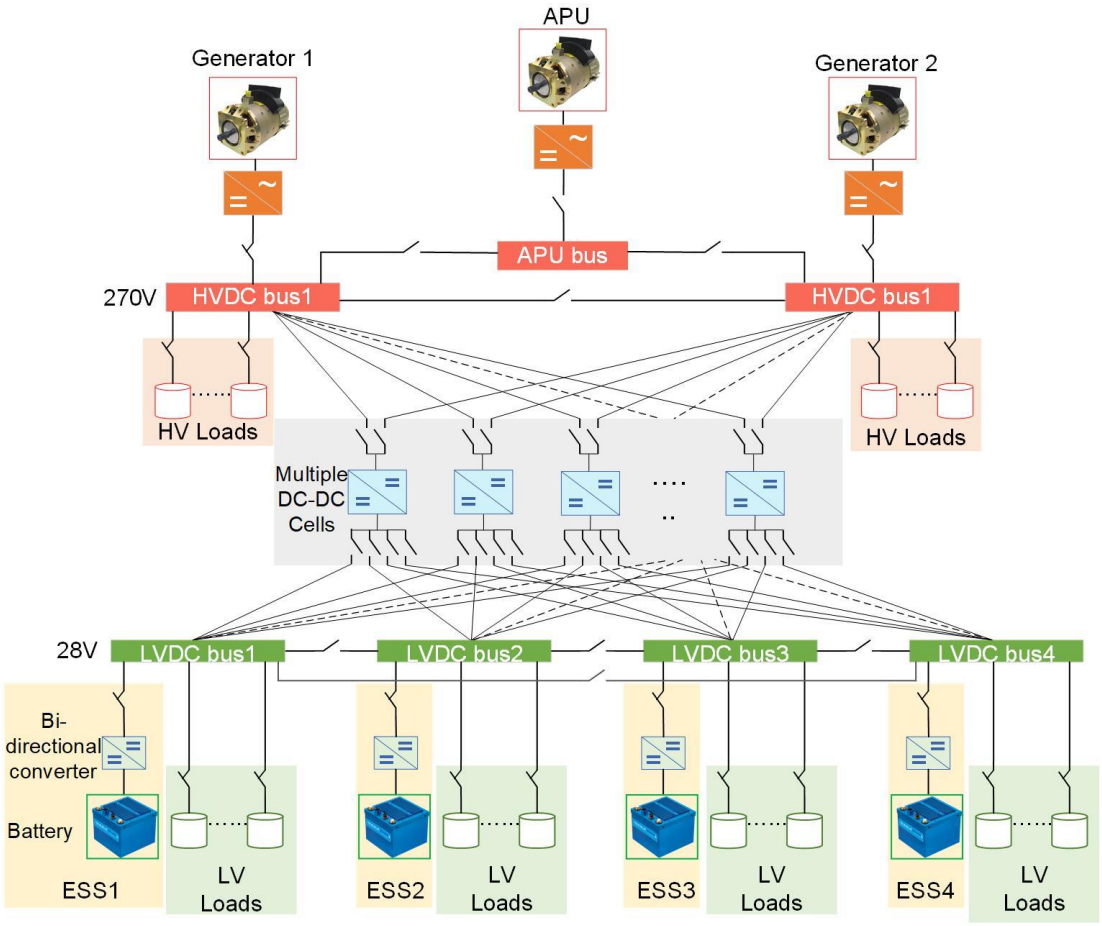


Figure 1.7 A novel flexible EPS architecture using modular power electronic converters [20]

1.1.4 Operational control problems with the novel MEA EPS

As mentioned in Section 1.1.2, different EPS architectures arise various operational control problems according to the functions of the subsystems. For the studied EPS architecture presented in Figure 1.7, four control functions require to be exploited. Firstly, different types of loads allocated in both HV and LV buses need to be supplied. Load shedding for deciding their connections is essential for operational control to avoid overload in EPS faulty conditions. Secondly, modular DC/DC converters and multiple buses increase the configuration and power scheduling flexibility in both normal and faulty conditions, which require operational control to provide reconfiguration and PAS strategies to ensure power availability. Moreover, ESSs are adopted in LV side controlled by ESM for power supply and energy reserving for EPS. To clarify the main issues in each control functions, the following subsections introduces the targets discussed in literature.

1.1.4.1 Load shedding

Motivated by grid stabilization, load shedding cuts off loads in emergencies. The state-of-the-art load shedding system uses real-time system-wide data acquisition that continually

updates a computer-based real-time system model, including power transmission, generator dynamics, updated status and actual loading of each sheddable load, and dynamic characteristics of the system loads. This system produces the optimum solution for EPS preservation by shedding only the necessary amount of load and is called intelligent load shedding [23]. To conduct load shedding strategy, the operational control determines the on/off status of load contactors, which are represented by integer control variables (i.e. 0, 1) in load shedding formulations.

For the MEA EPS, the load profile is related to flight stages. Automatic load shedding and load curtailment have to be ensured in case of power source overload and power shortage scenarios, whereas automatic reconnection of loads should be established, when enough power is available on the power source, respecting the available power and the priority levels of each load [33], [34]. Typically, each controllable load has a predefined priority, and the higher the priority of a load the less time it is preferred to be shed [30]. Fixed priority indices are commonly applied to present different load priorities, which are applied to penalize the load shedding in the objective function when optimization models are applied, such as the studies in [35], [36], [30] and [34]. However, faulty loads are not considered in the aforementioned studies, while the authors in [37] propose adaptive load priority to consider a trade-off between a high-priority faulty load and a lower-priority healthy loads.

When dealing with shedding and reconnections, there is always a trade-off between switching activities and usable generator capacity. Figure 1.8 illustrates the situation when periodical switching activities happen. The load is controlled to be shed when the power consumption exceeds some max value, while reconnection takes place when the power consumption is below min. When the load is shed in Figure 1.8, the power consumption drops below min which triggers reconnection, which consequently leads to unwanted periodical switching activities, causing EPS transient issues [38]. This can also be reduced by solving an optimization problem for minimizing the switching activities considering future status [39], or make decisions based on the memory of previous status [34].

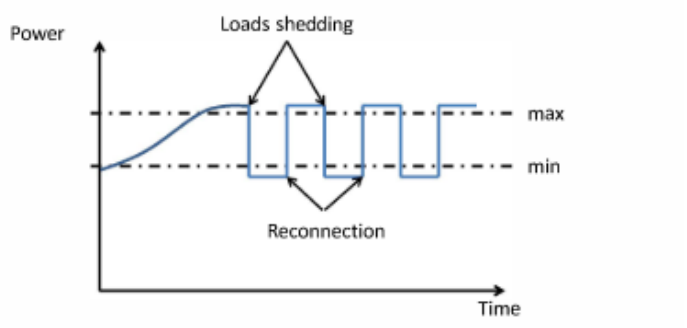


Figure 1.8 Chattering occurring if max and min power levels are too close [38]

1.1.4.2 Reconfiguration

1) In EPS normal condition

One common goal of reconfiguration of the distribution network is to find an operating structure that minimizes the power losses in the distribution system. This optimization problem is subjected to a group of operation constraints, such as power balance for each bus, power capacity of each device/cable, and connection requirements [40]. Among the constraints, power balance and power capacity constraints integrate both binary variables for configuration and continuous variables for power, ensuring the calculated configuration is applicable for supplying power from energy sources to loads because only the connected transmission paths can be used for transferring power. The constraints for connection requirements only contain the binary variables for EPS configuration, depending on the EPS architecture features and safety operation rules.

In addition to the power losses minimization, the EPS reconfiguration can be optimized targeting other operation costs, such as minimization of the number of times for reconfiguration, which indicates avoiding the transients caused by the switching activities [30]. However, this can increase the total power losses, which requires the balance between the two objectives [41].

2) In EPS faulty condition

Achieving flight safety is critical for airborne applications, therefore, when failures occur in the MEA EPS, operational control is required to provide strategies to isolate the failures, maintain the safety-related critical loads, and reduce the impact of the failures to the EPS. In section 1.1.4.1, load shedding is introduced as one strategy to cope with the power shortage scenarios which can be caused by EPS failures. Furthermore, by starting the redundant energy sources (e.g. APU) or using redundant transmission branches (e.g. bus interconnections, DC/DC cells), reconfiguring the system appropriately can ensure the critical loads being supplied and less loads are shed/reduced.

In addition to the operation constrains mentioned in EPS normal condition, the EPS faulty condition introduces further operation constraints to the control design: the fault devices are inapplicable for power generation/transmission, some configurations are only applicable in EPS faulty condition, such as bus interconnections and APU starting. Subjected to these constraints, the EPS reconfiguration in faulty condition is exploit to respond quickly to isolate the EPS fault and provide applicable configuration to improve the power availability [30], [42], and [43], while minimizing the power losses [44] and the starting up cost of the power source [45], such as APU on MEA.

1.1.4.3 Power allocation and scheduling for multi-bus EPS architecture

When the EPS configuration has been decided, PAS provides power references to each connected power source and converters, which automatically schedule the power flow through transmission cables. Optimal PAS commonly aims to reduce the power losses of the EPS or reduce the cost of power sources. For example, the fuel consumption can be considered as one cost function for a generator, which is traditionally assumed to be a quadratic function of generator output power [39], [46]. Quadratic functions can be applied for estimating the power losses of converters and cables as proposed in [47] and [48], which are considered as the cost of transmission power loss. In different applications with the author defined targets, a variety of formulations are proposed to represent the power-related cost functions for PAS. For instance, in [49], authors aim to control the main generators to save fuel in the main engines during various flight phases, therefore, they defined an optimal range for the generators, to confine the generators to work within the ranges. In the residential grid, authors formulated carbon dioxide emission cost [50] and grid pricing cost [51] as objectives, which are proposed as linear functions of output power.

PAS calculation is based on the principle of power balance, reducing power losses, and the limitations of power capacity of each device/branch when the EPS configuration is known. In addition, power transmission and generation can introduce further constraints with regard to their characteristics. In [52], voltages, phase angles and frequency requirements are formulated when PAS is studied for an AC systems. In addition, generator ramping limits are discussed for a residential grid in [53].

1.1.4.4 Energy storage management

ESSs are used to share the loads with generators, as hybrid energy sources (HESs), which requires the PAS to consider different response dynamics. On the other hand, ESSs, such as batteries and SCs, allow for both charging/discharging, hence, can be used for energy shifting, i.e. storing at times of energy surplus and releasing at times of energy deficit. When generators can provide more power than the load demands, batteries and SCs can store and keep the redundant energy for supporting higher power demands in other flight stages and in emergency scenarios. Intelligently scheduling the ESS is one target for the operational control of energy storage management (ESM).

To describe the ESSs mathematically, the dynamics of ESSs are formulated in addition to the PAS requirements. For example, the hydrogen consumption estimation equations related to fuel cell output power [54], [55], and the change of state of charge (SOC) for batteries and SCs are required to be kept within preferred operation ranges [49]. Following these limitations, researchers exploit strategies to improve the ESS applications in various aspects, such as

avoiding over charging, deep discharge, fast charge, and fast discharge [56]. In [57], the authors provide the ESS with sequential target energy references in PAS of the ESS, which leads to power losses reduction and load sharing improvement. The cost function is formulated as a quadratic equation similar to the function in terms of ESS energy. Moreover, one particular target in the ESS management is lifespan improvement for the energy storage (ES) devices. In [58], the proposed ESM keeps the depth of discharge (DOD), i.e. minimum SOC level, of the battery within certain limits to maximize the lifetime of the battery. The DOD related degradation is considered to be the capacity fade resulting from the daily minimum SOC level achieved during battery operation. In [59], the battery lifetime is considered to be impacted by battery current magnitude/variations. Hence, the battery current magnitude and variations are minimized in the cost function. To evaluate aging of a battery, state of health (SOH) is another index which has been recently used. SOH is a figure of merit that indicates the battery level of degradation, which is defined as the ratio of the maximum battery charge to its rated capacity [60], [61]. In [62], The SOH value of the battery is estimated by a current counting method using the measurable parameters of the battery, such as current and temperature.

1.2 Research aims and objectives

As discussed in Section 1.1.4, the operational control for the EPS in Figure 1.7 contains various requirements and control targets. This study aims to provide methods to design an optimized operational controller for the studied modular converter-based EPS in Figure 1.7. This controller is required to provide efficient, reliable, and robust operating strategies regarding various targets of LS, reconfiguration, PAS, and ESM issues, while satisfying all the requirements in EPS normal and faulty conditions. To this end, the following research objectives should be achieved:

- To propose a feasible MILP mathematical model for the multi converter-based power distribution system, targeting optimal PAS and reconfiguration with a group of operation constraints and nonlinear efficiency.
- To bring clearer and deeper insights into MILP based model predictive control (MPC) design for optimal ES and load management problems, considering the flexibility of MILP-MPC objective formulations and horizon selections.
- To extend the MILP-MPC method to a fault-tolerant hierarchical supervisory control of the entire EPS, considering long-term (i.e., the entire flight stages) and short-term (i.e., a sample time interval of the high-level controller) control targets.

- To consider the uncertainty of load demands in the operational control of the entire EPS in normal/faulty conditions, which requires the formulation of deterministic and probabilistic constraints in a chance-constrained stochastic MPC (CC-SMPC) model.

1.3 Summary of research contributions

Novel contributions from this work are summarized in the following points:

- This work investigates the optimal PAS and reconfiguration problem for the modular converter-based power distribution architecture, which introduces bidirectional power flow, nonlinear characteristics of modular DC/DC power converters, and flexible EPS configurations. MILP is an effective method for solving optimization problems if they can be described as mathematical MILP models – i.e. that variables are integer or continuous and both constraints and objectives are (at least mostly) linear. In this work, a solvable mathematical model in MILP is formulated for two PAS objectives when subjected to the power system operation constraints with both continuous and binary variables. In addition, linearization techniques such as piecewise functions are applied to deal with nonlinear efficiency characteristics.
- Focusing on the LM and ESSs, an MPC scheme is proposed to intelligently schedule the ESS and to exploit flexibility in the demand-side while satisfying time-varying operational requirements, such as power balance constraints and SOC requirements of ESSs. To achieve different control targets, a MILP formulation is integrated in the MPC scheme, which is designed with different objective functions. In addition, the technique of soft constraints is applied to improve the feasibility of the model. An evaluation framework is proposed to analyze the effects of various objective functions and the prediction horizon on system performance, which provides the designers and users of MEA and other complex systems with new insights into operation management problem formulation.
- Based on the studies of different operational control problems for the subsystems mentioned above, this thesis proposes a two-level hierarchical controller design for supervising the entire EPS operation in different time scales and operational scenarios (normal and multiple faulty scenarios). The high level (HL) control is based on the optimization scheme of MILP-MPC to improve the long-term EPS performance with future predictions. The long-term EPS performance here includes a variety of optimization objectives, such as reducing total power losses and generator sizing, intelligent ESM and load shedding, and reducing switching activities. To provide quick responses to short-term system changes, such as load demands and failure occurrence,

a low level (LL) control is proposed with a faster clock, reducing the violation of the EPS operational constraints caused by the short-term system changes. A group of rules are designed for this LL controller to allow it both to cooperate with HL and to operate alone in any scenario.

- In the study of MPC, EPS future prediction is one fundamental precondition, such as load demand predictions. However, real-time load demands can have disturbances, resulting in the aforementioned MPC (which is a deterministic MPC (DMPC)) model providing invalid strategies, with constraint violations. Hence, in this study, a CC-SMPC (i.e. chance-constrained stochastic MPC) method is proposed to improve both the system operation cost optimization, and the ability to cope with uncertainties due to fluctuating load demands on multiple buses. Both normal and faulty operating conditions are investigated with multi-failure cases, resulting in different uncertainty propagation paths. To verify the effectiveness of the proposed strategy, a comprehensive comparison study is conducted for comparing the performance of the proposed CC-SMPC and DMPC techniques.

1.4 Thesis outline

This thesis is structured into seven chapters, covering topics related to the operational control of the MEA EPS, taking a novel modular converter-based EPS architecture in Figure 1.7 as an example. Figure 1.9 presents the problems included in each subsystem and the research in each chapter of this thesis. To better demonstrate the control problems, this work focuses on different subsystem functions first. The PAS and reconfiguration functions for the modular DC/DC converters is firstly studied. This inspires the ESM and load shedding study for the LV side taking one ESS and LV bus as an example. Based on the studies of these subsystems, the operational control for the entire EPS is finally explored. The rest of this thesis is organized as follows.

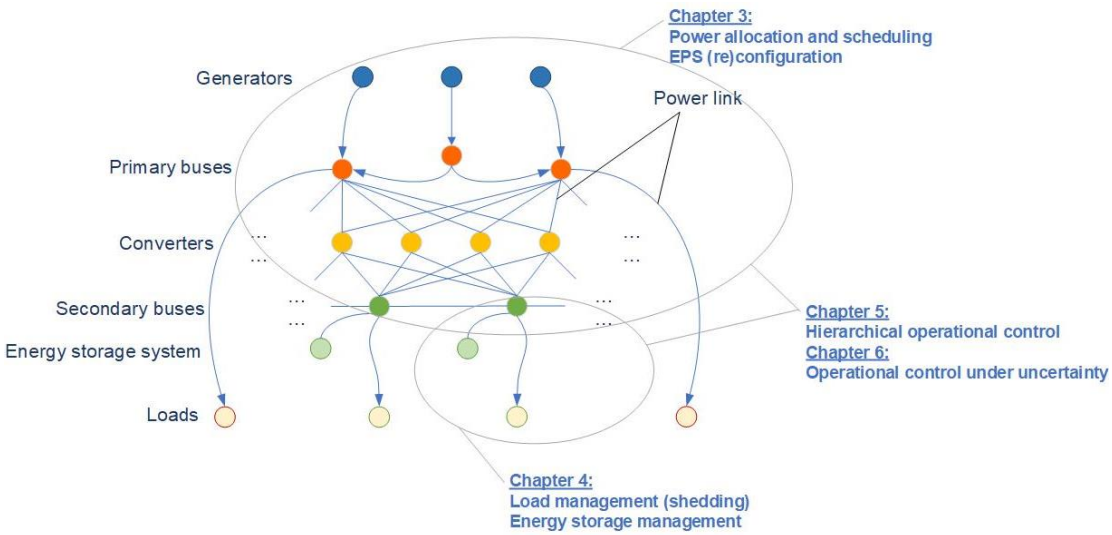


Figure 1.9 Research map of the operational control problems for the novel MEA EPS

Chapter 2 reviews the techniques for the operational control problems discussed in Section 1.1.2 and 1.1.4 (i.e. LM, EPS reconfiguration, PAS, and ESM), which are proposed to benefit the controller in different aspects, such as mathematical formulations and solution calculations, acting to future predictions, responding to EPS dynamics in different time scale, and uncertainty considerations, etc. Among all techniques, the basis of the methods adopted in this thesis include deterministic rule-based methods, MILP/MINLP, MPC, hierarchical control, and SMPC. Hence, these methods are introduced in detail and compared with other optional methods, showing both advantages and disadvantages.

In Chapter 3, the modular converter-based power distribution architecture is studied. The optimized PAS integrated with EPS reconfiguration is discussed in this section. The optimization model is firstly proposed to work out the most efficient paths to transfer the power with minimum total power losses, subject to the power system operation constraints, including power balancing and the limitations for each bus/converter, the bus/converter connection logic, the transmission losses in the cables and the nonlinear converter efficiency characteristics. Then the model is utilized for reducing each generator sizing, and the modification in the model is presented. The detailed MILP model and numerical simulation results are presented in this section.

In Chapter 4, MPC-based optimal ESM and load management is studied for a subsystem consisting of input power from HV side, ESS, and several loads on an LV bus. The proposed online control strategy aims to maintain ES and prolong the battery life cycle, while minimizing load shedding, with fewer switching activities to improve device lifetimes and to avoid unnecessary transients. Using a MILP formulation, three objective functions are proposed with various cost function terms, where each objective function can perform differently for each

control target as the horizon changes, with soft constraints improving the feasibility of the model. An evaluation framework is proposed to analyse the effects on system performance of various objective functions and of the prediction horizon. A real-time experiment is conducted with the final selection of the objective function and the length of the prediction horizon.

In Chapter 5, an intelligent two-level hierarchical supervisory control method for the entire EPS is presented. An HL controller based on MILP-MPC model is firstly formulated for the EPS for the optimization targets studied in Chapter 3 and 4. Then, a rule-based LL controller with a faster clock is designed to deal with load changes and fault occurrence over a short time during the HL sample intervals. Four control modes are designed for the LL controller, allowing the LL to work in EPS normal/faulty conditions by collaborating with the HL, as well as by deciding control sequence independently when online MPC in HL is unavailable, e.g. in case of communication failure between different control levels. The performance of each control mode is simulated and evaluated when the EPS operates in both normal/faulty conditions. Based on the evaluation results, the effectiveness and the benefits of the proposed hierarchical control are demonstrated.

In Chapter 6, a CC-SMPC method is proposed based on the MPC model formulated in Chapter 5 to improve the ability to cope with uncertainties due to fluctuating load demands. The system's operational and technical requirements are formulated as a set of deterministic and probabilistic constraints in the CC-SMPC model. To verify the effectiveness of the proposed strategy, a comparison study is conducted for comparing the performance of the proposed CC-SMPC and DMPC techniques. Three uncertainty/failure cases are taken into account and simulations are performed for both offline and online control strategies while the Monte-Carlo algorithm is used for scenario generation. The results are evaluated by the proposed evaluation framework, showing the performance improvement by adopting the proposed CC-SMPC.

To conclude the thesis, Chapter 7 summarizes the contributions and findings, and suggests potential future works to extend this research, in the area of operational control of MEA EPS.

Chapter 2 State of the Art: Operational controller design techniques

The previous chapter has presented an introduction and background to the work described in this thesis, initially introducing the problems considered in the system-level operational control. The control strategy can be concentrated on different aspects, such as mathematical formulations and solution calculations, acting on future predictions, responding to EPS dynamics in different time scales, and uncertainty considerations, etc. A variety of techniques are proposed for these aspects in dealing with the operational control problems of EPSs in literature. In this chapter, techniques adopted in the following chapters are reviewed and compared with other typical optional techniques.

2.1 Control design techniques

As introduced in Sections 1.1.2 and 1.1.4, operational control is needed to solve the issues, including load management (LM), reconfiguration, power allocation and scheduling (PAS), and energy storage management (ESM), which are proposed, with various targets and EPS operation limitations. For designing an effective control, a number of techniques are proposed, with novelties in different aspects, while four aspects are highly focused upon in this study, as presented in Figure 2.1.

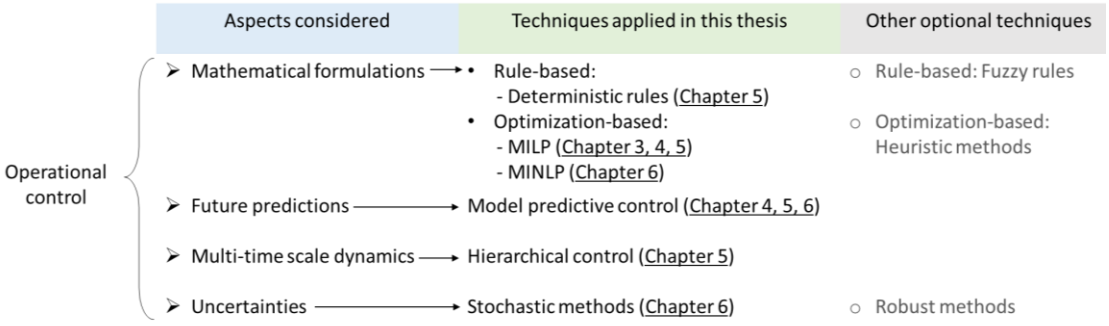


Figure 2.1 Control design techniques with the consideration of different aspects

Firstly, it is essential for operational control to mathematically model the control targets and EPS requirements, as well as to solve this model to provide operational strategies. Rule-based methods and optimization-based methods are two main types of techniques. Since rule-based methods are based on predefined logics, they cause less run-time computational burden compared to optimization-based methods (the optimization having been effectively done offline, to generate the rules), while the latter potentially provide more flexible optimization strategies,

for better performance. In this research, deterministic rule-based methods and exact optimization-based methods are applied, which are reviewed and compared with the other optional methods in Section 2.2, including fuzzy rules and heuristic optimization methods. The adopted exact optimization-based methods include mixed-integer linear programming (MILP) and mixed-integer nonlinear programming (MINLP).

Secondly, to improve the control ability for future EPS changes, researchers propose model predictive control (MPC) to make strategies based on the predicted future EPS status. Combined with the optimization techniques, MPC is studied to provide optimized control sequences for a future time period in the literature, as presented in Section 2.3. In addition, an EPS contains a variety of components and subsystems, resulting to different dynamics and requirements in multiple time scales, hence, researchers propose hierarchical control architecture as discussed in Section 2.4. These studies inspire this study when short-term responses to failures are considered in combination with the future long-term performance improvements.

Finally, uncertainty design in operational control is necessary for an onboard EPS to meet strict flight safety requirements. Stochastic methods and robust methods are studied in the literature, as discussed in Section 2.5. Based on the review and comparisons, a stochastic MPC method is finally proposed in this thesis in Chapter 6.

2.2 Techniques for mathematical formulations

If the operational problems introduced in Sections 1.1.2 and 1.1.4 (i.e. LM, reconfiguration, PAS, ESM), are formulated as a group of “if-then” logic in the controller, these techniques are known as rule-based methods, which are straightforward to apply when the designers have the knowledge of the EPS and the control rules. Rule-based methods are classified as deterministic rule-based and fuzzy ruled-based, based on the application of crisp logic or fuzzy logic. In this thesis, only deterministic rule-based methods are applied based on the review in Section 2.2.1.

Although rule-based methods are theoretically applicable with the knowledge of the EPS in any cases, it can be difficult to apply in practice when the EPS is complex with lots of rules or defining rules for optimal decisions. In this case, rather than setting up rules, the control problem can also be formulated as an optimization model containing operational constraints and objective functions, therefore an optimal control sequence can be provided to the system by solving the model with different optimization methods [63]. The optimization algorithms contain exact methods and heuristic methods. In this thesis, two exact methods, including MILP and MINLP, are applied based on the review in Section 2.2.1.2.

2.2.1 Rule-based methods

Rule-based methods consist of deterministic rule-based and fuzzy ruled-based methods. Section 2.2.1.1 introduces deterministic rule-based methods in the literature, which are adopted in this thesis in Chapter 4 as low-level control in the proposed hierarchical control framework. Then in Section 2.2.1.2, fuzzy rule-based methods are briefly introduced, and the comparisons of the two methods are presented.

2.2.1.1 Deterministic rule-based

The deterministic rule-based controllers operate on a set of rules that have been defined by human expertise, and implemented prior to actual operation [64], for example, [65] proposes a rule-based power distribution strategy to schedule the power among hybrid power sources by selecting different predefined modes according to the "if-then" conditions. To cope with the reconfiguration in the EPS design stage of MEA, research in [66] builds up the rules as an expert system to provide several reconfiguration solutions to different failure scenarios. In [19], a rule-based energy management controller is proposed for an aircraft power distribution system, which integrates power allocation and scheduling (PAS), energy storage management (ESM), reconfiguration, and energy regeneration. The proposed strategy is formulated by safety and reliability rules considering the potential for eliminating the 5 min overload capability of the generators. The following diagram in [33] presents an example of the rule-based load management algorithm for aircraft.

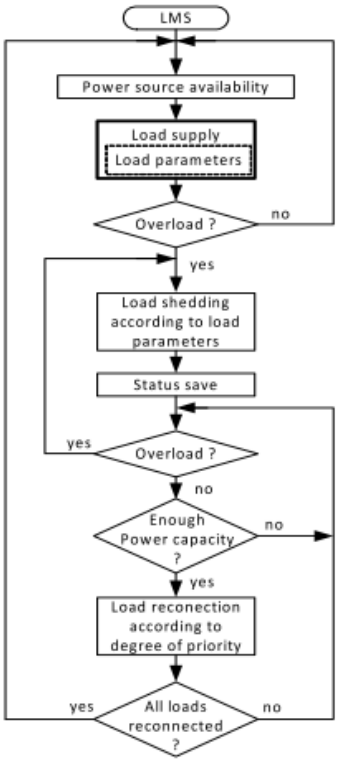


Figure 2.2 Rule-based algorithm for load management [33]

Compared to direct application of the "if-then" rules, finite state machine (FSM) transfers between different states with sequential logic. [70] proposes an energy management strategy based on the FSM to apply the predefined rules for hybrid energy sources on a single bus of vehicles, and Figure 2.3 presents the diagram with the state transfer. The system working mode is divided into 9 states (S1-S9), aiming for deciding the power of the battery (P_b) and the fuel cell system (P_{fc}). The transition conditions are formulated by comparing the decision variables (P_b and P_{fc}) with the power limitations ($P_{fc.\max}$) and the power demand (P_m), as well as the comparison of the battery SOC (z_b) to its limitation (z_{b*}). In [67], [68], and [69], the authors compile the rules in a FSM for the power distribution management of aircraft ESP to decide load shedding and charging batteries. In these studies, several sets of safety rules are defined to cope with different failure cases to ensure uninterrupted power supply to the high-priority loads. However, this method relies on accurate measurements to change the operational state and it is hard to integrate multiple operating goals. In addition, setting optimal rules by hand can be difficult for complex systems because of the large number of system states.

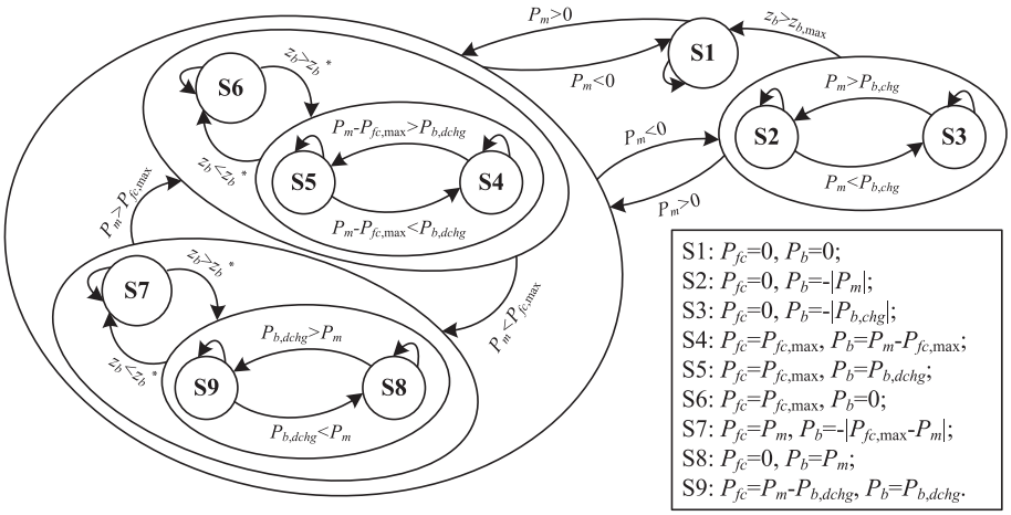


Figure 2.3 Rule-based energy management for battery/fuel cell system with finite state machine [70]

2.2.1.2 Comparison with fuzzy rule-based methods

In deterministic rule-based algorithms, the crisp logic is applied in which a proposition is either true or false (1 or 0). In contrast, fuzzy rule-based algorithms apply fuzzy logic in which propositions are presented with degrees of truthfulness or falsehood, i.e., fuzzy logic uses a continuous range of truth values from 0 to 1 [71]. The conventional fuzzy system requires expert knowledge of the process operation for the parameter setting, and the controller can be only as good as the expertise involved in the design [72]. To avoid the inadequacy in applications with fixed parameters, adaptive fuzzy controllers are proposed to generate and modify the control protocol by a learning process based on measuring performance [73].

Conventional fuzzy rule-based methods have been applied for onboard ESM and PAS problems for a common bus in [74] and [75], and load management in [37]. In [76] and [77], an adaptive fuzzy rule-based mechanism is developed to validate the integrity of the critical data for the power/energy control of an emergency power system of MEA and detect potential cyber-attacks.

Table 2.1 presents the advantages and disadvantages when comparing deterministic rule-based methods to fuzzy rule-based methods. Based on the application requirements in this research, deterministic rule-based methods are adopted as low-level control in the proposed hierarchical control framework, to collaborate with high-level optimization-based control. The proposed deterministic rule-based methods and the hierarchical control framework are introduced in detail in Chapter 5.

Table 2.1 Comparison of deterministic and fuzzy rule-based methods

Methods	Deterministic rule-based	Fuzzy rule-based
Advantages	1. Less design complexity, especially when the EPS is complex with multiple decision variables 2. More straightforward to collaborate with other controllers, such as optimization-based control 3. Less computational complexity	1. More tolerant to imprecise measurements and variations 2. Require less expert knowledge for adaptive fuzzy methods
Disadvantages	1. Less tolerant to imprecise measurements and variations 2. Require complete expert knowledge	1. Additional design complexity, such as fuzzification and defuzzification, therefore less adopted when the EPS is complex with multiple decision variables 2. Not common to collaborate with optimization-based control 3. More computational complexity

2.2.2 Optimization-based methods

Exact methods and heuristic methods are two classifications of optimization techniques. The exact methods formulate the objectives and constraints by linear programming (LP), MILP, MINLP, and etc., which are solved for global optimal solutions. However, exact methods are feasible only when the model is convex with limited nonlinearity, such as quadratic functions. In contrast, heuristic methods rely on random searching, which are applicable when the exact methods are infeasible, such as genetic algorithms, Tabu search, etc.

2.2.2.1 Exact methods

Exact optimization method takes advantage of the analytical properties of the problem to generate a sequence of points that converge to a global optimal solution [78]. These methods benefit from a variety of commercial optimization solvers, such as CPLEX, Gurobi, Xpress, etc, to effectively provide reliable solutions to the power system problems [79], [80]. The following subsections introduce the applications of MILP and MINLP, which are the highlighted methods in this research.

1) Mixed-integer linear programming

LP-based techniques are used to linearize nonlinear power system optimization problems so that objective functions and constraints in these problems have linear forms [81]. LP has been widely used in various engineering disciplines, such as flow control and power management, because it provides a guaranteed solution to a well-formulated problem, and it is possible to solve a large-scale problem in a reasonable time [82],[83]. In the 1990s, M. Mangoli et al. applied an LP formulation for both active and reactive power optimization modules, utilizing the revised simplex method [84]. In [85], LP is used for the optimization of operating cost for a single-phase high-frequency AC microgrid with distributed energy sources.

The LP only contains continuous variables such as power/energy and SOC. In real applications, binary/integer variables are often required, to present connection or on/off activities in the EPS, such as load shedding, generator starting, etc. To decide these integer variables, MILP techniques are proposed. Compared to LP, MILP involves problems in which only some of the variables, are constrained to be integers, while other variables are allowed to be non-integers. In addition, all of the constraints and objective functions are formulated as linear functions. Similar to LP, the MILP output is predictable, being mathematically calculated, and can be used for both stability and reliability studies, thanks to its strong mathematical formulation; this is a great advantage for aeronautical applications [86]. Hence, MILP techniques are adopted in various EPS optimization problems for simultaneously providing decisions of EPS configurations, load connections, and power/energy flow.

A MILP-based dynamic load balancing for civil aircraft is proposed in [87], to reduce the peak currents of the power feeder and to minimize the return current. To solve the problem within a limited time, i.e. 10ms, this study proposes to add a break condition and reduce the number of loads by defining a threshold for the load level. In [30], the authors formulate the EPS connectivity, safety and performance requirements in terms of MILP constraints, which are combined with the MPC framework. The proposed method optimizes the number of generators used, load shedding, battery usage, and switching activities in the presence of one generator fault. The load management of the aircraft EPS is also studied in [86] with a MILP

formulation for the constraints of voltage and power. In this study, to overcome the quadratic problem formulation when the grid is expressed in terms of the conductance matrix, the authors propose to express the voltage limits in terms of power, giving a homogeneous formulation to the problem. The authors of [88] introduce MILP methods for optimal PAS and unit commitment for diesel-electric marine vessels to reduce the power, starts/stops and running hours of gensets. To reduce the computational burden, [89] proposes a MILP model for fuel reduction of the powertrain on a hybrid electric vehicle, which is relaxed to a LP, and devises an iterative algorithm for rapid computation. MILP has also been widely used in various optimization problems for residential EPSs. For example, it has been applied to schedule the thermal generators in [90] and [80], and cope with optimal power flow calculation for real-time control in [91] and [92]. In [93], the MILP is compared and aided the fuzzy logic methods for the ESM and PAS problems.

2) Mixed-integer nonlinear programming

In some cases, nonlinear functions are required to describe the EPS. As introduced in Section 1.1.4, quadratic functions are applied for modelling the cost functions, such as fuel consumption and transmission power losses. Nonlinear programming (NLP)-based techniques are applied to handle power systems operation problems with nonlinear objective and constraint functions. Quadratic programming (QP) is the most commonly used form of NLP in real applications, where the objective function of the QP model is quadratic, and the constraints are in a linear form. In [94], a QP-based method is proposed for optimal ES management and power allocation strategies, and optimal flight paths for the fuel cell-powered hybrid unmanned aerial vehicles (UAV). To minimize fuel consumption for hybrid electric aircraft (HEA), the study in [95] uses QP to formulate the system subject to the constraints of the ESS, electric motors, and gas turbines.

The aforementioned NLP and QP based methods only contain continuous variables. Considering both continuous and integer variables, such as the power allocation and EPS connectivity decisions respectivly, MINLP and mixed-integer quadratic programming (MIQP) are introduced. Compared to other NLP and MINLP models, QP and MIQP models have less computational complexity. Some solvers, such as CPLEX, Gurobi, can solve QP and MIQP problems as long as they have the right kind of structure. In [49], the cost for the generators in PAS is proposed as a quadratic function to confine the generators to work within a preferred range. Considering the connection of three HVDC buses, the optimal PAS is formulated as a MIQP and is solved by Gurobi solver. An AC/DC hybrid EPS system with multiple buses is studied in [21] and [96], which aims to reduce the costs of fuel burn and energy storage (ES), both being formulated as quadratic functions considering the bus interconnections. To reduce

the computational complexity, Lagrangian relaxation and sub-gradient methods are applied to distribute the PAS into four QP problems in the corresponding subsystems, resulting in a computation time reduction of 95% compared to the conventional centralized MIQP method. Targeting appropriately selecting the operation modes of a DC microgrid with renewable energy sources and the ESS, a MIQP method is proposed in [97] to minimize the perturbation of the small signal branch current and the operation cost.

2.2.2.2 Comparison with heuristic methods

Due to the complexity of the EPS operation problems, accurate formulation of the system characteristics, such as battery degradation, generator efficiency curves, transmission losses, combined switching decisions, etc., leads to the highly non-linear and non-convex optimization model, for which the exact methods become less applicable or infeasible. In these cases, heuristic algorithms based on random search mechanisms can potentially be applied to obtain good (i.e. near-optimal) solutions at a reasonable computation cost without being able to guarantee optimality [98]. Heuristic algorithms include evolutionary-based algorithms (e.g. genetic algorithms), swarm-based algorithms (e.g. particle swarm optimization), and Tabu search [99]. In [100] and [101], the operational control of the MEA EPS is solved by genetic algorithms aiming to improve the efficiency of the generators and converters with nonlinear cost functions. The power allocation and scheduling for hybrid onboard energy sources is solved by particle swarm optimization in [102] and [54] to minimize hydrogen consumption. Residential distribution systems are reconfigured by Tabu search in [25], [103], [104] to reduce power losses.

Table 2.2 compares the advantages and disadvantages of exact and heuristic optimization algorithms. In most practical applications, exact optimization-based methods are adopted when the problem can be formulated in a solvable model, therefore it is unnecessary to resort to heuristic methods. In this thesis, two exact optimization methods are adopted . Based on the problems formulated, MILP is adopted in Chapter 3-Chapter 5, while MIQP is adopted in Chapter 6 when uncertainties are studied.

Table 2.2 Comparison of exact and heuristic optimization methods

Methods	Exact	Heuristic
Advantages	1. Guarantee the global optimality 2. Commercial solvers give solutions efficiently with high accuracy 3. A benchmark to verify the performance of the heuristic methods	1. Fewer limitations in mathematical formulization of control problems 2. Better ability to cope with nonlinear and nonconvex problems 3. Pareto optimality for multi-objective functions
Disadvantages	1. Often highly reliant on the structure of the mathematical formulization of the problem - e.g. some methods have limited ability to cope with nonlinear and nonconvex problems, some rely on being able to decompose the problem into stages, or to be able to quickly eliminate/prune infeasible areas of the search space.	1. The global optimality cannot be guaranteed 2. Additional verifications of the performance is needed 3. Computation time cannot be foreseen

2.3 Model predictive control for future status considerations

Instead of solving the optimization problem for a single time step, model predictive control (MPC), also named receding horizon control, computes the optimization problem over a future time horizon to optimize forecasts of behavior [105]. This leads to the system acting in advance to (predicted) future system changes, thereby avoiding operating based on the worst-case scenarios, with potentially high costs. The inherent feedback mechanism of MPC, stemming from its receding horizon mechanism, makes the system more resilient to predictable future changes [39].

In the application for MEA, on the one hand, the robustness of controller design can benefit from the intrinsic robust characteristics of MPC due to the rolling horizon strategy. On the other hand, the system operational and time-coupling constraints can be integrated into the MPC model. As mentioned in Section 2.2.2.1, [30] integrates the MILP model with the MPC framework for optimal PAS and load management of aircraft EPS, which reduces the switching of the APU and loads when generator faults occur, based on EPS prediction of loads and ESS dynamics. In [106], a stochastic MPC method is proposed based on the MILP model in [30], with the consideration of load demand and connection fault uncertainty. When the quadratic cost functions are proposed for generators, MIQP models are adopted into MPC in [107] and

[21], while [21] reduces the computation complexity by introducing adaptive horizons. In [108], a QP based MPC model is proposed, to reduce fuel consumption considering electrical and mechanical powertrain losses and constraints on the battery, electric motor and gas turbine for a HEA. Rather than solving a MIQP model by exact methods in MPC controller for one objective function, [100] and [101] apply NSGA-II (Non-dominated Sorting Genetic Algorithm II) to calculate the Pareto optimum of the EPS level efficiency with multi-objectives, while considering generator and transmission cable faults. In [57], a hierarchical MPC framework for a hybrid propulsion system is presented to minimize the power generation costs and delivery losses, decoupling the slow energy management from dynamic power management in a holistic optimized manner, which is implemented on heterogeneous real-time computing hardware. However, the possibility of load shedding and system failure is not considered. With regard to different time scale and design entities of different subsystems, [109] proposes a distributed MPC to exploit the differing rates of the control updates of the engine and power subsystem controllers while preserving subsystem privacy, which matches the performance of a fully centralized MPC.

The benefits of MPC also inspire its application in the EPS of EV and residential grids. In [110] and [111], the NLP-based MPC controller attempts to minimize the vehicle equivalent fuel consumption and the battery capacity fade at the same time. To enhance the battery lifespan and power performance, [112] and [113] propose a QP-based MPC approach to reduce the battery power variation and maintain supercapacitors' SOC at their desired values. In [58], MILP-MPC is proposed to supervise a rule-based controller for optimizing a household energy cost by scheduling load power and ESS, which considers battery degradation. In [114], [115], MILP-MPC is applied for achieving economic efficiency in residential microgrids. In [114], the quadratic cost function of fuel consumption is linearly approximated, while in [115], a hierarchical MPC architecture is applied to coordinate a group of microgrids.

In this thesis, MPC is adopted in Chapter 4, Chapter 5, and Chapter 6. In Chapter 4, when ESS and load management are studied, MPC is introduced to provide optimal decisions considering future energy and load power predictions, and the improved performance compared to instantaneous framework is studied. Based on the conclusions in Chapter 4, in Chapter 5, MPC is adopted in the HL optimization for the entire EPS operation with multi-objectives. In Chapter 6, the MPC model proposed in Chapter 5 is combined with chance constraints to cope with uncertainties.

2.4 Hierarchical control for various dynamics

To cope with the control targets in different time scales and deal with computational complexity appropriately, hierarchical control architecture is commonly used, which consists of controllers in different levels, and in each level, different control techniques can be adopted [116]. In this thesis, a hierarchical control architecture is proposed in Chapter 5 to improve the long-term performance and quick responses to short-term power/faulty changes, which is inspired by the following studies.

In [117], [118], and [14], a two-level fuzzy rule-based supervisory controller is designed for embedded EPS, with the first level to determine the total required power, while the second level has to minimize the dissipated power and compensate for the slower dynamic behavior of the storage system. Considering the load operative mode and health level of MEA, a three-level hierarchical fuzzy rule-based method is studied in [37] for fault-tolerant load management, which consists of a task level, an optimization level, and a detection level. In [57], for the aircraft EPS supplying loads with hybrid power sources, the authors propose a hierarchical MPC framework with two levels to reduce long-term energy costs and the transients for voltage regulation and current following. In [30] and [106], the authors assume a rule-based low-level (LL) controller to collaborate with a high-level (HL) MPC controller for MEA EPS, without introducing the details of the LL controller design. For an HEV EPS, a two-level MPC method is proposed to overcome the computation burden in [119]. The HL MPC computes the travel time and battery energy for the entire route by using an abstracted powertrain model, while the LL computes the optimal control for a short horizon following the target sets from HL.

In residential microgrids, the hierarchical operational control can be used both in multiple cooperative microgrids as well as within a single microgrid. Loads and ESS are managed for a household EPS in [58] and in [120] with renewable generation, which introduce a hierarchical two-layer control to reduce daily household energy costs with the upper layer using MPC and the lower layer comprises a rule-based real-time controller, compensating for the effects of forecast uncertainties and sample time resolution. In [51], a 4-level MIQP-MPC controller is designed, coping with the time scale from long-term, medium-term, short-term, and very short-time, to reduce the operational cost and ESSs degradation for a microgrid, in which the ESS is scheduled to start-up/shut-down with power scheduling. For an isolated microgrid with renewable energy, energy storage, and interruptible loads, [121] proposes a two-stage MILP based robust MPC controller, which solves the unit commitment in the first stage and solves the final power dispatch commands in the second stage.

2.5 Techniques for uncertainty considerations

Without considering the uncertainty during the sample intervals and future predictions, the deterministic operational control, such as deterministic MPC (DMPC), can provide ineffective strategies to the EPS, resulting to violations of EPS operation requirements and safety limitations. Hence, stochastic and robust methods are proposed to model the EPS uncertainty, which can be combined with the aforementioned techniques. Both methods are reviewed and compared in the following subsections.

2.5.1 Stochastic methods

Rather than estimating the worst-case scenario, the uncertain parameters are modeled by probability density functions (PDFs) and are coped with by different stochastic strategies [122]. In these strategies, loads are commonly modeled as a Gaussian PDF, the wind speed of a wind turbine is commonly modeled as a Weibull PDF, the generated power of a PV generator is commonly modeled by Beta distribution [123], and failures can be modeled by a Bernoulli distribution [124], [125] or uniform distribution [126]. Chance constrained (CC) methods and scenario-based methods are two typical stochastic programming methods for modeling optimization problems with uncertainties. When stochastic programming is integrated with MPC, it is also known as stochastic MPC (SMPC), which is increasingly studied nowadays in the studies of optimal operational control of EPS under uncertainties [127].

In [30], when DMPC is applied for optimal load management of an aircraft power distribution system, the uncertainty in load demand leads to poor performance of the DMPC due to imprecise load predictions. Therefore, the authors in [106] propose a chance-constrained stochastic MPC (CC-SMPC) method, solved by MILP, to optimize the same onboard load management problem, considering the load demand uncertainty and contactor failures. Day-ahead scheduling is studied in [128] and [129] for residential microgrids, considering forecast errors of renewable energy resources as well as load demand. In [128] a CC-based strategy, solved by MIQP, is proposed for reconfigurable microgrids, which models the probability constraints of islanding capability, aiming to reduce the costs of fuel, reliability, purchasing power, and switching. In [129], a hierarchical chance-constrained strategy solved by MILP is proposed for ESM and PAS, considering the degradation cost of energy storage elements. Focusing on the unit commitment problem, the chance constraint is used to restrict the probability of load imbalance in [130], where the authors propose a bilinear MILP formulation method for CC-SMPC to reduce the computational complexity for large-scale systems. Without configuration decisions, CC-SMPC solved by QP is applied for the coordinated energy management of terrestrial multi-microgrids for ESM and PAS in [131] by a distributed

framework and in [132] by centralized framework, while different distribution characteristics of uncertainty sources are considered in [131].

Rather than directly formulating uncertainty with chance constraints, some studies solve the optimization problem for a number of predefined uncertain scenarios at each time step, which is known as scenario-based stochastic optimization [133]. When combined with MPC, the MPC model is solved for all scenarios at each time step, which is known as scenario-based SMPC. This method is applied for operational scheduling and hourly reconfiguration of distribution systems of residential grids in [134], and for energy management of ESS and distributed energy sources in [135], [136], and [137]. Moreover, in [138], a scenario-based SMPC strategy is proposed for coordinated engine and power management of MEA. Compared to CC-SMPC, scenario-based SMPC methods heavily rely on the selection of predefined uncertain scenarios at each time step. More scenarios normally indicate better representations of uncertainties; however, this can result in a dramatic increase in the computational time for large-scale systems or systems that contain a large number of decision variables.

2.5.2 Comparison with robust methods

Robust optimization (RO) was relatively recently introduced as a method to incorporate uncertainty into mathematical programming models (Ben-Tal et al., 2009). By the very nature of the methodology, robust optimal solutions are highly conservative, aiming to hedge against all possible worst-case realizations of the uncertainty [141]. It essentially targets finding the decision variables that would maximize the minimum possible objective function value under uncertainties. For the PAS and ESM of a fuel cell/ ultra-capacitor HEV, a RO-based EMS solved by PSO is studied in [142] to improve fuel economy, FC system slow dynamics, and solutions' robustness under uncertainty parameters such as the propulsion demanded power. In [143], power exchanges between distribution systems and networked microgrids are formulated using two-stage robust optimization in a decentralized framework to address the uncertainties of renewables and load demands.

Table 2.3 Comparison of probabilistic and robust methods

Methods	Probabilistic	Robust
Advantages	1. Better cost-risk trade-offs 2. Better approximation to real probabilistic distributions	1. Less nonlinearity in the model 2. Ability to cope with the scenarios when probabilistic distributions are unknown
Disadvantages	1. Computation complexity with more nonlinearity in the model	1. Highly conservative

Table 2.3 compares the advantages and disadvantages of probabilistic and robust methods. In Chapter 6, uncertainties in both HV and LV sides are considered as Gaussian distributions when adopting CC-SMPC.

2.6 Chapter summary

This chapter firstly introduced four aspects focused on the operational control design, including mathematical formulations and solution calculations, acting according to future predictions, responding to EPS dynamics in different time scales, and uncertainty considerations, which are studied in the following chapters. After that, the techniques adopted in the following chapters are reviewed and compared with other typical optional techniques, which provides a deep insight into developing operational control with different techniques, referring to their advantages and applications in literature. In addition, from this literature review, it is found that there are few studies considering applications in airborne EPSs. This research gap is filled in this thesis.

Chapter 3 Optimal power allocation and scheduling by MILP in the distribution system

In this chapter, the optimal power allocation and scheduling (PAS) is studied for a modular converter-based EPS distribution system for two vital targets: routing the power in the system with less transmission losses; and reducing the generator sizing by minimizing the required overload capabilities for lighter main generators. The PAS is initially integrated with reconfiguration of the studied EPS, which introduces constraints and objective functions with both continuous and binary decision variables. By linearizing the nonlinear transmission efficiencies, using piecewise-linear functions, the proposed MILP model can be formulated and solved efficient by MILP solvers, which provides optimal solutions for both PAS and reconfiguration simultaneously.

3.1 Introduction

3.1.1 Modular converter-based distribution architecture

In Section 1.1.3, the EPS architecture with modular power converters is introduced. In this chapter, power transmission from generators/APU to loads is studied with a simplified case presented in Figure 3.1, which is comprised of four 28V LVDC buses, two 270V HVDC buses, and one APU bus. The main generators/auxiliary generator power the HV buses, and a group of HV loads, via AC/DC rectifiers. The LV buses are connected with the HV buses through bidirectional DC/DC power converters (named cells), which supply LV loads. In this chapter, the modular DC/DC converters are assumed to consist of eight cells, giving an example of PAS formulation for this type of architecture. Each cell is rated at 3kW. In addition, the energy storage system and load shedding are not investigated, but these will be discussed in Chapter 4.

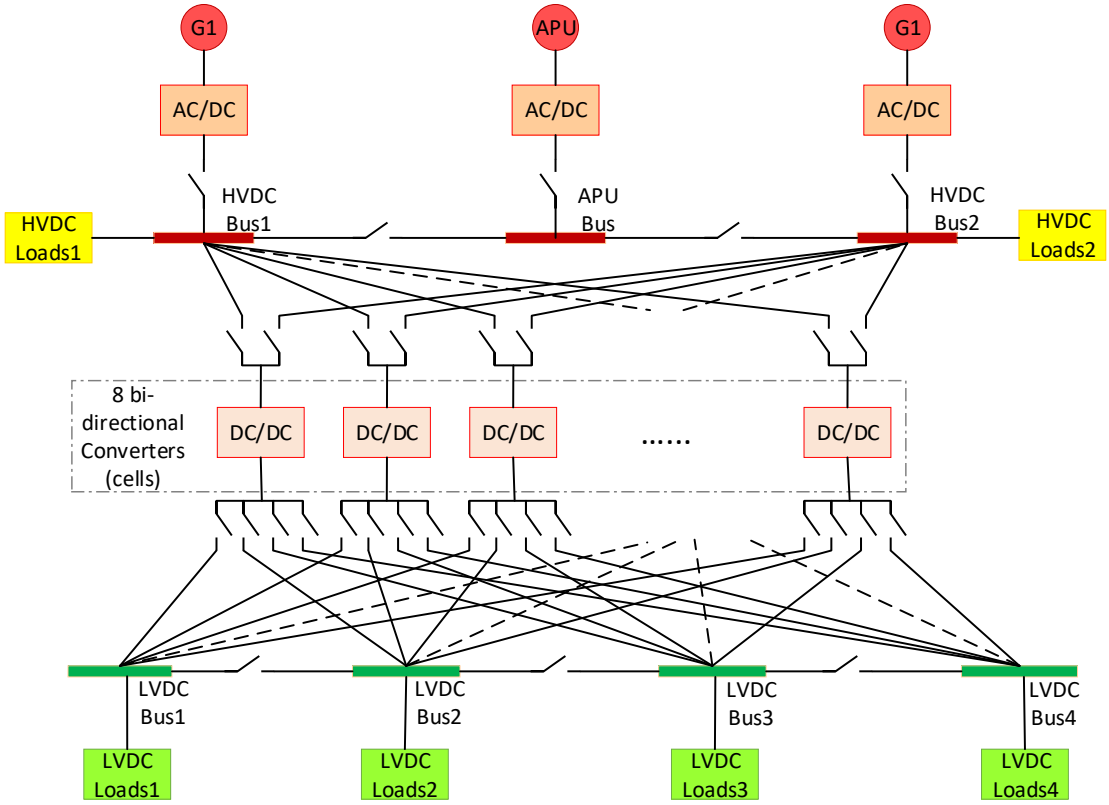


Figure 3.1 Modular converter-based EPS distribution architecture

3.1.2 Targets of optimal PAS with EPS reconfiguration

Based on the load requirements and system operation constraints, operational control for this distribution system aims to configure the EPS to allocate power in each generator and transmission branch. Two control targets are studied in this work. Firstly, EPS total power loss is minimized. Then, a generator sizing problem is studied by minimizing the power requirement on each generator. The EPS reconfiguration requirements are integrated into the constraints in the PAS.

3.1.2.1 Minimizing power losses in different flight stages

In this study, the optimized PAS has to work out the most efficient paths to transfer the power and minimize the total power demand for the generators. For example, modular power converters/cells can be used in the power distribution system, and for each converter/cell the efficiency is a non-linear function of input power. The optimal PAS provides power references to the converters/cells to make them operate at a higher efficiency range, based on the system operation constraints including generator failures. The detailed problem formulation and numerical simulation results will be presented in Section 3.2. The optimal PAS are illustrated for several cases of different load requirements, to present the effectiveness of the proposed model.

3.1.2.2 Size reduction of each generator

Generator sizing is a system design optimization problem which aims to select the most suitable generator size. In general, the generator sizing depends on load requirements and distribution losses, thus the power requirements allocated to a generator dramatically influence its size. The main objective for this problem is to reduce generator power rating, hence, to reduce the total weight, but with load satisfaction over the whole flight. Despite reducing the total power demands from the generators, this problem requires the minimum power demand from each generator. Because the two problems are based on similar power limitations, in this study we propose the method to solve the generator sizing problem based on the optimal PAS for loss reduction by introducing new constraints and objectives.

Three scenarios are simulated in Section 3.3 to present the power required from each generator during different flight stages with various loads. In each scenario, the generator operation range and the maximum output power are compared for both optimal PAS problems, i.e. power loss and generator sizing reduction. This comparison presents the effectiveness of the modelling techniques for different objectives.

3.1.3 Contributions

As introduced in Section 2.2.2.1, although optimal PAS has been studied for aircraft EPS in [30], [107] and [96], none of these considered the converters, nor included the transmission losses in their models. In [101] and [100], the generators are controlled to operate at high efficiency, while the power loss during power conversion is considered in power balance equations. However, the transmission efficiencies are simplified by treating them as constant values, and the model only considered the generator and HV bus side. In addition, the constraints for the operation of modular converters have not been studied in the literature. The generator sizing problem has been investigated for terrestrial EPS, for instance, the optimal location and sizing of distributed generation sources are formulated in [144] and [145] to minimize the network power losses and improve voltage regulation within the framework of system security constraints in a radial distribution system. However, these studies contain load flow analysis in their models and they both focus on AC terrestrial grids, while EPS in MEA should consider different constraints and modelling methodologies.

In this study, two optimization problems with regards to optimal PAS are addressed, as defined in Section 3.1.2. These two problems are investigated for the distribution architecture shown in Figure 3.1, where each bidirectional DC/DC converter (cell) can operate in buck or boost mode, allowing bidirectional power flow. The objective is therefore to formulate a solvable mathematical model for both problems, subject to the power system operation constraints, including the power balancing and the limitations for each bus/converter, the

bus/converter connection logic, the transmission losses in the cables and the nonlinear converter efficiency characteristics. In addition, this is not really a static problem: when the load requirements change during different flight stages, the optimal solutions will change to accommodate the changing loads. This study proposes a formulation method for optimal PAS with modified cost functions and constraints, as well as providing mathematical models for both loss reduction and generator sizing problems. The nonlinear functions caused by efficiencies and losses in the models are modelled using a piecewise linearization method to deal with these nonlinear constraints. Using the proposed method, the models can be formulated as MILP models and solved using the CPLEX MILP solver.

3.1.4 MILP model

As the PAS and reconfiguration problems are integrated in this study, MILP is proposed to formulate the problems mathematically, which benefits from effective solvers for global optimal solutions, as introduced in Section 2.2.2. In addition, compared with nonlinear programming, MILP models has fewer feasibility issues. Hence, it is preferable to model the EPS with less nonlinearity. In this study, linearization techniques are proposed in the model formulation.

The generic form of deterministic MILP problem can be presented as follows, where x is a set of integer variables, y is a set of continuous variables, $g(x, y)$ is the objective function, A, B, C, D, E are parameters describing the system, such as load demands, maximum power, efficiency factor, etc. In the following sections, the models are formulated in this form.

$$\min_{x,y} g(x, y) = Ax + By \tag{3.1}$$

Subject to

$$Cx + Dy \leq E$$

$$x \in \{0, 1\}$$

3.2 Optimal PAS for minimizing power losses in different flight stages

3.2.1 Model formulation

To concentrate on power flow analysis, a single line power flow diagram, as shown in Figure 3.2, is built for the studied architecture. In this diagram, the devices, such as generators, buses, cells, and loads, are represented by nodes, the power flows are given as lines where the arrow indicates flow direction. The system consists of two main generator nodes G1 and G2,

one APU generator node, two HVDC bus nodes HVB1 and HVB2, one APU bus node APUB, eight cell nodes from Cell1 to Cell 8, four LVDC bus nodes from LVB1 to LVB4, two HVDC load nodes HVL1 and HVL2, and two LVDC nodes LVL1 and LVL2. The unidirectional power flows from the main generators/APU generator to HV/APU buses, and from the buses to loads, are represented by blue arrows. Bidirectional power flows between the buses and cells and among LV buses are represented by red lines. The notations for the parameters and the decision variables (including the binary and continuous variables) used for the model formulation is shown in Table 3.1-Table 3.3.

Table 3.1 Notation for parameters

Connection status	
$\alpha_i^G \in \{0,1\}$	the connection status between the generator i and corresponding HV bus
$\gamma_p \in \{0,1\}$	the connection status between HV load p and corresponding HV bus
$\delta_q \in \{0,1\}$	the connection status between LV load q and corresponding LV bus
Efficiency parameters	
η_c	the efficiency of cell c in buck mode
η'_c	the efficiency of cell c in boost mode
η_j^{AHV}	the cable efficiency between the APU bus and HV bus j
$\eta_{kk'}^{LV}$	the cable efficiency of LV bus connection between bus k and k'
η_{jc}^{HVC}	the cable efficiency between the HV bus j and cell c
η_{ck}^{LVC}	the cable efficiency between the cell c and LV bus k
Power limits	
$P_{i_max}^G$	the maximum power can be produced from each generator
P_{max}^{APU}	the maximum power can be produced from APU generator
P_{max}^C	the capacity of cell
$P_{p_max}^{HVL}$	the maximum HV load
$P_{q_max}^{LVL}$	the maximum LV load
$P_{kk'_max}^{LV}$	the maximum power can be transferred between LV bus nodes

Table 3.2 Notations for binary decision variables

Connections status between layers	
$\alpha^{APU} \in \{0,1\}$	the connection status between APU to APU bus
$x_j \in \{0,1\}$	the connection status between the APU bus and HV bus j
$\beta_{jc} \in \{0,1\}$	the connection between HV bus j and cell c
$f_{jc} \in \{0,1\}$	The variables of indicators for power flow direction from HV bus j to cell c, the cell operates in buck mode
$f'_{jc} \in \{0,1\}$	the variables of indicators for power flow direction from cell c to HV bus j, the cell operates in boost mode
$\theta_{ck} \in \{0,1\}$	the connection between LV bus k and cell c
$f_{ck} \in \{0,1\}$	the variables of indicators for power flow direction from cell c to LV bus k, the cell operates in buck mode
$f'_{ck} \in \{0,1\}$	the variables of indicators for power flow direction from LV bus k to cell c, the cell operates in boost mode
Connections in the same layer	
$y_{kk'} \in \{0,1\}$	the connection status between the LV bus k and LV bus k'
$f^{HV}_{kk'} \in \{0,1\}$	the variables of indicators for power flow direction from LV bus k to LV bus k'

Table 3.3 Notations for continuous decision variables

Power flow at/between nodes	
$P_i^G \in [0, P_{i_max}^G]$	the power from generator i to corresponding HV bus
$P^{APU} \in [0, P_{max}^{APU}]$	the power from APU to the APU bus
$P_j^{AHV} \in [0, P_{max}^{APU}]$	the power from APU bus to the HV bus j
$P_{jc}^{HVC} \in [0, P_{max}^C/\eta_{jc}^{HVC}]$	the power from HV bus j to cell c, the cell operates in buck mode
$P_{jc_in}^{HVC} \in [0, P_{max}^C]$	the power injected into the cell c from HV bus j, the cell operates in buck mode
$P_{ck}^{LVC} \in [0, P_{max}^C]$	the power from cell c to LV bus k, the cell operates in buck mode
$P'^{HVC}_{jc} \in [0, P_{max}^C]$	the power from cell c to HV bus j, the cell operates in boost mode
$P'^{LVC}_{ck} \in [0, P_{max}^C/\eta_{ck}^{LV}]$	the power from LV bus k to cell c, the cell operates in boost mode
$P'^{LVC}_{ck_in} \in [0, P_{max}^C]$	the power injected to cell c from LV bus k, the cell operates in boost mode
$P_p^{HVL} \in [0, P_{p_max}^{HVL}]$	the power of HV load p
$P_q^{LVL} \in [0, P_{q_max}^{LVL}]$	the power of LV load q
$P_{kk'}^{LV} \in [0, P_{kk'_max}^{LV}]$	the power from LV bus k to LV bus k'

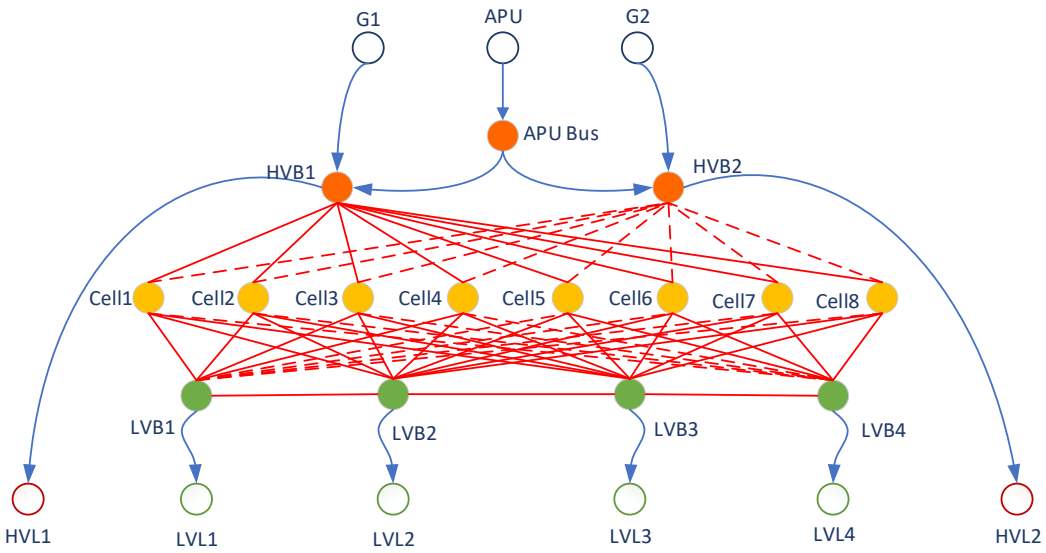


Figure 3.2 Simplified power flow diagram of the studied system

3.2.2 Objective functions

The objective of power allocation is to minimize the total power demand from generators while satisfying load demands. In different flight stages, the loads change, thus the optimal EPS configures power contactors on/off status, and the power flowing through each component to achieve a more efficient topology, in other words reducing the power losses from the generators to the loads. The objective function can be expressed in (3.2), where N^G is the total number of main generators.

$$J(P) = \frac{1}{N^G + 1}\left(\sum_i^{N^G} P_i^G + P^{APU}\right) \tag{3.2}$$

3.2.3 Constraints

1) Power balance constraints

Power balance for each node is essential to maintain voltage stability. The power flowing through each node should strictly comply with this rule – the sum of power into/out each node equals zero (Kirchhoff's Current Law for a given voltage).

For the APU bus node, the power balance equation in (3.3) should be satisfied. The equation represents the power drawn from the APU equals the power flowing into the HV buses.

$$P^{APU} - \sum_j P_j^{AHV} = 0 \tag{3.3}$$

For all HV bus nodes, the power balance equation is presented in (3.4), where N^{HVB} is the number of HV buses. The input power for each HV bus includes the power from the connected

generator/APU bus, and the cells when in boost mode, and the output power flows to the connected HV loads and the cells when in buck mode. The cell can only operate in either buck or boost mode, which means either P'^{HVC}_{jc} or P^{HVC}_{jc} is 0. This constraint is demonstrated in unidirectional constraints.

$$P^{G}_{j} + \eta^{AHV}_{j} P^{AHV}_{j} + \sum_{c}\left(\eta^{HVC}_{jc} P'^{HVC}_{jc} - P^{HVC}_{jc}\right) - \sum_{p} P^{HVL}_{p} = 0, \forall j \in \{1, \dots, N^{HVB}\} \tag{3.4}$$

For all cell nodes, the power balance equation is presented in (3.5), where N^{C} is the number of cells. In (3.5), the first term indicates the power between HV buses to cell *c*; the second term indicates the power between LV buses to cell *c*. The input power for each cell includes the power from the HV buses (buck mode) and the LV buses (boost mode), and the output power includes the power flowing to HV buses (boost mode) and the LV buses (buck mode).

$$(\eta_{c} \sum_{j} P^{HVC}_{jc_{in}} - \sum_{j} P'^{HVC}_{jc}) - (\sum_{k} P^{LVC}_{ck} - \eta'_{c} \sum_{k} P'^{LVC}_{ck_in}) = 0, \forall c \in \{1, \dots, N^{C}\} \tag{3.5}$$

where $P^{HVC}_{jc_in} = P^{HVC}_{jc}\eta^{HVC}_{jc}$, $P'^{LVC}_{ck_in} = P'^{LVC}_{ck}\eta^{LVC}_{ck}$.

For all LV bus nodes, the power balance equation is presented in (3.6), where N^{LVB} is the number of LV buses. In (3.6), The first term indicates the power between cells and the LV bus *k*; the second term indicates the load power allocated on LV bus *k*; the third term indicates the power between LV bus *k* and LV bus k'. The input power for each LV bus includes the power from cells (buck mode) and the adjacent LV bus nodes $P^{LV}_{k'k}$, and output power includes the power flowing to cells (boost mode) and the adjacent LV bus nodes $P^{LV}_{kk'}$. Power exchange between the LV buses is bidirectional, but it cannot flow in both directions simultaneously. Hence, either $\sum_{k\neq k'} P^{LV}_{k'k}$ or $\sum_{k\neq k'} P^{LV}_{kk'}$ should be 0.

$$\sum_{c}(\eta^{LVC}_{ck} P^{LVC}_{ck} - P'^{LVC}_{ck}) - \sum_{q} P^{LVL}_{q} - \sum_{k\neq k'}(P^{LV}_{kk'} - \eta^{LV}_{kk'} P^{LV}_{k'k}) = 0, \quad \forall k \in \{1, \dots, N^{LVB}\} \tag{3.6}$$

2) Component efficiency and linearization

In the power balance equations (3.3) - (3.6), the cable losses and the cell efficiencies are taken into consideration.

- Cable losses and efficiency coefficient

The cable losses in LV bus interconnections, between APU bus and HV buses, and the connections between HV/LV buses and converters are considered. In the DC grid, the power losses for cables are mainly copper losses, which can be calculated as

$$P_{Cu} = I^{2} r \tag{3.7}$$

where P_{Cu} is the cable/copper losses, I is the current flowing through this cable, and r is the cable resistance. Hence, the cable efficiency coefficient can be calculated as follow:

$$\eta = \frac{P_{trans}}{P_{total}} = \frac{P_{trans}}{P_{trans} + P_{Cu}} \tag{3.8}$$

where P_{total} is the total power flowing into this cable, P_{trans} is the power transferred to the next node.

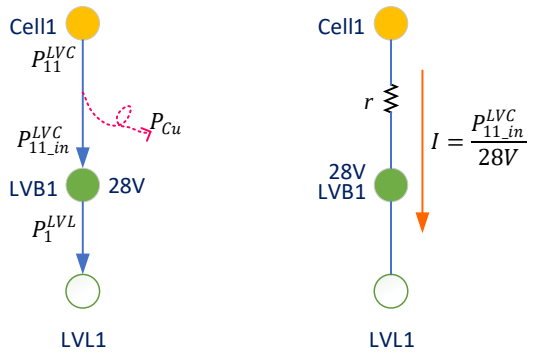
Taking the cable between one cell and one LV bus as an example to calculate the cable efficiency coefficient η_{ck}^{LVC}, the power flows and cable losses are presented in Figure 3.3 (a), where P_{11}^{LVC} represents the power out of the converter 1 to LV bus 1, $P_{11_in}^{LVC}$ represents the power into the LV bus 1, P_{Cu} represents the power losses on the cable between Cell 1 and LV bus 1 (LVB1), and the P_1^{LVL} is the LV load power demand. The efficiency coefficient for this cable η_{11}^{LVC} can be calculated as follow:

$$\eta_{11}^{LVC} = \frac{P_{11_in}^{LVC}}{P_{11}^{LVC}} = \frac{P_{11_in}^{LVC}}{P_{11_in}^{LVC} + P_{Cu}} = \frac{1}{1 + \frac{P_{Cu}}{P_{11_in}^{LVC}}} \tag{3.9}$$

where $P_{11_in}^{LVC} = P_1^{LVL}$.

In this study, the LV bus voltage is assumed to be kept constant at 28V, the current in this routing can be calculated, thus the cable loss can be derived. The functions are shown in (3.10), where r is the resistance of the cable. The current and the resistance of this cable in this route is presented in Figure 3.3 (b).

$$P_{Cu} = I^2 r = \left(\frac{P_{11_in}^{LVC}}{28V}\right)^2 r = \left(P_{11_in}^{LVC}\right)^2 \frac{r}{(28V)^2} \tag{3.10}$$



(a) (b)

Figure 3.3 Example to introduce cable loss and efficiency coefficient: (a) example of power flows and cable loss from Cell 1 to load 1 (LVB1); (b) the current and resistance in this power route

Based on equations (3.9) and (3.10), the cable efficiency can be rewritten as shown in (3.11). It can be observed that $\eta_{11}^{LVC} \propto \frac{1}{P_{11_in}^{LVC} \cdot r}$, which presents a nonlinear function to the decision variable. This introduces nonlinearity to the power balance constraints (3.6). Similar derivations can be addressed for other cables.

$$\eta_{11}^{LVC} = \frac{1}{1 + \frac{P_{11_in}^{LVC} \cdot r}{(28V)^2}} \tag{3.11}$$

Assuming that cable resistance is small, the cable efficiency can be approximated to a constant value to simplify the model formulation. For example, in this study, the cell is rated at 3kW, which means $P_{11_in}^{LVC} < 3kW$, hence if the resistance r is 1mΩ, then $0.9962 \leq \eta_{11}^{LVC} \leq 1$. In this case, an average efficiency 0.9981 is adopted as the constant efficiency coefficient for this cable.

- Cell (modular DC/DC converter) efficiency

In contrast to cable efficiencies, the cell efficiency is typical a nonlinear function of input power, as illustrated in Figure 3.4. This will lead to a nonlinear problem instead of a MILP, unless it is reformulated in a linearized format. Therefore, a piecewise function is proposed to linearize this nonlinear relationship.

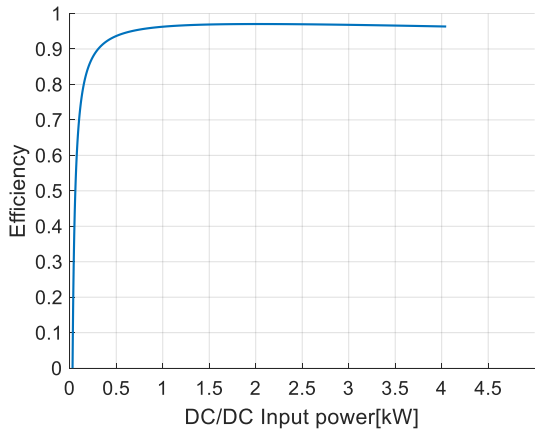


Figure 3.4 A typical cell efficiency curve dependent on input power

In this study, it is assumed that the cell efficiency curve in both buck and boost operation modes are the same. Their relationship is given in (3.12).

$$\eta_c = f(\sum\nolimits_j P_{jc_in}^{HVC})$$
$$\eta'_c = f(\sum\nolimits_k P'^{LVC}_{ck_in}) \tag{3.12}$$

where $\sum_j P_{jc_in}^{HVC}$ and $\sum_k P'^{LVC}_{ck_in}$ are the total power flowing to the cell from HV buses and LV buses respectively.

Equation (3.5) can consequently be presented in the format of (3.13) resulting, in nonlinearity in the constraints, which is unsolvable in CPLEX.

$$(f(\sum_j P_{jc_in}^{HVC}) \cdot \sum_j P_{jc_in}^{HVC} - \sum_j P'^{HVC}_{cj}) - (\sum_k P_{ck}^{LVC} - f(\sum_k P'^{LVC}_{ck_in}) \cdot \sum_k P'^{LVC}_{ck_in}) = 0 \quad (3.13)$$

In this case, a new decision variable $P_{c_out}^{HVC}$ is introduced to represent the cell's output power in buck mode, and $P'^{HVC}_{c_out}$ to present the output power in boost mode. Taking the variable $P_{c_out}^{HVC}$ as an example, it can be approximated by a piecewise function, and each segment is a linear function relating to the input power as demonstrated in (3.14).

$$\begin{aligned} P_{c_out}^{HVC} &= \eta_c \sum_j P_{jc_in}^{HVC} \approx f_p\left(\sum_j P_{jc_{in}}^{HVC}\right) \\ &= \begin{cases} k_1 \sum_j P_{jc_in}^{HVC} + b_1\,,\ if\ m_0 \le \sum_j P_{jc_in}^{HVC} \le m_1 \\ k_2 \sum_j P_{jc_in}^{HVC} + b_2\,,\ if\ m_1 \le \sum_j P_{jc_in}^{HVC} \le m_2 \\ k_3 \sum_j P_{jc_in}^{HVC} + b_3\,,\ if\ m_2 \le \sum_j P_{jc_in}^{HVC} \le m_3 \\ \vdots \\ k_n \sum_j P_{jc_in}^{HVC} + b_n\,,\ if\ m_{n-1} \le \sum_j P_{jc_in}^{HVC} \le m_n \end{cases} \end{aligned} \quad (3.14)$$

Taking the typical efficiency curve in Figure 3.4 as an example, the corresponding output power $P_{c_out}^{HVC}$ can be illustrated in regarding to the input power $\sum_j P_{jc_in}^{HVC}$ in blue, while the piecewise linear approximation of $P_{c_out}^{HVC}$ is in red with 5 segments. The piecewise output power curve is very close to the original one.

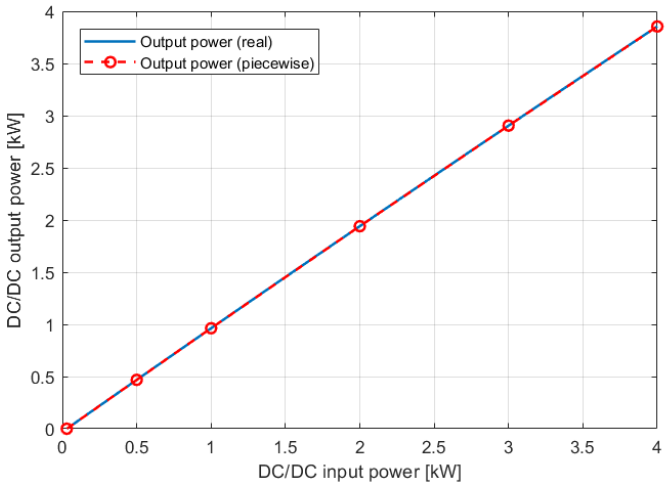


Figure 3.5 Piecewise output power curve compared to the original one based on the typical efficiency curve in Figure 3.4

To verify its accuracy, the approximated converter efficiency $\widetilde{\eta_c}$ is derived in (3.15), which is compared to the actual one in Figure 3.6. The figure shows that the approximated efficiency $\widetilde{\eta_c}$ is very close to the original.

$$\widetilde{\eta_c} = \frac{k_m \sum_j P_{jc_in}^{HVC} + b_m}{\sum_j P_{jc_in}^{HVC}} = k_m + \frac{b_m}{\sum_j P_{jc_in}^{HVC}} \tag{3.15}$$

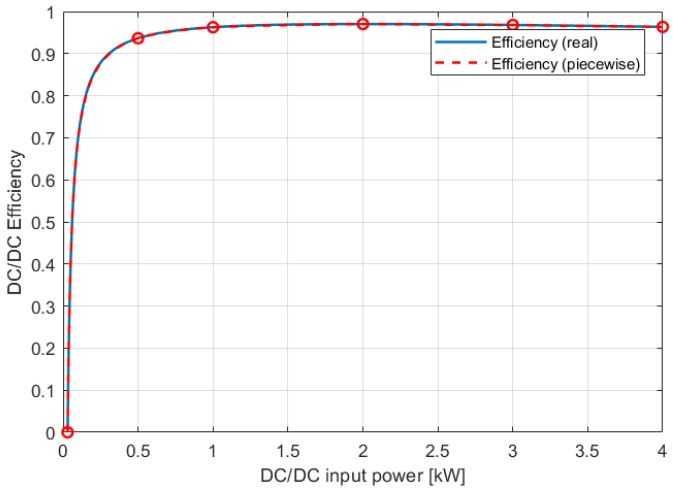


Figure 3.6 The piecewise function derived efficiency curve compared to the original one

When the cell operates in the boost mode, the output power $P'^{HVC}_{c_out}$ has a similar relationship with the input power $\sum_k P'^{LVC}_{ck_in}$. A similar procedure could be adopted, and thus no detail is presented here.

3) Power limitation constraints

As defined in Table 3.1, each connection/power flow direction has its power limitation – a non-negative upper bound. The power in each connection also depends on its connection status, when the connection status is 0, the power through this connection line is restricted to be 0. This principle is similarly applied to the bidirectional power flow, i.e. when the power flow in one direction is restricted to be 0 when the indicator of this direction is 0. The following inequalities are proposed to present the power in connection lines.

Limitations of the generator power in (3.16) and APU in (3.17)

$$0 \le P_i^G \le \alpha_i^G P_{i_max}^G \tag{3.16}$$

$$0 \le P^{APU} \le \alpha^{APU} P_{max}^{APU} \tag{3.17}$$

Limitations of the power from the APU bus to HV buses

$$0 \le P_j^{AHV} \le x_j P_{max}^{APU} \tag{3.18}$$

Limitations of the power into and out of the cells in buck mode

$$0 \le P_{jc_in}^{HVC} \le f_{jc} P_{max}^{C} \tag{3.19}$$

$$0 \le P_{ck}^{LVC} \le f_{ck} P_{max}^{C} \tag{3.20}$$

Limitations of the power into and out of the cells in boost mode

$$0 \le P'^{LVC}_{ck_in} \le f'_{ck} P_{max}^{C} \tag{3.21}$$

$$0 \le P'^{HVC}_{jc} \le f'_{jc} P_{max}^{C} \tag{3.22}$$

Limitations of power out of and into the LV bus node k between the adjacent LV bus nodes

$$0 \le P_{kk'}^{LV} \le f_{kk'}^{LV} P_{kk'_max}^{LV} \tag{3.23}$$

4) Unidirectional constraints

In Figure 3.2, the red lines presented the connections where the power has two optional directions, but the power cannot flow in both directions simultaneously. Therefore, the unidirectional constraints are set to avoid the conflicts in the power directions.

- Operation mode constraints of cells

Each cell can operate in either buck mode or boost mode, but it cannot operate in both modes simultaneously. Thus, if a cell works in buck mode, the power flows from an HV bus to an LV bus through it, and the power in the reverse direction is 0. This can be formulated as: if $P_{jc_in}^{HVC}, P_{ck}^{LVC} > 0$, then $P'^{LVC}_{ck_in}, P'^{HVC}_{jc} = 0$. The binary power indicators could be 0 or 1, in buck mode, the binary variables $f_{jc} = 1, f_{ck} = 1$, the boost mode indicators are forced to be 0. If the cell is not connected to the buses, then variables are forced to 0. This *if…then…* function can be realized when the constraints in (3.24) - (3.25) are combined with the power balance constraints (3.4) - (3.6) and the power limitation constraints in (3.19) - (3.22).

$$f_{jc} + f'_{jc} = \beta_{jc} \tag{3.24}$$

$$f_{ck} + f'_{ck} = \theta_{ck} \tag{3.25}$$

- Bus interconnection power constraints

In practice, bus interconnections are connected only when any bus is in the faulty condition. For example, an LV bus interconnection is connected when one LV bus is in the faulty condition, which is studied in Chapter 5. In this chapter, the LV bus failures are not considered. However,

to present the formulations of the bus interconnections and the configuration changes when considering a wider range of options, it is assumed that the LV bus can be connected in the EPS normal condition in this chapter. Hence, there is a situation that the LV bus interconnections are adopted to supply one LV bus to provide sufficient power to the connected loads on this LV bus when the EPS operates normally, despite the fact that this is unlikely in practice. The LV buses are considered to be able to be connected together under this assumed situation. For an interconnection of LV bus node k and k', the power could flow either from k to k', or from k' to k. Similar to the converter operation mode constraint, the power flow constraints can be realized by combining (3.26) with the power balance constraints (3.6) and the power limitation constraints in (3.23).

$$f_{kk'}^{LV} + f_{k'k}^{LV} = y_{kk'} \tag{3.26}$$

5) Physical connection constraints

Besides the aforementioned constraints for the power flow perspective, some other physical connection constraints should also be considered.

The APU connects to the APU bus only when a main generator failure has occurred, which can be presented as in (3.27) where N^G is the number of the generators.

$$\alpha^{APU} + \sum_i \alpha_i^G \leq N^G \tag{3.27}$$

Each cell cannot be connected to more than one HV and LV bus, as presented in (3.28) - (3.29).

$$0 \leq \sum_j \beta_{jc} \leq 1 \tag{3.28}$$

$$0 \leq \sum_k \theta_{ck} \leq 1 \tag{3.29}$$

For the LV bus interconnection, only neighboring nodes can be connected together, as presented in (3.30), where N^{LVB} is the number of LV buses. It is noted in this study that LV bus interconnections are assumed to be applicable in any EPS scenarios to present more potential configuration results. However, in the following chapters, both HV and LV bus interconnections are allowed only in an EPS faulty condition.

$$k' = k \pm 1, \text{ and } N^{LVB} \geq k, k' \ldots \geq 1 \tag{3.30}$$

- Other physical connection assumptions

Some other physical connection assumptions are taken into consideration to simplify the studied system, they are listed as follows:

a) Each generator only connects to one specific HV bus.
b) Each HV/LV load only connects to one specific HV/LV bus.
c) The APU only connects to the APU bus.

3.2.4 Case study

To verify the effectiveness of the proposed model and algorithms, three cases will be studied in this section, considering different load profile of MEA EPS, such as symmetric HV/LV load allocation on the left and rights side of the aircraft. Case 1 and Case 2 show how the EPS allocates power intelligently to symmetric and asymmetric load demands respectively when all generators work well, while Case 3 shows the power allocation under one generator failure. The topology used in these cases is given in Figure 3.1, and the adopted converter efficiency curve is shown in Figure 3.4. Other parameters are listed in Table 3.4 and Table 3.5. The values are assumed to consider the power losses caused by different cable resistance, considering cable length, cross-sectional area, and resistivity.

Table 3.4 Cable efficiencies for bus connections

Parameters	Values
η_j^{AHV}	0.9998
$\eta_{kk'}^{LV}$	0.9000

Table 3.5 Cable efficiencies between HV/LV buses and DC/DC cells

Cable efficiencies η_{jc}^{HVC} between HV bus j and cell c								
η_{jc}^{HVC}	Cell 1	Cell 2	Cell 3	Cell 4	Cell 5	Cell 6	Cell 7	Cell 8
HVB1	0.9963	0.9962	0.9961	0.9960	0.983	0.982	0.981	0.980
HVB2	0.980	0.981	0.982	0.983	0.9963	0.9962	0.9961	0.9960
Cable efficiencies η_{ck}^{LVC} between cell c and LV bus k								
η_{ck}^{LVC}	Cell 1	Cell 2	Cell 3	Cell 4	Cell 5	Cell 6	Cell 7	Cell 8
LVB 1	0.9963	0.9962	0.9961	0.9960	0.983	0.982	0.981	0.980
LVB 2	0.9960	0.9961	0.9963	0.9962	0.9835	0.9825	0.9815	0.9805
LVB 3	0.9805	0.9815	0.9825	0.9835	0.9963	0.9962	0.9961	0.9960
LVB 4	0.980	0.981	0.982	0.983	0.9960	0.9961	0.9963	0.9962

3.2.4.1 Case 1: symmetric load demands with generators in normal condition

In this case, the system has symmetric HV/LV load demands as listed in Table 3.6. From the aforementioned constraints, it can be seen that the HV loads can be powered directly by the

corresponding HV buses, while the LV loads are supplied by the LV buses which requires DC/DC converters/cells to transfer the needed power, and each LV load can be supplied by only one cell in this case. Based on the connection efficiency provided in Table 3.5, only Cell1, Cell3, Cell5, Cell7 need to be used.

The simulation results are presented in Figure 3.7 and the derived converter efficiency points are marked as red triangles on the efficiency curve. It can be observed that the power balance is realized for all of the nodes and the most efficient connections are achieved as expected. In addition, all of the converters are working in the high efficiency operation range.

Table 3.6 Loads in the system

Parameters	Values(kW)
HV Loads	{40,40}
LV Loads	{1,2,2,1}

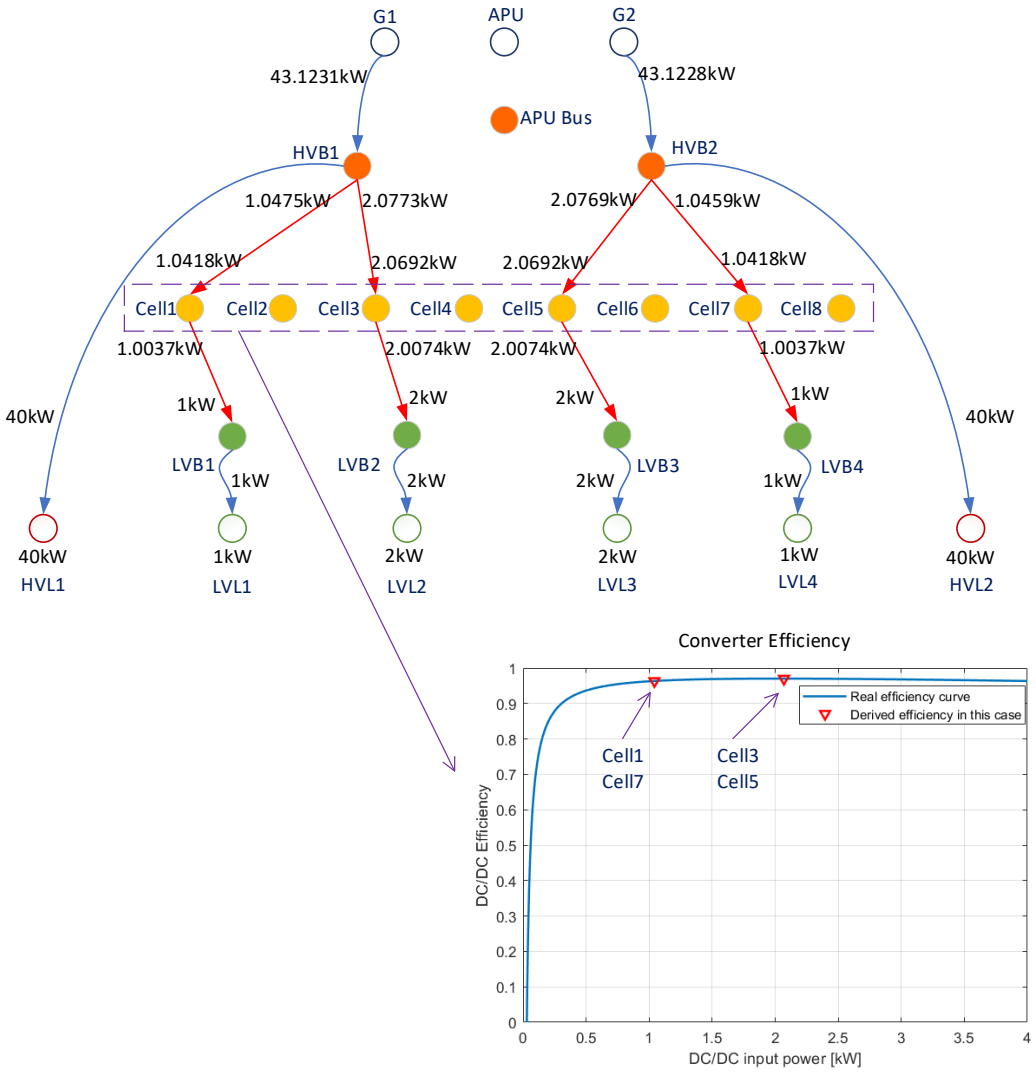


Figure 3.7 Optimal PAS in Case 1

3.2.4.2 Case 2: asymmetric load demands with generators in normal condition

In this case, the system has asymmetric HV/LV load demands as listed in Table 3.7, and the LV loads demands more power compared to those of case 1, hence more cells will be used in this case. One cell can meet the power requirement of LV load1 while either LV load2 or load4 needs two cells, and LV load3 is so large that three cells would be required. The LV buses could be connected together to optimize the usage of the cells.

The simulation results are presented in Figure 3.8 and the derived converter efficiency points are marked as red triangles in the efficiency curve. It can be observed that the power balance is realized for all the nodes and the most efficient connections are achieved by connecting LVB2 and LVB3 together to compensate for the power needs of LV load3. In addition, all of the cells are working in the high efficiency range.

Table 3.7 Loads in the system

Parameters	Values(kW)
HV Loads	{40,30}
LV Loads	{2,3,6,4}

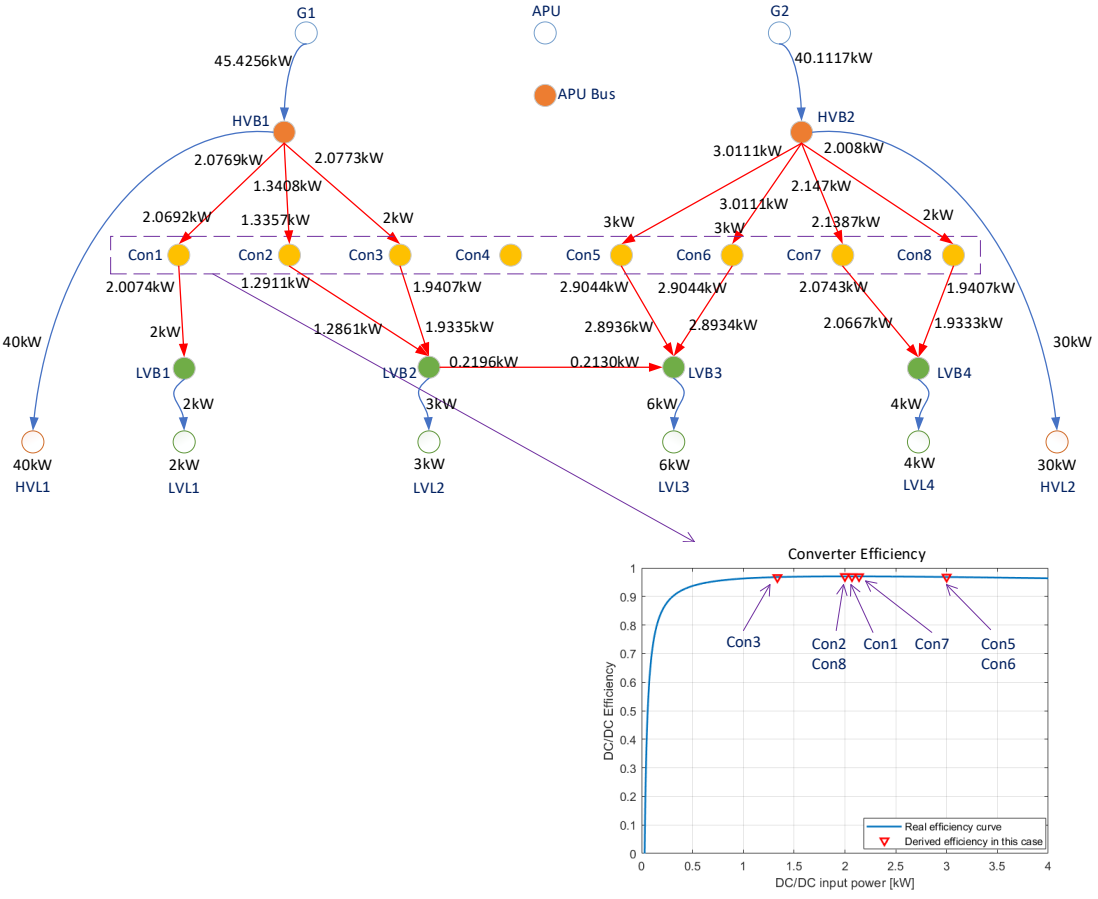


Figure 3.8 Optimal PAS in Case 2

3.2.4.3 Case 3: symmetric load demands with one faulty generator

In this case, the same symmetric load demands of case 1 are used. It is assumed that generator 1 fails, therefore, to support the HV load1 and LV load1 and load2, either the APU is needed or one or more cells could operate in boost mode to support HV bus1 and HV load1. As the connection of the APU bus and HV buses have high efficiency, the APU should be connected, and the other parts are similar as those in case 1. The simulation results are presented in Figure 3.9, which are consistent with the previous analysis.

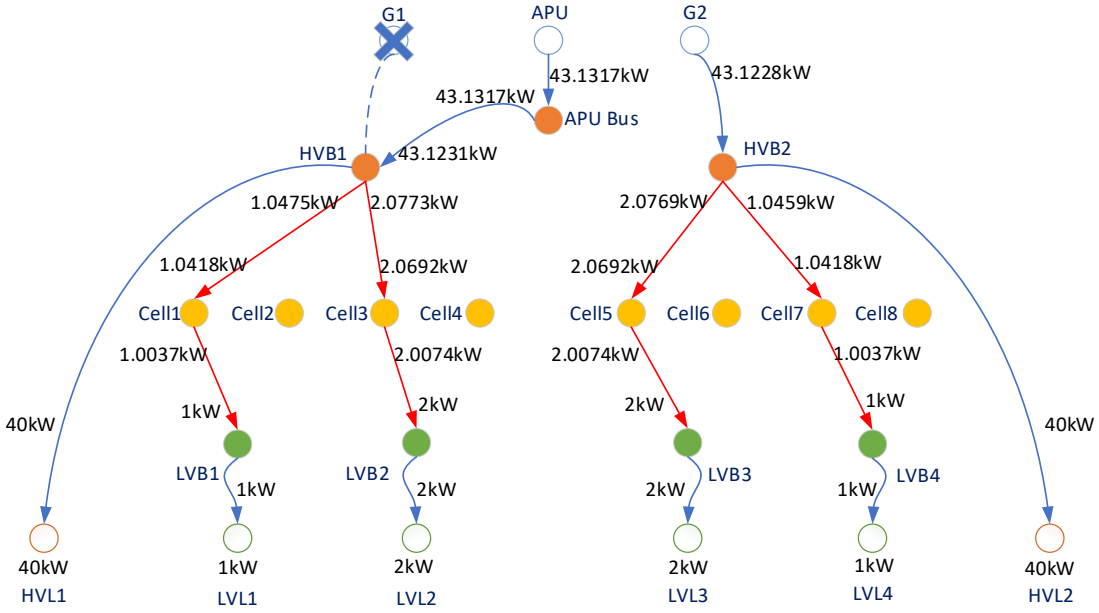


Figure 3.9 Optimal PAS in Case 3

3.3 Optimal PAS for generator sizing

Generators should provide for all of the demanded power in all flight stages, and the size of generators is essentially related to the load requirements and the PAS. In the Section 3.2, the PAS aims for higher efficiency and lower power losses. Combining some other constraints and objective functions, the model can also be adopted to deal with the generator sizing problem. In this section, the generator failures and APU connection are not considered, to simplify explanations.

3.3.1 Model formulation

To formulate the problem, a new constant decision variable P_{cap}^{G} needs to be introduced. This denotes the maximum power required from each generator. Combining the model in Section 3.2, the generator sizing problem can be formulated as follows:

3.3.1.1 Objective functions

The objective is to minimize the maximum power required from each generator. Hence, the objective functions can be presented in (3.31), where N^G is the number of generators, and P_{max}^G is an initial value of the maximum generator power to provide an upper bound to P_{cap}^G.

$$J(P) = \frac{1}{P_{max}^G} \sum_{N^G} P_i^G + \frac{P_{cap}^G}{P_{max}^G} \tag{3.31}$$

3.3.1.2 Constraints

To minimize the power from each generator, the limitations of the power flowing out of the generators in (3.16) should be rewritten. For each generator, the power flowing out should not exceed the maximum needed power, which is presented in (3.32):

$$\begin{aligned} 0 \leq P_i^G &\leq \alpha_i^G P_{i_max}^G \\ 0 \leq P_i^G &\leq P_{cap}^G \\ 0 \leq P_{cap}^G &\leq P_{max}^G \end{aligned} \tag{3.32}$$

Combined with the other constraints of power balance, power limitation, and connections constraints, which are discussed in Section 3.2.3, the generator sizing problem can be solved by optimizing the maximum required power for each generator across all flight stages, having different load requirements in each stage.

3.3.2 PAS during flight stages with different objectives

Targeting EPS power loss reduction, optimal PAS is required in the different flight stages regarding different load requirements. Despite targeting a lighter generator, optimal PAS is also required for all flight stages, ensuring generators can provide all of the demanded power in each flight stage. In this section, 3 scenarios are used to verify the effectiveness of the proposed models with two different objectives. In each scenario, a specific load profile is assumed as an example about how the optimization results are accordingly changed. Their results will be compared to see how much power is produced by each generator in each flight stage under symmetric/asymmetric load demands.

3.3.2.1 Scenario 1: asymmetric LV loads and symmetric HV loads

One typical flight cycle has several flight stages with different load demands. In this scenario, it is assumed that during the overall flight stage (7 flight stages) the loads varies as shown in Figure 3.10 (1), and the power of HV load1 and HV load2 are symmetric while the power of the LV loads are asymmetric. The detailed load power demands are listed in Appendix A Table 7.1. The optimal PAS of the two main generators for reducing power loss is presented in Figure 3.10 (2-a), while the results for generator sizing are presented in Figure 3.10 (2-b).

It can be observed that both generators reach the maximum output power during stage 4, because the HV loads are much higher than the LV loads and dominate the output power. Compared to Figure 3.10 (2-a), when the objective of minimizing the maximum power of each generator is added to the optimal PAS model, the power produced from each generator gets balanced, as presented in Figure 3.10 (2-b). Both generator powers are lower than 60 kW in Figure 3.10 (2-b), while in Figure 3.10 (2-a) without the sizing optimization, the generators produced maximum powers of 61 kW and 57 kW respectively.

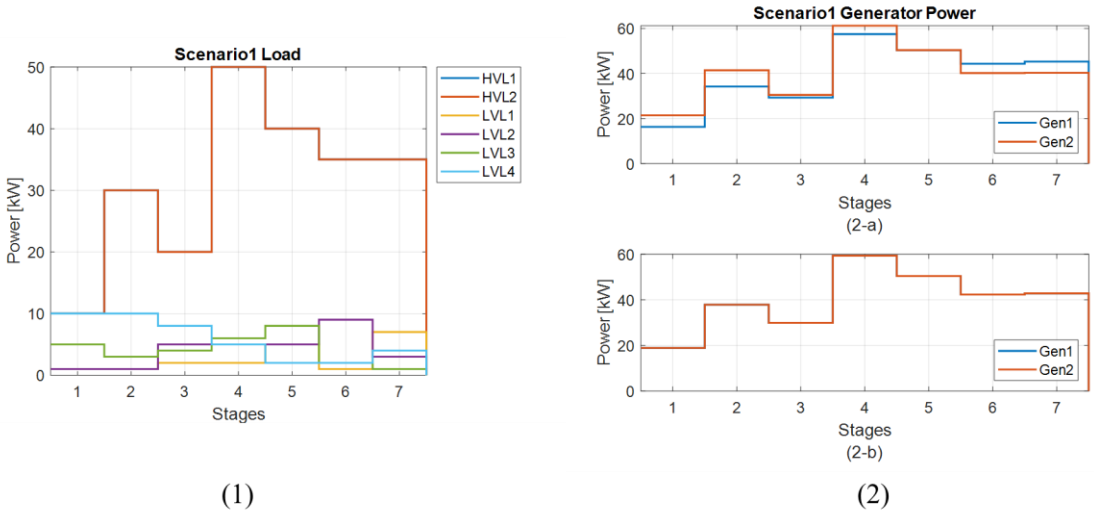
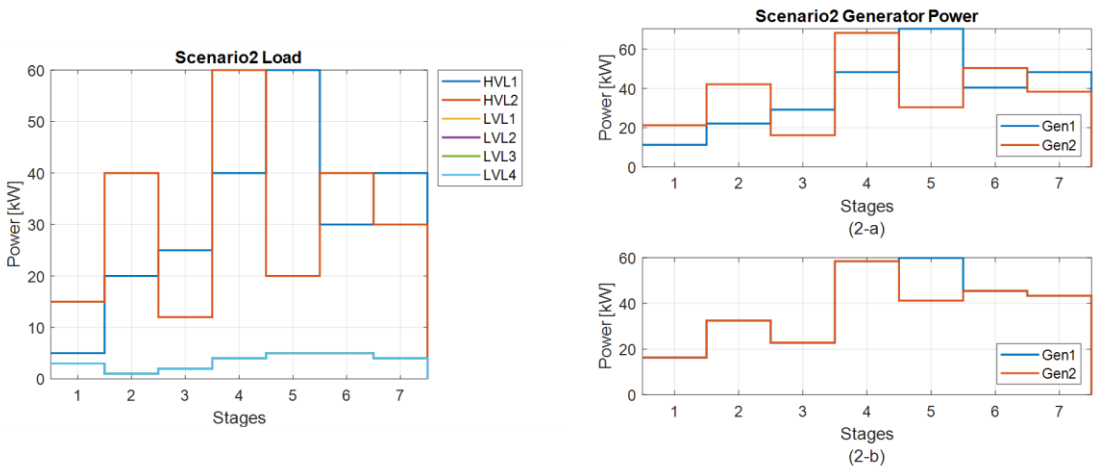


Figure 3.10 Generator power in Scenario 1: (1) load profile; (2-a) generator power targeting power loss reduction; (2-b) generator power targeting generator sizing reduction

3.3.2.2 Scenario 2: asymmetric HV loads and symmetric LV loads

In this scenario, the loads are assumed to vary during seven flight stages as shown in Figure 3.11 (1), and the HV loads are asymmetric while the LV loads are symmetric. The detailed load power demands are listed in Appendix A Table 7.2.

Based on the load requirements, generator 2 reaches the peak power during stage 4 while generator 1 reaches its peak point during stage 5. Compared to Figure 3.11 (2-a), when the objective of minimizing the maximum power of each generator is added to the optimal PAS model, the power produced from each generator gets balanced as presented in Figure 3.11 (2-b). Both generator powers are lower than 60 kW in Figure 3.11 (2-b), while in Figure 3.11 (2-a) without the sizing optimization, the generators produced maximum powers of 70.4 kW and 68 kW respectively.

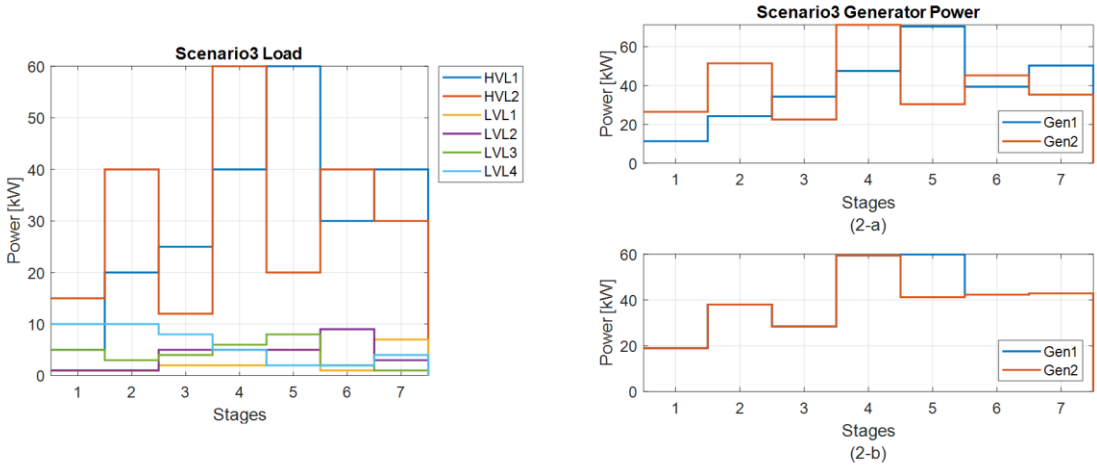


(1) (2)

Figure 3.11 Generator powers in Scenario 2: (1) load profile; (2-a) generator power targeting power loss reduction; (2-b) generator power targeting generator sizing reduction

3.3.2.3 Scenario 3: asymmetric HV and LV loads

In this scenario, the loads are assumed to vary during seven flight stages as shown in Figure 3.12 (1), and all HV and LV loads are asymmetric. The detailed load power demands are listed in Appendix A Table 7.3. Based on the load requirements, generator 2 reaches the peak output power during stage 4 while generator 1 reaches its peak power during stage 5.



(1) (2)

Figure 3.12 Generators power in Scenario 3: (1) load profile; (2-a) generator power targeting power loss reduction; (2-b) generator power targeting generator sizing reduction

Compared to Figure 3.12 (2-a), when the objective of minimizing the maximum power of each generator is added to the optimal PAS model, the power produced from each generator gets balanced, as presented in Figure 3.12 (2-b). The maximum power of each generator is 60

kW in Figure 3.12 (2-b), while in Figure 3.12 (2-a) without the sizing optimization, the generators produced maximum powers of 70 kW and 71 kW respectively.

The simulation results for optimal generator sizing for the 3 scenarios revealed that, compared to the results in optimal PAS for power loss minimization, the maximum power of each generator has been obviously minimized. This proves the effectiveness of the proposed sizing method by added objectives and constraints in the optimal PAS problem.

3.4 Chapter summary

In this chapter, a mathematical model of the modular converter-based EPS distribution architecture was formulated for optimal PAS and reconfiguration control, which constituted the system constraints of power balancing and limitations for each bus/converter, the bus/contactor connection logic, the transmission power losses in the cables and the nonlinear converter efficiency characteristics. By using the piecewise linearization techniques, the proposed model can be formulated as a MILP and solved by MILP solvers to reduce the computational complexity. By formulating objective functions and adding more constraints, the model can be applied to two targets, including reducing the total power needs from the power sources and minimizing the required overload capabilities for each generator. Simulation results have shown that the optimization model and the approach can achieve good performance and that optimal solutions can be obtained for different flight stages. The proposed modelling techniques to formulate the EPS as a MILP in this chapter are applied in the following chapters of this thesis.

The modelling methods proposed in this chapter provide other researchers with solutions to problems relating to PAS and reconfiguration in various EPS architectures. For example, when the EPS contains only one single HV bus with two parallel generators, the MILP model can be modified by eliminating the HV bus connection variables and constraints. In addition, the objective functions can be adjusted to balance the power sharing between two generators. When modular converters are not used in an EPS, the MILP model is changed by removing constraints for the power balance of cells and their connectivities. If nonlinear power losses in cables are highlighted, the piecewise functions proposed in this chapter for cells can be adapted to each cable. In summary, although this study focuses on a specific EPS architecture, researchers can use this study to efficiently propose a feasible MILP model for their applications.

Chapter 4 Model predictive control-based ESS and load management system

In Chapter 3, MILP is applied to power allocation and scheduling (PAS) and reconfiguration problems in a power distribution system. A similar mathematical model can be applied to describe the energy storage systems (ESSs) and loads onboard, providing optimized load and energy management strategies. In addition, when MILP is integrated within a model predictive control (MPC) framework, an optimal operating strategy can be provided based on predicted future system trajectories, thereby avoiding operating based on the worst-case scenarios with high costs, as discussed in Section 2.3. This chapter presents a MILP-MPC method to schedule the ESS and exploit flexibility on the demand side while satisfying time-varying operational requirements.

4.1 Introduction

4.1.1 Main source-energy storage-load subsystem architecture

In this chapter, energy storage (ES) and load management are studied for the system presented in Figure 4.1. As can be seen in this figure, the studied system includes a main source (MS) consisting of power from HV side, an ESS, DC/DC power converters, one LV bus and several loads. The MS powers the loads which are connected to a low voltage (LV) bus. In this system, the ES, which consists of one battery, one bidirectional DC/DC converter, and one contactor, is connected to the same LV bus, to both maintain the bus voltage and supply the loads when faults result in insufficient power available from the MS. It is worth mentioning that this chapter focuses on the load and ES management for the LV bus as an example to study the objective formulations. However, the proposed method can be applied to the HV side or other EPS architectures [6].

The loads can be classified into critical and non-critical loads. Critical loads link with flight safety status and avionics systems, such as environment control system and flight control system, etc. The non-critical loads are the other classes of loads that provide a comfortable environment for passengers and some of them are more essential, which are assigned with a higher priority. For example, the in-flight entertainment and galley services are considered as lower priority loads compared to other non-critical loads such as water and waste systems [146],

[107]. Therefore, in this study, three types of loads are considered, namely, critical loads (Load1) which must be supplied under all circumstances, high-priority loads (Load2), which can be shed but should not where possible, and low-priority loads (Load3), which should be shed in preference to high-priority loads when load shedding is needed.

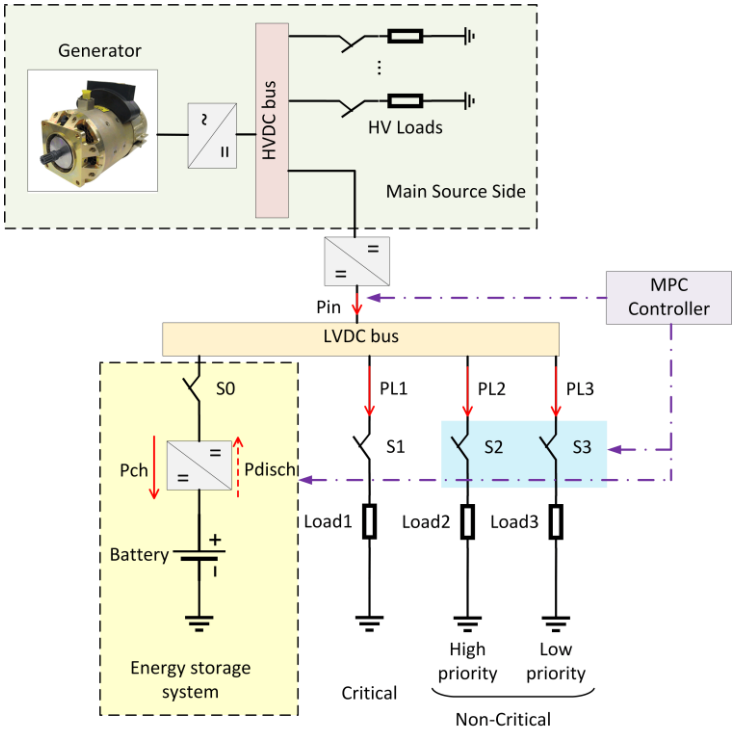


Figure 4.1 The architecture of main source-energy storage-load (MS-ES-L) subsystem

4.1.2 Energy storage and load management

Intelligently combining the load shedding with the ESS capabilities is essential for safe onboard EPS operation. As introduced in Section 1.1.4, critical loads must be powered in all flight scenarios regardless of high-power peaks or fault-causing emergencies. The ESS has an important role in MEA, not only for supporting bus voltages, but also as a backup to deal with power shortages during faults occurring in generation or transmission systems, or high-power peaks. In addition, shedding of non-critical loads is also used to reduce peak power usage, helping to maintain power for safety-critical loads [147]. In this study, operational control aims to keep the battery energy storage highly charged, with fewer power variations to prolong the battery life cycle, and to minimize load shedding, with less contactor switching.

4.1.3 Contributions

As mentioned in Section 2.3, MPC has drawn the attention of the power system community for the operation management of EPSs based on future predictions. The inherent feedback mechanism of MPC, stemming from its receding horizon mechanism, makes the system more resilient to predictable future changes [39]. To enhance the battery lifespan and power

performance, [112] and [113] propose an MPC approach to reduce the battery power variation and maintain supercapacitors' SOC at their desired values. In [148], the battery capacity fading is described by an online least-squares identification method, and the degradation cost function is used in the MPC scheme to increase the battery lifetime. In [57], a hierarchical MPC framework for a hybrid propulsion system is presented to minimize power generation costs and delivery losses. However, the possibility of load shedding and system failure is not considered. In [149] and [30], MPC is used for both power scheduling and load shedding optimization to cope with scenarios with one generator and one transmission cable failure. In [150] and [151], set-based hierarchical MPC strategies are proposed to control the ESS considering multi-time scale dynamics for hybrid-electric aircraft, aiming to achieve mission objectives including a desired vehicle velocity and avionic load current, minimize fuel consumption, and regulate the fast under-damped dynamics in the EPS. However, in these papers, MPC for battery management is not the focus, and the control problem is formulated without much detail about, for example, how to cope with different control targets and increase algorithm feasibility, which has left considerable scope for further investigation and analysis here. Hence, this chapter aims to address these issues in the proposed MPC strategy for MEA EPS.

In the previous works of the MPC applications, the flexibility of the MPC design including the objective function formulation, prediction horizon length, weighting factors to prioritize different operating criteria, and the related impacts on the system performance have been neglected by adopting empirical settings for these parameters. Although some tuning may have been conducted in these works to obtain the setting, there is no systematic research for tuning and deciding these settings. Investigating how these degrees of freedom can affect the control system performance will help to better decide the appropriate settings to use for MPC depending upon the system requirements. This chapter will contribute to this investigation by designing a system-level MPC-based operation management strategy for an MEA MS-ES-L subsystem. The analysis in this study can be extended to other complex systems including storage systems and load management, such as those studied for the entire EPS in Chapter 4 and Chapter 6.

In this chapter, to solve the multi-objective optimal operation management problem of the studied EPS, an MPC-based operation management strategy is introduced which aims to intelligently manage the onboard energy storage systems and exploit flexibility in the demand-side while satisfying time-varying operational requirements. Different objective functions are proposed with various cost function terms to reach the operating goals, where each objective function can perform differently for each control target. To evaluate the designed control system performance, an evaluation index for each target is proposed, to quantify system performance across all flight stages. All objective functions are evaluated by the proposed

indices, varying the prediction horizon from short to long; hence, the impact of various prediction horizons for each objective function can be compared. This evaluation procedure is conducted with the load profiles having different changing frequencies and variations so that the analysis can consider different load cases. Based on the proposed index for each target, a multi-objective evaluation index is also proposed as an overall performance criterion, by which the final selection of the objective function and the length of the prediction horizon can be performed.

In addition to analysis of the degrees of freedom in an MPC setting, this work also improves the feasibility of the MPC-based control strategy to adapt the controller to real-time operating conditions. On the one hand, soft constraints are introduced to cope with the non-accurate estimation of the battery SOC. The optimization problem to be solved by the control system is formulated as a MILP problem, which includes both objective functions and system constraints related to the system power flow, energy conversion, and connection constraints, benefitting from certainty for global optimal solutions [152]. As the system only operates normally when the MILP-MPC algorithm provides a feasible solution, the algorithm should tolerate (soft) bounds-exceeding situations (i.e., SOC exceeds the target range). On the other hand, the real-time application requires that the sample time of the MPC can meet the possible computation time variations when dealing with different operating conditions. For each objective function, the worst-case values of the maximum computation time are recorded for various prediction horizon lengths. The sample time can be selected appropriately by considering the maximum computation time at the design stage, which guarantees that the MPC can be adopted for online optimization in real time. Finally, a real-time test is conducted for the studied system, to verify the real-time application of the proposed MPC-based operation strategy.

4.2 System description and MILP-MPC control

4.2.1 Nomenclature

All the main symbols used in this chapter are listed in Table 4.1-Table 4.4.

Table 4.1 Notations of parameters for this chapter

Parameters			
k	Time intervals, k∈$\mathbb{Z}_{\geq 0}$	LO/HI	Lower/upper bounds of the battery SOC target range
H	Prediction horizon (s)	P_{in}^{max}	Maximum input power from the MS-side (kW)
T_s	Sampling time (s)	$P_{Li}^{shed}(k)$	The *i*th non-critical load power (kW)
T	Total simulation time (s)	γ_{Li}	The priority of the *i*th non-critical load
η_{ch} / η_{disch}	Battery charging/discharging efficiency	P_{ch}^{max} / P_{disch}^{max}	Maximum charging/discharging power (kW)
B_{cap}	Battery capacity (kWh)	$P_{Li}^{nonshed}(k)$	The *i*th critical load power (kW)
N_{Li}	Total number of non-critical loads		

Table 4.2 Notations of variables for this chapter

Continues Variables			
$P_{in}(k)$	Input power from the MS-side (kW)	$SOC(k)$	Battery state of charge
$P_{ch}(k)$	Battery charging power (kW)	$\varepsilon(k)$	Tolerance for lower bound of battery *SOC*
$P_{disch}(k)$	Battery discharging power (kW)	$\vartheta(k)$	Tolerance for upper bound of battery *SOC*
$P_{batt}(k)$	Battery overall power (kW)		
Binary Variables			
$\zeta_{ch}(k)$	Indicator for charging the battery	$\zeta_{disch}(k)$	Indicator for discharging the battery
$S_{Li}(k)$	Contactor connection status of the *i*th non-critical load		

Table 4.3 Notations of cost function terms for this chapter

Cost functions			
J_{SLi}	Cost function for minimizing total load shedding	J_{Δ}	Cost function for keeping SOC within the target range
$J_{\delta Li}$	Cost function for minimizing switching activities	J_{SOC}	Cost function for maximizing SOC to the upper bound
J_{Pch}	Cost function for maximizing charging power	J_{Pbatt}	Cost function for minimizing battery power variations
J_{Pdisch}	Cost function for minimizing discharging power		
Weighting factors			
w_S	Weighting factor for J_{SLi}	w_{Δ}	Weighting factor for J_{Δ}
w_{δ}	Weighting factor for $J_{\delta Li}$	w_{SOC}	Weighting factor for J_{SOC}
w_{Pch}	Weighting factor for J_{Pch}	w_{Pbatt}	Weighting factor for J_{Pbatt}
w_{Pdisch}	Weighting factor for J_{Pdisch}		

Table 4.4 Notations of evaluation terms for this chapter

Evaluation Indices			
G_{SLi}	Evaluation index for total load shedding	G_{Pbatt}	Evaluation index for battery power variations
$G_{\delta Li}$	Evaluation index for contactor status change	$G_{\overline{SOCR}}$, $G_{\underline{SOCR}}$	Evaluation index for SOC target range: upper and lower range bounds, respectively
G_{SOC}	Evaluation index for battery energy storage level		
Weights for multi-objective evaluation index			
v_S	Weight for G_{SLi}	v_{Pbatt}	Weight for G_{Pbatt}
v_{δ}	Weight for $G_{\delta Li}$	$v_{\overline{SOCR}}$,$v_{\underline{SOCR}}$	Weight for $G_{\overline{SOCR}}$, $G_{\underline{SOCR}}$ correspondingly
v_{SOC}	Weight for G_{SOC}		

4.2.2 System description

The controller is responsible for optimizing the control commands related to the MS (P_{in}) and ES (P_{batt}) as well as determining the connection/disconnection status of non-critical loads (S_{Li}) to guarantee power balance in the system while following operational goals. To do so, the power from the MS and the battery should equal the power required by the connected critical and non-critical loads, as shown below. In (4.1), the binary decision variable $S_{Li}(k)$ indicates

that the entire load will be supplied/shed by connecting/disconnecting the associated switch and there is no partial shedding. However, based on the load characteristics, it is straightforward to modify the model to shed part of the load if required.

$$P_{in}(k) - P_{batt}(k) - \sum_i S_{Li}(k) P_{Li}^{shed}(k) - \sum_j P_{Lj}^{nonshed}(k) = 0 \tag{4.1}$$

$$P_{batt}(k) = P_{ch}(k) - P_{disch}(k) \tag{4.2}$$

Equation (4.2) shows that the battery power is equal to either $P_{ch}(k)$ or $P_{disch}(k)$, during charging and discharging times, respectively (at least one of these values will be zero). The charging/discharging power of the battery is the control command that needs to be determined by the EPS control system, by directly adjusting the P_{in} as the load power changes. The SOC of the battery, as a system state variable, is evaluated using the discrete dynamic equation in (4.3), which is essential for predicting the future status of the ESS.

$$SOC(k+1) = SOC(k) + T_s \cdot \eta_{ch} \cdot \frac{P_{ch}(k)}{B_{cap}} - T_s \cdot \frac{P_{disch}(k)}{\eta_{disch} \cdot B_{cap}} \tag{4.3}$$

According to (4.1)-(4.3), the system model includes both continuous variables related to the power from the MS and the ESS as well as binary variables representing the connection/disconnection status of the noncritical loads. In addition, to avoid simultaneous charging/discharging of the battery, additional binary variables are introduced to show the charge/discharge status of the battery at each stage, which are formulated in (4.18)-(4.20) in Section 4.3.2 as charging/discharging mode constraints. The system dynamics introduced above, together with operational limitations over the prediction horizon, are considered as constraints in an MPC-based controller, which is presented in detail in Section 4.3. The core of the MPC strategy is a model of the system under control to predict the evolution of system output over the desired horizon. Thus, the system model introduced in this section is repeatedly updated based on the most recent information obtained from the system. In addition, a prediction of the system load over the prediction horizon is required.

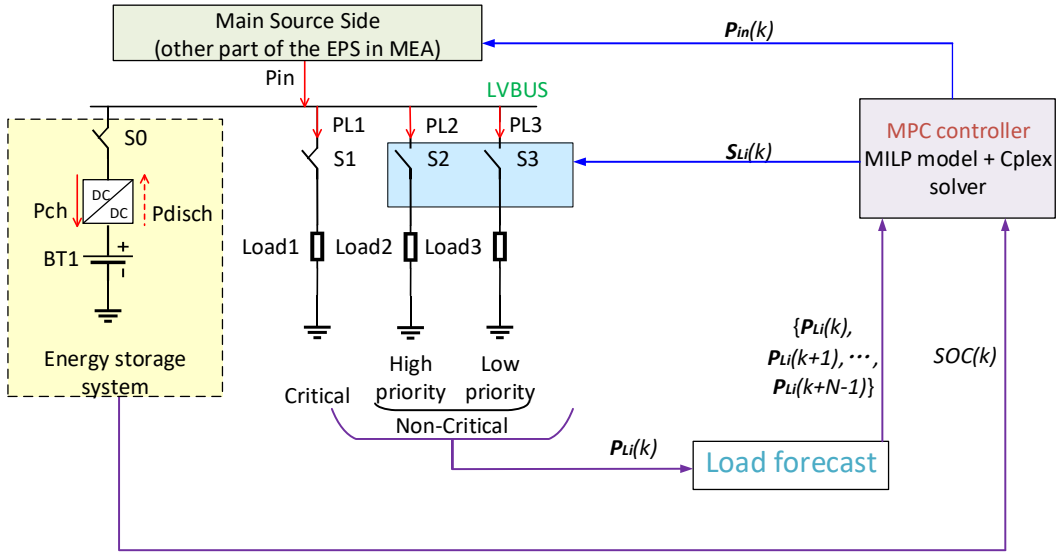
The MEA load can potentially be predicted by online machine learning-based methods combining the adjustment of the flight stages, and historical data [153], [58], which is outside of the scope of this study. In this thesis, the sampled load profile is used for prediction without adjustment for real-time flight power changes, and the deviations between the predicted load and the real values are ignored to simplify the analysis.

4.2.3 MILP-MPC controller framework

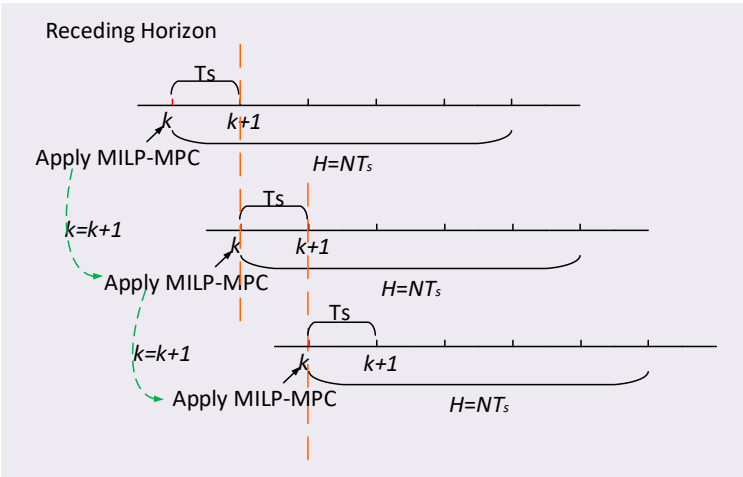
The proposed MPC-based control architecture is represented in Figure 4.2. This chapter concentrates on the system-level MPC controller, with a slow time scale in the order of 1 minute

to optimize the long-term performance (i.e., a variety of optimization targets for the entire fight stages) of the system. As can be seen in Figure 4.2, the controller received the updated information of the system at the beginning of each control cycle defined by the desired sampling time. This information includes the updated network constraints, battery status, and the prediction of the load demands and associated priorities.

The control problem for the target MEA is formulated as a dynamic MILP optimization problem similar to (3.1), and the CPLEX solver [154] is used to solve the problem at each time step, guaranteeing to find an optimal solution for each time step. The MS-ES-L system is modeled as a discrete-time dynamic system with sampling time T_s as introduced in the previous section. The structure of the MILP-MPC controller framework will now be explained.



(a) MILP-MPC controller diagram



(b) Receding horizon framework

Figure 4.2 Online MILP-MPC optimization procedure with receding horizon

As illustrated in Figure 4.2 (b), at each time step k, $k = 0, 1, \ldots, N\text{-}1$, an online optimization problem is solved over the finite prediction horizon H. The prediction horizon indicates the time it will look ahead into the future to evaluate the current cost function, subject to several technical and operational constraints. This can be calculated as $H = N \cdot T_s$ [155]. The MPC works based on a receding horizon scheme presented in Figure 4.2. At each time step k, the MPC controller receives the updated status of the system and finds the solution of a finite horizon optimization problem. The result is an optimal control sequence over the optimization horizon. However, only the first sample of the optimal control sequence is applied to the system, and the control problem is shifted to the next time step $k + 1$ as shown in Figure 4.2. The MILP-MPC controller is explained in detail in the rest of this section. The controller aims to keep the battery energy storage highly charged, with fewer power variations to prolong the battery life cycle, and to minimize load shedding, with fewer contactor switching operations needed, and this need to be appropriately modeled in the MPC optimization problem. The optimization problem including these operating criteria and system constraints is introduced in the next section.

MILP-MPC controller

(1) Update system state at time step k

(a) Initialize the model with the measured/estimated state of the components, e.g., $SOC(k)$, load power measurement $\boldsymbol{P}_{Li}(k)$

(b) Predict load demands over the prediction horizon H at each future sampling time $T_{s,}$ e.g., $\boldsymbol{P}_{Li}(k)$, $\boldsymbol{P}_{Li}(k+1)$, ..., $\boldsymbol{P}_{Li}(k+N-1)$

(2) Perform optimization: the high-level controller computes the optimal input sequence for the prediction horizon H, based on the updated system status and the predictions of the future system behavior. The optimal input sequence includes the decision of load shedding or not ($\boldsymbol{S}_{Li}$, $k = 0, 1, \ldots, N\text{-}1$, $H = NT_s$) and the input power reference on the MS-side P_{in} ($k = 0, 1, \ldots, N$, $H = NT_s$). The optimization problem, which is formulated by MILP, is solved using the CPLEX solver.

(3) Apply the first sample of the optimal control sequence.

(4) Set $k = k+1$, go to step 1, and repeat the process with the new state.

4.3 Formulation of objectives and constraints in MPC

As presented in Section 3.2, the system control problem can be mathematically modeled using a set of technical and operational constraints and objective functions. In this section, three different objective functions are proposed for multiple control targets, and the system constraints are introduced.

4.3.1 Designing the Objective Functions

There are several control targets which are being followed by the system under study. Firstly, the controller needs to minimize the total time for which loads are shed while maximizing the time duration for which the energy stored in the battery is kept within the target range (SOC(k)∈[LO, HI]). In addition, it needs to be ensured that the high-priority loads are shed less than the low-priority loads. Regarding the load management, instead of shedding/connecting loads continually, it is preferable to keep the contactors' switching activity as low as possible to prolong the components lifetime, and to avoid the transients and instabilities in the system, even though this may potentially increase the total time for which loads are disconnected. Moreover, the battery is preferred to be charged/discharged smoothly rather than constantly changing the status between charging and discharging modes to improve the life span of the battery [156]. Apart from load shedding targets, the battery management-related goals could be formulated with different cost functions as well as different weighting factors for battery charging/discharging power, maintaining battery SOC, and minimizing battery power variation. The following three objective functions are therefore proposed to formulate the desired operating criteria and to analyze the effects of different cost functions on the system performance.

4.3.1.1 The first proposed objective function (Obj1)

Obj1 in (4.4) denotes the first objective function combining the cost functions in (4.5)-(4.9) for each target by different weighting factors w_S, w_δ, w_{Pch}, w_{Pdisch}, and w_Δ. Cost function (4.5) indicates minimizing the total load shedding time by penalizing the shedding of loads with the load priorities. The change in load connections (connected/disconnected) for each time interval is minimized in (4.6). Since the energy stored in the battery can be calculated from the net power flowing to the battery, the cost function (4.7) and (4.8) can lead to maximizing the energy stored by penalizing the discharging and rewarding charging of the battery: the cost function in (4.7) encourages the system to charge the battery with as much power as is available, up to the rated value, while the cost function in (4.8) encourages the system to avoid battery discharging by minimizing the discharging power for every time interval. The charging speed of the battery can be changed by adopting different weighting factors for (4.7) and (4.8). For example, when $w_{Pch} > w_S$, the system will allow more load shedding to use power from the MS to charge the battery. When $w_{Pdisch} \gg w_S \gg w_{Pch}$, the system will shed loads when the battery is needed, but the charging will be slow as the MS priority is to supply loads rather than charging the battery.

$$Obj1 = w_S J_{S_{Li}} + w_\delta J_{\delta_{Li}} + w_{Pch} J_{P_{ch}} + w_{Pdisch} J_{P_{disch}} + w_\Delta J_\Delta \tag{4.4}$$

where

$$J_{S_{Li}} = \sum_{k=0}^{N-1} \sum_{i=1}^{N_{Li}} \gamma_{Li}(1 - S_{Li}(k))/N \sum_{i=1}^{N_{Li}} \gamma_{Li} \tag{4.5}$$

$$J_{\delta_{Li}} = \left(\sum_{k=0}^{N-1} \sum_{i=1}^{N_{Li}} |S_{Li}(k+1) - S_{Li}(k)|\right)/(N \cdot N_{Li}) \tag{4.6}$$

$$J_{P_{ch}} = \left(\sum_{k=0}^{N-1} \left(P_{ch}^{max} - P_{ch}(k)\right)\right)/(NP_{ch}^{\max}) \tag{4.7}$$

$$J_{P_{disch}} = \left(\sum_{k=0}^{N-1} \left(P_{disch}(k)\right)\right)/(NP_{disch}^{\max}) \tag{4.8}$$

$$J_{\Delta} = \left(\left(\sum_{k=0}^{N-1} \left(\varepsilon(k) + \vartheta(k)\right)\right)\right)/N \tag{4.9}$$

For battery management, the battery SOC is preferred to be kept in a target range (LO, HI) that can be modeled as a constraint. However, when there is a deviation between the predicted load and the actual load, the battery SOC might be temporarily out of the target range, which would prevent the solver from finding a feasible solution if modelled as a hard (inflexible) constraint. Hence, rather than enforcing this requirement as a hard constraint, two slack variables ($\varepsilon(k)$ and $\vartheta(k)$) are introduced to penalize the deviation of the battery SOC from the target's lower and upper bounds in the objective function as presented in (9). In this way, the controller will try to keep the SOC within the target range, or minimize the deviations when this is not possible. These variables are explained further in Section 4.3.2 below.

4.3.1.2 The second proposed objective function (Obj2)

Adding the cumulative battery SOC to the objective function will increase the average energy stored in the battery. Equation (4.8) represents a normalized cost function to increase the battery SOC to be as close as possible to the upper bound. Hence, Obj2 in (4.10) is formed by adding the battery SOC cost function to Obj1 in (4.4), with its weighting factor w_{SOC}. Compared to the cost for charging/discharging power in (4.7) and (4.8), including SOC in the cost function will directly control SOC to maintain the desired reference value, which can be adjusted according to the applications. In this work, the desired reference value is set to be HI. Moreover, the charging will speed up more when longer prediction horizons are selected, as the SOC is a time-accumulated value, reflecting the accumulated charge for the whole prediction horizon.

$$Obj2 = w_{\delta} J_{\delta_{Li}} + w_{S} J_{S_{Li}} + w_{SOC} J_{SOC} + w_{Pch} J_{P_{ch}} + w_{Pdisch} J_{P_{disch}} + w_{\Delta} J_{\Delta} \tag{4.10}$$

where

$$J_{SOC} = \left(\sum_{k=0}^{N-1} |HI - SOC(k+1)|\right)/(N \cdot HI) \tag{4.11}$$

4.3.1.3 The third proposed objective function (Obj3)

The aforementioned objective functions control the energy stored in the battery. However, proposing a cost function to prolong the battery life is also important for aircraft EPS for longer-term safe flights, for example, reducing the battery charging/discharging current variations and reducing charging/discharging operations [59]. In this work, it is assumed that the battery voltage has small deviations, so that reducing the battery charging/discharging current variations is equivalent to reducing the charging/discharging power variations. This also reduces the charging/discharging operations to reduce the charging cycle, which also benefits the battery lifetime. The cost for minimizing the battery charging/discharging power change $J_{P_{batt}}$ is presented in (4.13), where $P_{batt}(k) = P_{ch}(k) - P_{disch}(k)$ presents the battery net power. Obj3 represented in (4.12) is formulated by adding this prolonging battery lifetime cost to Obj2 in (4.10) with the weighting factor w_{Pbatt}.

$$Obj3 = w_{\delta}J_{\delta_{Li}} + w_{S}J_{S_{Li}} + w_{SOC}J_{SOC} + w_{Pch}J_{P_{ch}} + w_{Pdisch}J_{P_{disch}} + w_{Pbatt}J_{P_{batt}} + w_{\Delta}J_{\Delta} \tag{4.12}$$

where

$$J_{P_{batt}} = \left(\sum_{k=0}^{N-1}|P_{batt}(k+1) - P_{batt}(k)|\right)/\left(N(P_{ch}^{max} + P_{disch}^{\max})\right) \tag{4.13}$$

4.3.2 System constraints

(1) Power balance constraints

For the LV bus, the sum of power flowing into/out of it equals zero (Kirchhoff's Current Law for a given voltage), assuming no losses within the bus itself. Hence, for the system presented in Figure 4.1, the power from the MS and the battery equals that required by the connected critical and non-critical loads, which can be formulated as (4.1) and (4.2), which is mentioned in Section 4.2.2.

(2) Storage dynamics

The battery SOC can be calculated from the charging/discharging power over time using (4.3) presented in Section 4.2.2.

(3) Hard and soft constraints of SOC

Battery $SOC \in [0,1]$, where *SOC* = 1 indicates a fully charged battery, while *SOC* = 0 corresponds to a depleted battery. In the aircraft, *SOC* is preferred to be kept within a target range [LO, HI]. Therefore, upper and lower bounds are defined in (4.14), where LO = 0.3, HI = 0.9 is selected in this case, which could be presented as hard constraints for the optimization.

$$0.3 \leq SOC(k) \leq 0.9 \tag{4.14}$$

However, the hard constraints (4.14) increase the sensitivity of the algorithm to imprecise load predictions, i.e., the actual load power fluctuations from the predicted mean load power demand. Because SOC is related to the stored or released energy, which is influenced by power fluctuations, it is necessary to allow SOC to vary slightly outside of this range in real situations, due to unpredicted power consumption variations. In this case, the hard constraints (4.14) would prevent finding a feasible solution. Therefore, soft constraints in (4.15) - (4.17) are proposed in our model to improve the feasibility of the solution strategy of the MILP-MPC algorithm. Variables $\varepsilon(k)$ and $\vartheta(k)$ are introduced to relax the hard upper and lower bounds in (4.14). The maximum allowed deviation for both bounds is 0.1 in this case. By adding two large weight factors to $\varepsilon(k)$ and $\vartheta(k)$ in the cost function as presented in Obj1 (4.4) and (4.9), SOC will usually be kept within the target range [0.3, 0.9], while allowing some tiny deviations when necessary.

$$0.3 - \varepsilon(k) \leq SOC(k) \leq 0.9 + \vartheta(k) \tag{4.15}$$

$$0 \leq \varepsilon(k) \leq 0.1 \tag{4.16}$$

$$0 \leq \vartheta(k) \leq 0.1 \tag{4.17}$$

(4) Charging/discharging mode constraints

The battery can be either charged or discharged by the system. Therefore, two binary indicators are introduced to represent different modes in (4.18), (4.19), and (4.20), allowing the modes to be treated differently.

$$\zeta_{ch}(k) + \zeta_{disch}(k) = 1, \zeta_{ch}(k), \zeta_{disch}(k) \in \{0,1\} \tag{4.18}$$

$$0 \leq P_{ch}(k) \leq \zeta_{ch}(k) \cdot P_{ch}^{max} \tag{4.19}$$

$$0 \leq P_{disch}(k) \leq \zeta_{disch}(k) \cdot P_{disch}^{max} \tag{4.20}$$

(5) Bounds of input power from the MS-side

The input power from the MS-side is limited by the maximum power that can be transferred by the DC/DC converters, and these input power bounds are presented in (4.21).

$$0 \leq P_{in}(k) \leq P_{in}^{max} \tag{4.21}$$

4.4 Evaluation for various objectives

The objective functions designed in Section 4.3.1 lead to different control problems and consequently different operating strategies for the MS-ES-L system, which are also impacted by the prediction horizon and the load profile. To compare the differences caused by these factors, an evaluation framework is proposed in this section to quantify the control results for all flight stages. The overall flight time is $T = M \cdot T_s$, where M is the total number of time intervals. Moreover, to verify that the proposed method is suitable for real-time applications, the computation time for the MILP-MPC controller should be less than the sample time T_s. As the computation time can be impacted by the objective function formulation, prediction horizon, and load samples, the impact of these factors on the computation time is also studied in this section.

4.4.1 Model parameters

The model parameters, including the MS-ES-L system component parameters, are listed in Table 4.5, and the weighting factors are listed in Table 4.6. These weighting factors are selected by the method proposed in [157] – weighting factors are tuned to achieve the optimized performance of the multi-objective index. This will be further discussed in Section 4.4.7. The MILP-MPC controller sample time T_s is selected as 1 min, the verification for the sample time selection will be demonstrated in Section 4.5.1. The total flight time is 150 min.

Table 4.5 Parameters for the MS-ES-L system

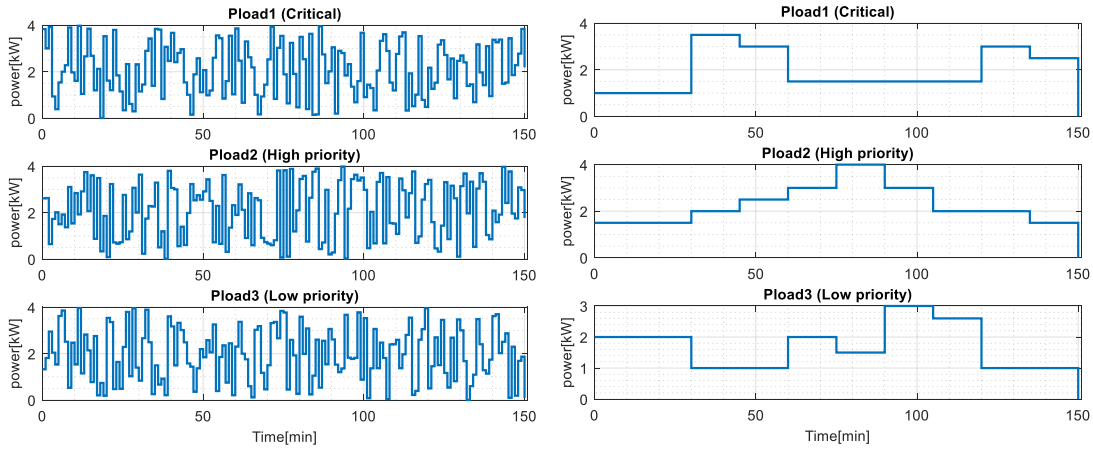
B_{cap}	4kWh	P_{ch}^{max}, P_{disch}^{max}	4kW
P_{in}^{max}	4kW	η_{ch}, η_{disch}	90%
P_{Load}^{max}	4kW	$SOC(0)$	0.3

Table 4.6 Weighting factors in objective functions

w_S	5	w_δ	34.7
w_{SOC}	16	w_Δ	10^5
w_{Pbatt}	2	w_{Pdisch}	5.1
w_{Pch}	3.1 in Obj1, 2.8 in Obj2 and Obj3		

For evaluating the load profile impacts on the results, two types of load profiles are used. In Figure 4.3(a), a randomly changing load profile is considered, while Figure 4.3(b) demonstrates the load profiles based on different flight stages. The flight stages include ground (pre-departure and taxiing-out), takeoff, climb, cruise, descent, loiter, and landing. Each load

system requires a different amount of power at each flight stage. For example, the cabin power demand reaches the highest level at the cruise stage, which can be several times larger than the power demand at other stages. In addition, the power demand of the environment control system increases dramatically as soon as the aircraft takes off and keeps almost the same value for the following stages, while the landing gear only requires power during the ground, takeoff and landing stages [21], [158]. Therefore, compared to the load profiles in Figure 4.3(a), which change every minute, the profiles in Figure 4.3(b) change much slower where each load level lasts at least for 15 min. However, an average load power of 2 kW can be seen in both cases.



(a) Case 1: Random load profiles

(b) Case 2: Load profiles based on flight stages

Figure 4.3 Different load cases

In the following subsections, eight evaluation indices are proposed. The control results are evaluated by each of the proposed indices for both load scenarios when objectives Obj1-Obj3 are adopted for prediction horizons, H, varying from $1T_s$ to $30T_s$ (N = 1, 2, …, 30). Each evaluation index represents the quantified performance in the corresponding area, and in all cases lower values indicate better performance.

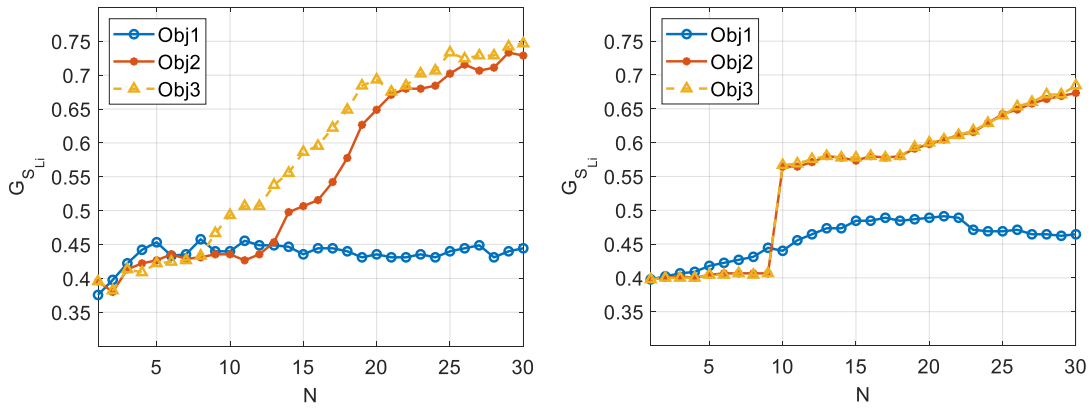
4.4.2 Load shedding index

The normalized load shedding index quantifies the average proportion of shed loads throughout the whole flight time T = 150 min, as shown in (4.22).

$$G_{S_{Li}} = \left(\sum_{k=0}^{M-1}\sum_{i=1}^{N_{Li}}\left[\gamma_{Li}\left(1 - S_{Li}(k)\right)\right]\right)/\left(M \cdot \sum_{i=1}^{N_{Li}}(\gamma_{Li})\right) \tag{4.22}$$

In Figure 4.4, the load shedding index values are compared when adopting different prediction horizons and objective functions, with case 1 and case 2 showing the results for adopting different load profiles. For both load cases, Obj2 and 3 have similar changes: when the prediction horizon is short, load shedding remains lower than for Obj1, while load shedding increases quickly as the prediction horizon becomes longer, causing Obj2 and 3 to have more

load shedding than Obj1 with long prediction horizons. Although the load shedding for Obj1 also has an incrementally increasing tendency when N increases for the second load case, the growth rate is much slower compared to Obj2 and 3. This difference between Obj1 and Obj2-3 is caused by the cost function J_{SOC} - more loads are shed to speed up the SOC that accumulates when N increases.



(a) Case 1 (b) Case 2

Figure 4.4 Comparison of different prediction horizons and objective functions based on the normalized shedding index for two load cases.

Comparing Obj2 and Obj3, when the loads frequently vary, as presented in case 1, the load shedding for Obj3 increases at a higher rate than Obj2, while Obj3 has less load shedding than Obj2 when $N \leq 6$. This is caused by the cost function J_{Pbatt} in Obj3. By changing the load shedding scheduling and adjusting the input power from MS, the battery can be charged/discharged smoothly. Combining with J_{SOC}, more load shedding will be conducted as N increases so that the system keeps charging the battery with fewer power fluctuations. When the load varies less and slowly, as load profiles in case 2, the load shedding curves for Obj2 and Obj3 mostly overlap, because the stable load profile lacks the scheduling possibilities while the WF for J_{Pbatt} is small; hence, J_{SOC} dominates J_{Pbatt} in this case. Comparing the results for $N = 9$ in Figure 4.4, there is a sharp rise in the index value at $N = 10$, which indicates that the shedding of high-priority loads is increased.

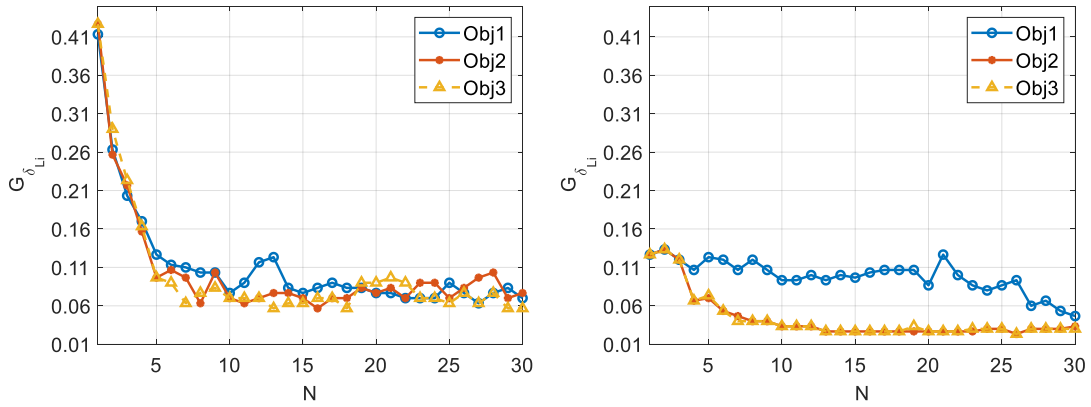
In summary, Obj1 has better performance in load shedding compared to Obj2 and 3 on average. However, when the selected prediction horizon is not too long, e.g., $N \leq 9$ in our case, Obj2 and 3 can have better load shedding performance.

4.4.3 Contactor status change index

The average number of connection status changes for each contactor in the whole period is presented in (4.23), where N_{Li} indicates the total number of non-critical sheddable loads.

$$G_{\delta_{Li}} = \left(\sum_{k=0}^{M-1}\sum_{i=1}^{N_{Li}}|S_{Li}(k+1) - S_{Li}(k)|\right)/\left((M \cdot N_{Li})\right) \tag{4.23}$$

These index values are compared in Figure 4.5 when adopting different prediction horizons and objective functions, with case 1 and case 2 showing the results for different load profiles. In general, the change in contactor status is reduced as N increases in both cases for Obj1-Obj3, while the curve for Obj1 in case 2 fluctuates the most. In both load cases, the contactor change values for Obj2 and 3 decrease very quickly when $N < 10$ and then remain at a low level when the prediction horizon is longer. Moreover, when N is in this range, compared with the results for load shedding in Figure 4.4, Obj2 and 3 also have good performance for the load shedding index. This also benefits from the inclusion of J_{SOC}, as it takes the results of power integration over time into consideration within the prediction horizon.



(a) Case 1 (b) Case 2

Figure 4.5 Comparison of different prediction horizons and objective functions based on the contactor status change index for two load cases

It can be concluded that Obj2 and 3 perform better than Obj1 for maintaining the contactor status in different load cases. Moreover, for the contactor status change index, a very long prediction horizon is unnecessary for Obj2 and 3, saving computation time while still achieving good results.

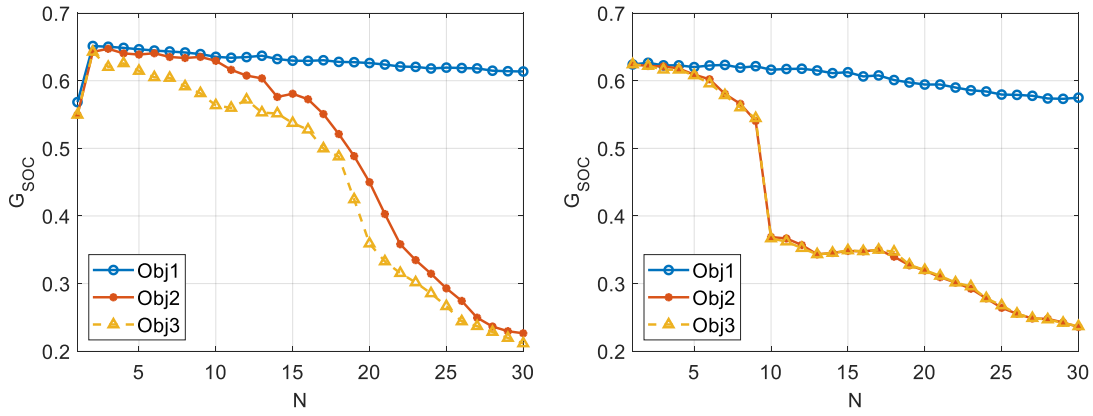
4.4.4 Battery energy storage level index

In aircraft applications, it is preferable to keep the battery highly charged to cope with emergency cases and unforeseen situations. Hence, when designing the optimization algorithms, the objective functions are designed to maximize the average energy stored in the battery. This index, presented in (4.24), is proposed to evaluate the average level of the energy stored during the studied scenarios.

$$G_{SOC} = \left(\sum_{k=0}^{M-1}|0.9 - SOC(k)|\right)/\left((M \cdot 0.9)\right) \tag{4.24}$$

Figure 4.6 shows the comparison of the G_{SOC} index values with different prediction horizons and objective functions, with case 1 and case 2 showing the results for adopting different load profiles. In general, the energy storage level index value is reduced as N increases in both cases for Obj1-Obj3, while for the load case 1, the index values for MILP (N = 1) are less than the ones for MILP-MPC ($N \geq 2$) when $N \leq 12$ for Obj3, $N \leq 16$ for Obj2, and $N \leq 30$ for Obj1. When N = 1, the contactor status changes will not impact the optimization results for each time step. Combined with the frequently varying loads, the SOC is therefore improved by shedding/connecting loads with high power demands continuously. However, when N = 2, the number of contactor status changes is much reduced (the index value is reduced by more than 31.7%) compared to the value when N = 1. In the meantime, the battery will be used for supporting loads even the loads' demands could be high, which slows down the SOC accumulation.

Comparing the SOC changing rate for Obj1-3 with the MILP-MPC method, for both load cases, Obj2 and 3 improve SOC level at a higher rate than Obj1 when N increases, since both Obj2 and Obj3 benefit from the cost function J_{SOC} to speed up the energy storage in the long term. For load case 1, Obj3 speeds up the SOC accumulation with a higher rate than Obj2, as the cost function J_{Pbatt} in Obj3 tends to keep the battery charging with few power fluctuations.



(a) Case 1 (b) Case 2

Figure 4.6 Comparison of different prediction horizons and objective functions based on the battery energy storage level index for two load cases

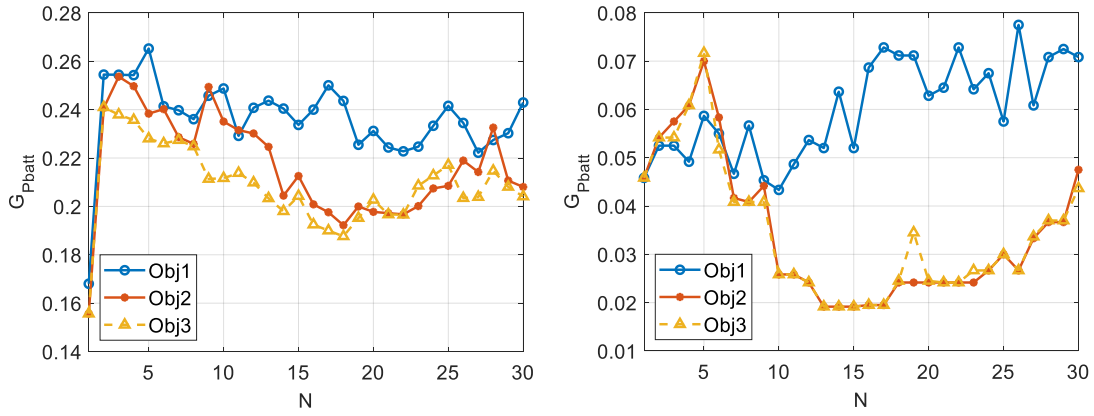
This suggests that Obj3 has the best performance for the battery storage level index. When adopting Obj3, the prediction horizon selected does not necessarily need to be very long, as it charges the battery much faster than Obj1.

4.4.5 Battery power change index

The battery life will be shortened when the battery power is frequently changed [59]. Index (4.25) is therefore proposed to calculate the total battery power change for all flight stages.

$$G_{P_{batt}} = \left(\sum_{k=0}^{M-1} |P_{batt}(k+1) - P_{batt}(k)|\right) / \left(M\left(P_{ch}^{max} + P_{cisch}^{max}\right)\right) \tag{4.25}$$

Figure 4.7 presents the comparison of the battery power change index values with different prediction horizons and objective functions, with case 1 and case 2 showing the results for adopting different load profiles. In both load cases, for each *N*, Obj3 usually has a better performance compared to Obj1, because Obj1 does not contain the cost function J_{Pbatt} to minimize the power change. However, as Obj2 has the cost function J_{SOC} in common with Obj3 with relatively high WF, the index value curve of Obj2 has similar trends as Obj3—the value is reduced to the minimum value and then slightly rises with variations when *N* increases from 2 to 30. Because the load shedding and the reduction in the load on/off changes can avoid the battery changing between the charging and discharging modes, Obj2 and Obj3 perform similarly in these indices. By adding the cost function J_{Pbatt} in Obj3, the charging power can be smoothed whenever it is possible. On the other hand, when *N* increases ($N > 20$) to keep accumulating SOC, more power will be injected into the battery, thereby increasing the battery charging power variation. Moreover, J_{Pbatt} and J_{SOC} can impact the results for load shedding and the contactor status changes, which results in the battery power change fluctuations, as can be seen in Figure 4.7.



(a) Case 1 (b) Case 2

Figure 4.7 Comparison of different prediction horizons and objective functions based on the battery power change index for two load cases

Based on this comparison, Obj3 has the best performance for the index of battery power change, which also indicates that this objective function is preferred when battery life is important.

4.4.6 SOC target range index

Since the soft constraints of SOC are introduced to improve the feasibility of the solution strategy, the real SOC might exceed the target range of [0.3, 0.9]. The SOC target range index

is built to evaluate the proportion of the spare SOC (difference between the real (hard) SOC limit and the soft target) that the out-of-range SOC is using. Equations (4.26) and (4.27) are considered for the upper and lower bounds respectively, where *S* is the set of all time intervals that satisfy the desired ranges. The SOC can be out of range in the following situations: 1) when there are deviations between the predicted and realized load which the controller cannot handle in time; or 2) the controller has a delay in sending and receiving signals. In this section, the ideal situation is considered; hence, the SOC target range index will be observed to remain 0.

$$G_{\overline{SOCR}} = \left(\sum_{k \in S:(SOC(k)>0.9)} (SOC(k) - 0.9)\right)/(1 - 0.9) \tag{4.26}$$

$$G_{\underline{SOCR}} = \left(\sum_{k \in S:(SOC(k)<0.3)} (0.3 - SOC(k))\right)/0.3 \tag{4.27}$$

4.4.7 Index for multi-objective problem

Although the performance of each objective function has been analyzed in subsection 4.4.2-4.4.6 for each index, the overall performance of each objective function concerning the length of prediction horizon *N* still needs to be investigated. For a multi-objective problem with conflicting cost functions, e.g., J_{SOC} and J_{SLi}, there are trade-offs among the evaluation indices. Hence, weight parameters for each index are selected to represent the practical requirements, i.e., the priorities of each optimization target. The final overall index is formed with the full knowledge of system performance throughout the whole operation, by using the above-mentioned indices, which are combined with appropriate user-specified weight parameters. The WFs utilized by the MPC to get the best overall results may differ from the weights used in the final evaluation. A neural network-based method in [157] is adopted for selecting WFs and weights in the overall index. The multi-objective evaluation index is presented in (4.28) with the adopted weights listed in Table 4.7.

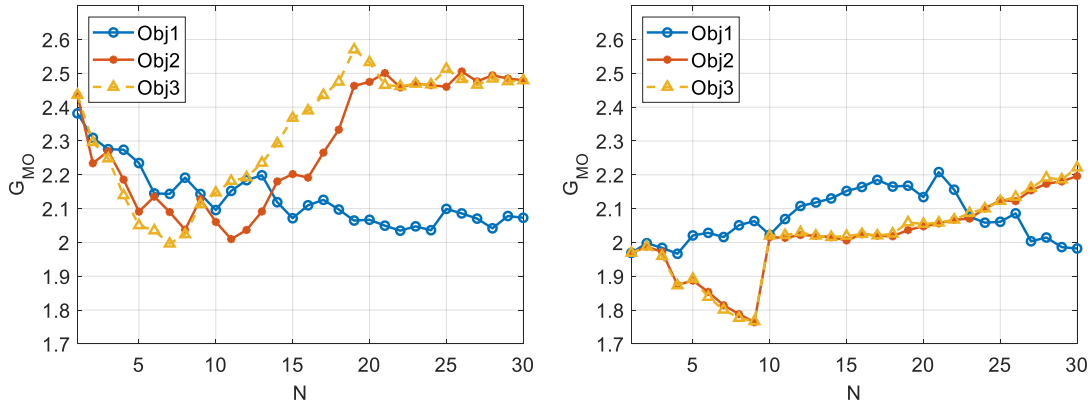
$$G_{MO} = v_S G_{S_{Li}} + v_\delta G_{\delta_{Li}} + v_{SOC} G_{SOC} + v_{Pbatt} G_{P_{batt}} + v_{\overline{SOCR}} G_{\overline{SOCR}} + v_{\underline{SOCR}} G_{\underline{SOCR}} \tag{4.28}$$

Table 4.7 Weights for the multi-objective index

v_s	2.8	v_δ	1.68
v_{SOC}	1	v_{Pbatt}	0.4
$v_{\overline{SOCR}}$	10^4	$v_{\underline{SOCR}}$	10^4

Figure 4.8 presents the comparison of the proposed multi-objective evaluation index values with different prediction horizons and objective functions; case 1 and case 2 show the results for adopting different load profiles. The figure shows that Obj2 and 3 can provide the optimal solutions with a shorter prediction horizon compared with Obj1. Compared to Obj2, Obj3

reaches a lower index value with a shorter horizon for load case 1. These results are heavily based on the selection of the weights for each index, but with the adjustment of the weights by the users according to their application requirements, the optimal objective function with a suitable prediction horizon can be selected.



(a) Case 1 (b) Case 2

Figure 4.8 Comparison of different prediction horizons and objective functions based on the multi-objective index for two load cases

4.4.8 Discussions

To summarize the results of the comparison study performed in the previous section, the best objective functions for each evaluation index with short and long horizons are listed in Table 4.8. In addition, the performance change based on horizon selections of the objective functions in Section 4.4.1 is presented in the table.

Table 4.8 Objective function with the best performance and key features for each index when the horizon changes

Index	**Best Obj with a Short Horizon**	**Best Obj with a Long Horizon**	**Key Features of Performance Tendency When Horizon Increases**	**Combinations for Best Performance**
Load shedding	Obj2-Obj3	Obj1	1. Performance of Obj1-Obj3 is better when a shorter horizon is applied (e.g., N < 10) 2. Performance of Obj2-Obj3 is reduced rapidly after the inflection point (N = 10) when horizon increases	Obj2-Obj3 with a short horizon (e.g., N < 10)

Contactor status change	Obj2-Obj3	Obj2-Obj3	1. Before the inflection point (N = 5), the performance of Obj1-Obj3 is improved rapidly when the horizon increases 2. After the inflection point, the performance has few changes when the horizon increases	Obj2-Obj3 at and after the inflection point (N ≥ 5)
Battery energy storage level	Obj3	Obj3	1. Performance of Obj1-Obj3 is better when a longer horizon is applied (e.g., N > 10) 2. Performance of Obj2-Obj3 is improved rapidly after the inflection point (N = 10) when horizon increases	Obj3 with a long horizon (e.g., N > 10)
Battery power change	Obj3	Obj3	1. Before the inflection point (N = 13), the performance of Obj2-Obj3 is improved when the horizon increases 2. After the inflection point, the performance of Obj2-Obj3 is reduced when the horizon increases 3. Obj1 doesn't show relativity to horizon changes	Obj2-Obj3 at inflection point (N = 13)
Multi-objective	Obj2-Obj3	Obj1	1. Before the inflection point (N = 9), the performance of Obj2-Obj3 is improved when the horizon increases 2. After the inflection point, the performance of Obj2-Obj3 is reduced when the horizon increases 3. Obj1 requires a long horizon to improve the performance (e.g., N > 25)	Obj2-Obj3 at inflection point (N = 9)

4.5 Real-time experiment

4.5.1 Computational time analysis

For real-time MPC applications, computation time is the key issue to be considered, as the time required to complete the computation should be less than the sampling time. When adopting the CPLEX solver, the computation time is influenced by several factors: 1) more

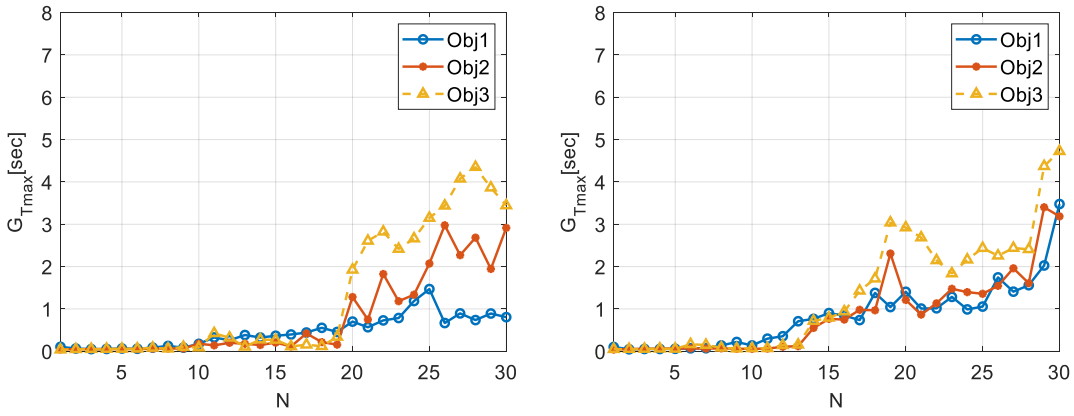
complex models will often take a longer time; 2) longer prediction horizons will take a longer time; and 3) different input values, such as different load data as inputs to the MPC controller, can cause different computation times. Hence, to verify the MPC real-time application, the worst-case analysis of the computation time is conducted for Obj1-3. For each objective function and each N, the MPC controller will finally adopt 150 optimal solutions (one sample at each time step), and the maximum computation time for the MPC controller in any step is recorded as the worst-case.

Figure 4.9 presents the maximum computation time G_{Tmax} changes for each objective function with respect to N. In both load cases, the maximum computation time for Obj1-3 has similar incrementally increasing tendencies as N increases: when $N \leq 10$, the computation time is less than 0.2 s; when $10 < N \leq 15$, the computation time is less than 1s; and when $N > 15$, the computation time will go above 1 s with the maximum value of less than 8 s. This indicates that the proposed MPC method could be adopted for real-time applications with selected sample times T_s larger than 10 s, during which the optimization would be completed, with the additional time being used for data measuring and communicating [159]. It is worth noting that a maximum computation time can be set in CPLEX. In this case, if the solver ran out of time, it would return the best solution that has been found in that time, rather than the optimal solution. In our case, T_s is set to 1 min because of the following reasons:

(1) A 1-minute sample time can provide the controller with enough time to obtain the measured status and updated load prediction, complete the optimization, and send the control signals to the system.
(2) The proposed MPC method is mainly designed to satisfy the long-term battery SOC and load management requirements in the high-level control system. Since the SOC and average loads will not change very much in a few seconds, the MPC controller would not be required to update the control references frequently in small time intervals in the order of seconds. On the other hand, if the MPC is required to run every few seconds to update the reference to cope with transients, the battery power and loads might change with every load fluctuation, which might cause instability in the system. In fact, instead of using MPC with long-term operating goals to act fast in response to the transient load changes, another real-time controller is usually added to the system at a lower control level, which will respond to the transient issues. For example, in Chapter 5, a low-level controller is proposed to cope with load changes within 1 s.

In summary, when adopting the proposed multi-objective evaluation index as the index for our overall preferred performance, Obj3 will have the best performance with a suitable

prediction horizon (N = 7 and N = 9 for the corresponding load cases), with a computation time of lower than 0.2 s.



(a) Case 1 (b) Case 2

Figure 4.9 Comparison of the worst-case computation time of different prediction horizons and objective functions for two load cases.

4.5.2 Real-time test

A real-time experiment was implemented in the "Aerospace Electrical Power Systems Innovations Laboratory" at the Aerospace Technology Centre at the University of Nottingham. The experimental setup is presented in Figure 4.10. The MS-ES-L system model was implemented in dSPACE 1006 for real-time simulation. The MILP-MPC controller was run in Matlab on a host PC, connected with the dSPACE. Every T_s (1 min), Matlab on the host PC uses the XIL API interface to read the measured data from dSPACE, including the load power $P_{Li}(k)$ and battery $SOC(k)$. The MILP-MPC controller in Matlab takes these values as inputs and calls the CPLEX solver to provide the optimal power reference on the MS side $P_{in}(k)$ and load shedding $S_{Li}(k)$. Finally, these optimal values are sent to the system implemented in dSPACE by the XIL API interface to realize real-time control. This experiment validates the suitability of the proposed system-level control framework for real-time implementation and the capability of the controller to provide the system with optimal control commands at specified control intervals to achieve the desired operating performance. It also verifies the coordination of the controller with the communication interfaces and local controllers at the lower level. This configuration (using PC and dSPACE) and using XIL API to read/write data and communicate between two levels, provides the opportunity to test the two-level control structure in real time. The physical system and local controllers are running all the time, and the system-level controller receives measurements from the system and updates its control commands on a regular basis (every one minute). In other words, they work in parallel. Otherwise, in a conventional series implementation with a PC and non-real-time simulation, the system and local controllers have to be stopped while running the system-level controller.

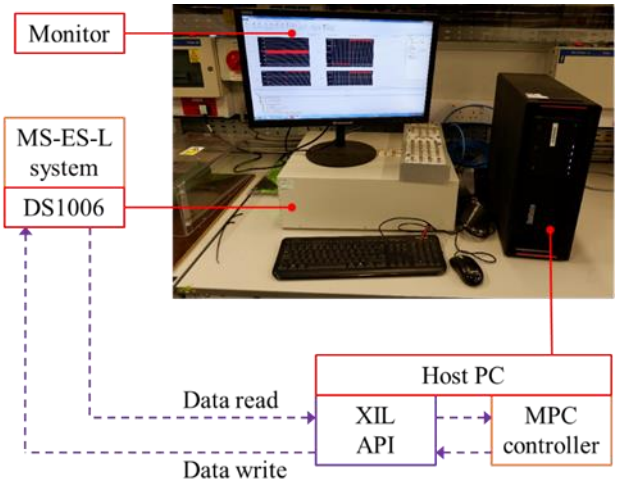
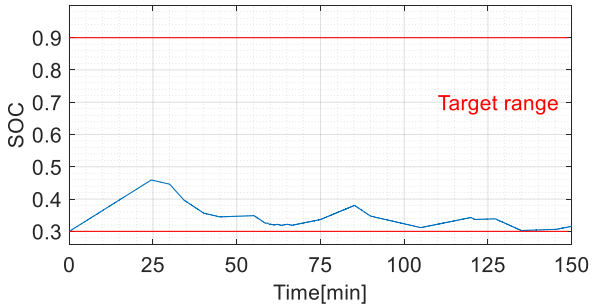


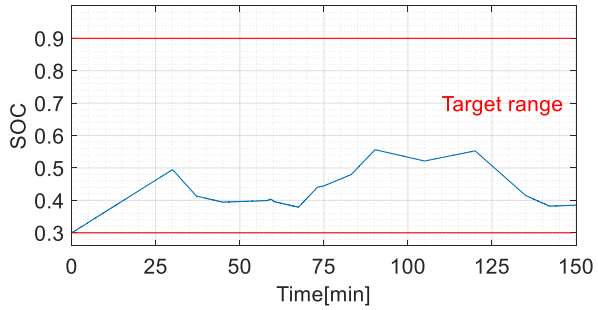
Figure 4.10 Experimental setup

The control results of MPC with Obj1-Obj3 for all flight stages were compared in this experiment. During the flight, the loads were changed following the profile in Figure 4.3 (b). According to the analysis in Section 4.4, the MPC for Obj3 performed best when $N = 9$ with a computation time of less than 0.2s. To verify this analytic conclusion based on the mathematical model, the MPC with Obj1-3 when $N = 9$ was applied in the experiment. The performance of each objective function can be visualized by observing the SOC changes, load shedding results, and battery power change. The real-time application of MPC was also verified. It should be noted that the duration of the flight time slot was scaled down from the 60 s to 3 s for these experiments, to complete them within 7.5 min instead of 150 min. The battery capacity was accordingly scaled down to 0.2 kWh during the experiment. From both analyses in Figure 4.8 and the experiment, Obj2 and Obj3 had the same control results when $N = 9$ for this load profile. Hence, in the following comparisons, only the control results for Obj1 and Obj3 are considered to study the differences.

Figure 4.11 presents the SOC measurement results during the flight stages, while Figure 4.11 (a) shows the results when MPC adopts Obj1, and Figure 4.11 (b) is related to Obj3. When Obj3 is adopted, the battery SOC is kept within 0.4-0.6 for most time intervals, with a maximum value of 0.56, while SOC is kept within 0.3-0.36 for most time intervals when adopting Obj1, with a maximum value of 0.46. As the SOC is close to the lower limit when adopting Obj1, the system will be less stable for coping with unexpected failure scenarios.

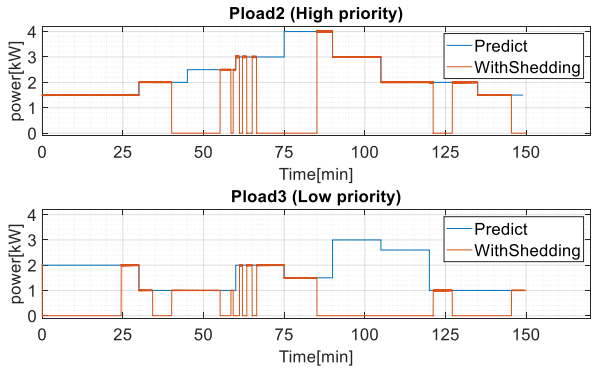


(a) SOC change with Obj1

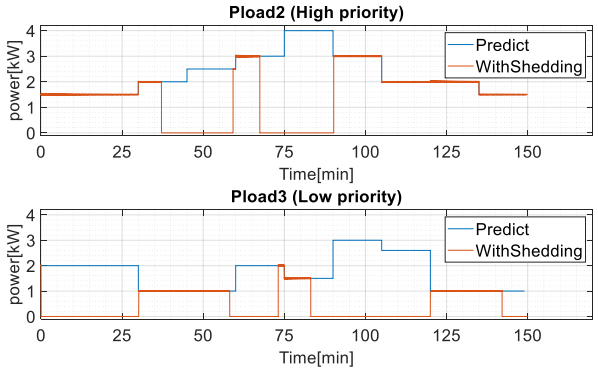


(b) SOC change with Obj3

Figure 4.11 SOC comparison for Obj1 and Obj3 when $N = 9$



(a) Load shedding with Obj1

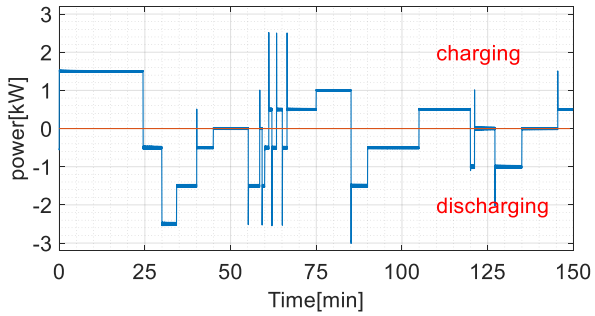


(b) Load shedding with Obj3

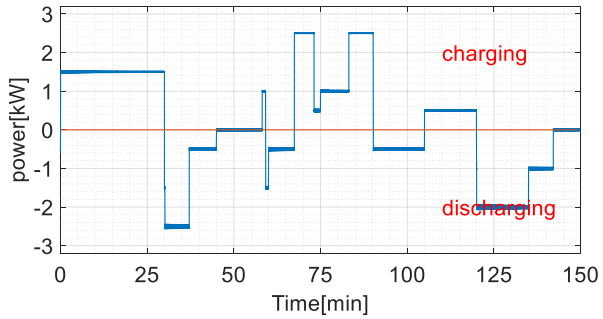
Figure 4.12 Load shedding comparison for Obj1 and Obj3 when $N = 9$

The predicted and scheduled results for shedding of non-critical loads are presented in Figure 4.12, indicating load shedding in the system when adopting Obj1 in Figure 4.12 (a) and Obj3 in Figure 4.12 (b). The load contactors have more frequent on/off activities when adopting Obj1 compared to the case of adopting Obj3. Moreover, when adopting Obj1, the minimum time for keeping loads connected is 1 min, while Obj3 will keep loads connected for at least 8 min, which is preferred for reducing transient issues. Although Obj3 has less load on/off activities, it still has less load shedding time for both high and low-priority loads: the load shedding index for Load 2 is 0.317 with Obj1 compared to 0.299 with Obj3, while the load shedding index value for Load 3 is 0.617 with Obj1 compared to 0.599 with Obj3. In conclusion, Obj3 outperforms Obj1 in both load shedding and switching activities in the experiment.

The battery charging/discharging power measurements are presented in Figure 4.13, where Figure 4.13 (a) presents the results with Obj1, while Figure 4.13 (b) presents the results with Obj3. Comparing the two figures, when adopting Obj3, the battery has fewer cases of switching between the charging and discharging modes, and the charging/discharging power is changed less during each mode. In addition, the battery power curve with Obj1 has several transient peaks, which happen when Load2 is connected/disconnected simultaneously with the Load3 connection action being reversed. This verifies that Obj3 performs better in terms of battery lifecycle as well as system stability.



(a) Battery power with Obj1



(b) Battery power with Obj3

Figure 4.13 Battery power comparison for Obj1 and Obj3 when $N = 9$

In summary, the MPC model with Obj1-3 proposed in Sections 4.2 and 4.3 is applicable for real-time applications. In addition, it was found that the MPC with Obj3 performs better than Obj1 in the real-time experiment when N is selected as 9 for the given load profile. This supports the analysis and conclusions in Section 4.4.

4.6 Chapter summary

This chapter proposed an MPC framework to optimize the control and management of the energy storage and flexibility on the load side for an MEA system. Following the control targets, three different objective functions were presented, and the importance of the different objective functions and prediction horizons was identified by analyzing the simulation results with the proposed evaluation framework including different performance indices. By assessing the impacts of different objectives, the work provided the readers with a reference for selecting the most applicable objective function combination, as well as its potential impacts on deciding prediction horizons for different use cases.

The value of this study lies in its broad applicability when investigating energy storage and load management issues for EPSs containing battery-based ESSs. On the one hand, when a complex EPS contains an MS-ES-L subsystem, the model proposed in this chapter can be conveniently integrated with other objective functions and constraints. In addition, the findings in this chapter can be used to guide the selection of objective functions relating to energy storage and load shedding. For instance, this research inspires the following work in the later chapters of this thesis when the system extends to the whole complex MEA power system configuration, such as HV buses, APU, multiple bidirectional converters, etc. In Chapter 5, a hierarchical controller based on the MPC method is proposed to cope with more operational constraints and scenarios, where the idea and findings mentioned in this work are adopted to design the objective function. On the other hand, when the architecture of the ESS is changed in another research, such as containing paralleled batteries, the model proposed in this study can be adapted from case to case, such as by adding voltage regulation constraints and battery scheduling objectives. The findings in this chapter can also be used to help decide objective functions when optimizing the energy storage dynamics of each battery.

Chapter 5 Fault-tolerant hierarchical operational control

Different subsystems of the EPS presented in Figure 1.7 were studied in Chapter 3 and Chapter 4, which inspired the application of MILP modeling and MPC design techniques to different operational control functions. Based on these studies, the MPC-based methods are applied in Chapter 5 and Chapter 6 to the entire EPS for multi-objective optimal control. In this chapter, a hierarchical control framework is proposed with the MILP-MPC control applied in the high level (HL), while the rule-based methods are applied in the low level (HL). The proposed hierarchical control method is able to provide quick responses to short-term system changes, such as failures and load fluctuations, while also improving long-term system performance.

5.1 Introduction

5.1.1 Modular converter-based EPS architecture

In Chapter 3, a modular converter-based power distribution system is studied, where power allocation and scheduling (PAS) and configuration problems are studied by formulating a MILP model. By applying the MILP techniques to the model predictive control (MPC) framework, optimal management of an energy storage system (ESS) and loads on a bus is studied in Chapter 4. Referring to these studies, in this chapter, operation management of the entire modular converter-based EPS with multiple ESSs is studied as mentioned in Section 1.1.4. The EPS architecture in Figure 1.7 can be extracted as the power flow diagram in Figure 5.1.

In the architecture presented in Figure 1.7 and Figure 5.1, two generators, with the associated rectifiers, are connected to the corresponding HV buses (HVB), each of which supplies several HV loads (HVLs). In addition, one auxiliary power unit (APU) is connected to the APU bus (APUB) to support the system power demand under emergency conditions. For transferring power from the HV side to the LV side, modular DC/DC converters/cells can be connected to any HV/LV bus. Each LV bus (LVB) is connected to an ESS comprised of one lithium-ion battery and one bidirectional DC/DC power converter, as well as several LV loads (LVLs).

Figure 5.1 presents the potential power flow in the system. System buses and components, such as generators, converters, batteries, and loads, are demonstrated as nodes. The potential power flows are demonstrated by lines with arrows, which show the direction of the power flow. The blue arrows demonstrate the unidirectional power flow, while the red arrows represent the bidirectional power flow.

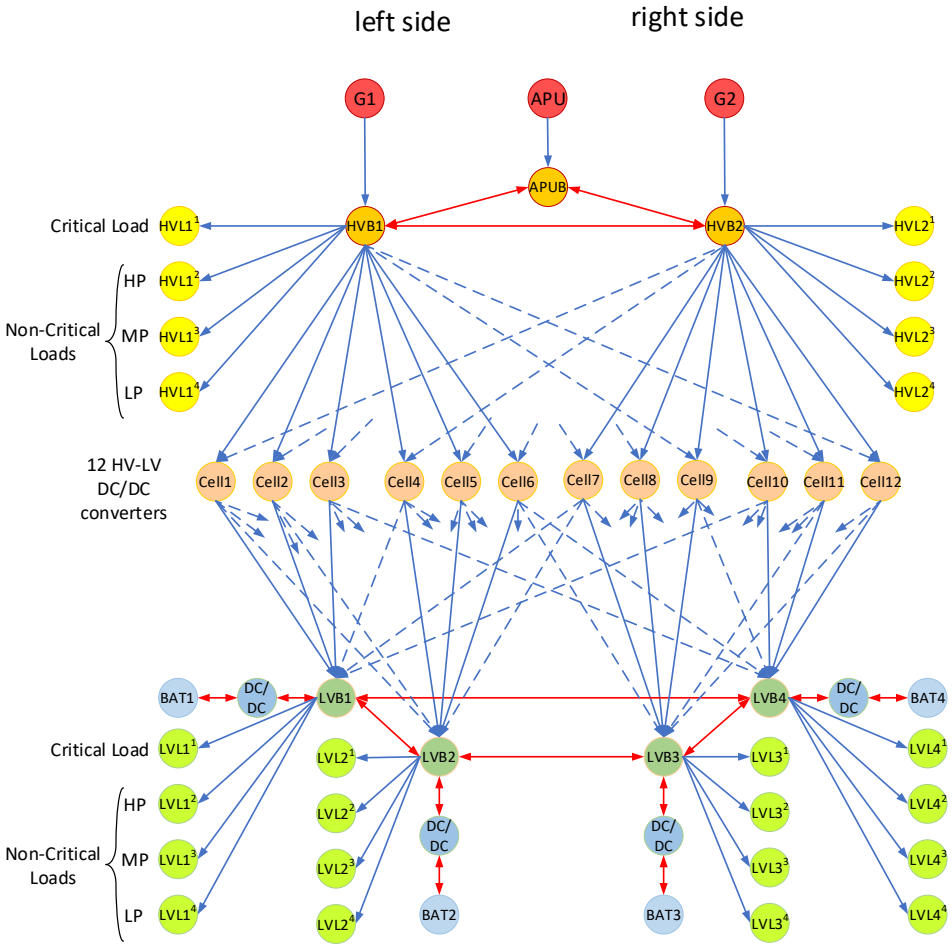


Figure 5.1 Power flow diagram of the modular converter modular converter-based EPS

5.1.2 Control functions

To coordinate the operation of every component and subsystem operation in the EPS, a system-level supervisory controller is required to configure the system and distribute power from power supplies to the loads following the real-time operating requirements, while also reducing the operating costs for all flight stages. In addition, for the application of MEA EPS, safety issues are essential in EPS operational control. For example, despite the components being out of service because of faults, such as failures of generators, ESS, and transmission links, the critical loads responsible for flight safety must be powered in all flight scenarios. Hence, the operational controller is required to provide strategies to cope with the EPS operation in faulty conditions. Moreover, it is preferable to design the controller with higher

reliability to cope with faults with regard to the controller (internal or external), such as computation or communication faults, to maintain appropriate EPS operation. Therefore, this chapter investigates supervisory control to cope with the control targets at two different time scales, in different failure scenarios. On the one hand, the controller ensures the EPS operating requirements with short-term system changes, such as keeping power balance within component power capacity when load demand changes or faults occur. On the other hand, in the long term, the EPS performance is improved in regard to minimizing power losses, switching activities, load shedding, and maintaining sufficient energy in the ESS, based on the operating requirements. In addition, as introduced in Section 3.3, when minimizing the output power for each generator during all flight stages, the power requirements of both generators are balanced, leading to less maximum power on each generator for the minimum generator sizing. In this chapter, the generator sizing is also considered in the long-term objective functions.

5.1.3 Contributions

In this chapter, a fault-tolerant hierarchical operational control framework is proposed for the novel multi-converter-based onboard EPS, aiming to achieve both short-term and long-term control functions presented in Section 5.1.2. As reviewed in Chapter 2, hierarchical control is commonly used to cope with the control targets in different time scales. In each control layer, techniques such as rule-based methods, MILP and MPC can be adopted to collaborate with different benefits. Particularly focusing on the hierarchical control of an onboard EPS, [117], [118], [14], and [57] study the cost reduction and voltage/current regulations for aircraft subsystems. However, none of these explores the fault operation scenarios for the entire EPS. In [37], hierarchical control is designed for fault-tolerant load management, which lacks the discussion of multiple component failures and the reconfiguration under this condition for the onboard EPS. Although multiple component failures are considered in [30] and [106], the authors assume a rule-based LL controller to collaborate with a MPC control at the HL for an MEA EPS, without introducing the details of the LL controller design. In addition, in the hierarchical operational control framework, none of these mentions how the low-level (LL) controls the system in different scenarios when the optimization level is out of service.

Motivated by these research gaps, this chapter proposes an intelligent two-level hierarchical supervisory control method for the EPS presented in Figure 5.1, which is able to deal with multiple failure scenarios while including optimization. An HL controller based on a MILP-MPC scheme is proposed to cope with the optimization of power loss, energy storage within the ESS, generator sizing, and the long-term management of failure impacts on the system, regarding switching and load shedding. An LL controller with a faster clock is designed to cope with changes of loads and fault occurrences over a short timeframe during the HL sample intervals. This LL controller is designed based on a set of predefined rules, which can

work in both collaboration modes with the HL controller, as well as independent modes when the online MPC at the HL is unavailable, e.g. communication failure between different control levels. Hence, the LL controller can keep the system operating in both normal and failure scenarios following the safety criteria and operational constraints. The contributions of this research are listed as follows.

1) In the HL controller, an online MPC model is built with the optimization model integrated into it. A MILP formulation is used to express the system operation requirements as a set of constraints, including power balance with nonlinear efficiencies, maximum power limitations, ESS dynamics, power flow directions, health status constraints presenting component availability, and EPS operational connection constraints. In this optimization model, the objective functions are formulated to minimize the costs related to the preferred system performance. According to the updates of the system status, the optimal decisions of the configuration and power references are provided as recommendations to the LL controller. The HL optimization MILP-MPC model operates in both offline and online modes. Before the flight, the aforementioned MILP-MPC model is conducted offline with the initial system status and average load profile. Therefore, the configuration for all flight stages based on the offline optimization can be saved as a backup database, which is applicable as recommendations when the online MILP-MPC is not available. During the flight, when the online MILP-MPC is available to EPS, it provides control strategies based on long-term optimization with a slow clock following the status changes in the EPS.

2) When the online MILP-MPC is available, a LL controller must provide quick responses to the EPS short-term status changes, i.e. real-time load disturbances and failure occurrences, during the HL control intervals. When the online MILP-MPC is unavailable, the LL controller is required to control the EPS following the operation constraints by referring to the configuration database prepared by the HL offline optimization. Hence, in this study, a rule-based LL controller is designed with four modes - two of the modes operate collaboratively, when the online MPC is available to deal with EPS normal and failure scenarios respectively, while the other two modes operate independently, when the online MPC is unavailable.

3) Two different rule-based methods are proposed for each LL independent mode. A basic rule (BR)-based method is firstly proposed for LL controller independent modes, which conducts a set of “if-then” rules based on the measurement of the system status at each time step. Although this method acts fast to the EPS changes, it can potentially increase the continuous switching of charging/discharging of ESS and connection/disconnection of loads. To avoid this, a finite state machine (FSM)-based method is introduced for LL independent modes by adding the sequential logic, i.e. SOC change sequence in ESS, and a finite number

of states are defined to conduct a set of “if-then” rules in each state. When the online MPC is available, only the BR method is used in the LL controller benefiting from the optimal strategies from online MPC.

4) A comprehensive comparison study is conducted with three cases, including the EPS in a normal operational scenario with both ideal and imprecise load prediction, and the EPS failure operation scenario with ideal load prediction. In each case, the simulation is conducted with the LL controller in the independent modes using both BR and FSM methods, as well as in the HL and LL collaboration modes. The simulation results are presented to illustrate the power and configuration changes, and the performances of each method are evaluated based on the designed evaluation framework. Furthermore, comparisons are made between the performances of the proposed methods in each case.

5.2 EPS description and assumptions

5.2.1 EPS description

The architecture of the studied EPS has been introduced in Section 5.1.1 and Figure 5.1. Two operating scenarios are considered for the EPS, namely the normal scenario and the faulty scenario, which are defined according to the health status of the EPS components. In the normal scenario, there is no failure in the system, while at least one of the system components is out of service in the faulty scenario. Accordingly, the role of the system components will change in different cases to ensure the power supply requirements of the HV/LV loads are met. A detailed description of the EPS components/subsystems' roles is given in Table 5.1.

As discussed in Chapter 4 Section 4.4.1, in an MEA system, the onboard loads usually change according to different flight stages, including ground, take off, climb, cruise, descent, loiter, and landing [21]. In this study, critical loads and non-critical loads are also included. In Figure 5.1, the critical loads, such as flight control systems, essential environment control, and communication systems, should be supplied in all scenarios. The non-critical loads can be shed if needed in faulty conditions with power shortage following load priorities, which means loads with higher priority are less preferred for load shedding. In this work, the non-critical loads are classified into high-priority (HP in Figure 5.1) loads (e.g. ice protection unit and sheddable parts of the environment control), mid-priority (MP in Figure 5.1) loads (e.g. some galley loads), and low-priority ((LP in Figure 5.1)) loads (such as lights and entertainment loads).

Table 5.1 EPS components' roles in normal and faulty operation cases

EPS Component	EPS normal scenario	EPS faulty scenario
Generators/APU	Generators/APU are controlled based on voltage regulation to stabilize the HV/APU bus voltage	
	1) HV/LV loads are supplied by the two main generators. 2) The generator output power is used to charge the batteries according to the ESS operating strategy.	1) In a generator failure scenario, the APU can be used to supply the loads and charge batteries. 2) The APU has a starting time of about 20 s before it is available to be connected to the APU bus.
ESS	An ESS is used to stabilize the LV bus voltage for each LV bus.	
	The ESS manages the power deviations between the loads and power transferred by cells.	ESSs can be used to supply LV loads when there is insufficient available power from the HV side, for instance, in case of failures in generators, transmission lines, and cells.
HVBs to LVBs transmission links	The LV buses are supplied by the generators, receiving power from the HV buses via the transmission links. One DC/DC cell can be connected to any HV or LV bus by controlling the on/off status of the contactors.	By reconfiguring the system with redundant links, the LV side power shortage in transmission failure scenarios is mitigated. For example, one contactor failure will not lead to the cell's availability to power transmission as the connections can be reconfigured to avoid the failed contactor.
HV/LV bus interconnections	The bus interconnections are disconnected to isolate different loads when bus voltages are controlled.	The bus interconnections are connected to maintain bus voltage and to keep critical loads supplied in the case of failures of generators or ESSs.

5.2.2 Assumptions

The following assumptions are considered for designing the control system.

1) Loads at both HV and LV sides are predictable, and there are limited deviations between the predicted and real-time load demand. As mentioned in Section 4.2.3, load prediction techniques can be deployed to predict the aircraft load at different flight stages, for example, in [160], [58], online machine learning-based methods are adopted. In this work, a simplified load prediction method is adopted in which loads are predicted by sampling the historical load without adjustment for real-time flight power changes.

2) The generators in the normal condition supply all of the loads in the EPS with load disturbances, i.e., the deviations between the actual load power and the predicted mean value load power.
3) The health status indicates the availability of the component, i.e., 1 for a normal condition or 0 for faulty conditions. It is assumed that any faulty component will not be recovered within the flight time. In addition, three types of component failures are considered in this work, including one generator failure, one ESS failure, and different transmission link failures, including contactors and cells.
4) The faulty controller represents the online MPC control in HL not being available for some reason, such as communication errors.

5.2.3 Nomenclature

All of the main symbols used in this chapter are listed in Table 5.2-Table 5.4.

Table 5.2 Notations of EPS and controller indices for this chapter

Indices of EPS architecture	
j, l	Index for HV and LV buses respectively
c	Index for cells (modular DC/DC converters)
p, q	Index for HV and LV loads respectively
N^{APU}	Number of APU
N^{HVB}	Number of HV buses
N^{LVB}	Number of LV buses
N^{C}	Number of cells
N^{BAT}	Number of batteries
N^{HVLcri}, $N^{HVLncri}$	Number of HV critical/noncritical loads
N^{LVLcri}, $N^{LVLncri}$	Number of LV critical/noncritical loads
Indices of hierarchical controller	
H	Prediction horizon
k	Time intervals, k$\in\mathbb{Z}_{\geq 0}$
T_s	Sampling time
N	Total time steps
$\mathbf{\Gamma}^{on}\{*\}$	The recommendation values from the online MPC to the LL controller
$\mathbf{\Gamma}^{off}\{*\}$	The recommendation values from the offline dataset to the LL controller
$\mathbf{M}\{*\}$	The measurement value from EPS to the controller
$(*)^{HL}$	Parameters/variable values in HL, such as T_s^{HL}, k^{HL}
$(*)^{LL}$	Parameters/variable values in LL, such as T_s^{LL}, k^{LL}

Table 5.3 Notations of EPS and controller parameters for this chapter

Parameters of EPS		
Power limitations	$PMAX^G$	Initial estimation of maximum generator and APU output power [kW]
	P^{AHVmax}	Maximum output power of APU bus to HV buses [kW]
	$P_{jj'}^{HVmax}$	Maximum power of HV buses [kW]
	P_{jc}^{HVCmax}	Maximum power of connection link between HV bus j and cell c [kW]
	P^{Cmax}	Capacity of DC/DC converter cells [kW]
	P_{cl}^{LVCmax}	Maximum power of connection link between celll c and LV bus j [kW]
	$P_l^{dismax}, P_l^{chmax}$	Maximum charging and discharging power for each battery l [kW]
	$P_{l'l}^{LVmax}$	Maximum power of LV buses [kW]
ESS limitations	B_l^{cap}	Capacity of battery l [kWh]
	HI, LO	Upper/Lower boundary for battery state of charge
Efficiency	η_j^{AHV}	Transmission efficiency in cables between the APU bus and HV bus j
	$\eta_{jj'}^{HV}$	Transmission efficiency in cables of HV bus connection between bus j and j'
	η_{jc}^{HVC}	Transmission efficiency in cables between the HV bus j and cell c
	η_c	Efficiency of cell c
	η_{cl}^{LVC}	Transmission efficiency in cables between the cell c and LV bus l
	$\eta_l^{ch}, \eta_l^{dis}$	Charging/ Discharging efficiency of battery l
	$\eta_{ll'}^{LV}$	Transmission efficiency in cables of LV bus connection between bus l and l'
Load priority	$\lambda_{jp}^{HVLncri}$	The priority of the pth non-critical load on HV bus j
	$\lambda_{jq}^{LVLncri}$	The priority of the qth non-critical load on LV bus l
Parameters of the controller		
Load power	$P_{jp}^{HVLcri}(k)$	The pth critical load power on HV bus j [kW]
	$P_{jp}^{HVLncri}(k)$	The pth non-critical load power on HV bus j [kW]
	$P_{lq}^{LVLcri}(k)$	The qth critical load power on LV bus l [kW]
	$P_{lq}^{LVLncri}(k)$	The qth non-critical load power on LV bus l [kW]
Failure	$\gamma_j^G(k)$	Indicator for the failure of generator j
	$\gamma_{jc}^{HVC}(k)$	Indicator for the failure of connection link between HV bus j and cell c
	$\gamma_{cl}^{LVC}(k)$	Indicator for the failure of connection link between cell c and LV bus l
	$\gamma^C(k)$	Indicator for the failure of cell c
	$\gamma_l^{BAT}(k)$	Indicator for the failure of battery l
APU status	$R^{APU}(k)$	Indicator for the starting status of APU: when $R^{APU}(k) = 0$, APU is not ready for connection, when $R^{APU}(k) = 1$, APU is ready for connection

Table 5.4 Notations of controller variables for this chapter

Continuous decision variables of the controller		
Power	$P^{Gmax}(k)$	Maximum output power of generator/APU [kW]
	$P^{APU}(k)$	Power flowing from APU to the APU bus [kW]
	$P_j^{AHVp}(k)$	Power flowing from APU bus to the HV bus j [kW]
	$P_j^{AHVn}(k)$	Power flowing from HV bus j to the APU bus [kW]
	$P_j^{G}(k)$	Power flowing from generator j to corresponding HV bus j [kW]
	$P_{jj'}^{HV}(k)$	Power flowing from HV bus j to HV bus j' [kW]
	$P_{jc}^{HVC}(k)$	Power flowing from HV bus j to cell c [kW]
	$P_{cl}^{LVC}(k)$	Power flowing from cell c to LV bus l [kW]
	$P_l^{ch}(k)$, $P_l^{dis}(k)$	Charging/ Discharging power of battery on LV bus l [kW]
	$P_{ll'}^{LV}(k)$	Power flowing from LV bus l to LV bus l' [kW]
ESS	$SOC_l(k)$	State of charge of battery on LV bus l
	$\vartheta_l(k)$	Tolerance for upper bound of state of charge of battery on LV bus l
	$\varepsilon_l(k)$	Tolerance for lower bound of state of charge of battery on LV bus l
Binary decision variables of DMPC/SMPC		
Connections	$S^{APU}(k)$	Connection status of the link between APU and APU bus
	$S_j^{AHV}(k)$	Connection status of the link between APU bus and HV bus j
	$S_j^{G}(k)$	Connection status of the link between generator j and corresponding HV bus j
	$S_{jj'}^{HV}(k)$	Connection status of the link between HV bus j and HV bus j'
	$S_{jp}^{HVLncri}(k)$	Connection status of the pth non-critical load power on HV bus j
	$S_{jc}^{HVC}(k)$	Connection status of the link between HV bus j and cell c
	$S_{cl}^{LVC}(k)$	Connection status of the link between cell c and LV bus l
	$S_l^{BAT}(k)$	Connection status of the link between LV bus l and its corresponding battery
	$S_{ll'}^{LV}(k)$	Connection status of the link between LV bus l and LV bus l'
	$S_{lq}^{LVLncri}(k)$	Connection status of the qth non-critical load power on LV bus l
	$\boldsymbol{S^{Phy}}(k)$	Vector of physical connections allowing bidirectional power, including $S_j^{AHV}(k)$, $S_{jj'}^{HV}(k)$, $S_l^{BAT}(k)$ and $S_{ll'}^{LV}(k)$
	$\boldsymbol{S^{h}}(k)$	Vector of physical connections related with failure isolations, including $S_j^{G}(k)$, $S_l^{BAT}(k)$, $S_{jc}^{HVC}(k)$, and $S_{cl}^{LVC}(k)$.
Indicators of Power direction	$s_j^{AHVp}(k)$	Indicator for power flow direction from APU bus to the HV bus j
	$s_j^{AHVn}(k)$	Indicator for power flow direction from HV bus j to the APU bus
	$s_{jj'}^{HV}(k)$	Indicator for power flow direction HV bus j to HV bus j'
	$s_{j'j}^{HV}(k)$	Indicator for power flow direction HV bus j' to HV bus j
	$s_l^{ch}(k)$	Indicator for charging the battery on LV bus l
	$s_l^{disch}(k)$	Indicator for discharging the battery on LV bus l
	$s_{ll'}^{LV}(k)$	Indicator for power flow direction from LV bus l to LV bus l'
	$s_{l'l}^{LV}(k)$	Indicator for power flow direction from LV bus l' to LV bus l

APU starting decisions	$ST^{APU}(k)$	Indicator for the starting of APU: when $ST^{APU}(k) = 0$, do not start APU, when $ST^{APU}(k) = 1$, start APU

5.3 Hierarchical framework

The hierarchical framework proposed in this work includes two levels. Rule-based LL control is conducted every T_s^{LL} (i.e. 0.1 s in this work), which is the fast clock. In contrast, the optimization-based HL controller is sampled based on the slow clock T_s^{HL} (i.e. 1 min in this work). With the fast clock, the LL controller can use predefined rules to guarantee the EPS safety in any scenario, providing quick responses: when maintaining instantaneous power balance and capacity limitations, configuring the EPS to supply loads in normal scenarios and maintain critical loads in faulty scenarios. Under the condition of this assured safety, the EPS is preferred to be controlled for minimizing operational costs. The rules in the LL controller could be modified continuously to achieve as good a performance as possible, however, this increases the computational and design complexity dramatically, and cannot ensure global optimality. In addition, defining rules for this EPS architecture is challenging because of the coupling of configuration and PAS with a variety of constraints.

The HL controller is proposed for two reasons. Firstly, to provide real-time recommendations to the LL controller to optimize the EPS long-term performances, such as load shedding, power losses, switching activities, and energy storage. Secondly, it aids the LL in working out EPS configurations to decouple the problem from PAS calculations, which improves the feasibility of rules in the LL controller. The HL controller contains one online MILP-MPC strategy in main usage to optimize the EPS behaviors during flight, and one offline database for EPS configuration backup to provide quick configuration references when the online strategy is not available because of real-time communication failures or computation failures.

According to the availability of the online MILP-MPC for the HL controller, different operation modes are designed in the LL controller to apply the HL recommendations/references to the EPS according to the short-term dynamics. Figure 5.2 presents the framework of this hierarchical operational control for the MEA EPS proposed in this chapter, and the roles for each control level are presented in Table 5.5.

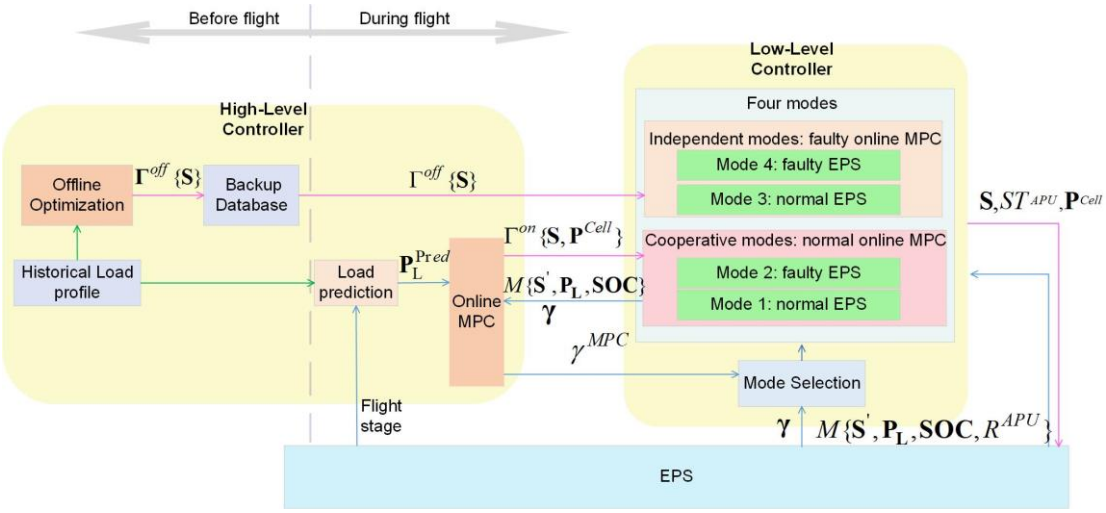


Figure 5.2 Architecture for two-level hierarchical operational control

Table 5.5 Control roles in each level

Functions	LL controller roles	HL controller roles
Load management	Shed sufficient loads if a power shortage happens to keep critical loads being supplied	**Online:** Minimize load shedding and switching activities
EPS reconfiguration	Respond immediately to EPS component failures: 1) isolate faults 2) if needed, reconfigure the EPS by providing available connections based on EPS symmetry 3) consider APU starting time for APU connection	**Online:** Provide configuration allowing minimum transmission power losses and switching activities in both normal and faulty scenarios **Offline:** Provide configuration allowing minimum transmission power losses and switching activities in normal scenarios, which can be referred to by the LL in EPS faulty scenarios to guide the optimization
PAS	Maintain instantaneous power balance and power limitations	**Online:** 1) Minimize transmission power losses 2) Maintain average power balance and power limitations
ESS management	Keep SOC within the limitations	**Online:** 1) Optimize ESS usage 2) Keep SOC within the desired limits

As presented in Figure 5.2, at each time step k^{LL}, the LL controller receives the real-time system status, including measurement matrices **M**{**PL, S', SOC,** R^{APU}} the information matrices **γ**, and the indicator γ^{MPC}, where **PL** consists of the power demands of all loads, **S'** consists of on/off status of all switches, **SOC** matrix consists of SOC of all ESS, R^{APU} indicates the APU availability, **γ** consists of all failures in the system, and γ^{MPC} indicates the availability of online MPC in the HL controller. The measurement and fault detection techniques are not discussed in this work; however, it is noted that SOC is not measured/estimated based on the fast clock because of its slow dynamics. Therefore, SOC is actually sampled based on the same clock as the HL controller, which indicates that the same values will be adopted for LL control for all of the time steps k^{LL} during each HL time interval T_s^{HL}.

The LL controller firstly selects its operation mode according to γ^{MPC} and **γ**. When γ^{MPC}=1, the LL controller refers to recommendations from the online MILP-MPC in HL, which are the cooperative modes, containing Mode 1 and Mode 2 for EPS normal and faulty operation scenarios, respectively, which it is being indicated by **γ**. In contrast, when γ^{MPC}=0, the LL controller operates with HL databases, in independent mode, containing Mode 3 and Mode 4 for EPS normal and faulty scenarios, respectively.

5.3.1 When online MPC is available

As illustrated in Figure 5.2, at each time step k^{HL}, the online MPC receives the status of the system from the LL controller, i.e. the tuple **M**{**PL, S', SOC**, R^{APU} } and the value of **γ**, to update the system state and constraints of the controller. In addition, the load prediction module updates the online MPC with load predictions for the horizon, e.g. $\boldsymbol{P}_{Li}(k^{HL})$, $\boldsymbol{P}_{Li}(k^{HL}+1)$, ..., $\boldsymbol{P}_{Li}(k^{HL}+N-1)$. An online optimization problem is solved with multi objectives to obtain an optimized control sequence for k^{HL}, $k^{HL}+1$, …, $k^{HL}+N-1$, where N indicates the total time steps contained in the finite prediction horizon H. However, only the first sample of the optimized control sequence is applied, and the horizon is shifted to the next time step $k^{HL}+1$. The online MPC provides the reference values of the configuration/connection matrix and power references of all cells to the system, which are represented by $\boldsymbol{\Gamma}^{on}\{\mathbf{S}, \mathbf{P^{Cell}}\}$. Since the generators/APU and ESS are all operated in voltage control mode, other power flows in the system are automatically determined based on Kirchhoff's Current Law, with the desired configurations, cell powers, and load powers.

In every time step k^{HL}, the LL controller receives recommendations $\boldsymbol{\Gamma}^{on}\{\mathbf{S}, \mathbf{P^{Cell}}\}$ from the online MPC, and compares these with the real-time status information, measured based on the fast clock T_s^{LL}, such as the health status of components and real-time load demands, to check the applicability of the recommendations to any EPS short-term behaviors during the HL sample time interval. If the recommendation values are expected to lead to the power of

components/links exceeding the limitations or resorting to the failed components, the LL controller (running in Mode 1 or Mode 2) adjusts the recommendation values to fit the real-time status; otherwise, the LL controller (in Mode 1 or Mode 2) directly adopts the recommendation values and applies these to the EPS.

5.3.2 When online MPC is unavailable

Before the flight, an offline optimization is conducted based on load predictions for all flight stages, with the sample time T_s^{HL}, by adopting the same optimization model as online MPC. The system configuration database is stored to provide configuration information ($\mathbf{\Gamma}^{off}\{\boldsymbol{S}\}$) for each flight stage in the system's normal scenario. In the EPS normal condition, the LL controller in Mode 3 calculates power references for the cells ($\mathbf{P}^{\mathbf{Cell}}$) based on the configuration extracted from the database. In EPS faulty scenarios, the LL controller in Mode 4 reconfigures the system by referring to the configuration in the database. Although the configuration references cannot be directly applied to the EPS, rules are defined in the LL controller to calculate the potential symmetric available connections. Therefore, the LL controller provides the EPS with a new configuration to resolve the power shortage caused by failures. Accordingly, power references for the cells ($\mathbf{P}^{\mathbf{Cell}}$) are calculated based on this updated configuration.

Because the LL controller cannot be supervised by online MPC for optimized decisions when independent modes (Mode 3 and 4) are required, an FSM rule-based method is proposed based on the basic rule (BR)-based method to improve the performance of the LL controller. The performances of both FSM and BR methods are compared in Section 5.7, together with other modes.

5.4 HL controller design

In this section, the HL optimization model is presented, which is formulated using MILP, following the MPC framework to provide optimized online strategies. By solving this model offline, the HL database is constructed. The MILP model formulates the EPS operational rules and targets, which can be solved at each time step k^{HL} using available solvers, such as CPLEX or GUROBI**.**

5.4.1 Objective functions

As shown in Chapter 4, adding SOC considerations, i.e. maximizing SOC, to the cost function of (Obj2 and 3 in Chapter 4) avoids the need for a long prediction horizon. In addition, compared to Obj3 which reduces battery power changes, Obj2 tends to require less computation time while being able to achieve similar performance. Hence, in this chapter, the objective

functions are designed similar to Obj2 in Chapter 4. For the optimal operation management of EPS, the following six control targets are considered:

1) *Minimize total power consumption from all power sources*: The power sources in the studied system include generators, an APU, and batteries in ESSs. Reducing the total output power of the power sources is the first control goal because, with the same load power demands, the minimization for the output power of power sources indicates less power loss in the system for the power distribution system, which leads to less fuel consumption. Compared to formulating all of the power losses directly, the formulation in (5.1) avoids nonlinear formulations to improve the model feasibility.

$$J_{P^{supply}} = \sum_{k^{HL}=0}^{N-1}\left(\frac{\left(\sum_{j}^{N^{HVB}} P_j^G(k^{HL}) + P^{APU}(k^{HL})\right)}{N^{G}\cdot PMAX^{G}} + \frac{\sum_{l}^{N^{LVB}} P_l^{dis}(k^{HL})}{N^{BAT}}\right) \tag{5.1}$$

2) *Maximizing the energy stored in ESS*: For ESS management, it is preferable to keep the aircraft battery at a high SOC value, within the target range, thereby being prepared for abnormal conditions which may later require stored power. According to Chapter 4, increasing the energy stored in ESSs can be achieved by either increasing the battery charging power or SOC in the objective function. In this study, increasing SOC is formulated in the objective function (5.2).

$$J_{SOC} = \sum_{k^{HL}=0}^{N-1} \frac{\sum_{l}^{N^{LVB}} |HI - SOC_l(k^{HL})|}{N^{BAT}\cdot HI} \tag{5.2}$$

3) *Minimizing the load shedding*: When the EPS is in a faulty condition, the power supply might be insufficient to support all of the loads. Therefore, load shedding can be conducted to maintain the system safe operation. The cost function in (5.3) minimizes the total load shedding by penalizing the shedding of loads, considering load priorities. In (5.3), the top has two factors; the first indicates the minimization of HV noncritical loads following their priorities, while the second indicates the minimization of LV noncritical loads. The bottom contains all priorities of the HV and LV noncritical loads for normalization.

$$J_{SL} = \sum_{k^{HL}=0}^{N-1} \frac{\sum_{j}^{N^{HVB}} \sum_{p}^{N^{HVLncri}} \lambda_{jp}^{HVLncri}\left(-s_{jp}^{HVLncri}(k^{HL})\right) + \sum_{l}^{N^{LVB}} \sum_{q}^{N^{LVLncri}} \lambda_{lq}^{LVLncri}\left(-s_{lq}^{LVLncri}(k^{HL})\right)}{\sum_{j}^{N^{HVB}} \sum_{p}^{N^{HVLncri}} \lambda_{jp}^{HVLncri} + \sum_{l}^{N^{LVB}} \sum_{q}^{N^{LVLncri}} \lambda_{lq}^{LVLncri}} \tag{5.3}$$

4) *Minimizing the switching activities*: Switching activities include the following changes: connecting/disconnecting the APU, configuration changes in the transmission system (e.g. bus connection, cell connection, etc.), and connecting/disconnecting loads. Switching activities are preferred to be avoided in the EPS of the aircraft as they might lead to unnecessary transients and can negatively affect the components' lifetimes. Cost functions (5.4)-(5.6) are adopted to minimize various types of switching activities.

$$J_{\delta APU} = \sum_{k^{HL}=0}^{N-1} |S^{APU}(k^{HL}+1) - S^{APU}(k^{HL})| \tag{5.4}$$

$$J_{\delta tran} = \sum_{k^{HL}=0}^{N-1} \sum |\boldsymbol{S^{tran}}(k^{HL}+1) - \boldsymbol{S^{tran}}(k^{HL})| \tag{5.5}$$

$$J_{\delta L} = \sum_{k^{HL}=0}^{N-1} \sum |\boldsymbol{S^{L}}(k^{HL}+1) - \boldsymbol{S^{L}}(k^{HL})| \tag{5.6}$$

where $\boldsymbol{S^{tran}}$ denotes the vector of all power transmission line switches, including all of the connections represented by S_j^{AHV}, $S_{jj'}^{HV}$, S_{jc}^{HVC}, S_{cl}^{LVC}, S_l^{BAT}, $S_{ll'}^{LV}$. Similarly, $\boldsymbol{S^{L}}$ denotes the vector of all load switches, including $S_{jp}^{HVLncri}$ and $S_{lq}^{LVLncri}$.

5) *Minimize generator sizing*: As introduced in Section 3.3, when minimizing the output power for each generator during all flight stages, the power requirements of both generators are balanced, leading to less maximum power on each generator. This is also known as minimizing the generator sizing.

$$J_{P^{GMAX}} = \sum_{k^{HL}=0}^{N-1} \frac{P^{Gmax}(k^{HL})}{PMAX^{G}} \tag{5.7}$$

6) <u>*Minimize SOC outside target range*</u>: For battery management, the battery SOC is preferred to be kept in a target range [LO, HI] that can be modeled as a constraint. In Section 5.4.2., soft constraints on the SOC and the corresponding objective function are discussed, which are also applied in (5.8).

$$J_{\Delta} = \sum_{k^{HL}=0}^{N-1} \sum_{l}^{N^{LVB}} (\varepsilon_l(k^{HL}) + \vartheta_l(k^{HL})) \tag{5.8}$$

Finally, a multi-objective cost function is formed by combining all of the cost functions introduced in (5.1)-(5.8) with different weighting factors $w_{P^{supply}}$, w_{SOC}, w_{SL}, $w_{\delta APU}$, $w_{\delta tran}$, $w_{\delta L}$, $w_{P^{GMAX}}$, and w_{Δ} correspondingly as follows.

$$\begin{aligned} J_{MO} = {} & w_{P^{supply}} J_{P^{supply}} + w_{SOC} J_{SOC} + w_{SL} J_{SL} + w_{\delta APU} J_{\delta APU} \\ & + w_{\delta tran} J_{\delta tran} + w_{\delta L} J_{\delta L} + w_{P^{GMAX}} J_{P^{GMAX}} + w_{\Delta} J_{\Delta} \end{aligned} \tag{5.9}$$

5.4.2 Constraints

To demonstrate the EPS operational requirements, six groups of constraints are proposed as follows:

5.4.2.1 Power balance constraints

For each bus node, the power flowing through should comply with the rule that the sum of powers flowing into/out of each node equals zero (Kirchhoff's Current Law for a given voltage). For the converter nodes, the power flowing out of each node is less than the power flowing into it because of the nonlinear converter efficiency. In addition, power losses across the transmission lines are considered by adding a constant transmission efficiency parameter to the

model. For all of the bidirectional power flow presented in Figure 5.1, the power in each direction is represented by a non-negative variable, hence all power variables are non-negative.

1) Power balance for the APU bus node: The power from the APU equals the total power between the APU bus and all HV buses, including the power that flows into and out of the HV buses. The APU bus receives less power than the total output power from the HV buses to the APU bus, accounting for transmission power losses using a constant efficiency factor multiplier η_j^{AHV} . Hence the power balance equation can be written as follows:

$$P^{APU}(k) - \sum_j^{N^{HVB}} P_j^{AHVp}(k) + \sum_j^{N^{HVB}} \eta_j^{AHV} P_j^{AHVn}(k) = 0 \tag{5.10}$$

2) Power balance for HV bus nodes: The input power for an HV bus includes the power from a generator, APU bus, and adjacent HV buses, while the output power includes the power to the HV loads, cells (to power the LV buses), and adjacent HV buses, formalized as (5.11), where $\forall j \in \{1, \dots, N^{HVB}\}$. In (5.11), the first term is the power from the generator *j*; the second term is the power between the HV bus *j* and the APU bus; the third term is the power between the HV bus *j* and the adjacent HV bus *j'*; the fourth term is the power from HV bus *j* to the cells; the fifth term is the critical loads' power allocated on HV bus *j*; the last term is the noncritical loads' power connected on HV bus *j*.

$$\begin{aligned} P_j^G(k^{HL}) + \left(\eta_j^{AHV} P_j^{AHVp}(k^{HL}) - P_j^{AHVn}(k^{HL})\right) + \left(\sum_{j \neq j'} \left(\eta_{jj'}^{HV} P_{j'j}^{HV}(k^{HL}) - \right.\right. \\ \left.\left. P_{jj'}^{HV}(k^{HL})\right)\right) - \sum_c^{N^C} P_{jc}^{HVC}(k^{HL}) - \sum_p^{N^{HVLcri}} P_{jp}^{HVLcri}(k^{HL}) - \\ \sum_p^{N^{HVLncri}} S_{jp}^{HVLncri}(k^{HL}) P_{jp}^{HVLncri}(k^{HL}) = 0 \end{aligned} \tag{5.11}$$

3) Power balance for cells' nodes: The cells operate in buck mode to transfer power from the HV side to the LV side, and the output power of each cell is less than its input power due to the power losses in the nodes, formulated as (5.12), where $\forall c \in \{1, \dots, N^C\}$. Although the function for the losses, $\eta_c = f(\sum_j^{N^{HVB}} \eta_{jc}^{HVC} P_{jc}^{HVC}(k^{HL}))$, is a nonlinear function, piecewise-linear functions will be used for linearization, to ensure that the problem can be solved by the MILP solver (in Section 5.7), as presented in Chapter 3.

$$\eta_c \sum_j^{N^{HVB}} \eta_{jc}^{HVC} P_{jc}^{HVC}(k^{HL}) - \sum_l^{N^{LVB}} P_{cl}^{LVC}(k^{HL}) = 0 \tag{5.12}$$

4) Power balance for LV bus nodes: For each LV bus, the battery operates in voltage control mode to maintain the constant voltage. Therefore, the power into/out of the ESS is decided by the power between the cells, adjacent LV buses, and LV loads, formulated as (5.13), where $\forall l \in \{1, \dots, N^{LVB}\}$. In (5.13), the first term is the power

from cells to the LV bus *l*; the second term is the power between LV bus *l* and the adjacent LV bus *l'*; the third term is the power between LV bus *l* and the corresponding ESS; the fourth term is the critical loads' power allocated on LV bus *l*; the last term is the noncritical loads' power connected on LV bus *l*.

$$\sum_{c}^{N^C} \eta_{cl}^{LVC} P_{cl}^{LVC}(k^{HL}) + \sum_{l \neq l'} \left(\eta_{ll'}^{LV} P_{l'l}^{LV}(k^{HL}) - P_{ll'}^{LV}(k^{HL}) \right) + \left(P_{l}^{dis}(k^{HL}) - P_{l}^{ch}(k^{HL}) \right) - \sum_{q}^{N^{LVLcri}} P_{lq}^{LVLcri}(k^{HL}) - \sum_{q}^{N^{LVLncri}} S_{lq}^{LVLncri}(k^{HL}) P_{lq}^{LVLncri}(k^{HL}) = 0 \quad (5.13)$$

5.4.2.2 ESS constraints

For each battery (in an ESS), the SOC at time step k^{HL}+1 can be estimated from the battery power and SOC value at the previous time step k^{HL}, as shown below, where $\forall l \in \{1, \dots, N^{LVB}\}$. η_l^{ch} and η_l^{dis} are assumed constant indicating the charging and discharging efficiencies.

$$SOC_l(k^{HL}+1) = SOC_l(k^{HL}) + \frac{T_s \eta_l^{ch} P_l^{ch}(k^{HL})}{B_l^{cap}} - \frac{T_s P_l^{dis}(k^{HL})}{\eta_l^{dis} B_l^{cap}} \quad (5.14)$$

In the aircraft system, *SOC* is preferred to be kept within a target range [LO, HI]. In this work, LO=0.3 and HI=0.9 are considered. As mentioned in Section 4.3.2, instead of adopting the hard constraints to limit the SOC target range, soft constraints in (5.15) - (5.17) are proposed in our model to improve the robustness of the MILP-MPC algorithm, which allows SOC to vary slightly outside of this range in real situations due to unpredicted power requirements.

$$0.3 - \varepsilon_l(k^{HL}) \leq SOC_l(k^{HL}) \leq 0.9 + \vartheta_l(k^{HL}) \quad (5.15)$$

$$0 \leq \varepsilon_l(k^{HL}) \leq 0.1 \quad (5.16)$$

$$0 \leq \vartheta_l(k^{HL}) \leq 0.1 \quad (5.17)$$

5.4.2.3 Boundary constraints

Each component and each transmission link have its maximum power limitation for safe operation. For the potential unidirectional power flow, when its physical transmission path is connected, the power should not exceed its limitation; otherwise, the power is restricted to 0. Similarly, for the potential bidirectional power flow, the power is limited by the direction indicator, i.e. only the selected power direction can reach its maximum power limitation. This set of constraints is presented below.

$$\boldsymbol{S}(k^{HL}) \times \boldsymbol{P_{min}} \leq \boldsymbol{P}(k^{HL}) \leq \boldsymbol{S}(k^{HL}) \times \boldsymbol{P_{max}} \quad (5.18)$$

where $\boldsymbol{P}(k)$ denotes the vector of power flow variables, including $P_j^G(k)$, $P^{APU}(k)$, $P_j^{AHVp}(k)$, $P_j^{AHVn}(k)$, $P_{jj'}^{HV}(k)$, $P_{j'j}^{HV}(k)$, $P_{jc}^{HVC}(k)$, $P_{cl}^{LVC}(k)$, $P_{ll'}^{LV}(k)$, $P_{l'l}^{LV}(k)$, $P_l^{ch}(k)$, and $P_l^{dis}(k)$; $\boldsymbol{S}(k)$ denotes the vector of binary variables of physical connections and power flow direction indicators, including $S_j^G(k)$, $S^{APU}(k)$, $s_j^{AHVp}(k)$, $s_j^{AHVn}(k)$, $s_{jj'}^{HV}(k)$, $s_{j'j}^{HV}(k)$, $S_{jc}^{HVC}(k)$, $S_{cl}^{LVC}(k)$, $s_{ll'}^{LV}(k)$, $s_{l'l}^{LV}(k)$, $s_l^{ch}(k)$, and $s_l^{dis}(k)$. In (5.18), $\boldsymbol{P_{max}}$ and $\boldsymbol{P_{min}}$ denote the vector of the corresponding power limitations. $\boldsymbol{P_{max}}$ includes the maximum power limitations for each term of $\boldsymbol{P}(k)$, including $PMAX^G$ for $P_j^G(k)$ and $P^{APU}(k)$, P^{AHVmax} for $P_j^{AHVp}(k)$ and $P_j^{AHVn}(k)$, $P_{jj'}^{HVmax}$ for $P_{jj'}^{HV}(k)$ and $P_{j'j}^{HV}(k)$, P_{jc}^{HVCmax} for $P_{jc}^{HVC}(k)$, P_{cl}^{LVCmax} for $P_{cl}^{LVC}(k)$, $P_{l'l}^{LVmax}$ for $P_{ll'}^{LV}(k)$ and $P_{l'l}^{LV}(k)$, P_l^{chmax} for $P_l^{ch}(k)$, P_l^{dismax} for $P_l^{dis}(k)$. Considering all power flow variables are non-negative, $\boldsymbol{P_{min}} = \boldsymbol{0}$ is applied in (5.18) for each term of $\boldsymbol{P}(k)$**.** The details of the power limitation constraints are listed in Section 3.2.3 and 4.3.2.

As presented in Section 3.3.1.2, to minimize the generator sizing by reducing the power of each generator, power limitation constraints in (5.19) are introduced. Therefore, when combined with the objective function (5.7), the maximum power of each generation and APU can be reduced during the flight.

$$\begin{gathered} 0 \le P^{Gmax}(k^{HL}) \le S_j^G(k^{HL}) \cdot PMAX^G \\ P_j^G(k^{HL}) \le P^{Gmax}(k^{HL}), \forall j \in \{1, \dots, N^{HVB}\} \\ P^{APU}(k^{HL}) \le P^{Gmax}(k^{HL}) \end{gathered} \tag{5.19}$$

5.4.2.4 Unidirectional constraints

For the potential bidirectional power flow, two non-negative variables are introduced to present the power flow in each direction. As presented in Section 3.2.3, the unidirectional constraints in (5.20) combined with (5.18) are proposed to avoid power flow in both directions simultaneously. Eq (5.20) and (5.18) indicate that when the physical transmission link is connected, the power can be transferred in either direction with the given maximum value while the maximum power in the opposite direction is restricted to 0. Additionally, when the physical transmission link is disconnected, power flow in both directions is set to zero.

$$\boldsymbol{s^p}(k^{HL}) + \boldsymbol{s}(k^{HL})^{\boldsymbol{n}} \le \boldsymbol{S^{Phy}}(k^{HL}) \tag{5.20}$$

In (5.20), $\boldsymbol{s^p}(k)$ and $\boldsymbol{s^n}(k)$ consist of the binary variables that denote the vector for the positive and negative direction indicators respectively. For example, $\boldsymbol{s^p}(k)$ includes the direction indicators $s_j^{AHVp}(k)$, $s_{jj'}^{HV}(k)$, $s_l^{ch}(k)$ and $s_{ll'}^{LV}(k)$, while $\boldsymbol{s^n}(k)$ includes the direction indicators $s_j^{AHVn}(k)$, $s_{j'j}^{HV}(k)$, $s_l^{disch}(k)$ and $s_{l'l}^{LV}(k)$. In addition, $\boldsymbol{S^{Phy}}(k)$ is related to the

vector of their corresponding physical connections, including $S_j^{AHV}(k)$, $S_{jj'}^{HV}(k)$, $S_l^{BAT}(k)$ and $S_{ll'}^{LV}(k)$.

5.4.2.5 Health status constraints

As mentioned in Section 5.2, several failure scenarios in system components, such as generators, ESS, and cells, are considered in this study. To make the MPC controller capable of coping with the failure scenarios, the health status constraints in (5.21)-(5.23) are introduced, indicating that the components are disconnected in case of failure. In particular, (5.22) and (5.23) demonstrate that when one cell fails, the switches to this cell are all disconnected to isolate the failure.

$$\boldsymbol{S^h}(k^{HL}) \leq \boldsymbol{\gamma}(k^{HL}) \tag{5.21}$$

$$\sum\nolimits_j^{N^{HVB}} S_{jc}^{HVC}(k^{HL}) \leq \gamma^C(k^{HL}) \tag{5.22}$$

$$\sum\nolimits_l^{N^{LVB}} S_{cl}^{LVC}(k^{HL}) \leq \gamma^C(k^{HL}) \tag{5.23}$$

where $\boldsymbol{S^h}(k)$ denotes the vectors of connections status, including $S_j^G(k)$, $S_l^{BAT}(k)$, $S_{jc}^{HVC}(k)$, and $S_{cl}^{LVC}(k)$; $\boldsymbol{\gamma}(k)$ denotes the failure status matrix consisting of all failures of the terms in $\boldsymbol{S^h}(k)$.

5.4.2.6 Operational connection constraint

The power contactors should be connected properly to provide the system with all possible operation topologies and prevent unexpected connection conditions. The connection constraints are proposed for APU connection, buses interconnections, and the cells' connections as follows:

1) The APU is connected to the APU bus only when any of the main generators fails. As formulated in (5.24), if all of the values of $\gamma_j^G(k^{HL})$ are 1, then right hand side is 0, hence, the APU is not running; whereas if any value of $\gamma_j^G(k^{HL})$ is 0, then right hand side is 1, hence, the APU could be running.

$$S^{APU}(k^{HL}) \leq \left(1 - \prod\nolimits_j^{N^{HVB}} \gamma_j^G(k^{HL})\right) \tag{5.24}$$

2) The HV and APU bus interconnections are only allowed when any generator failure occurs. HV buses and the APU bus should also be connected without creating loops. As formulated in (5.25), if all of the values of $\gamma_i^G(k^{HL})$ are 1, the HV and APU buses are not connected; whereas if any value of $\gamma_i^G(k^{HL})$ is 0, then the maximum number of N^{HVB} bus interconnections can be adopted to connect the maximum number of $N^{HVB}+1$ buses ($N^{HVB}=2$ for the number of HV buses, $N^{APU}=1$ for the number

of APU bus). In addition, because the bus interconnections are applied to replace the faulty generators, the number of faulty generators indicates the maximum number of bus interconnections required, as formulated in (5.26). For example, one faulty generator indicates a maximum of 1 bus interconnection can be adopted to supply the HV bus.

$$\sum_{j}^{N^{HVB}} S_j^{AHV}(k^{HL}) + S_{jj'}^{HV}(k^{HL}) \leq N^{HVB} \cdot (1 - \prod_{j}^{N^{HVB}} \gamma_i^G(k^{HL})) \tag{5.25}$$

$$\sum_{j}^{N^{HVB}} S_j^G(k^{HL}) + S^{APU}(k^{HL}) + \sum_{j}^{N^{HVB}} S_j^{AHV}(k^{HL}) + S_{jj'}^{HV}(k^{HL}) \leq N^{HVB} + N^{APU} \tag{5.26}$$

3) Each HV bus should be supplied by only one healthy power source, either one main generator or the APU. As formulated in (5.27), if $S_j^G(k^{HL}) = 1$, indicating a normal generator for HV bus *j*, then this bus can adopt one interconnection (either $S_j^{AHV}(k^{HL})$ or $S_{jj'}^{HV}(k^{HL})$) to supply another HV bus *j'* in its generator faulty scenario. In contrast, if $S_j^G(k^{HL}) = 0$, indicating a faulty generator *j*, then at least one bus interconnection (any of $S_j^{AHV}(k^{HL})$ and $S_{jj'}^{HV}(k^{HL})$) will be adopted to supply the HV bus *j*.

$$1 \leq S_j^G(k^{HL}) + S_j^{AHV}(k^{HL}) + S_{jj'}^{HV}(k^{HL}) \leq 2, \forall j \in \{1, \dots, N^{HVB}\} \tag{5.27}$$

4) Although the cells are flexible enough to be connected with any HV/LV bus, during the system operation, each cell cannot be connected with more than one HV and one LV bus:

$$0 \leq \sum_{j}^{N^{HVB}} S_{jc}^{HVC}(k^{HL}) \leq 1 \tag{5.28}$$

$$0 \leq \sum_{l}^{N^{LVB}} S_{cl}^{LVC}(k^{HL}) \leq 1 \tag{5.29}$$

5) The LV bus interconnections are only allowed when any battery failure occurs. Again, LV buses should be connected without creating loops, as formulated in (5.30)-(5.31). The principle of the formulation is similar to the HV/APU bus interconnections in (5.25)-(5.26).

$$\sum_{l}^{N^{LVB}} S_{ll'}^{LV}(k^{HL}) \leq (N^{BAT} - 1)(1 - \prod_{j}^{N^{HVB}} \gamma_l^{BAT}(k^{HL})) \tag{5.30}$$

$$\sum_{l}^{N^{LVB}} S_l^{BAT}(k^{HL}) + \sum_{l}^{N^{LVB}} S_{ll'}^{LV}(k^{HL}) \leq N^{BAT} \tag{5.31}$$

6) Each LV bus should be supplied by only one healthy battery to maintain the bus voltage, as formulated in (5.32). The principle of the formulation is similar to the HV side in (5.26).

$$1 \leq S_l^{BAT}(k^{HL}) + S_{l(l-1)}^{LV}(k^{HL}) + S_{l(l+1)}^{LV}(k^{HL}) \leq 2 \tag{5.32}$$

5.5 LL controller design

As presented in Figure 5.2 and Section 5.3, all system status values are updated for the LL controller every time step k^{LL}, and the operating mode is selected based on the health status of the components and the availability of the HL controller, which is proposed in the Main Algorithm below. In each mode, a group of rules are defined to work as an expert system to either collaborate with online MPC (Mode 1 and 2) or supervise the system independently (Mode 3 and 4). In the independent modes, two different rule-based methods are proposed, i.e. BR and FSM.

As presented in the Main Algorithm, the LL controller provides the three groups of control signals to the EPS, including variables for the system configuration $\boldsymbol{S^{conf}}(k^{LL})$, load shedding $\boldsymbol{S^{shed}}(k^{LL})$, power references of all cells $\boldsymbol{P^C}(k^{LL})$. The system configuration variables include $S_j^G(k^{LL})$, $ST^{APU}(k^{LL})$, $S^{APU}(k^{LL})$, $S_j^{AHV}(k^{LL})$, $S_{jj'}^{HV}(k^{LL})$, $S_{jc}^{HVC}(k^{LL})$, $S_{cl}^{LVC}(k^{LL})$, $S_l^{BAT}(k^{LL})$, and $S_{ll'}^{LV}(k^{LL})$. Load shedding variables include $S_{jp}^{HVLncri}(k^{LL})$, and $S_{lq}^{LVLncri}(k^{LL})$. Power reference variables of cells include $P_c^C(k^{LL})$.

Main Algorithm for LL controller
1) Update system status at time step k^{LL}: a) System health status $\boldsymbol{\gamma}(k^{LL})$, MPC controller availability $\gamma^{\mathrm{MPC}}(k^{LL})$ b) Load power measurement: $P_{jp}^{HVLcri}(k^{LL})$, $P_{jp}^{HVLncri}(k^{LL})$, $P_{lq}^{LVLcri}(k^{LL})$, $P_{lq}^{LVLncri}(k^{LL})$ c) SOC measurement: $SOC_l(k^{LL})$ d) APU status: $R^{APU}(k^{LL})$, $R^{APU}(k^{LL}) = 1$ indicates APU is ready to use, 0 indicates the reverse
2) Select LL controller mode: $(\forall\gamma(k^{LL}) = 1) \wedge (\gamma^{\mathrm{MPC}}(k^{LL}) = 1)$, start Mode 1 $(\exists\gamma(k^{LL}) = 0) \wedge (\gamma^{\mathrm{MPC}}(k^{LL}) = 1)$, start Mode 2 $(\forall\gamma(k^{LL}) = 1) \wedge (\gamma^{\mathrm{MPC}}(k^{LL}) = 0)$, start Mode 3 $(\exists\gamma(k^{LL}) = 0) \wedge (\gamma^{\mathrm{MPC}}(k^{LL}) = 0)$, start Mode 4
3) Send control references to the system: a) System configuration: $\boldsymbol{\Psi}\{\boldsymbol{S^{conf}}(k^{LL})\}$ b) Load shedding: $\boldsymbol{\Psi}\{\boldsymbol{S^{shed}}(k^{LL})\}$ c) Power reference of cells: $\boldsymbol{\Psi}\{\boldsymbol{P^C}(k^{LL})\}$
4) $k = k+1$, go to step 1) and continue to the new state

5.5.1 LL Mode 1: collaboration mode in EPS normal scenarios

In this mode, online MPC in the HL provides recommended control decisions based on average load prediction at each timestep k^{HL}. In EPS normal scenarios, short-term power disbalance and the consequent violations of power capacity constraints can be caused when

applying the recommendations because of the deviations between the real-time load power demands and the predicted average power during the sample time interval T_s^{HL}. Therefore, Algorithm I is proposed for the LL in Mode 1, which adopts the recommendations of configurations $\boldsymbol{\Gamma}^{on}\{\boldsymbol{S}^{\boldsymbol{conf}}(k^{HL})\}$ and load shedding $\boldsymbol{\Gamma}^{on}\{\boldsymbol{S}^{\boldsymbol{shed}}(k^{HL})\}$, and calculates the power references $\boldsymbol{P}^{\boldsymbol{C}}(k^{LL})$ based on the load power deviations. It is noted that HV load deviations are directly compensated for by the generators. In addition, based on assumption 2) in Section 5.2.2, HV and LV load disturbances will not cause the overload of generators. Therefore, when calculating the cells' power in Algorithm I, the constraints of power balance and capacity limitations on HV sides are already guaranteed based on HL recommendations.

Algorithm I for LL Mode 1

1) Consider system state at time step k^{LL}
   a) Load power measurement: $P_{jp}^{HVLcri}(k^{LL})$, $P_{jp}^{HVLncri}(k^{LL})$, $P_{lq}^{LVLcri}(k^{LL})$, $P_{lq}^{LVLncri}(k^{LL})$
2) Keep MPC controller recommendation of system configuration references and load shedding: $\boldsymbol{\Psi}\{\boldsymbol{S}^{\boldsymbol{conf}}(k^{LL})\} = \boldsymbol{\Gamma}^{on}\{\boldsymbol{S}^{\boldsymbol{conf}}(k^{HL})\}$, $\boldsymbol{\Psi}\{\boldsymbol{S}^{\boldsymbol{shed}}(k^{LL})\} = \boldsymbol{\Gamma}^{on}\{\boldsymbol{S}^{\boldsymbol{shed}}(k^{HL})\}$
3) Calculate power references $\boldsymbol{P}^{\boldsymbol{C}}(k^{LL})$ to control the battery charging/discharging and load supporting:
   For each LV bus *l*, do the following:
   a) Calculate the deviations $P_l^{LVdev}(k^{LL})$ between the recommended input power from cells and real-time load demands, as presented in (5.33)
   b) Calculate the power capacity remained from cells to the LV bus *l*, i.e. $P_{cl}^{LVCrem}(k^{HL})$, when recommended power references were allocated, as presented in (5.34)
   c) **If**
   $-P_l^{dismax} \le P_l^{LVdev}(k^{LL}) \le P_l^{chmax}$: the ESS for LV bus *l* can compensate for the deviations between predicted and real-time loads.
   Then
   Adopt recommended power references for cells connected to bus *l*, i.e. $P_{cl}^{LVC}(k^{LL}) = P_{cl}^{LVC}(k^{HL})$
   d) **If**
   $P_l^{LVdev}(k^{LL}) > P_l^{chmax}$: the real-time loads are less than the predicted ones, and the battery is over-charged when adopting the HL recommended power of cells which are connected with LV bus *l*.
   Then
   Reduce power of the corresponding cells proportionally (based on the HL recommendations), to avoid battery being over-charged, as presented in (5.35)
   e) **If**
   $P_l^{LVdev}(k^{LL}) < -P_l^{dismax} < 0$: the real-time loads are more than the predicted ones, leading to the battery being over-discharged when adopting the HL recommended power of the cells connected with LV bus *l*.
   Then
   Increase power of the corresponding cells proportionally (based on the power capacity remained from cells to the LV bus *l* calculated in b)), to avoid battery over-discharging, as presented in (5.36)
4) Obtain updated control references for the system: $\boldsymbol{\Psi}\{\boldsymbol{S}^{\boldsymbol{conf}}(k^{LL})\}$, $\boldsymbol{\Psi}\{\boldsymbol{S}^{\boldsymbol{shed}}(k^{LL})\}$, $\boldsymbol{\Psi}\{\boldsymbol{P}^{\boldsymbol{C}}(k^{LL})\}$, the cells' power is calculated by (5.37)

In Algorithm I, the following calculations are conducted in a)-e) in step 3) respectively. In (5.33) (for rule 3)-a)), $\sum_{c=1}^{N^C} P_{cl}^{LVC}(k^{HL})$ indicates the total recommended input power from cells to the LV bus *l*; $\sum_{q=1}^{N^{LVLcri}} P_{lq}^{LVLcri}(k^{LL})$ and $\sum_{q=1}^{N^{LVLncri}} S_{lq}^{LVLncri}(k^{LL}) \cdot P_{lq}^{LVLncri}(k^{LL})$ indicate the real-time critical loads and connected non-critical loads on the LV bus *l*, respectively. In (5.34) (for rule 3)-b)), $P_{cl}^{LVCmax} \cdot S_{cl}^{LVC}(k^{LL})$ indicates the maximum power can be obtained from the cell *c* to the LV bus *l*; $P_{cl}^{LVC}(k^{HL})$ indicates the recommended power allocation from cell *c* to the LV bus *l*. In (5.35), $P_l^{LVdev}(k^{LL}) - P_l^{chmax}$ indicates the total power should be reduced among the cells for rule 3)-d); $P_{cl}^{LVC}(k^{HL})/\sum_{c=1}^{N^C} P_{cl}^{LVC}(k^{HL})$ indicates the recommended proportion of power allocation from the cell *c* to the LV bus *l*. In (5.36), $-P_l^{LVdev}(k^{LL}) - P_l^{dismax}$ indicates the total power should be increased among the cells for rule 3)-d); $P_{cl}^{LVCrem}(k^{HL})/\sum_{c=1}^{N^C} P_{cl}^{LVCrem}(k^{HL})$ indicates the proportion of the power capacity remained from cells to the LV bus *l* based on (5.34). In (5.37) for step 4), the cells' power is calculated by the output power from cells to the LV bus *l* considering the efficiency of cells.

$$P_l^{LVdev}(k^{LL}) = \sum_{c=1}^{N^C} P_{cl}^{LVC}(k^{HL}) - \sum_{q=1}^{N^{LVLcri}} P_{lq}^{LVLcri}(k^{LL}) - \sum_{q=1}^{N^{LVLncri}} S_{lq}^{LVLncri}(k^{LL}) \cdot P_{lq}^{LVLncri}(k^{LL}) \tag{5.33}$$

$$P_{cl}^{LVCrem}(k^{HL}) = P_{cl}^{LVCmax} \cdot S_{cl}^{LVC}(k^{LL}) - P_{cl}^{LVC}(k^{HL}) \tag{5.34}$$

$$P_{cl}^{LVC}(k^{LL}) = P_{cl}^{LVC}(k^{HL}) \cdot (1 - (P_l^{LVdev}(k^{LL}) - P_l^{chmax})/\sum_{c=1}^{N^C} P_{cl}^{LVC}(k^{HL})) \tag{5.35}$$

$$P_{cl}^{LVC}(k^{LL}) = P_{cl}^{LVC}(k^{HL}) + P_{cl}^{LVCrem}(k^{HL})/\sum_{c=1}^{N^C} P_{cl}^{LVCrem}(k^{HL}) \cdot (-P_l^{LVdev}(k^{LL}) - P_l^{dismax}) \tag{5.36}$$

$$P_c^C(k^{LL}) = \sum_l^{N^{LVB}} P_{cl}^{LVC}(k^{LL}) / \eta_c \tag{5.37}$$

5.5.2 LL Mode 2: collaboration mode in EPS faulty scenarios

When a component failure occurs, the online MPC in the HL cannot respond to it immediately because the online MPC samples the EPS based on a slow clock. However, after the EPS failure status is updated to the online MPC, the online MPC provides optimized decisions to reduce the operational costs in an EPS faulty condition. To reduce the response time to the failure occurrence and apply the optimized decisions following the EPS real-time status, the LL Mode 2 is proposed to cooperate with the online MPC in the HL. Algorithm II is designed for Mode 2, based on the assumptions in Section 5.2.2, which defines the number of failure cases and the failure persistence during the flight stages.

Algorithm II for LL Mode 2

1) Consider system state at time step k^{LL}
   a) system health status $\boldsymbol{\gamma}(k^{LL})$
   b) Load power measurement: $P_{jp}^{HVLcri}(k^{LL})$, $P_{jp}^{HVLncri}(k^{LL})$, $P_{lq}^{LVLcri}(k^{LL})$, $P_{lq}^{LVLncri}(k^{LL})$
   c) APU availability status: $R^{APU}(k^{LL})$
2) Receive online MPC recommendations of system configuration references and load shedding: $\boldsymbol{\Gamma}^{on}\{\boldsymbol{S}^{\boldsymbol{conf}}(k^{HL})\}$ and $\boldsymbol{\Gamma}^{on}\{\boldsymbol{S}^{\boldsymbol{shed}}(k^{HL})\}$
3) Decide system configuration $\boldsymbol{\Psi}\{\boldsymbol{S}^{\boldsymbol{conf}}(k^{LL})\}$ based on $\boldsymbol{\gamma}(k^{LL})$ and $\boldsymbol{\Gamma}^{\boldsymbol{on}}\{\boldsymbol{S}^{\boldsymbol{conf}}(k^{HL})\}$
   a) Check each generator's health status, decide the configuration of the HV sides, refer to the applicability of the recommendations, and calculate any load shedding caused by the generator failure. The details are presented in Section 5.5.2.1 and Algorithm II-A in Appendix B.1.
   b) Check each battery's health status, decide the configuration of the LV sides, refer to the applicability of recommendations. The details are presented in Section 5.5.2.2 and Algorithm II-B in Appendix B.2.
   c) Check the transmission health status between the HV and LV sides, decide upon the configuration of modular cells, refer to the applicability of the MPC recommendations. The details are presented in Section 5.5.2.3 and Algorithm II-C and Algorithm II-D in Appendix B.3 and B.4 respectively.
4) Decide the HV side load shedding: according to step 3)-a), the load shedding on the HV side, i.e. $S_{jp}^{HVLncri}(k^{LL})$, is decided based on the generator/APU status.
5) Decide the LV side load shedding $S_{lq}^{LVLncri}(k^{LL})$ and calculate the power references $\boldsymbol{P^C}(k^{LL})$ to control the battery charging/discharging and load supply:
   For each LV bus *l* (or set of connected buses, noting that when the LV bus *l* is connected to the LV bus *l'*, the two buses are regarded as a new combined single bus *l*), do the following:
      a) Calculate the power deviation $P_l^{LVdev}(k^{LL})$ between the recommended available input power and real-time load demands when adopting the EPS configuration $\boldsymbol{\Psi}\{\boldsymbol{S}^{\boldsymbol{conf}}(k^{LL})\}$ decided in step 3), as presented in (5.38).
      b) Calculate the power capacity remained from the cells to the LV bus *l*, i.e. $P_{cl}^{CLVrem}(k^{HL})$, when available recommended power references which were allocated and the EPS configuration $\boldsymbol{\Psi}\{\boldsymbol{S}^{\boldsymbol{conf}}(k^{LL})\}$ decided in step 3) is adopted, as presented in (5.39).

      c) **If**
      $-P_l^{dismax} \le P_l^{LVdev}(k^{LL}) \le P_l^{chmax}$, which indicates that the ESS for LV bus *l* can compensate for the deviations between predicted and real-time loads
      Then
      Adopt recommended power references for cells connected to bus *l*, i.e. $P_{cl}^{CLV}(k^{LL}) = P_{cl}^{CLV}(k^{HL}) \cdot S_{cl}^{LVC}(k^{LL}) \cdot \sum_{j=1}^{N^{HVB}} S_{jc}^{HVC}(k^{LL})$

      d) **If**
      $P_l^{LVdev}(k^{LL}) > P_l^{chmax}$: The real-time loads are less than the predicted ones, and the battery is overcharged when adopting the HL recommended power of cells connected with LV bus *l*
      Then
      Reduce the power of the corresponding cells proportionally (based on the HL recommendations and the EPS configuration), aiming to avoid battery overcharging, as presented in (5.40)

      e) **If**
      $P_l^{LVdev}(k^{LL}) < -P_l^{dismax} < 0$ and $|P_l^{LVdev}(k^{LL}) + P_l^{LVdismax}(k^{LL})| \le P_l^{CLVrem}(k^{LL})$: The battery will be over-discharged because of the load disturbances and the transmission failures, when adopting the HL recommended power of cells connected with LV bus *l*. In addition, the over-discharge can be avoided by increasing the cells' power within their limitations.
      Then

Increase the power of the corresponding cells proportionally (based on the power capacity remained from cells to the LV bus l and the EPS configuration), aiming to avoid battery over-discharging, as presented in (5.41).

f) **If** $P_l^{LVdev}(k^{LL}) < -P_l^{dismax} < 0$ and $\left|P_l^{LVdev}(k^{LL}) + P_l^{LVdismax}(k^{LL})\right| > P_l^{CLVrem}(k^{LL})$: The battery will be over-discharged because of the load disturbances and the transmission failures, when adopting the HL recommended power of cells connected with LV bus *l*. In addition, the over-discharge cannot be avoided by increasing the cells' power, which requires the load shedding on LV bus *l*.

Then

1) Cells connected with the LV bus *l* are set to rated power, i.e. $P_{cl}^{CLV}(k^{LL}) = P_{cl}^{LVCmax} \cdot S_{cl}^{CLV}(k^{LL}) \cdot \sum_{j=1}^{N^{HVB}} S_{jc}^{HVC}(k^{LL})$.

2) Sufficient LV loads are shed to avoid the battery discharge exceeding the limitation. The loads connected to the LV bus *l* are shed following the load priorities, from low to high, which is presented in Algorithm II-Shed-LVL. The load shedding is stopped until the connected loads on the LV bus *l* can be supplied by the maximum available input power from the cells and ESS, where $P_l^{LVinmax}(k^{LL})$ represents the maximum available input power from the HV side to *l* in (5.42), and $P_l^{LVLtot}(k^{LL})$ represents the total power of the loads connected to the LV bus l in (5.43).

6) Obtain updated control references for the system: $\boldsymbol{\Psi}\{\boldsymbol{S^{conf}}(k^{LL})\}$, $\boldsymbol{\Psi}\{\boldsymbol{S^{shed}}(k^{LL})\}$, $\boldsymbol{\Psi}\{\boldsymbol{P^{C}}(k^{LL})\}$, the cells' power is calculated by (5.37)

In Algorithm II, the calculations mentioned in step 5) are presented as follows. The equations in (5.38)-(5.41) for the rules in a)-e) in step 5) are similar to (5.33)-(5.36) in Algorithm I. While in Algorithm II, the real-time configuration changes in LL (in step 3)-4)) are considered in (5.38)-(5.41) when calculating the recommended power, i.e. $P_{cl}^{LVC}(k^{HL})$ is replaced by $P_{cl}^{LVC}(k^{HL}) \cdot S_{cl}^{LVC}(k^{LL}) \cdot \sum_{j=1}^{N^{HVB}} S_{jc}^{HVC}(k^{LL})$. This indicates the recommended power can be allocated when the cell *c* is connected to the LV bus *l*, as well as when the cell *c* is supplied by any of HV bus. This principle is also applied in (5.42), when calculating the maximum available input power from the HV side to *l*. For calculating the load shedding in step 5)-f), the total power demand in (5.43) on bus *l* is updated in the LL controller.

$$P_l^{LVdev}(k^{LL}) = \sum_{c=1}^{N^C} P_{cl}^{LVC}(k^{HL}) \cdot S_{cl}^{LVC}(k^{LL}) \cdot \sum_{j=1}^{N^{HVB}} S_{jc}^{HVC}(k^{LL}) - \sum_{q=1}^{N^{LVLcri}} P_{lq}^{LVLcri}(k^{LL}) - \sum_{q=1}^{N^{LVLncri}} S_{lq}^{LVLncri}(k^{LL}) \cdot P_{lq}^{LVLncri}(k^{LL}) \tag{5.38}$$

$$P_{cl}^{CLVrem}(k^{HL}) = P_{cl}^{LVCmax} \cdot S_{cl}^{LVC}(k^{LL}) \cdot \sum_{j=1}^{N^{HVB}} S_{jc}^{HVC}(k^{LL}) - P_{cl}^{LVC}(k^{HL}) \tag{5.39}$$

$$P_{cl}^{LVC}(k^{LL}) = P_{cl}^{LVC}(k^{HL}) \cdot S_{cl}^{CLV}(k^{LL}) \cdot \sum_{j=1}^{N^{HVB}} S_{jc}^{HVC}(k^{LL}) \cdot \left(1 - \frac{P_l^{LVdev}(k^{LL}) - P_l^{chmax}}{\sum_{c=1}^{N^C} P_{cl}^{LVC}(k^{HL}) \cdot \sum_{j=1}^{N^{HVB}} S_{jc}^{HVC}(k^{LL})}\right) \tag{5.40}$$

$$P_{cl}^{LVC}(k^{LL}) = P_{cl}^{LVC}(k^{HL}) \cdot S_{cl}^{CLV}(k^{LL}) \cdot \sum_{j=1}^{N^{HVB}} S_{jc}^{HVC}(k^{LL}) + \frac{P_{cl}^{CLVrem}(k^{HL}) \cdot (-P_{l}^{LVdev}(k^{LL}) - P_{l}^{dismax})}{\sum_{c=1}^{N^{C}} P_{cl}^{CLVrem}(k^{HL})} \tag{5.41}$$

$$P_{l}^{LVinmax}(k^{LL}) = P_{cl}^{LVCmax} \sum_{c}^{N^{C}} \eta_{cl}^{LVC} S_{cl}^{LVC}(k^{LL}) \cdot \sum_{j=1}^{N^{HVB}} S_{jc}^{HVC}(k^{LL}) \tag{5.42}$$

$$P_{l}^{LVLtot}(k^{LL}) = \sum_{q}^{N^{LVLcri}} P_{lq}^{LVLcri}(k^{LL}) + \sum_{q}^{N^{LVLncri}} S_{lq}^{LVLncri}(k^{LL}) P_{lq}^{LVLncri}(k^{LL}) \tag{5.43}$$

In Algorithm III step 5)-f), load shedding is introduced, which applies Algorithm II-Shed-LVL as follows.

Algorithm II-Shed-LVL Load shedding for LV bus *l*

Start from low-priority LV load $q = N^{LVLncri}$

While $q \geq 1$, Do the following calculation for LV bus *l*:

$S_{lq}^{LVLncri}(k^{LL}) = 0$

IF $P_{l}^{LVLtot}(k^{LL}) \leq P_{l}^{LVinmax}(k^{LL}) + P_{l}^{dismax}$, Break **While**;

Else $q = q - 1$;

End While

5.5.2.1 Supervision of generator status

In this study, one generator failure is considered. To supervise the generator failure and respond to it by reconfiguring the HV side network and shedding enough loads to avoid generator overload, Algorithm II-A is proposed for the LL Mode 2 in Algorithm II step 3)-a). Algorithm II-A is presented in detail in Appendix B.1. This algorithm controls the EPS in the following three ways:

a) The HV bus interconnection is used when a single generator supplies all of the power demands, when another generator has failed and the APU is not started or is not ready for connection. In contrast, when the APU is started and ready for connection, the APU is used to replace the faulty generator.

b) Although the online MPC determines the APU usage to reduce its switching activities and power losses as presented in Section 5.4.1, the LL controller is designed to start the APU before the online MPC even samples the generator failure. This reduces the shedding time of high-priority and mid-priority loads caused by the generator failure, and the delay in the MPC response.

c) Before the online MPC responds to the generator failure, the LL controller reduces sufficient loads when a single generator supplies the EPS, to avoid the overload of the single remaining normal generator.

5.5.2.2 Supervision of battery status

In this study, one battery failure is considered. When the failure happens, the faulty battery is isolated and LV bus interconnections are required to maintain the corresponding LV bus voltage. In Section 5.4, the online MPC can reconfigure the LV sides in the faulty scenarios with the operational costs minimized. However, before the failure is sampled by the online MPC, the LL controller connects the LV buses following the rules proposed in Algorithm II-B to reduce the response time to the failure occurrence, for safe EPS operation. In addition, the LL controller applies the optimized connection recommendations from online MPC when they are applicable to the failures. Algorithm II-B is presented in detail in Appendix B.2.

5.5.2.3 Supervision of transmission status

In this study, different transmission failures are considered, including the faulty scenarios of the links between the HV/LV buses and cells and the cells. These faults can lead to power shortage on the LV side causing load shedding. The online MPC proposed in Section 5.4 receives full knowledge of the EPS to reconfigure the links and cells for minimum load shedding, power losses, and switching activities. Before the online MPC responds to the failures, the LL controller uses symmetric links and disconnects the faulty links and cells to maintain EPS safety and avoid power shortage as a very quick response. The LL controller can apply the recommendations to the EPS when the online MPC recommendations are applicable to the failures. The following three aspects are considered in Algorithm II-C and Algorithm II-D, which are presented in detail in Appendix B.3 and B.4.

a) When a cell *c* is in the faulty condition, all of the links from HV/LV buses to this cell *c* are disconnected, regardless of the health status of these links.
b) In Figure 5.1, the left side and the right side of the EPS are symmetric. When cell c is in normal condition, while a link failure occurs between it and the HV bus *j*, the faulty link is disconnected instantly by the LL controller. Because cell *c* cannot be supplied by the power source on the HV bus *j*, the LL controller connects this cell to the symmetric HV bus *j'* to maintain the power transmission when this adopted link is itself in normal condition. In the meantime, to avoid the overload of the power source (e.g. generator/APU) on HV bus *j'*, cell *c'*, which is symmetric to cell *c*, is connected to HV bus *j*, as long as this adopted link and cell *c'* are working normally. This is presented in step 3) of Algorithm II-C in Appendix B.3.
c) When a link failure emerges between normal cell *c* and the LV bus *l*, the symmetry of the EPS is also applied. After disconnecting the faulty link, the LV bus *l* is connected to the symmetric cell *c'* as long as the adopted link and cell *c'* are in normal condition. In the meantime, cell *c* is connected to the LV bus *l'* to maintain the bus input power,

which is initially supplied by cell *c'*. This is presented in step 3) of Algorithm II-D in Appendix B.4

5.5.3 LL Mode 3: independent mode in EPS normal scenarios

As discussed in Section 5.3, when the online MPC is unavailable in the HL, the LL accesses the backup database to obtain the recommended EPS configurations, which are calculated based on the average load predictions. Assuming the real-time load demands have limited deviations from the predicted values according to Section 5.2.2-1), the EPS configurations calculated offline in HL based on load predictions can tolerate the deviations in normal EPS scenarios. Therefore, the LL in Mode 3 adopts the recommendations for configurations $\boldsymbol{\Gamma}^{off}\{\boldsymbol{S}^{\boldsymbol{conf}}(k^{HL})\}$ during each time interval T_s^{HL}. Two methods are proposed in the following subsection for Mode 3.

5.5.3.1 BR method for Mode 3

Algorithm III is proposed for LL Mode 3 to calculate power references and decide load shedding based on the configurations in the database.

The calculations conducted in Algorithm III in 4)-a) to 4)-e) are presented as below. (5.44) and (5.45) ensure that the power transmitted from the cell *c* to the LV bus *l* will not exceed its limitation P_{cl}^{LVCmax}. It is noted that $P_{cl}^{LVCmax} = P^{Cmax} \cdot \eta^{Cmax}$, where η^{Cmax} indicates the efficiency of the cells at rated capacity (P^{Cmax}). Consequently, the power demand allocated on the cell *c* will not exceed its capacity.

$$P_{cl}^{LVC}(k^{LL}) = \min(P_{cl}^{LVCmax}, P_{l}^{LVLtot}(k^{LL}) / \sum_{c}^{N^C} S_{cl}^{LVC}(k^{LL})) \cdot S_{cl}^{LVC}(k^{LL}) \tag{5.44}$$

$$P_{cl}^{LVC}(k^{LL}) = \min(P_{cl}^{LVCmax}, (P_{l}^{LVLtot}(k^{LL}) + P_{l}^{chmax}) / \sum_{c}^{N^C} S_{cl}^{LVC}(k^{LL})) \cdot S_{cl}^{LVC}(k^{LL}) \tag{5.45}$$

Algorithm III for LL BR-based Mode 3

1) Consider system state at time step k^{LL}
   a) Load power measurement: $P_{jp}^{HVLcri}(k^{LL})$, $P_{jp}^{HVLncri}(k^{LL})$, $P_{lq}^{LVLcri}(k^{LL})$, $P_{lq}^{LVLncri}(k^{LL})$
   b) SOC measurement: $SOC_l(k^{LL})$
2) Read dataset to extract system configuration references: $\boldsymbol{\Psi}\{\boldsymbol{S^{conf}}(k^{LL})\} = \boldsymbol{\Gamma}^{off}\{\boldsymbol{S^{conf}}(k^{HL})\}$
3) Initially, set all loads as being connected, $\boldsymbol{S^{shed}}(k^{LL}) = \mathbf{1}$
4) Calculate power references $\boldsymbol{P^C}(k)$ and shed loads if required (i.e. change $\boldsymbol{S^{shed}}(k^{LL})$ values from 1 to 0) to control the battery charging/discharging and load supporting:
   For each LV bus *l*, do the following:
   a) Calculate the maximum available input power from HV side to LV bus *l*: $P_l^{LVinmax}(k^{LL})$, as presented in (5.42)
   b) Calculate the total load demands $P_l^{LVLtot}(k^{LL})$, as presented in (5.43)
   c) **If**
      $SOC_l(k^{LL}) \geq 0.9$: SOC exceeds the upper bound
      Then (Corresponding to State 1 in FSM method in Figure 5.3)
      Stop charging the battery: Share LV loads among cells equivalently within the cells' power capacity, as presented in (5.44); Use the battery to automatically compensate for the additional power demands when $P_l^{LVinmax}(k^{LL}) < P_l^{LVLtot}(k^{LL}) \leq P_l^{LVinmax}(k^{LL}) + P_l^{dismax}$
   d) **If**
      $0.3 \leq SOC_l(k^{LL}) < 0.9$: SOC is within the target range
      Then (Corresponding to State 2 in FSM method in Figure 5.3)
      Charge the battery whenever possible without load shedding: share LV loads and charging power among cells equivalently within the cells' power capacity, as presented in (5.45)
   e) **If**
      $(SOC_l(k^{LL}) < 0.3)$: SOC exceeds the lower bound
      Then (Corresponding to State 3 in FSM method in Figure 5.3)
      Charge the battery whenever possible by (5.45) when $P_l^{LVLtot}(k^{LL}) \leq P_l^{LVinmax}(k^{LL})$, otherwise, shed sufficient loads to charge battery. When load shedding is required, the loads connected to LV bus *l* are shed, following the load priority from low to high. In addition, the load shedding is stopped until $P_l^{LVLtot}(k^{LL}) \leq P_l^{LVinmax}(k^{LL})$.
5) Obtain updated control references for the system: $\boldsymbol{\Psi}\{\boldsymbol{S^{conf}}(k^{LL})\}$, $\boldsymbol{\Psi}\{\boldsymbol{S^{shed}}(k^{LL})\}$, $\boldsymbol{\Psi}\{\boldsymbol{P^C}(k^{LL})\}$, the cells' power is calculated by (5.37)

5.5.3.2 FSM method for Mode 3

In Algorithm III, the battery can be quickly charged to its upper bound. However, the battery SOC is likely to vary around the upper bound because the battery keeps switching between the charging and discharging process, which leads to additional power losses, unnecessary power changes, and can be harmful to the battery lifetime. Compared to the BR method making decisions based on the inputs, the FSM decides outputs and the next state as a function of the inputs and the present state (allowing it to take the current state / previous decisions into consideration). To improve Algorithm III for Mode 3, removing the continuous switching of charging/discharging, FSM-based Mode 3 in Figure 5.3 is proposed, which consists of three states and a group of state transition conditions.

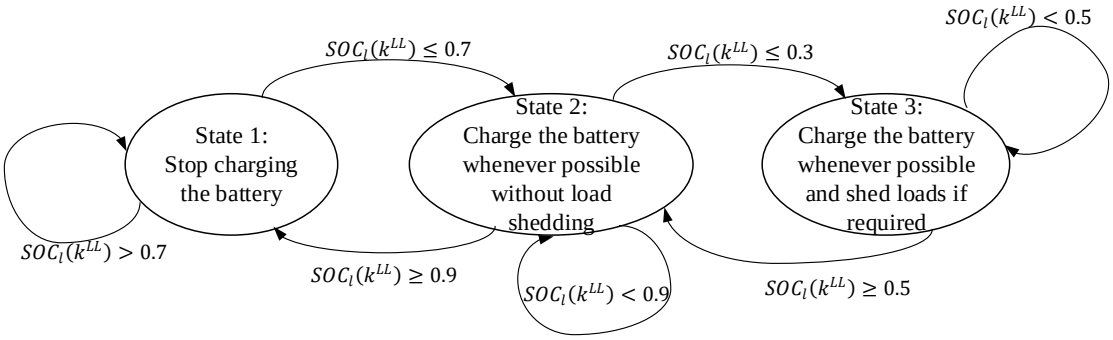


Figure 5.3 FSM-based Mode 3

In FSM-based Mode 3, states correspond to the 'Then' commands in BR-based Algorithm III for Mode 3. The controller continuously compares the inputs, i.e. the SOC of each battery, with the transition conditions. When a transition condition is satisfied, the controller transits from the present state to the next state for calculating the decision variables.

The FSM here introduces two more level boundaries, which are SHI=0.7, and SLO=0.5, dividing the SOC target range into three levels. When $SOC \in [0.7, 0.9]$, the energy stored in the battery is at a high level, allowing both State 1 and State 2. When $SOC \in [0.5,0.7]$, the energy stored in the battery is at the middle level, and the controller works in State 2. When $SOC \in [0.3,0.5]$, the energy stored in the battery is at a low level, allowing both State 2 and State 3.

According to Figure 5.3, if $0.7 \leq SOC_l < 0.9$ at the initial status, the controller enters State 2 to charge battery l whenever possible until $SOC_l \geq 0.9$. Then the controller transits to State 1 to stop charging the battery l until $SOC_l < 0.7$. Afterward, the controller enters State 2, if $P_l^{LVinmax} < P_l^{LVLtot}$, the battery l is applied to supply the loads leading to the reduction of SOC_l. When the reduction causes $SOC_l < 0.3$, the controller transits from State 2 to State 3 to charge the battery l with the potential load shedding. Load shedding is applicable to stop the discharge of the battery l until $SOC_l \geq 0.5$, and the controller enters State 2, which is the same as the initial status.

5.5.4 LL Mode 4: independent mode in EPS faulty scenarios

In faulty scenarios, although the online MPC is unavailable to provide optimized recommendations to the failures, the LL can adopt rules to configure the EPS. The rules are similar to the configuration algorithm in Mode 2 steps when the failures are not sampled by the online MPC and the LL responds to the failures. Similar to Mode 3, LL Mode 4 calculates the power in the EPS to manage loads and ESS to meet the operational constraints when the EPS configurations are decided. In addition, BR-based and FSM-based methods are proposed in Mode 4 similarly to Mode 3.

In BR-based Mode 3, the loads can be supplied by the input power from the HV sides and the ESS because the EPS is in faulty condition, and the load shedding is only conducted when there is insufficient energy in the ESS. However, in BR-based Mode 4, in addition to insufficient energy, load shedding is also conducted when there is power shortage caused by failures. The rules for the ESS charging/discharging and the load shedding are demonstrated in step 6) of Algorithm IV.

Similar to Mode 3, FSM-based Mode 4 is proposed based on BR-based Mode 4 in Algorithm IV. The transmission conditions and definition of the states are the same as illustrated in Figure 5.3, while the rules conducted in each state are replaced with the rules proposed in Mode 4 in step 6). Therefore, the FSM-based Mode 4 reduces the switching of the charging/discharging when the SOC is close to the upper/lower boundaries, and the continuous load shedding is reduced when the SOC is close to the lower boundary in the EPS faulty scenarios.

Algorithm IV for LL controller Mode 4

1) Consider system state at time step k^{LL}
   a) system health status $\boldsymbol{\gamma}(k^{LL})$
   b) Load power measurement: $P_{jp}^{HVLcri}(k^{LL})$, $P_{jp}^{HVLncri}(k^{LL})$, $P_{lq}^{LVLcri}(k^{LL})$, $P_{lq}^{LVLncri}(k^{LL})$
   c) APU starting status: $R^{APU}(k^{LL})$
2) Read dataset to extract system configuration references: $\boldsymbol{\Gamma}^{\boldsymbol{off}}\{\boldsymbol{S}^{\boldsymbol{conf}}(k^{HL})\}$
3) Initially, set all loads been connected, $\boldsymbol{S}^{\boldsymbol{shed}}(k^{LL}) = \mathbf{1}$
4) Decide system configuration $\boldsymbol{\Psi}\{\boldsymbol{S}^{\boldsymbol{conf}}(k^{LL})\}$ based on $\boldsymbol{\gamma}(k^{LL})$ and $\boldsymbol{\Gamma}^{\boldsymbol{off}}\{\boldsymbol{S}^{\boldsymbol{conf}}(k^{HL})\}$
   a) Check each generator health status, decide the configuration of the HV side, and calculate load shedding caused by the generator failure. The rules are similar to the ones discussed in Section 5.5.2.1 and Algorithm II-A (in Appendix B.1), while replacing the online MPC recommendations with the offline ones. In addition, the APU is always started in Mode 4 when one generator fails to cope with the worst scenarios.
   b) Check each battery health status, decide upon the configuration of the LV side. The rules are the same to the ones discussed in Section 5.5.2.2 and Algorithm II-B (in Appendix B.2) while replacing the online MPC recommendations with the offline ones.
   c) Check transmission health status between HV and LV sides, decide the configuration of modular cells. The rules are the same to the ones discussed in Section 5.5.2.3, Algorithm II-C and Algorithm II-D (in Appendix B.3 and B.4 respectively), while replacing the online MPC recommendations with the offline ones.
5) Decide HV side load shedding: according to step 3)-a), the load shedding on the HV side, i.e. $S_{jp}^{HVLncri}(k^{LL})$, is decided based on the generator/APU status.
6) Decide LV side load shedding $S_{lq}^{LVLncri}(k^{LL})$ and calculate power references $\boldsymbol{P}^{\boldsymbol{C}}(k^{LL})$ to control the battery charging/discharging and load supply:
   For each LV bus *l* (or set of connected buses, noting that when the LV bus *l* is connected to the LV bus *l'*, the two buses are regarded as a new combined single bus *l*), do the following:
      a) Calculate the maximum available input power $P_l^{LVinmax}(k^{LL})$ from HV side to *l* based on the EPS configurations decided in step 4), as presented in (5.42)
      b) Calculate the total load demands $P_l^{LVLtot}(k^{LL})$, as presented in (5.43)
      c) **If**
      $SOC_l(k^{LL}) \geq 0.9$: SOC exceeds the upper bound
      Then (Corresponding to State 1 in FSM method in Figure 5.3)

Stop charging the battery, and shed sufficient loads if the loads on the LV bus *l* cannot be supplied by the maximum available input power of the HV side and the ESS:
(1) If $P_l^{LVinmax}(k^{LL}) + P_l^{dismax} \geq P_l^{LVLtot}(k^{LL})$, share LV loads among cells equivalently within the cells' power capacity, and use the battery to automatically compensate for the additional power demands, as presented in (5.46).
(2) If $P_l^{LVinmax}(k^{LL}) + P_l^{dismax} < P_l^{LVLtot}(k^{LL})$, load shedding is conducted by Algorithm II-Shed-LVL until $P_l^{LVinmax}(k^{LL}) + P_l^{dismax} \geq P_l^{LVLtot}(k^{LL})$. Based on the load shedding, recalculate the cells' power to share the connected load demands without charging the battery.

d) **If**
$0.3 \leq SOC_l(k^{LL}) < 0.9$: SOC is within the target range
Then (Corresponding to State 2 in FSM method in Figure 5.3)
Charge the battery if possible, and shed sufficient loads if the loads on the LV bus *l* cannot be supplied by the maximum available input power of the HV side and the ESS:
(1) If $P_l^{LVinmax}(k^{LL}) + P_l^{dismax} \geq P_l^{LVLtot}(k^{LL})$, charge the battery whenever possible without load shedding: share LV loads and charging power among cells equivalently within the cells' power capacity, as presented in (5.47).
(2) If $P_l^{LVinmax}(k^{LL}) + P_l^{dismax} < P_l^{LVLtot}(k^{LL})$, load shedding is conducted by Algorithm II-Shed-LVL until $P_l^{LVinmax}(k^{LL}) + P_l^{dismax} \geq P_l^{LVLtot}(k^{LL})$. Based on the load shedding, recalculate the cells' power to share the connected load demands and charge the battery whenever possible, i.e. $P_l^{LVinmax}(k^{LL}) \geq P_l^{LVLtot}(k^{LL})$,

e) **If**
$(SOC_l(k^{LL}) < 0.3)$: SOC exceeds the lower bound
Then (Corresponding to State 3 in FSM method in Figure 5.3)
Charge the battery, and shed sufficient loads to avoid the battery discharge:
(1) If $P_l^{LVinmax}(k^{LL}) \geq P_l^{LVLtot}(k^{LL})$, charge the battery: share LV loads and charging power among cells equivalently within the cells' power capacity, as presented in (5.47)
(2) If $P_l^{LVinmax}(k^{LL}) < P_l^{LVLtot}(k^{LL})$, load shedding is conducted by Algorithm II-Shed-LVL until $P_l^{LVinmax}(k^{LL}) \geq P_l^{LVLtot}(k^{LL})$. Based on the load shedding, recalculate the cells' power to share the connected load demands and charge the battery.

7) Obtain updated control references for the system: $\boldsymbol{\Psi}\{\boldsymbol{S^{conf}}(k^{LL})\}$, $\boldsymbol{\Psi}\{\boldsymbol{S^{shed}}(k^{LL})\}$, $\boldsymbol{\Psi}\{\boldsymbol{P^{C}}(k^{LL})\}$, the cells' power is calculated by (5.37)

The calculations mentioned in step 6) of Algorithm IV, can be formulated as follows. The principle of (5.46) and (5.47) are similar to (5.44) and (5.45) in Algorithm III respectively. While in Algorithm IV, the real-time configuration changes in LL caused by failures are considered in (5.46) and (5.47) when calculating the recommended power, i.e. $\sum_{j=1}^{N^{HVB}} S_{jc}^{HVC}(k^{LL})$ is added in both equations. Both equations indicate that the power demand can be allocated when the cell *c* is connected to the LV bus *l*, as well as when the cell *c* is supplied by any of HV buses.

$$P_{cl}^{LVC}(k^{LL}) = \min(P_{cl}^{LVCmax}, \frac{P_l^{LVLtot}(k^{LL})}{\sum_c^{N^C}(S_{cl}^{LVC}(k^{LL})\sum_{j=1}^{N^{HVB}} S_{jc}^{HVC}(k^{LL}))}) \cdot S_{cl}^{LVC}(k^{LL}) \sum_{j=1}^{N^{HVB}} S_{jc}^{HVC}(k^{LL}) \quad (5.46)$$

$$P_{cl}^{LVC}(k^{LL}) = \min(P_{cl}^{LVCmax}, \frac{P_l^{LVLtot}(k^{LL}) + P_l^{chmax}}{\sum_c^{NC}(S_{cl}^{LVC}(k^{LL}) \sum_{j=1}^{NHVB} S_{jc}^{HVC}(k^{LL}))}) \cdot S_{cl}^{LVC}(k^{LL}) \sum_{j=1}^{NHVB} S_{jc}^{HVC}(k^{LL}) \quad (5.47)$$

5.6 Evaluation framework design

An evaluation framework is presented in this section for calculating the cost of operation as well as the cost of constraint violation. The operation costs include the costs of power loss, SOC, load shedding, switching activities, maximum generator power, and change of battery power. The violation costs include the violation costs of SOC limitations, generator power limitations, cells' power limitations, and battery power limitations. The mathematical formulation of each cost index is presented below. The total cost is proposed to evaluate all performance of the operational control, which is the sum of the overall operation cost and the overall violation cost.

Table 5.6 Notations for evaluation indices

Notation		Evaluation indices for the costs
Operation costs	G_{Ploss}	Cost of total power losses in the EPS
	G_{SOC}	Cost of SOC
	G_{SL}	Cost of load shedding
	G_{δ}	Cost of switching activities
	G_{Pmax}	Cost of the maximum generator power
	$G_{\delta Pbat}$	Cost of the battery power changes
	G_{op}	Overall operation cost
Violation costs	G'_{SOC}	SOC exceeding limited range
	G'_{Pgen}	Power exceeding the rated generator power, for checking the constraints violation
	G'_{Pcell}	Power exceeding the rated cell's power, for checking the constraints violation
	G'_{Pbat}	Power exceeding the rated battery power, for checking the constraints violation
	G'_{vio}	Overall constraints violation cost

5.6.1 Operation costs

The operation cost functions from the study in Chapter 4 are used to evaluate the performances of the controller across all of the flight stages. In this work, the following six evaluation indices are proposed:

1) *Cost of total power losses*: The power loss is calculated by the difference between the total output of the power sources (5.49) and the total load power (5.50). The power loss for all

flight stages is evaluated by (5.48), calculating the average power loss weighted by the weighting factor v_{Ploss}.

$$G_{Ploss} = v_{Ploss}(\frac{1}{T}\sum_{k^{LL}=0}^{T}(P_n^{source}(k^{LL}) - P_n^{load}(k^{LL})) \tag{5.48}$$

$$P_n^{source}(k^{LL}) = \sum_j^{N^{HVB}} P_j^G(k^{LL}) + P^{APU}(k^{LL}) + \sum_l^{N^{LVB}}(\frac{P_l^{dis}(k^{LL})}{\eta_l^{dis}} - \eta_l^{ch}P_l^{ch}(k^{LL})) \tag{5.49}$$

$$\begin{aligned} P_n^{load}(k^{LL}) = {} & \sum_p^{N^{HVLcri}} P_{jp}^{HVLcri}(k^{LL}) + \sum_p^{N^{HVLncri}} S_{jp}^{HVLncri}(k^{LL})P_{jp}^{HVLncri}(k^{LL}) \\ & + \sum_q^{N^{LVLcri}} P_{lq}^{LVLcri}(k^{LL}) + \sum_q^{N^{LVLncri}} S_{lq}^{LVLncri}(k^{LL})P_{lq}^{LVLncri}(k^{LL})) \end{aligned} \tag{5.50}$$

2) <u>*Cost of SOC*</u>: The ESS performance is evaluated from the SOC level in (5.51), weighted by v_{SOC}, which indicates better performance for any SOC average value which is closer to the upper bound within the target range.

$$G_{SOC} = v_{SOC}(\frac{1}{T}\sum_{k^{LL}=0}^{T}\sum_l^{N^{BAT}}|HI - SOC_{n,l}(k^{LL})| \tag{5.51}$$

3) <u>*Cost of load shedding*</u>: The load shedding is evaluated by calculating the average time for which loads are disconnected over the entire flight period, with their priorities, in (5.52).

$$G_{SL} = v_{SL}(\frac{1}{T}\sum_{k^{LL}=0}^{T}\frac{\sum_j^{N^{HVB}}\sum_p^{N^{HVLncri}}\lambda_{jp}^{HVLncri}\left(1-S_{jp}^{HVLncri}(k^{LL})\right)+\sum_l^{N^{LVB}}\sum_p^{N^{LVLncri}}\lambda_{jp}^{LVLncri}\left(1-S_{jp}^{LVLncri}(k^{l}\right.}{\sum_j^{N^{HVB}}\sum_p^{N^{HVLncri}}\lambda_{jp}^{HVLncri}+\sum_l^{N^{LVB}}\sum_p^{N^{LVLncri}}\lambda_{jp}^{LVLncri}} \tag{5.52}$$

4) <u>*Cost of switching*</u>: The average switching activities for connections are evaluated by (5.53), which combines the change of APU connection in (5.54), the change of transmission connections in (5.55), and the change of load connections in (5.56), with $v_{\delta APU}$, $v_{\delta tran}$, and $v_{\delta L}$ representing the weighting factors, respectively.

$$G_\delta = G_{\delta APU} + G_{\delta tran} + G_{\delta L} \tag{5.53}$$

$$G_{\delta APU} = v_{\delta APU}\frac{1}{T}\sum_{k^{LL}=0}^{T}|S^{APU}(k^{LL}+1) - S^{APU}(k^{LL})| \tag{5.54}$$

$$G_{\delta tran} = v_{\delta tran}\frac{1}{T}\sum_{k^{LL}=0}^{T}\sum|\boldsymbol{S^{tran}}(k^{LL}+1) - \boldsymbol{S^{tran}}(k^{LL})| \tag{5.55}$$

$$G_{\delta L} = v_{\delta L}\frac{1}{T}\sum_{k^{LL}=0}^{T}\sum|\boldsymbol{S^{L}}(k^{LL}+1) - \boldsymbol{S^{L}}(k^{LL})| \tag{5.56}$$

5) <u>*Cost of the maximum generator power*</u>: In the objective function, the maximum generator output power is minimized for each generator, which balances the load power demand

allocation amongst the generators. This is evaluated in (5.57), which finds the maximum output power during all flight stages amongst the generators and the APU. The value is compared to the pre-given value $PMAX^G$ to calculate the ratio, with $v_{P^{max}}$ adopted for its weight.

$$G_{P^{max}} = v_{P^{max}} \frac{\max\left\{P_j^G(k^{LL}), P^{APU}(k^{LL}), \forall j \in N^{HVB}, k^{LL}=0,1,\ldots,T\right\}}{PMAX^G} \tag{5.57}$$

5) *Cost of the battery power changes*: As discussed in Chapter 4, the battery life will be shortened when the battery power usage mode is frequently changed. The index (5.58) is proposed to calculate the total battery power change for all flight stages.

$$G_{\delta Pbat} = v_{\delta Pbat} \frac{1}{T} \sum_{k^{LL}=0}^{T} \frac{\sum |P_l^{bat}(k^{LL}+1) - P_l^{bat}(k^{LL})|}{P_l^{chmax} + P_l^{dismax}} \tag{5.58}$$

The overall operation cost includes all of the aforementioned operation costs, which is presented as:

$$G_{op} = G_{P^{loss}} + G_{SOC} + G_{\delta Pbat} + G_{SL} + G_{\delta} + G_{P^{max}} + G_{\delta Pbat} \tag{5.59}$$

5.6.2 Constraint violation costs

The EPS operation constraints can potentially be violated when there are deviations between the predictions and real-time values and delayed responses. Based on the control proposed in this study, there are four potential violations, including the violation of the SOC target range, the violation of the maximum power bounds for generator/APU output power, and the violation of maximum power bounds for cells and battery power. The evaluation indices for the violation costs are presented in (5.60)-(5.63). The violations are evaluated by calculating the average amount by which the values exceeded the boundaries during the flight stages, for all corresponding components. For example, (5.60) calculates the average SOC violation value for all batteries.

$$G'_{SOC} = v'_{SOC} \frac{1}{T} \sum_{l=1}^{N^{LVB}} \sum_{\{SOC_l(k^{LL}) \in S:(SOC_l(k^{LL}) > HI \vee SOC_l(k^{LL}) < LO)\}} (|SOC_l(k^{LL}) - HI| + |SOC_l(k^{LL}) - LO|) \tag{5.60}$$

$$G'_{Pgen} = v'_{Pgen} \frac{1}{T} \sum_{j=1}^{N^{HVB}} \sum_{\{P_j^{G,APU}(k^{LL}) \in S:(P_j^{G,APU}(k^{LL}) > P^{Gmax})\}} \left|P_j^{G,APU}(k^{LL}) - P^{Gmax}\right| \tag{5.61}$$

$$G'_{Pcell} = v'_{Pcell} \frac{1}{T} \sum_{c=1}^{N^C} \sum_{\{P_c^C(k^{LL}) \in S:(P_c^C(k^{LL}) > P^{Cmax})\}} |P_c^C(k^{LL}) - P^{Cmax}| \tag{5.62}$$

$$\begin{aligned} G'_{Pbat} = v'_{Pbat} \frac{1}{T} \Big(& \sum_{l=1}^{N^{LVB}} \sum_{\{P_l^{ch}(k^{LL}) \in S:(P_l^{ch}(k^{LL}) > P_l^{chmax})\}} \left|P_l^{ch}(k^{LL}) - P_l^{chmax}\right| \\ & + \sum_{l=1}^{N^{LVB}} \sum_{\{P_l^{dis}(k^{LL}) \in S:(P_l^{dis}(k^{LL}) > P_l^{dismax})\}} \left|P_l^{dis}(k^{LL}) - P_l^{dismax}\right| \end{aligned} \tag{5.63}$$

The overall violation cost includes all of the aforementioned violation costs, which is presented as:

$$G'_{vio} = G'_{SOC} + G'_{Pgen} + G'_{Pcell} + G'_{Pbat} \tag{5.64}$$

5.7 Case studies

To compare the performances of the proposed hierarchical control with different EPS scenarios, 3 cases are studied by simulating the EPS and the controller in Simulink. In Case 1 and 2, the EPS is in normal condition. In Case 1, the real-time load demands are assumed to be the same as the predictions, and the performances are compared when the controller works with the online MPC with the LL in Mode 1 (M1-BR-MPC), and the offline database with the LL in Mode 3 using both the BR method (M3-BR) and FSM method (M3-FSM). In Case 2, the real-time loads are assumed with fluctuations, causing a maximum deviation within $\pm$5% compared to the predictions. In Case 2, the three methods studied in Case 1 are also compared. In addition, the performance is also compared when the online MPC in the HL operates without the LL (NoLL-MPC), to study the impact of the response delay. Finally, Case 3 explores the controller performance when the EPS operates in faulty scenarios. Therefore, in Case 3, the performance is compared when the controller works with the online MPC with LL in Mode 2 (M2-BR-MPC), and the offline database with LL in Mode 4 with both the BR (M4-BR) and FSM (M4-FSM) based methods. In each case, the EPS performance is evaluated using the indices proposed in Section 5.6.

5.7.1 Parameters

In this subsection, the parameters adopted for the case studies are presented. As studied in Chapter 4, seven stages are considered for the load profile of the flight duration, for 150 minutes, as presented in Table 5.7. The load profile contains the mean value of the power demand of each load, which is forecasted for the online MPC in HL. In Case 1 and Case 3, the real-time loads are assumed the same to the mean values without disturbances, while in Case 2, the real-time load are assumed with disturbances based on the mean values. In the table, HP, MP, and LP represent High Priority, Mid Priority, and Low Priority respectively. The priority of loads can be represented by a group of prioritization parameters, such as 50, 30, 10 for HP, MP, and LP load respectively in this study.

Table 5.7 Load profile of power usage (kW) based on flight stages with indices in Figure 5.1

Load types [kW]	**Load indices**	**Ground (20min)**	**Take off (5min)**	**Climb (25min)**	**Cruise (60min)**	**Descent (10min)**	**Loiter (15min)**	**Landing (15min)**
HV Critical Loads	$HVL1^1$, $HVL2^1$	3.34	9.86	7.40	7.15	7.40	9.07	10.00
LV Critical Loads	$LVL1^1$, $LVL4^1$	1.78	1.94	2.07	3.00	2.07	2.07	1.94
	$LVL2^1$, $LVL3^1$	3.00	2.50	2.50	2.50	2.50	2.50	3.00
HV HP Loads	$HVL1^2$, $HVL2^2$	1.63	2.78	8.00	8.00	8.00	8.00	0.29
LV HP Loads	$LVL1^2$, $LVL4^2$	1.40	1.30	1.30	1.30	1.60	0.80	0.80
	$LVL2^2$, $LVL3^2$	0.50	0.50	0.50	0.50	1.50	1.00	2.20
HV MP Loads	$HVL1^3$, $HVL2^3$	5.00	1.14	4.72	4.87	4.72	4.72	1.14
LV MP Loads	$LVL1^3$, $LVL4^3$	0.50	0.35	0.35	2.00	0.35	0.35	0.35
	$LVL2^3$, $LVL3^3$	0.70	0.70	1.50	2.50	0.50	0.50	0.50
HV LP Loads	$HVL1^4$, $HVL2^4$	2.00	2.00	2.00	6.00	2.00	2.00	2.00
LV LP Loads	$LVL1^4$, $LVL4^4$	1.00	0.70	1.50	2.20	0.50	0.50	1.50
	$LVL2^4$, $LVL3^4$	2.00	1.50	2.00	3.00	2.00	2.00	2.00

In the EPS, the efficiency for the cells is considered to be nonlinear, as discussed in Chapter 3, and the efficiency curve and piecewise-linear techniques in Figure 3.4 and Figure 3.6 are adopted in this study. Cable efficiencies and battery charging/discharging efficiencies are assumed to be constant in the calculations of the controller. The maximum load power is 43.02 kW on the left/right side when the aircraft enters the cruising stage, while the rated generator power is 46 kW, which is designed to cover all of the MEA loads. The rated power for each DC/DC converter is 3 kW, and the battery capacity of all batteries is 6 kWh. The load demand peak appears at the cruise stage (from 50min to 110min), leading to less available power for battery charging during this stage. In contrast, before/after this stage, there is sufficient power to charge batteries with the maximum power from the generators when the EPS is in normal

condition. During the simulation, different SOC initial values are set for the batteries in the EPS, such as 0.35, 0.5, 0.7, 0.75.

The weighting factors in the HL objective function and evaluation indices are presented in Table 5.8 and Table 5.9 respectively, referring to the impact of each cost function studied in Chapter 4. In addition, $v_{*'}$ represents the penalty in the evaluation scheme of each violation cost.

Among the objectives in Section 5.4.1, increasing SOC and reducing the power losses are two conflict objectives, because charging a battery to increase SOC causes additional power losses. However, their importance changes in different conditions: when the SOC is close to the upper bound, reducing the power losses can be more prioritized than increasing SOC; otherwise, when the SOC is close to the lower bound, it improves the EPS safety to charge battery regardless the consequent power losses. A varying SOC weighting factor is therefore designed to balance the energy redundancy and power losses. In this study, the weighting factor for J_{SOC} is selected as a linear function in (5.65) to the SOC value initial value $SOC_l(0)$ at each time step *k*: when SOC is close to upper bound HI, its weighting factor is reduced. Conversely, when SOC is close to lower bound LO, its weighting factor is increased. In (5.65), W_{soc}^{max} and W_{soc}^{min} are the maximum and minimum weights selected for the varying SOC.

$$w_{SOC_l}(k) = W_{soc}^{min} + \frac{SOC_l(0)-LO}{HI-LO}(W_{soc}^{max} - W_{soc}^{min}) \tag{5.65}$$

Table 5.8 Weighting factors for the objective functions

$w_{Psupply}$	1	w_{SOC}	(5.62), $W_{soc}^{max} = 10, W_{soc}^{min} = 0$
w_{SL}	100	$w_{\delta APU}$	4
$w_{\delta tran}$	1	$w_{\delta L}$	8
w_{PGMAX}	0.5	w_{Δ}	10^5

Table 5.9 Weights for the evaluation indices

v_{Ploss}	2	v_{SOC}	(5.62), $W_{soc}^{max} = 2, W_{soc}^{min} = 0$
v_{SL}	50	$v_{\delta APU}$	4
$v_{\delta tran}$	1	$v_{\delta L}$	8
v_{Pmax}	0.2	$v_{\delta Pbat}$	0.4
$v_{*'}$	100		

5.7.2 Case 1: EPS normal scenario without load fluctuations

Figure 5.4 compares the operation costs and constraint violation costs for Case 1 when different control is applied. In Figure 5.4 (a), the overall operation cost, overall violation cost, and total cost are compared for each control method. Figure 5.4 (b) presents the breakdown of the overall operation cost in Figure 5.4 (a) when adopting three control methods, including six operation cost indices proposed in Section 5.6.1. In addition, Figure 5.4 (c) presents the breakdown of the overall violation cost in Figure 5.4 (a), including four violation cost indices proposed in Section 5.6.2.

As illustrated, when online MPC and the LL collaborate, the EPS achieves the best performance in both overall operation and violation cost. Compared to the LL in the independent mode, M1-BR-MPC leads to the minimum power loss and each generator output power, although M3-FSM performs the best in reducing battery power changes, while M1-BR performs the best in SOC. Consequently, M1-BR-MPC reduces the overall operation cost by 10.45% and 9.55% compared to M3-BR and M3-FSM respectively. In addition, the overall violation cost is reduced by 100% when adopting M1-BR-MPC. Therefore, when the LL collaborates with the online MPC, the minimum total cost is achieved, which is 17.84% and 10.62% less than the total costs when adopting the M3-BR and M3-FSM respectively.

When the online MPC is unavailable, M3-BR and M3-FSM perform similarly for the overall operation cost. However, compared to M3-BR, M3-FSM reduces costs of power losses and battery power changes, resulting in an overall operation cost improvement of 1% compared to M3-BR. Regarding the overall violation cost, the M3-FSM reduces the violation of SOC limitation by 88% compared to M3-BR, leading to the total costs reduced by 8.18%.

In Case 1, there is no load shedding, switching activities, and other violation costs for any of the three methods. The following subsections illustrate the simulation results for each cost index.

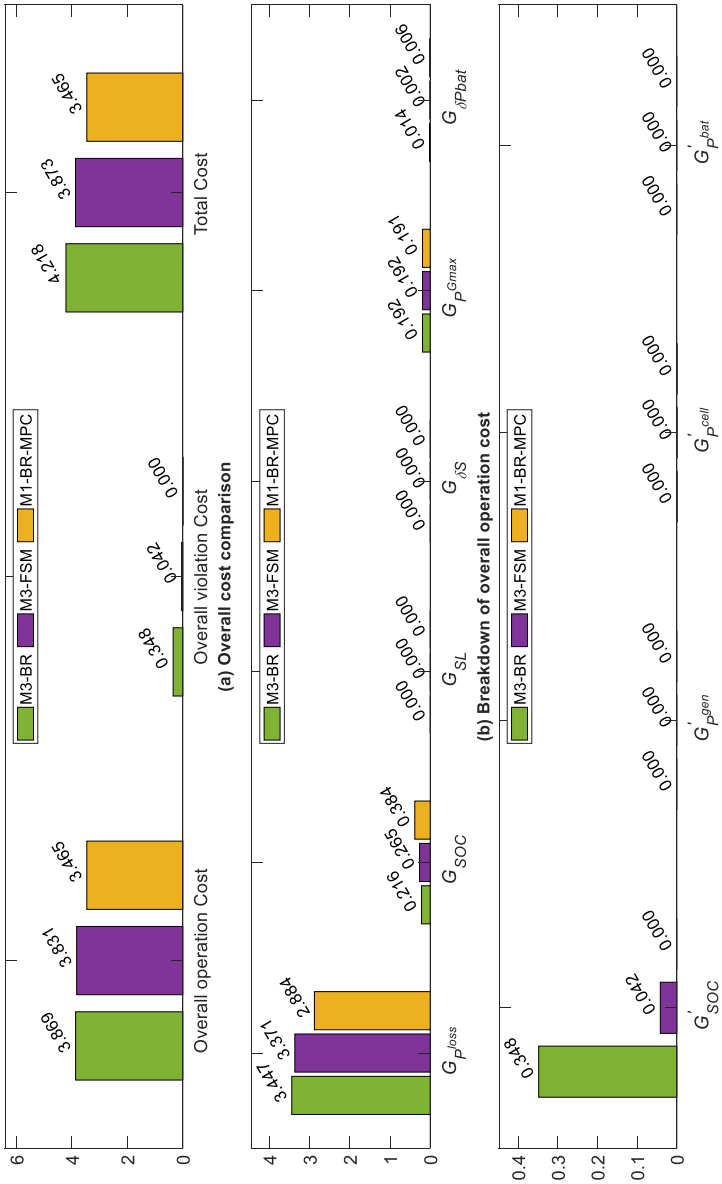


Figure 5.4 Cost comparison of different control for Case 1

5.7.2.1 Comparison of power loss

Figure 5.5 presents the total power loss of the EPS during the flight for Case 1 when adopting the aforementioned control methods. According to this figure, when the online MPC is available, the total power loss is the least in almost all flight stages compared to the LL in the independent mode. When adopting M1-BR-MPC, the average power loss is 1.44kW. Compared to power losses of 1.72kW and 1.69kW on average when adopting the M3-BR and M3-FSM methods, the online MPC reduces the cost of power loss by 16.34% and 14.45% respectively as presented in Figure 5.4.

When the online MPC is unavailable, M3-FSM reduces the power loss peaks during the flight compared to the M3-BR method. Referring to the SOC in Figure 5.6, battery

charging/discharging power in Figure 5.7, and cells' power in Figure 5.9, M3-BR leads to more battery charging time to keep the SOC around the upper boundary, which is avoided by M3-FSM. This leads to the power loss cost being reduced by 2.2% comparing M3-FSM to M3-BR.

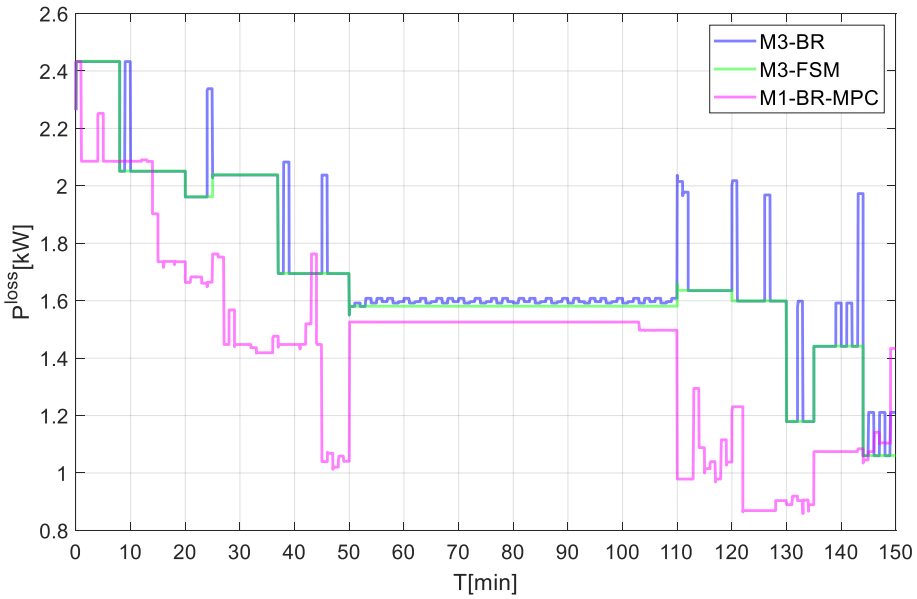


Figure 5.5 Total power loss during the flight for Case 1

5.7.2.2 Comparison of SOC and battery power

Figure 5.6 and Figure 5.7 demonstrate the SOC and the charging/discharging power of four batteries on LV buses for Case 1. In Figure 5.7, positive values indicate battery charging, while negative values indicate battery discharging. Since the loads are symmetrically allocated, the maximum power available for charging batteries 1 and 4 is equivalent, similarly for batteries 2 and 3. In addition, in contrast to the load demand, the maximum available power for battery charging on each LV bus increases before the cruising stage, after which the power decreases. During the cruising stage, the maximum available power for charging the battery on each LV bus is less than 0.2kW because of the load demand and cells' power limitations.

As presented in Figure 5.6, without online MPC, M3-BR and M3-FSM keep battery charging to the HI (0.9) level, whatever the initial values of SOC. When the SOC exceeds 0.9, although M3-BR maintains SOC to 0.9, battery 3 and 4 are switched between charging and discharging continuously during the cruising stage, while M3-FSM avoids this switching with the SOC of battery 3 and 4 decreasing to 0.8 approximately. This is observed in Figure 5.7. Compared to M3-BR, the M3-FSM leads the cost of SOC being increased by 22.69%, while the cost of battery power changes is reduced by 82.44%. In addition, as presented in Figure 5.4, M3-FMS reduces the violation of SOC limitations.

Rather than keep SOC charged to the upper bound, the online MPC provides optimized decisions to balance the power losses and SOC, because both battery charging and discharging cause power losses. As illustrated in Figure 5.6, the battery is charged for longer, to increase SOC when its SOC initial value is more approximated to the LO (0.3). In Figure 5.6, the SOC of battery 1 is increased from 0.35 to 0.69, while the SOC of battery 4 is maintained around 0.85 with the least charging/discharging activities. Although the M1-BR-MPC method results in a higher cost of SOC by 77.8% and 44.9% compared to M3-BR and M3-FSM methods, it charges batteries to increase the average SOC to 0.73, which maintains the SOC redundancy for the EPS safety. In addition, compared to the M3-BR method, M1-BR-MPC reduces the cost of battery power changes by 57.82%.

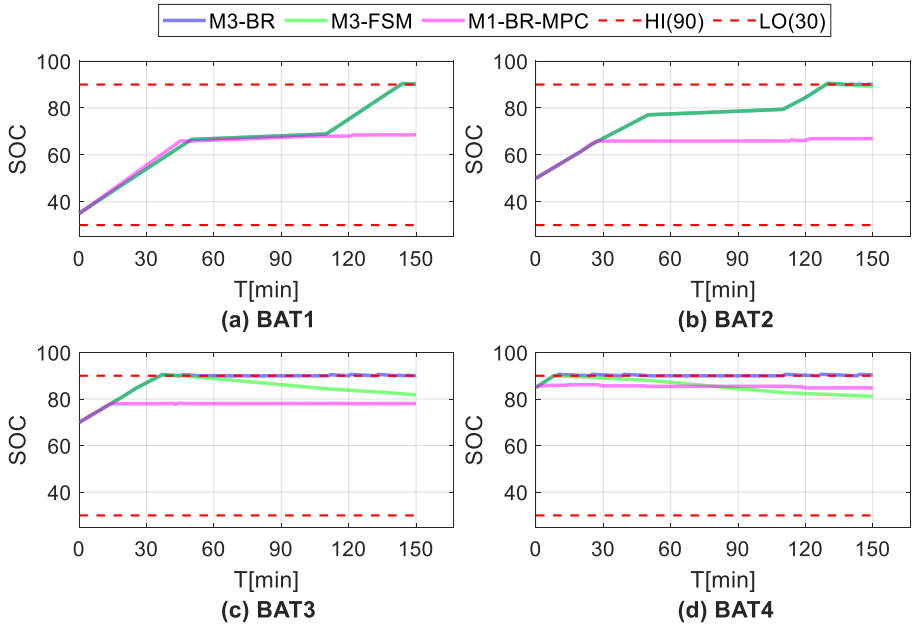


Figure 5.6 SOC results for Case 1

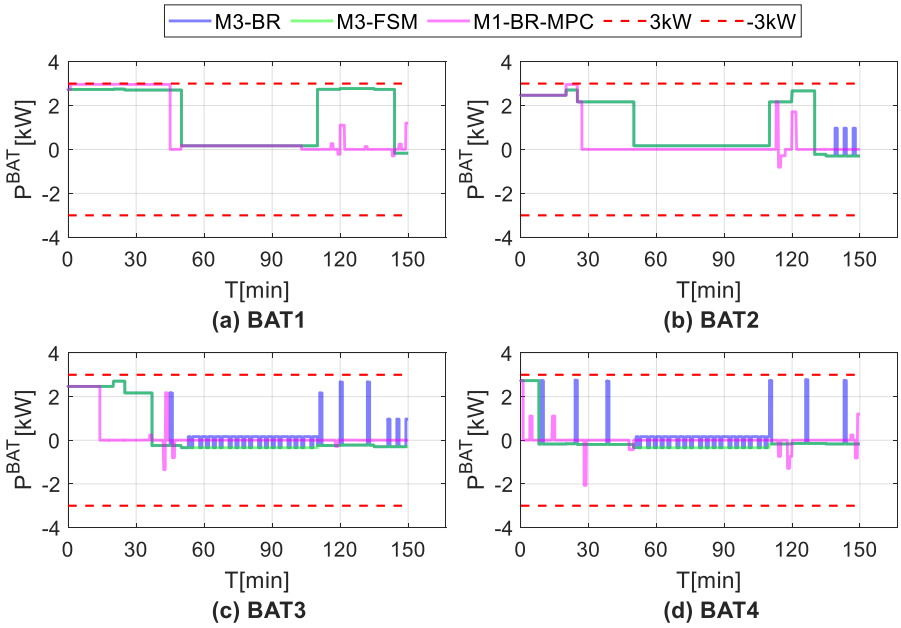


Figure 5.7 Battery charging/discharging power for Case 1

5.7.2.3 Comparison of generator output power

Figure 5.8 illustrates the generator power in the EPS for Case 1. The APU is not started in normal condition by all three methods. In general, the output power of generator 1 is more than generator 2 in most flight stages when adopting all control methods, because the batteries on LV bus 1 and 2 are supplied by generator 1 to increase the SOC to a higher value from the low initial value. During the cruising stage, both generators reach the maximum output power to supply the peak load demand. In addition, a small amount of power is available for charging batteries during this stage. Hence, the maximum generator output power is dominated by the load demand, leading to similar values when adopting different control methods. In Figure 5.8, the maximum generator output power is 44.13kW when adopting M3-BR and M3-FSM methods, while the value is 43.95kW by BR-M1-MPC with a cost (i.e., the evaluation index value of maximum generator output power) reduction by 0.4%.

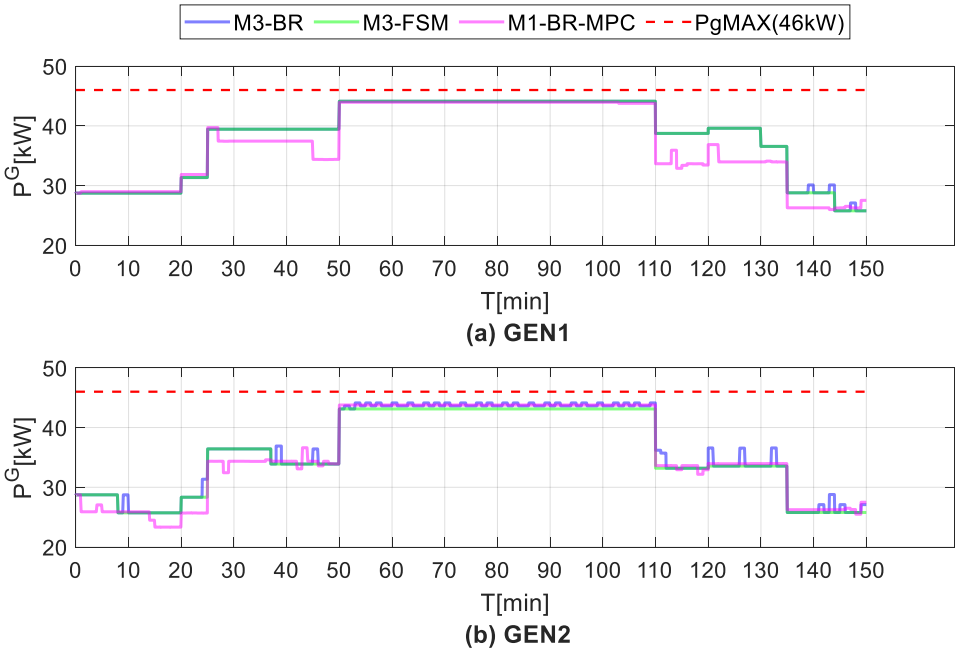


Figure 5.8 Generator output power for Case 1

5.7.2.4 Comparison of cells' power

The input power of each cell is illustrated in Figure 5.9. All control methods ensure that the power allocated to cells is within the rated power limitation, which is 3kW in the simulation. According to the configuration results, each LV bus is supported by three cells; for example, LV bus 1 is supplied by Cells 1-3. The power allocated for Cells 1-3 is the same when the M3-BR and M3-FSM methods are adopted because they apply rules to equivalently share the power among the cells connected to one LV bus. In contrast, after the cruise stage in Figure 5.9, Cell 3 is kept unused most of the time, while Cell 1 operates with the rated power when the online MPC is available (M1-BR-MPC), because it allocates power to cells differently to reduce the total power losses, which has been discussed in detail in Chapter 3. Similar comparisons and conclusions can be observed for the cells on other LV buses, which indicates that the EPS operates following the designed control strategies.

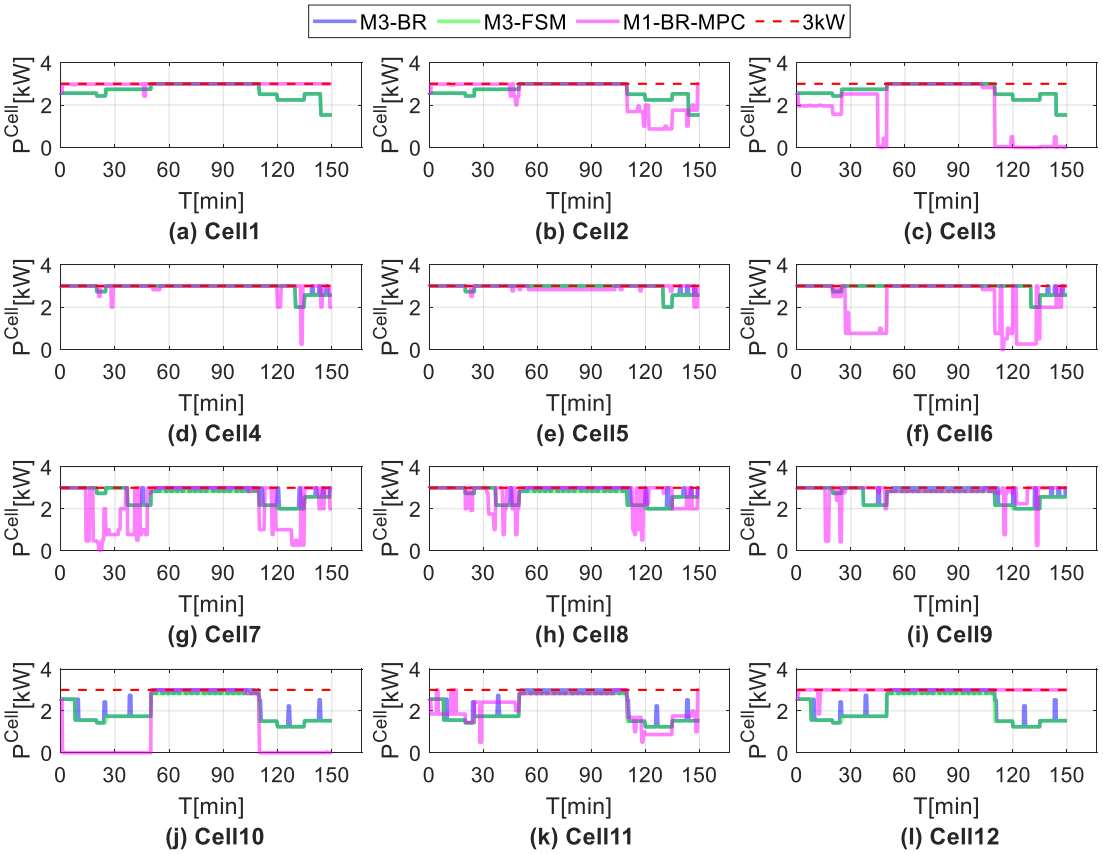


Figure 5.9 Cells' input power for Case 1

5.7.3 Case 2: EPS normal scenario with load fluctuations

In Case 2, the real-time loads are assumed to have a maximum 5% deviation compared to the predicted values. Since the online MPC provides control sequences based on the load predictions, the deviations between the real-time load demand and the predicted values lead to potential constraint violations when directly applying the recommendations of power references to the EPS. In Figure 5.10, results for directly applying the recommendations of online MPC is represented by the NoLL-MPC results, to compare these with the other methods which benefited from LL control.

Figure 5.10 illustrates the cost comparison for different control. In Figure 5.10 (a), the overall operation cost, overall violation cost, and total cost are compared for each control method. Figure 5.10 (b), presents the breakdown of the overall operation cost in Figure 5.10 (a) when adopting four control methods, including six operation cost indices proposed in Section 5.6.1. In addition, Figure 5.10 (c) presents the breakdown of the overall violation cost in Figure 5.4 (a), including four violation cost indices proposed in Section 5.6.2.

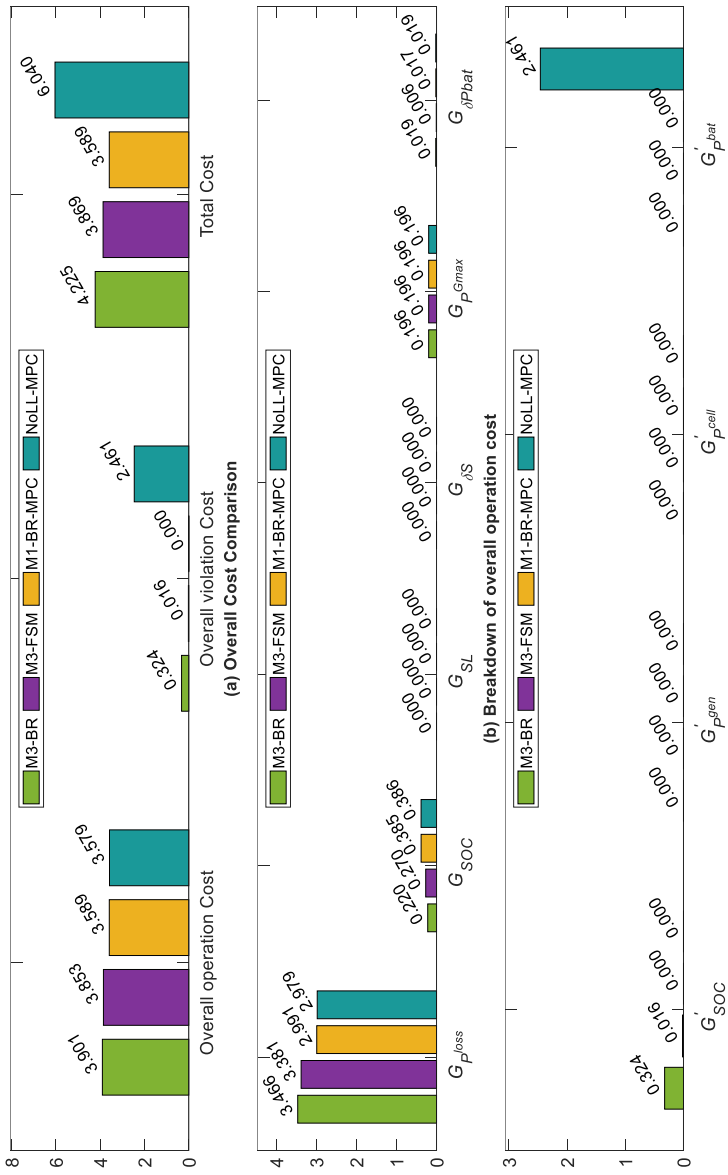


Figure 5.10 Cost comparison of different control for Case 2

Compared to Case 1, the overall operation cost is increased by a small proportion when adopting M3-BR, M3-FSM, and M1-BR-MPC, by 0.83%, 0.57%, 3.58% respectively. This shows that when the load prediction is imprecise, the performance when adopting M1-BR-MPC is impacted more than M3-BR and M3-FSM, although compared to the latter two methods, M1-BR-MPC reduces the overall operation cost by 8% and 6.85%, respectively.

Similar to Case 1, when online MPC is available, M1-BR-MPC performs the best in terms of power loss and battery power changes, resulting in the least operation cost compared to M3-BR and M3-FSM. NoLL-MPC performs similarly to M1-BR-MPC for the operation costs. However, the M1-BR-MPC method avoids constraint violations 100% of the time, while NoLL-MPC causes battery power violations because of the imprecise load predictions,

resulting in constraint violation costs which are 6.6 and 152.81 times higher than the ones when adopting the M3-BR and M3-FSM method. Consequently, the EPS achieves the minimum total cost by adopting the M1-BR-MPC method, which reduces the total costs by 15%, 7.24%, and 40.58% compared to adopting M3-BR, M3-FSM, and NoLL-MPC respectively. On the other hand, without the online MPC, M3-BR and M3-FSM perform similarly to Case 1, with M3-FSM reducing operation, violation, and total costs by 1.23%, 95.1%, and 84.3% respectively compared to M3-BR.

Based on these comparisons, the following facts are revealed:

1) Deviations between the real-time load and predictions impair the performance of the online MPC, resulting in higher overall operation and violation costs.

2) With the LL controller working in collaboration with the online MPC, the violation cost is reduced, while the operation cost is not improved compared to the ideal load predictions.

In practice, the LL controller provides quick reactions to the EPS changes. Therefore, the LL controller can cope with the inapplicable recommendations from online MPC. To improve the performance of the online MPC under the load uncertainties, a stochastic MPC method is proposed for HL in Chapter 6.

5.7.3.1 Comparison of power loss

Figure 5.11 presents the total power loss of the EPS during the flight for Case 2 when adopting the aforementioned control methods. Compared to the power loss result in Case 1, presented in Figure 5.5, a similar tendency can be observed in Figure 5.11 with more fluctuations because the loads fluctuate around the mean value listed in Table 5.7. When adopting M1-BR-MPC and NoLL-MPC, the average power loss is 1.5kW and 1.49kW accordingly. The two methods have similar values because the power losses are optimized by the online MPC. When NoLL-MPC is adopted, the maximum power loss is 2.8kW during the first minute of the flight, while the value is reduced to 2.38kW when M1-BR-MPC is adopted, because the LL controller avoids the power loss caused by the battery over-discharging. Furthermore, compared to power losses of 1.73kW and 1.69kW on average when adopting M3-BR and M3-FSM method, M1-BR-MPC method reduces the cost of power losses by 13.71% and 11.54% respectively, as presented in Figure 5.10 (b).

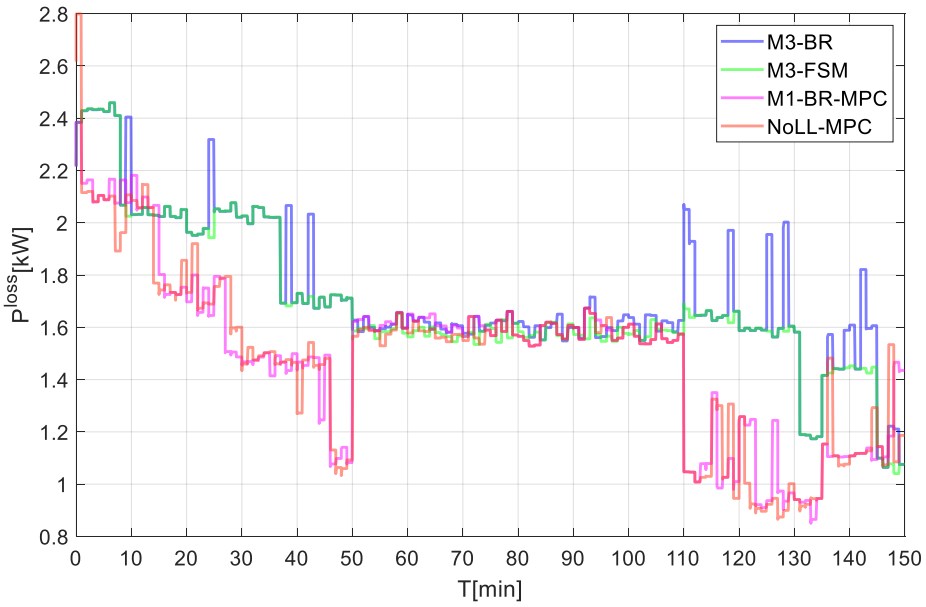


Figure 5.11 Total power loss during the flight for Case 2

5.7.3.2 Comparison of SOC and battery power

Figure 5.12 and Figure 5.13 demonstrate the SOC and the charging/discharging power of four batteries on LV buses for Case 2. The results have a similar tendency to Case 1 when adopting the same control methods. For example, M3-BR and M3-FSM methods keep the battery charging to increase the SOC to the upper bound (0.9) whatever the initial values of SOC, and M3-FSM stops charging after the SOC exceeds the upper bound. Compared to M3-BR, the cost of SOC is increased by 22.73% when adopting M3-FSM, while the SOC violation is reduced by 95% in this case. Aided by the online MPC, M1-BR-MPC charges the battery for longer when its SOC initial value is closer to the lower boundary (0.3). Compared to M3-BR and M3-FSM, the cost of SOC is increased by 75.32% and 42.65% respectively, without constraint violation when adopting M1-BR-MPC, while the average SOC of the ESSs is maintained at 0.73 for energy redundancy.

With the load disturbances, M3-FSM maintains the minimum amount of battery power changes, which is reduced by 66.68% in comparison to the cost index when adopting M3-BR. Although the M1-BR-MPC has a higher cost of battery power change than M3-FSM, it performs better than M3-BR with the cost reduction of 10.42%.

NoLL-MPC results in a similar change tendency of SOC and battery power to M1-BR-MPC, because both methods refer to decisions from the online MPC. However, without LL control for real-time load responses, battery 1, 2 and 4 exceed their maximum discharging limitations when adopting the online MPC as presented in Figure 5.13. Because battery 1 is charged the most with the minimum initial SOC, it encounters more violation time and value compared to other batteries. According to Figure 5.13 (a), battery 1 is overcharged for 17

minutes with the maximum exceeding power of 0.98kW. In contrast, when the LL controller operates in either independent or collaboration mode, there is no battery power violations.

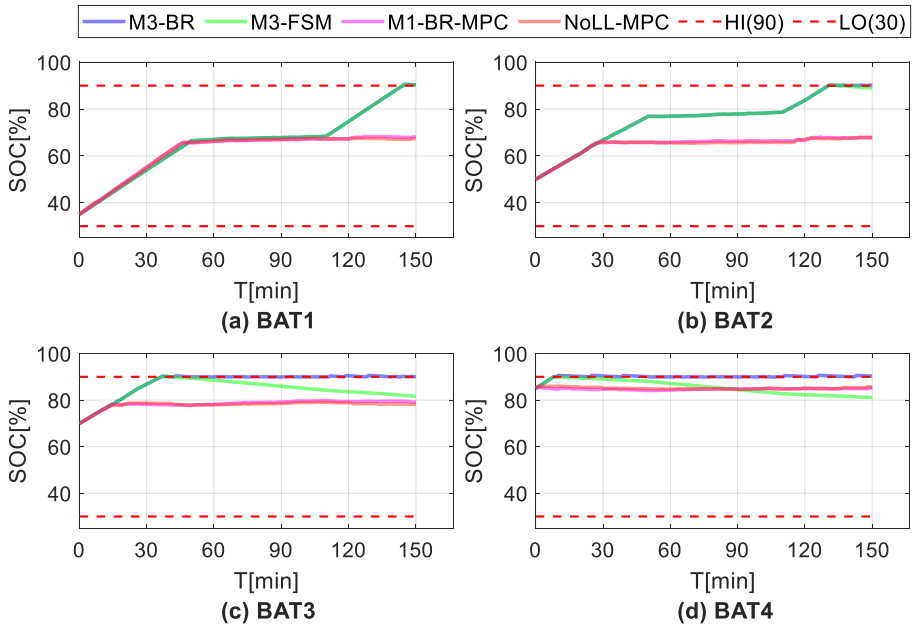


Figure 5.12 SOC results for Case 2

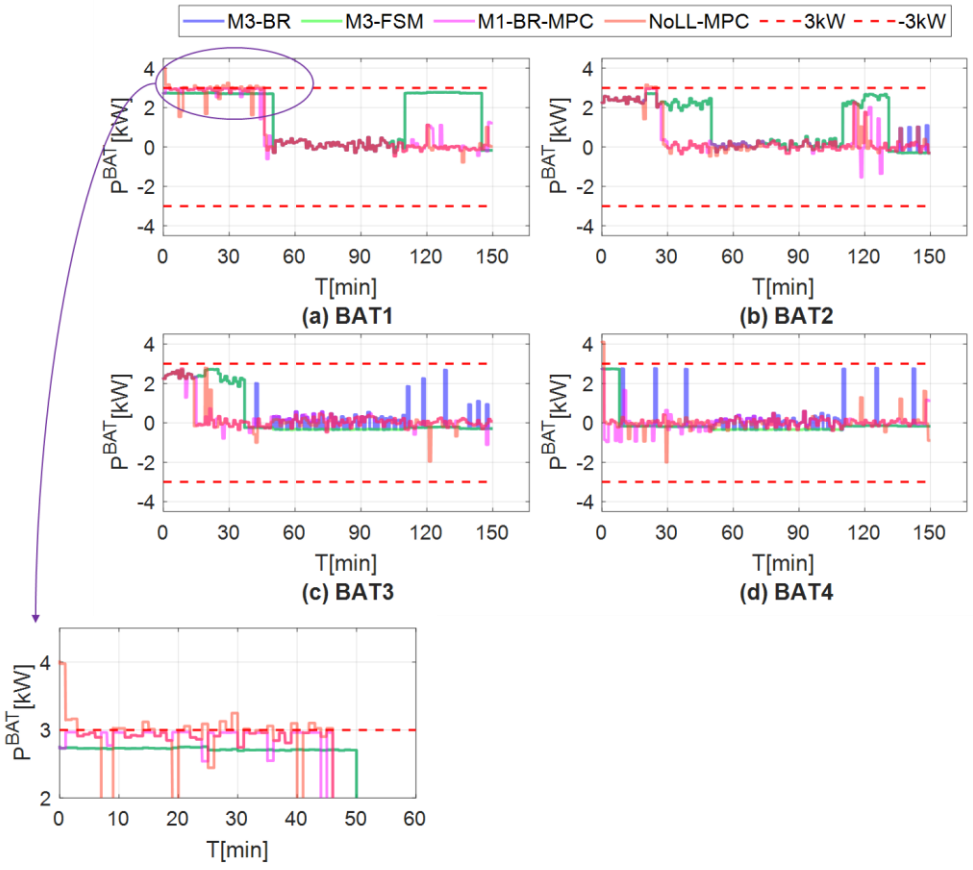


Figure 5.13 Battery charging/discharging power in Case 2

5.7.3.3 Comparison of generator output power

Figure 5.14 illustrates the generator output power in the EPS for Case 2, which has similar tendencies to Case 1 when adopting the same methods. In addition, NoLL-MPC provides similar results to M1-BR-MPC. In this study, the generators are assumed to be capable of supplying loads with the predefined fluctuations; hence, generators are not overloaded when adopting all of the four methods mentioned in this case. Moreover, because the generator output power is mostly applied for load supply rather than battery charging during the cruising stage under the study settings, the maximum generator power varies from 45.03kW to 45.1kW when adopting different methods, which results in a small (neglectable) difference of less than 0.15%.

Instead of assuming a limited amount of load fluctuation within generator capabilities, Chapter 6 presents further studies of the load uncertainties with the potential generator overload scenarios.

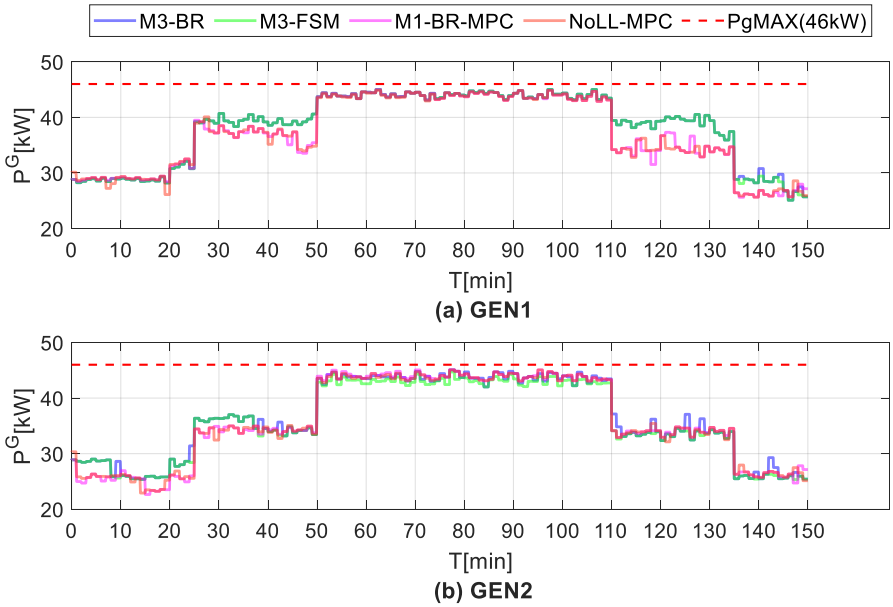


Figure 5.14 Generator power in Case 2

5.7.3.4 Comparison of cells' input power

Figure 5.15 illustrates the cells' input power in the EPS for Case 2, which has similar tendencies to Case 1 when adopting the same methods. In addition, NoLL-MPC shows a similar tendency to M1-BR-MPC. However, with the LL controller, the cells' power is adjusted to avoid the battery power exceeding the limits. For example, as illustrated in Figure 5.13(a), battery 1 is overcharged by NoLL-MPC during 0min-2min, which is supplied by Cell 1-3. Comparing the input power of Cell 1-3 in Figure 5.15 (a)-(c) when adopting M1-BR-MPC and NoLL-MPC, the former method reduces the power allocated to Cell 1-3 referring to the rule in step 3)-d) of Algorithm I. During the flight of 0 min-50 min, the same comparison results can be observed with other batteries and time intervals when power violation happens, which

verifies the effectiveness of the LL controller in the collaboration mode for responses to load fluctuations.

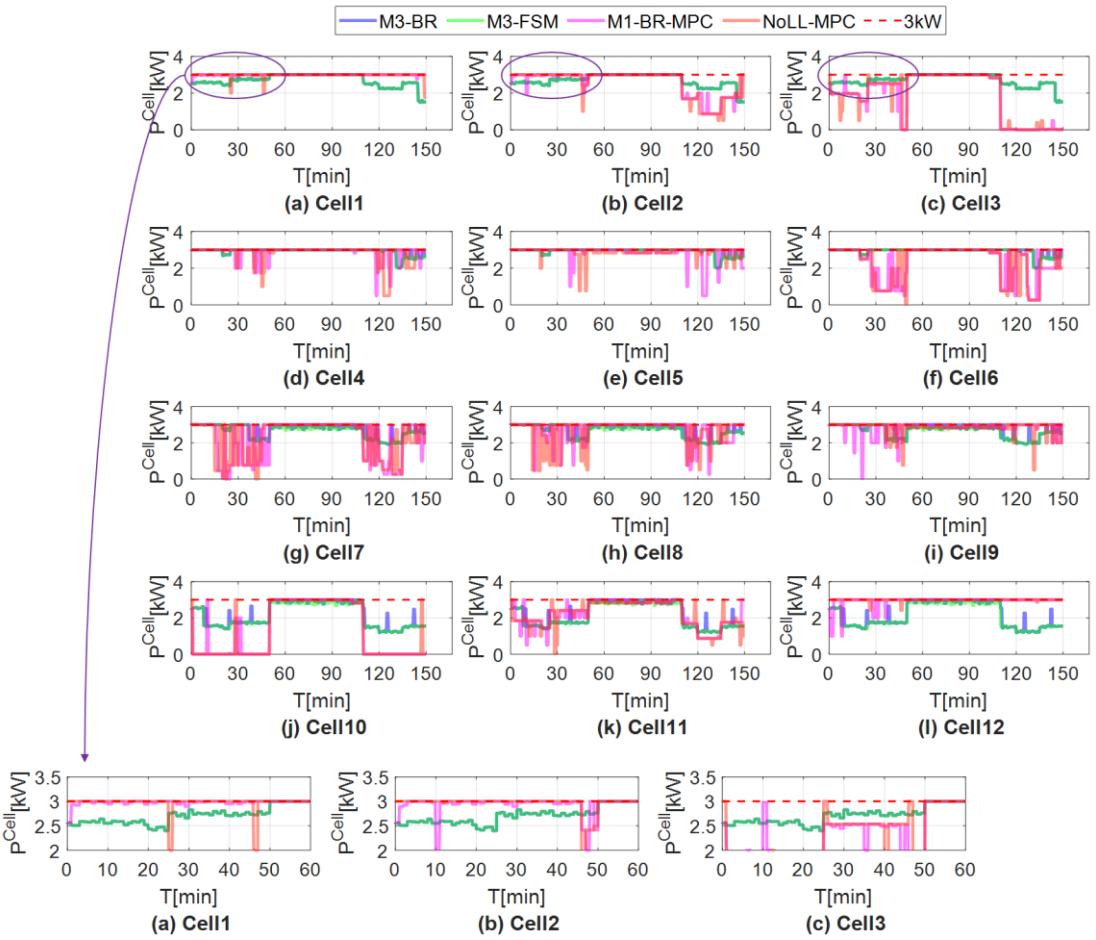


Figure 5.15 Cells' input power for Case 2

5.7.4 Case 3: EPS faulty scenario

In Case 3, faulty scenarios are assumed during different flight stages, including failure events for: Battery 4; Cell 10; Generator 1; the connection between HVB 2 and Cell 7 (S_{27}^{hvc}); and the connection between HVB 1 and Cell1 (S_{11}^{clv}). The failures are assumed to occur at the specified time instances as listed in Table 5.10. This case aims to verify the controller capability to respond to the component failures following the operational constraints, and to compare the performance in the faulty condition. The load demands are assumed to follow the load profile in Table 5.7 without considering load disturbances, aiming to focus on the performance in faulty conditions. Further study of the uncertain load demands with the EPS failures is presented in Chapter 6.

Table 5.10 Failure events during the flight

Instant of fault occurrence	1000s (16.67min)	2000s (33.33min)	3000s (50min)	4000s (66.67min)	5000s (83.33min)
Failed Component	Battery 4	Cell 10	Generator 1	S_{27}^{hvc}	S_{11}^{clv}

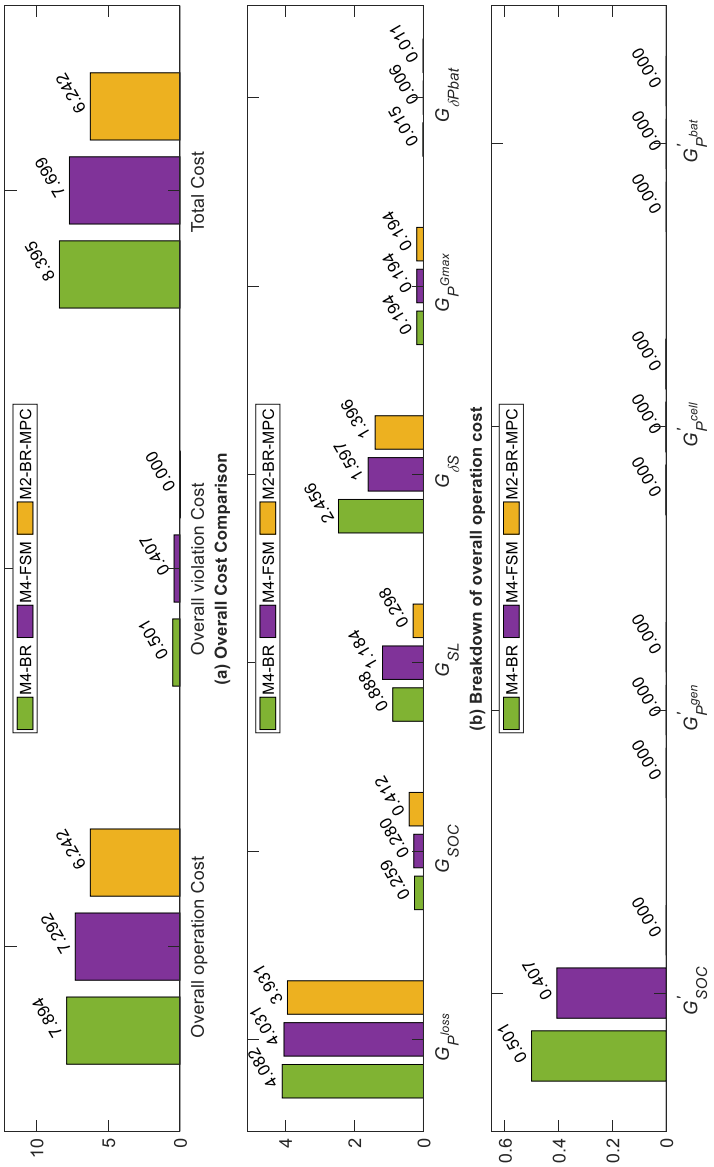


Figure 5.16 Cost comparison of different control for Case 3

The costs of different methods for Case 3 are presented in Figure 5.16. In Figure 5.16 (a), the overall operation cost, overall violation cost, and total cost are compared for each control method. Figure 5.16 (b), presents the breakdown of the overall operation cost in Figure 5.16 (a)

when adopting four control methods, including six operation cost indices proposed in Section 5.6.1. In addition, Figure 5.16 (c) presents the breakdown of the overall violation cost in Figure 5.16 (a), including four violation cost indices proposed in Section 5.6.2.

As illustrated in Figure 5.16, with the online MPC in HL, M2-BR-MPC achieves the minimum overall operation and violation costs among all methods studied. In particular, the EPS achieves the minimum cost of power loss, switching activities, and load shedding without violation costs when adopting M2-BR-MPC. In contrast, M4-FSM leads to the minimum cost of battery power changes, while M4-BR performs the best in the cost of SOC among all methods. When adopting M2-BR-MPC, the overall operation cost is reduced by 20.93% and 14.4% respectively, compared to M4-BR and M4-FSM, while the total cost is reduced by 25.64% and 18.92%.

When the online MPC is unavailable, M4-BR results in fewer costs in SOC and load shedding compared to M4-FSM. In comparison, M4-FSM performs better than M4-BR with fewer costs of power loss, switching activities and battery power changes, which leads to the reduction of overall operation cost by 7.63%. In addition, the violation of SOC limitations is reduced by 18.79% compared to the violation cost of M4-FSM to M4-BR, leading to an overall violation cost reduction by 8.3%.

5.7.4.1 Comparison of power loss

Figure 5.17 illustrates the total power loss of the EPS during the flight for Case 3 when adopting different control methods. The average power loss is 2.04kW, 2.02kW, and 1.97kW. Compared to Case 1, the average power loss is increased in Case 3 by 18.42%, 19.58%, and 36.3% when adopting M4-BR, M4-FSM, and M2-BR-MPC respectively. Because the component failures lead to different configurations, which are less efficient compared to normal scenarios for supplying the same load demands as Case 1. On the other hand, with the failure of a cell, less input power from generators is available at the LV side, resulting in more discharging in batteries during the cruising stage and more charging after the cruising stage, which can be observed in Figure 5.18 (a) and (c) compared to Figure 5.6 (a) and (c). In consequence, this results in more power losses in charging/discharging batteries compared to Case 1.

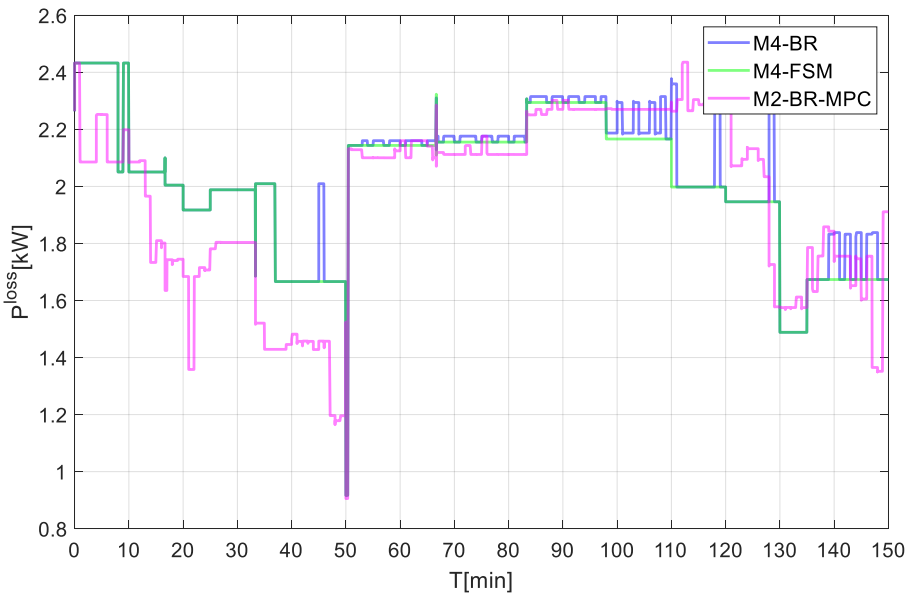


Figure 5.17 Total power loss during the flight for Case 3

When the online MPC is unavailable, the M4-BR and M4-FSM methods configure the EPS following the same rules, while the battery power and load shedding are determined using different rule conditions. In this case, M4-FSM causes less power loss compared to M4-BR, by about 1.23%, because M4-BR reduces the periodical charging beyond the SOC upper bound, as mentioned in Case 1. In addition, less load supply leads to less power loss. For example, the power loss is the minimum during 3000s-3020s (50min-50.33min) among all flight stages in Figure 5.17, when generator 1 is in the faulty condition and generator 2 supplies the EPS, resulting in load shedding of mid- and low-priority HV/LV loads as presented in Figure 5.23 and Figure 5.24. As evaluated in Figure 5.16 (b), M4-FSM sheds more loads compared to M4-BR, causing a reduction in power loss.

When the online MPC is available, the power loss is reduced by 3.69% and 2.49% compared to M4-RB and M4-FSM methods for the independent LL. Differing from the rule-based methods, M2-BR-MPC improves the power loss by changing the configuration of LV bus connections and charging batteries in a different manner without increasing load shedding. These are further discussed in the following subsections.

5.7.4.2 Comparison of SOC and battery power

Figure 5.18 and Figure 5.19 demonstrate the SOC and the charging/discharging power of four batteries on the LV buses for Case 3. Figure 5.20 presents the connection of LV buses. At 1000s (16.17min), battery 4 is out of service and disconnected. Hence, the power of battery 4 remains at 0 in the following flight stages in Figure 5.19 (d), and its SOC remains unchanged. To keep the voltage and supply the loads of LV bus (LVB) 4, the LL controller connects LVB 1 with LVB 4 following its rules in M2 and M4. Compared to Case 1, battery 1 is discharged

when the EPS enters the cruising stage. This is caused by the disconnection of Cell 10 which supplies HVB 4 before 2000s (33.33mim), resulting in insufficient power from the HV side to LVB 4 when the load peak occurs during the cruising stage. Therefore, the loads on LVB 1 and LVB 4 are supplied by battery 1 with the connection of LVB 1 and LVB 4.

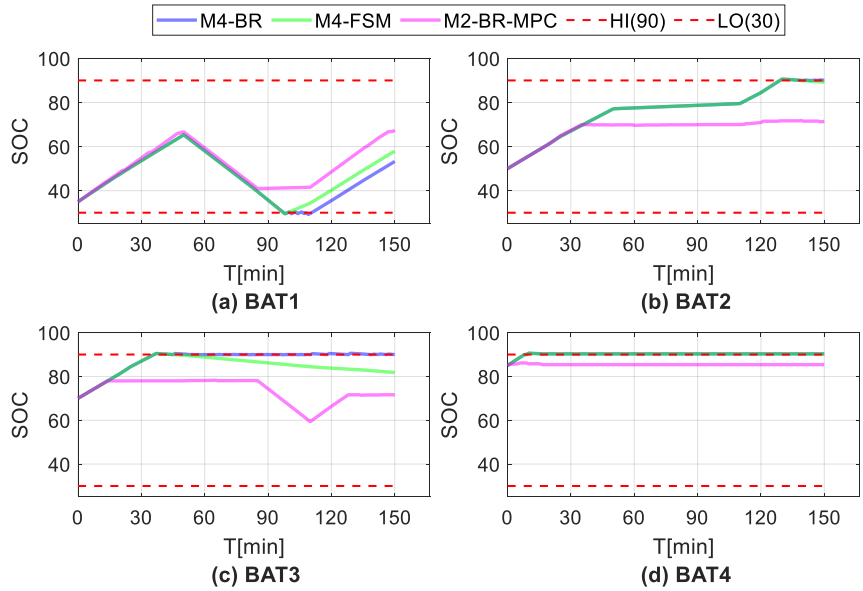


Figure 5.18 SOC results for Case 3

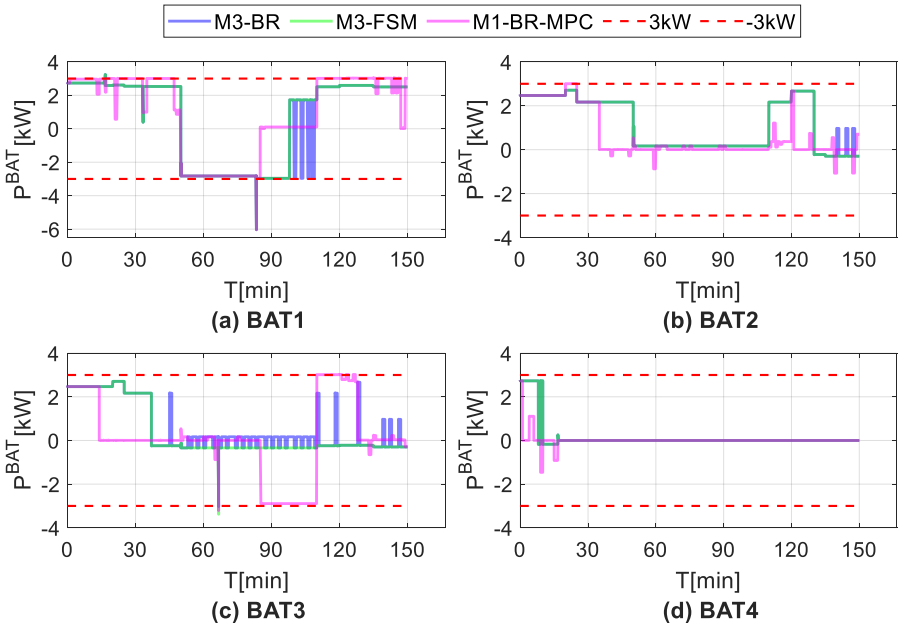


Figure 5.19 Battery charging/discharging power for Case 3

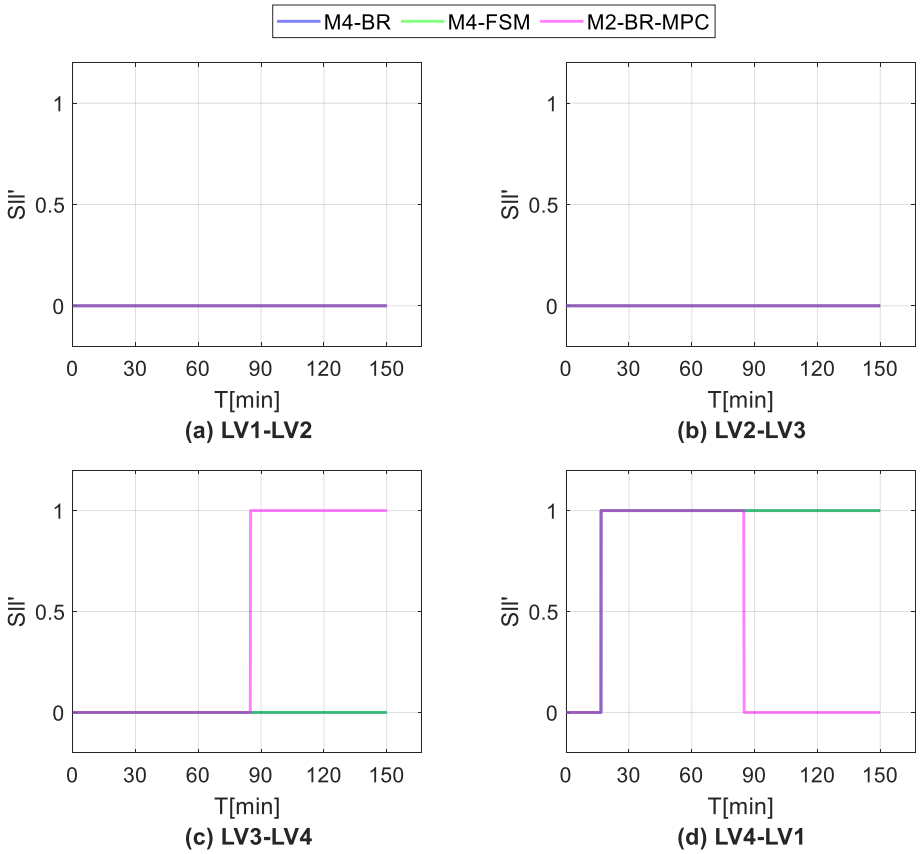


Figure 5.20 LV bus connections

Based on the optimization with the online MPC at HL, M2-BR-MPC maintains the connection decisions of M2 in the LL until 85min, to avoid the switching activities. After 85min, LVB 3 is connected with LVB 4 by M2-BR-MPC to supply the loads on both buses and stop the discharge of battery 1, avoiding the SOC violating the lower bound (0.3). However, without the online MPC considering future status, M4-BR and M4-FSM cause SOC violation of battery 1 at the lower bound, leading to load shedding as presented in Figure 5.23 (c) and (l) during the 98min-110min period. By shedding the low-priority loads on LVB 1 and LVB 4, battery 1 can be charged from the HV side. As presented in Figure 5.18, M4-FSM keeps load shedding during the 98min-110min period to maintain the charge of battery 1, while M4-BR alternates between charging the battery and reconnecting loads.

In summary, M4-BR maintains the maximum SOC for batteries 2-4, resulting in the cost of SOC being reduced by 7.5% and 37.14% compared to M4-FSM and M2-BR-MPC, respectively. However, for the worst case of battery 1, M2-BR-MPC performs the best to avoid the SOC dropping below the lower bound. In addition, M4-FSM performs better than M4-BR in recovering SOC from the lower bound. M2-BR-MPC and M4-FSM also reduce the cost of battery power changes by 26.7% and 60% compared to M4-BR accordingly. Similar to Case 1,

M2-BR-MPC avoids SOC exceeding limitations because of the future prediction, while M4-FSM reduces the excess by avoiding alternating around the boundaries.

5.7.4.3 Comparison of generator output power

Figure 5.21 illustrates the generator/APU power in the EPS for Case 3. Figure 5.21 (a) shows that the generator is disconnected because of the failure at 3000s (50min). The APU is started by the LL controller in both independent and collaboration modes and is connected to the HV bus 1 (HVB 1) to replace generator 1 after 20 seconds for starting up, which is presented in Figure 5.21 (c).

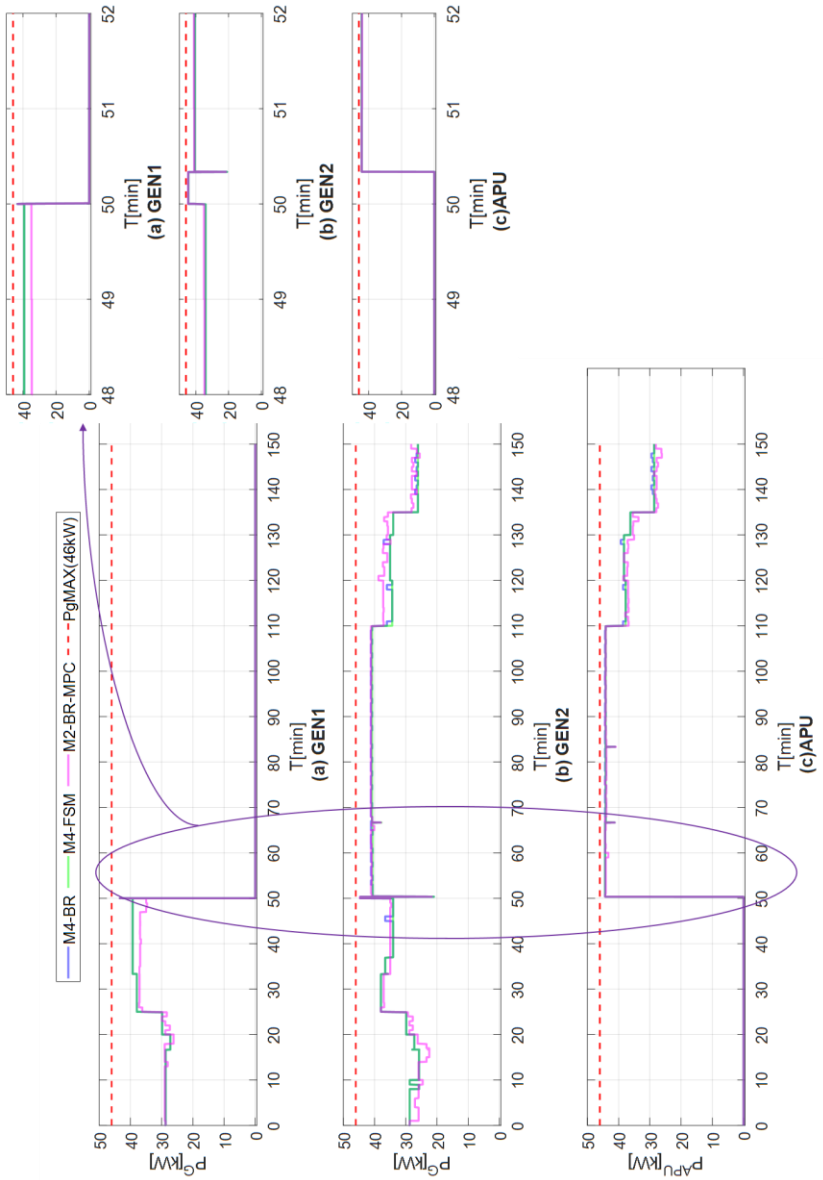


Figure 5.21 Generator/APU output power for Case 3

During the APU starting period (50min to 50.33min), generator 2 is connected to HVB 1 to supply the EPS. All of the methods shed sufficient loads to avoid the overload of generator

2. As presented in Figure 5.18 and Figure 5.19, mid (Load 3) and low (Load 4) priority HV/LV loads are shed. The maximum generator/APU power is reached during the APU starting period, when generator 2 supplies the EPS. The maximum output power of generator 2 is approximately equivalent across the studied methods.

5.7.4.4 Comparison of cells' input power

The input power of each cell is presented in Figure 5.22 to present the failure impacts on the cells. As presented in Figure 5.22 (j), failure occurs to Cell 10 at 2000 s (33.33 min), which is disconnected by LL in all methods. Therefore, the output power of Cell 10 remains at 0 afterwards. In addition, the power of all cells drops at 50 min when generator 1 fails, but is recovered once the APU has been connected. In Figure 5.22 (g) and (a), the power drops at 4000 s (66.67 min) and 5000 s (83.33 min) for Cell 7 and Cell 1 respectively, because of the connection failure. However, their connection is switched with Cell 6 and Cell 12 by the LL controller in all methods. Because the online MPC avoids transmission switching, the connection remains unchanged.

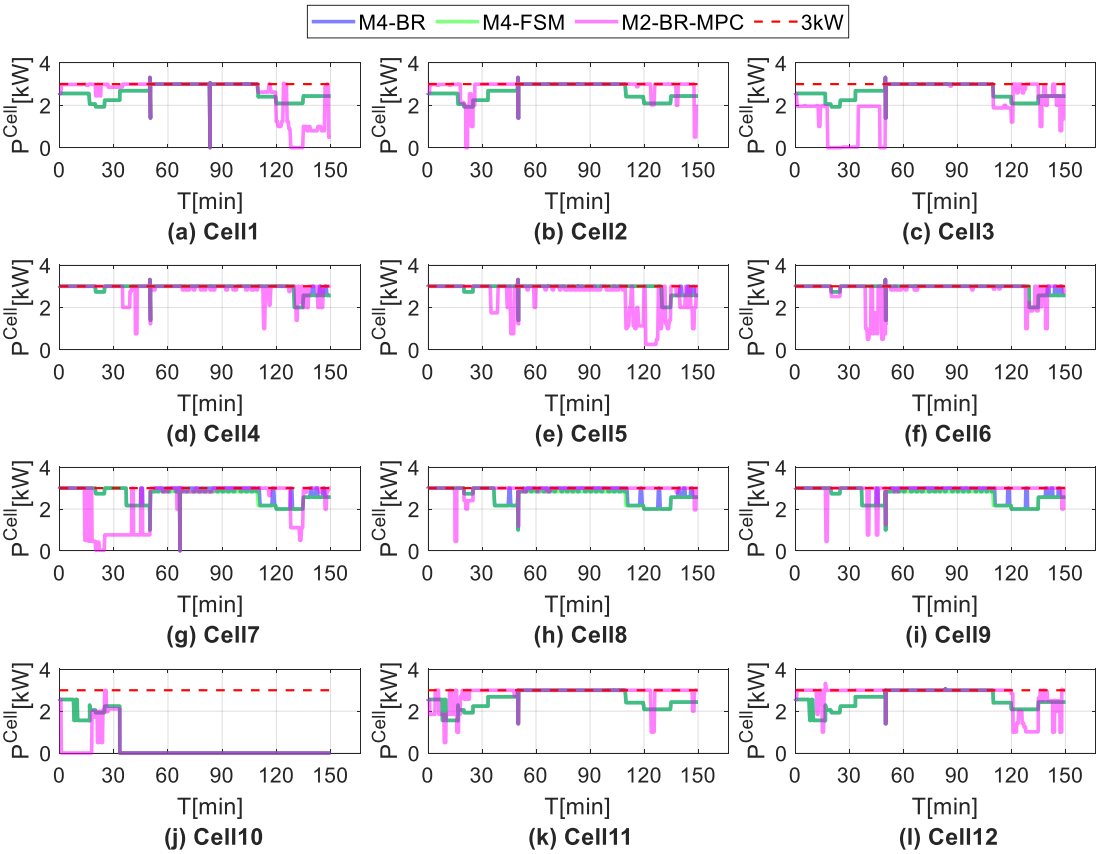


Figure 5.22 Cells' input power for Case 2

5.7.4.5 Comparison of load shedding and switching

Figure 5.23 and Figure 5.24 present the states of the noncritical load connections on LV and HV buses respectively. As mentioned in subsection 5.7.4.3, HV/LV mid and low-priority loads are shed after generator 1 failure (50 min) during the APU starting time (50 min to 50.33 min) by all three control methods. The studied control methods also provide decisions to reconnect the loads when the APU is connected to HVB 1. In the following flight stages, M2-BR-MPC controls the EPS without future load shedding, while load shedding is conducted for low-priority loads (Load 4) on LVB 1 and LVB 4 during the 98min-110min period by the LL in the independent mode. As mentioned in subsection 5.7.4.2, LBV 1 and LVB 4 are connected together and both supplied by battery 1, which requires charging in advance to avoid the SOC exceeding the lower bound. In summary, M2-BR-MPC performs the best among all of the methods in terms of the cost of load shedding, which is reduced by 66.49% and 74.85% compared to the cost when adopting the M4-BR and M4-FSM methods. Compared to M4-BR, the load shedding is increased by 33.25% when adopting M4-FSM methods.

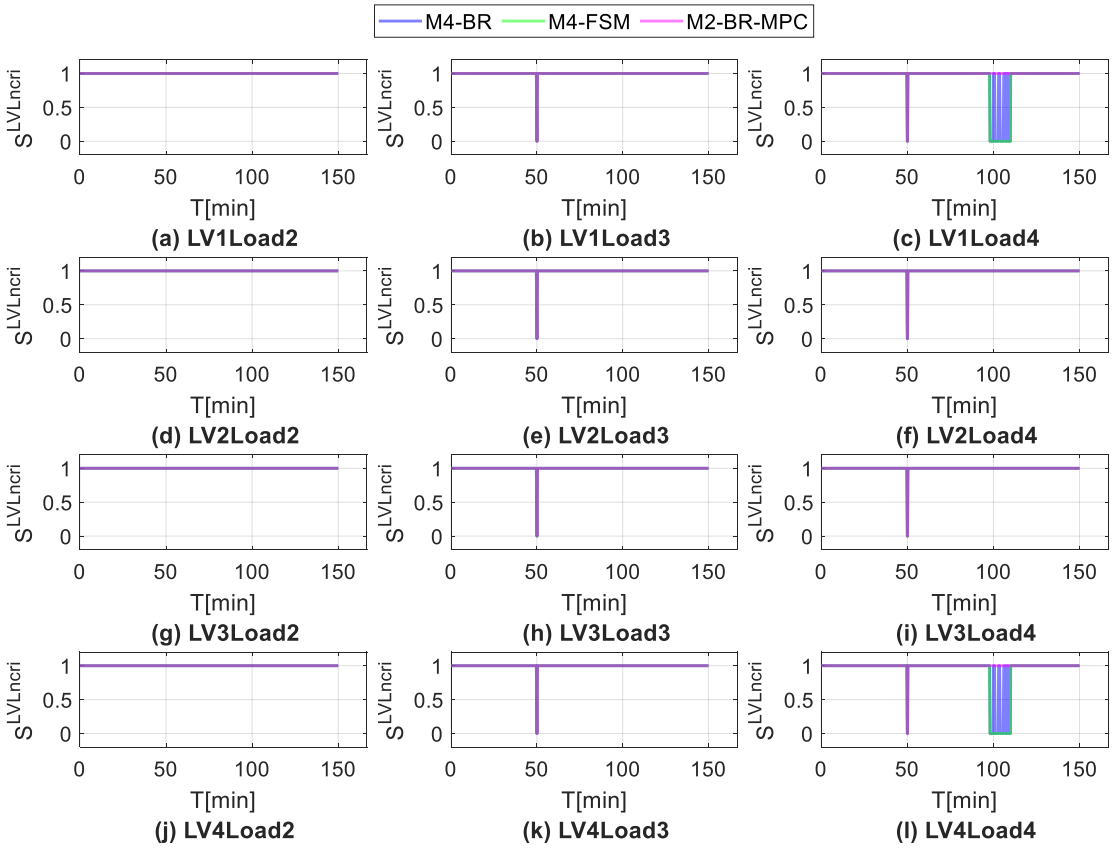


Figure 5.23 Connection of LV noncritical loads on LV buses for Case 3

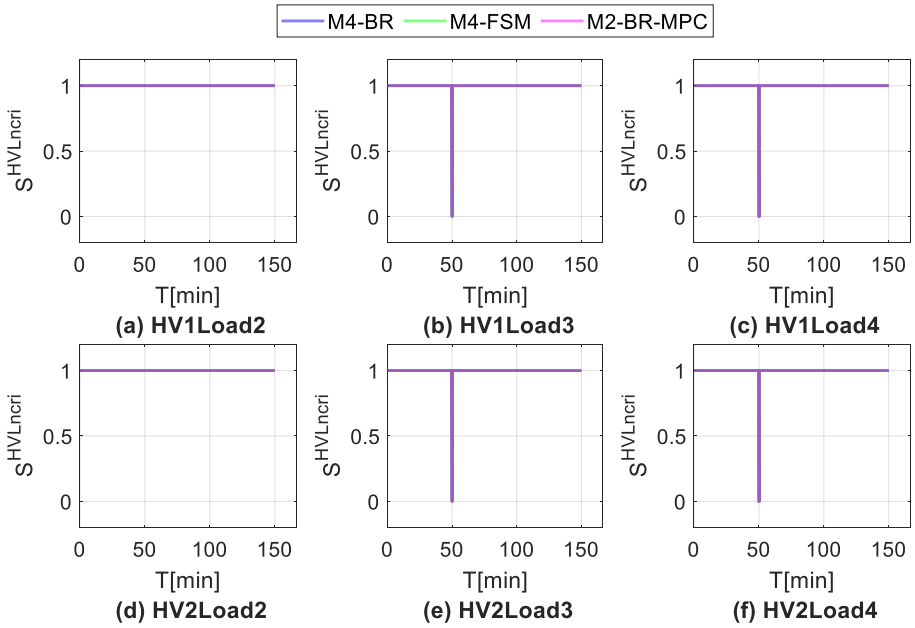


Figure 5.24 Connection of HV noncritical loads on HV buses for Case 3

In addition to load shedding, the count of switching activities is also compared for three control methods in Table 5.11. Compared to M4-BR and M4-FSM, M2-BR-MPC increases the switching of the transmission links by 15.38%, which is caused by the change of LV bus interconnections as discussed in subsection 5.7.4.2. However, the load switching is reduced by 45.45% and 14.29% compared to the other two methods when adopting M2-BR-MPC. When the online MPC is unavailable, M4-FSM reduces the load switching activities by 36.36% compared to M4-BR.

In summary, with the online MPC in HL, M2-BR-MPC performs the best in terms of both reducing load shedding and reducing switching activities. When the online MPC in the HL is unavailable, the LL controller in the independent mode can provide decisions for configurations and load shedding to meet the operational constraints. M4-FSM performs better than M4-BR in avoiding continuous load switching, although this can increase load shedding.

Table 5.11 Switching activities in Case 3

	M4-BR	M4-FSM	M2-BR-MPC
δ_{APU}	1	1	1
δ_{trans}	13	13	15
δ_L	44	28	24

5.7.5 Conclusions for the case study

As presented in Case 1-3, the EPS achieved the best overall operation and constraint violation performance when the online MPC in HL operated with the LL controller, because the collaboration improves the following aspects: 1) minimum power losses by balancing with restoring energy in ESSs; 2) minimum power requirements on each generator; 3) minimum load shedding; 4) minimum switching activities; 5) minimum constraint violations and quick response to EPS changes. However, when the online MPC is unavailable, the proposed controller can still manage the EPS operation following the real-time limitations. Although rule-based LL control cannot achieve the best overall performance, the performance can be improved by improving the rules, such as from the BR-based method to the FSM-based method.

5.8 Chapter summary

In this chapter, a two-level hierarchical controller was designed to supervise the entire EPS operation in different time scales and operation scenarios. The HL controller was based on the optimization scheme of MILP-MPC to improve the long-term EPS performance with future predictions. To provide quick responses to short-term system changes, such as load demands and failure occurrence, a rule-based LL controller was proposed with a faster clock. The LL contains four modes to allow it both cooperating with online MPC in HL and operating independently in EPS normal/faulty conditions. Moreover, two methods, BR-based and FSM based, were applied in the rule design for the LL independent modes. Three cases were simulated to verify the effectiveness of the proposed hierarchical control. In addition, the performance of the hierarchical control in different modes was evaluated and compared.

This study provides researchers with an innovative controller design methodology balancing the deterministic rules and the optimization flexibility for EPSs with extremely strict safety requirements, such as aircraft systems. For safety reasons, conventional operational controllers for aircraft EPSs completely rely on predefined rules to ensure all control strategies are deterministic. However, this makes it challenging to improve EPS performance. In contrast, by adopting the proposed hierarchical control framework in onboard EPSs, all predefined rules can be adapted in the LL controller; in the meantime, the HL is flexible to provide various optimized strategies. This study inspires each level controller design considering the coordination of different levels. Furthermore, because the LL controller ensures that the hard constraints are satisfied, the HL controller can adopt a variety of deterministic or nondeterministic techniques to achieve the optimization/preferred targets.

Chapter 6 Improved operational control with uncertainty considerations

In Chapter 3 to Chapter 4, the studies are based on the deterministic formulation of the optimal operational management problems. The uncertainty of the EPS component is not considered, such as uncertain load disturbances or component faults. In Chapter 4 and Chapter 5, since it does not take the uncertainty explicitly into account, the MPC proposed is known as deterministic MPC (DMPC), based on the assumption of precise load predictions. Although in Chapter 5, limited load disturbances are considered in the LL of the hierarchical control, two problems remain to be solved with the uncertainty in load demands. Firstly, the hierarchical control relies on the HL recommendations, which is based on the DMPC model. The uncertainty of the system can cause the DMPC to be ineffective in providing reliable control strategies to the LL because MPC relies on future predictions. Secondly, the LL controller provide strategies after the uncertainty occurrence, which can lead to higher costs compared to considering the uncertainty in advance. To cope with these issues, a chance-constrained stochastic MPC (CC-SMPC) method is proposed in this chapter for the same EPS architecture studied in Chapter 5. The proposed CC-SMPC is based on the DMPC model at the HL of the hierarchical control in Chapter 5, converting the deterministic constraints of power limitations and SOC range to chance constraints.

6.1 Introduction

6.1.1 Control functions

Uncertainty is an inseparable part of real systems and load forecasting is quite likely to be imperfect. Moreover, although most of the MEA loads are predictable, it is difficult to precisely predict the power consumption behavior of all parts of the system. This uncertainty in the system can lead to performance degradation of the DMPC methods that are based on the certainty equivalence principle (i.e. a model of the system is fit by observing its time evolution, and a control policy is then designed by treating the fitted model as the truth [159]). Hence, to overcome this limitation and explicitly take into account the uncertain nature of random parameters, CC-SMPC is used in this chapter for the operation of the same EPS architecture as in Figure 1.7 and the power flow diagram in Figure 5.1. With the ability to cope with uncertainties due to fluctuating load demands, the CC-SMPC model aims to improve the system

operation in terms of the system's cost and reconfiguration activities in both normal and faulty conditions of EPS, including minimizing power losses, load shedding, and switching activities in the system while optimizing ESS utilization. The system's operational and technical requirements are formulated as a set of deterministic and probabilistic constraints in the CC-SMPC model.

6.1.2 Contributions

In Section 2.5.1, the studies applying CC-SMPC to the operational management of the EPS are reviewed. There is a research gap with regard to normal and abnormal operating conditions with multiple failures of system components. In [106], the contactor failures are not taken into account while studying the load uncertainty. In contrast, when contactor failures are discussed, the load demand is assumed to be deterministic. In addition, the EPS architecture is a simple conventional one, where the propagation of uncertainty is simplified with isolated loads and buses. Regarding terrestrial power grid applications, in [131], [161], [162], [163], and [132], CC-SMPC is proposed for the coordinated energy management of microgrids, although the multi-uncertainty scenario is discussed in these papers, a common grid is applied to compensate for all of the uncertainty, avoiding the interactions of flexible configurations, power scheduling, and uncertainty propagation. None of the reviewed studies simultaneously combined both normal and multi-failure scenarios with multi-uncertainty issues and chance constraints, which is not only important at the moment, but will become even more so with the growing complexity as the MEA EPS develops, where flexible configurations, power scheduling, and uncertainty propagation interact with each other. Besides, the evaluation of the performance of the designed CC-SMPC must be improved. In the reviewed studies, online testing is conducted with only one uncertainty profile. This method consequently does not provide an understanding of how the uncertainty distribution impacts the results when the uncertainty profile changes. In addition, these impacts are not considered in the evaluation framework, leading to the incomplete performance evaluation for CC-SMPC compared to other methods.

The main contributions of the study in this chapter are summarized below:

1) A CC-SMPC model is proposed for three different cases: in the presence of uncertainty of load power demand on the LVBs in normal operation mode, and the presence of uncertainty of load power demand on both LVBs and HVBs in normal as well as faulty operation modes. In each case, the probabilistic constraints on power limitations and batteries' state of charge (SOC) are formulated based on the uncertainty propagations in the system, considering the power balance, components' health status, and system configuration.

2) A comprehensive Monte-Carlo-based offline and online simulation is conducted for both DMPC and SMPC methods, and the results are evaluated with the proposed multi-dimension

evaluation framework. In previous works, the analysis of the results for CC-SMPC is mostly conducted with offline simulations or a few online scenarios. However, for time accumulated variables such as SOC in CC-SMPC, the offline simulation is ineffective as the uncertainty accumulates with time, which leads to system divergence. In addition, the MPC method is initially based on the online scheme. Therefore, in this work, Monte-Carlo-based online simulation is conducted to improve the effectiveness of the comparative study for both methods. To compare the final results, the multi-dimension evaluation framework calculates both operation costs and constraint violation costs, which consist of average and maximum violation percentages and quantities.

6.2 CC-SMPC framework

Figure 6.1 represents the proposed CC-SMPC-based control framework for controlling the system operation. As illustrated in the figure, at each time step k, the CC-SMPC-based control system receives the EPS status to update the system state and constraints of the controller. An online optimization problem is solved with multi objectives to obtain an optimized control sequence for k, k+1, …, k+N-1, where N indicates the total time steps contained in the finite prediction horizon H. However, only the first sample of the optimized control sequence is applied, and the horizon is shifted to the next time step k+1.

As presented in Figure 6.1, at each time step k, the load prediction $\mathbf{P}^{\mathbf{Load}}(k,k+1,\ldots N-1)$ for the entire horizon is updated and sent to the controller, where $\mathbf{P}^{\mathbf{Load}}$ indicates the matrix of predicted average and standard deviation (SD) values of all loads. In addition, based on the new measurements of the system received at the current time step, the system status is updated and shared with the controller. The status information includes the failure status matrix $\boldsymbol{\gamma}$ consisting of all failures in the system, the connection status matrix **S**' consisting of the on/off status of all switches, and the **SOC** matrix consisting of the SOC of all ESSs. This information is used for updating the system dynamics and resetting the feasible region of the optimization problem included in the controller for the entire prediction horizon. After the optimization problem is solved, the CC-SMPC-based controller directly provides the reference values of the configuration/connection matrix **S** and the power references of all cells $\mathbf{P}^{\mathrm{Cell}}$ to the system. Since the generators/APU and ESS are operated in voltage control mode as introduced in Section 5.2.1, given these configurations, the cells' powers, loads' powers, and other power flows in the system can be determined based on Kirchhoff's Current Law.

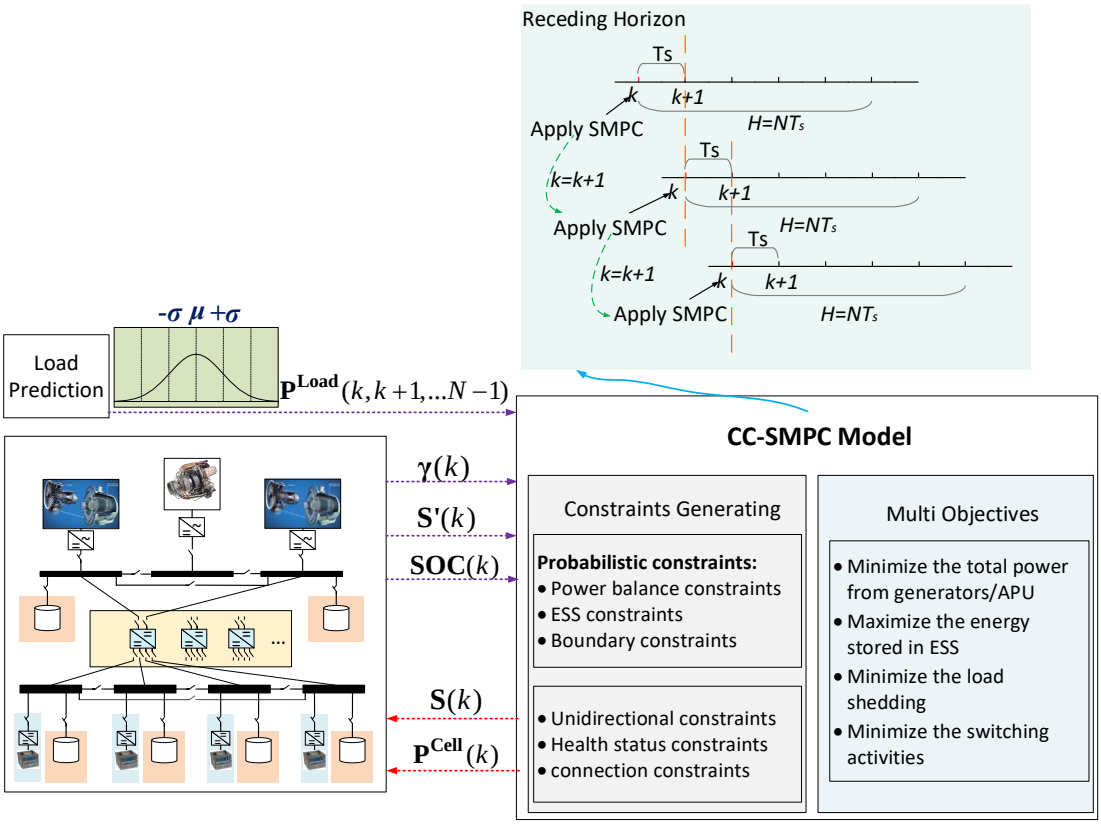


Figure 6.1 Flowchart of the proposed online CC-SMPC optimization framework

6.3 CC-SMPC formulation based on the DMPC which was proposed in Chapter 5

6.3.1 Objective functions

In this study for CC-SMPC, the focus is on the most highlighted objective functions in the DMPC, including: minimizing total power consumption from all power sources in (5.1), maximizing the energy stored in ESSs in (5.2), minimizing the load shedding in (5.3) and the switching activities in (5.4)-(5.6). As described in the following Section 6.3.2.1, battery charging/discharging power is represented by a variable $P_l^{BAT}(k)$, allowing both positive and negative values in this chapter, to reduce the nonlinearity and improve the feasibility of the model. Consequently, objective functions in (5.1) and (5.2) are replaced by simplified ones in (6.1) and (6.2), respectively, to reduce power losses and encourage battery charging. (6.1) indicates the objective to reduce the power from the generators and APU, combined with the reduction of power discharging in (6.2), total power consumption from all power sources can be minimized. In addition, battery charging is also encouraged by adopting (6.2), which maximizes the energy stored in ESSs.

$$J_{P^G} = \sum_{k=0}^{N-1} \frac{\sum_j^{N^{HVB}} P_j^G(k) + P^{APU}(k)}{N^G . pGmax} \quad (5.66)$$

$$J_{P^{bat}} = \sum_{k=0}^{N-1} \frac{\sum_l^{N^{LVB}} -P_l^{bat}(k)}{N^G . P_l^{batmax}} \quad (5.67)$$

6.3.2 Constraints

In CC-SMPC, constraints with random variables are replaced with probabilistic constraints, which means instead of guaranteeing the satisfaction of system constraints at all time instances, it is guaranteed that the probability of satisfying the probabilistic constraints is higher than a pre-specified confidence level. In this section, three cases are introduced to investigate the effects of uncertainty on different loads of the MEA system in various healthy and faulty operating conditions.

6.3.2.1 Case 1: Uncertainty on the LV-side loads

In this case, it is assumed that the system operates in a nominal operating condition (no failure is considered). Hence, the health status of each component is set to one. In addition, only the power uncertainty of the LV-side loads is taken into account ($\forall l \in \{1, \dots, N^{LVB}\}$, $\forall q \in \{1, \dots, N^{LVLcri}\}$, $\forall q \in \{1, \dots, N^{LVLncri}\}$). It is assumed that the uncertain parameters follow a Gaussian distribution with the expected value of $\bar{P}_{lq}^{LVLcri}$ and $\bar{P}_{lq}^{LVLncri}$ and the SD of $\sigma_{P_{lq}^{LVLcri}}$ and $\sigma_{P_{lq}^{LVLncri}}$, for each critical and non-critical loads on the LV buses, respectively as shown in (6.3) and (6.4), where $\mathcal{DN}$ represents the Gaussian probability distribution function (PDF).

$$P_{lq}^{LVLcri}(k) = \mathcal{DN}(\bar{P}_{lq}^{LVLcri}(k), \sigma_{P_{lq}^{LVLcri}(k)}) \quad (5.68)$$

$$P_{lq}^{LVLncri}(k) = \mathcal{DN}(\bar{P}_{lq}^{LVLncri}(k), \sigma_{P_{lq}^{LVLncri}(k)}) \quad (5.69)$$

Since in the normal operation scenario the LV buses will not be interconnected (according to constraints (5.30)-(5.32)), the LV loads uncertainty for each LV bus is independent of that of adjacent LV buses. In addition, the input power from cells to one LV bus is deterministic. Therefore, the battery on each LV bus is used for compensating for the LV loads' uncertainty independently.

To improve the feasibility of the CC-SMPC model with less nonlinearity, the battery power is represented by one variable $P_l^{BAT}(k)$: $P_l^{BAT}(k) > 0$ indicates charging the battery; $P_l^{BAT}(k) < 0$ indicates discharging the battery. Consequently, two binary variables for power direction and two non-negative power flow variables are avoided in the CC-SMPC model. Otherwise, the formulation can cause infeasible issues in practice because of the highly

nonlinearity. Based on the power balance equation in (5.13), for each battery, the mean value of battery power can be calculated using (6.5), with the SD value presented in (6.6).

$$\bar{P}_l^{BAT}(k) = \sum_c^{N^C} \eta_{cl}^{LVC} P_{cl}^{LVC}(k) + \sum_{l \neq l'} \left(\eta_{ll'}^{LV} P_{l'l}^{LV}(k) - P_{ll'}^{LV}(k) \right) - \sum_q^{N^{LVLcri}} \bar{P}_{lq}^{LVLcri}(k) - \sum_q^{N^{LVLncri}} S_{lq}^{LVLncri}(k) \bar{P}_{lq}^{LVLncri}(k) \tag{5.70}$$

$$\sigma^2_{P_l^{BAT}}(k) = \sum_q^{N^{LVLcri}} \sigma^2_{P_{lq}^{LVLcri}}(k) + \sum_q^{N^{LVLncri}} S_{lq}^{LVLncri}(k) \sigma^2_{P_{lq}^{LVLncri}}(k) \tag{5.71}$$

An approximate equation in (6.7) is applied in CC-SMPC model to calculate the SOC dynamic of each battery, where η_l^{BAT} indicates the charging/discharging efficiency. The mean value of SOC can also be calculated by (6.8), with the SD value calculated in (6.9). In this study, η_l^{BAT} is assumed to be 1; therefore, the estimation of SOC is simplified without considering charging/discharging separately to avoid the model infeasibility, regardless of the accuracy of the model. To resolve the aforementioned issues, more precise battery SOC estimation can be studied in future studies.

$$SOC_l(k+1) = SOC_l(k) + T_s \eta_l^{BAT} P_l^{BAT}(k) / B_l^{cap} \tag{5.72}$$

$$\overline{SOC_l}(k+1) = \overline{SOC_l}(k) + \frac{\bar{P}_l^{BAT}(k)}{B_l^{cap}} T_s \eta_l^{BAT} \tag{5.73}$$

$$\sigma^2_{SOC_l}(k+1) = \sigma^2_{SOC_l}(k) + (T_s \eta_l^{BAT})^2 \sigma^2_{P_l^{BAT}}(k) / B_l^{cap\,2} \tag{5.74}$$

Accordingly, for each battery, the constraints related to the SOC target range (5.15) as well as the boundary constraints of the battery power (5.18) are replaced with probabilistic constraints in (6.10)-(6.11). Satisfying the probabilistic constraints ensures that the probability of not violating the constraints will be higher than a pre-specified confidence level corresponding to constraints violation of ρ_l^{SOC} and ρ_l^{Pbat}.

$$Pr(LO \leq SOC_l(k+1) \leq HI) \geq 1 - \rho_l^{SOC} \tag{5.75}$$

$$Pr\left(-P_l^{batmax} \leq P_l^{BAT}(k) \leq P_l^{batmax}\right) \geq 1 - \rho_l^{Pbat} \tag{5.76}$$

With the assumption of the Gaussian PDF for the uncertain parameters, the probabilistic constraints can be replaced by two deterministic inequality constraints using the mean and SD values as shown in (6.12) and (6.13).

$$\begin{aligned} -P_l^{batmax} + \sqrt{2}\sigma_{P_l^{BAT}}(k) \mathrm{erf}^{-1}\left(1 - 2\rho_l^{Pbat}\right) &\leq \bar{P}_l^{BAT}(k) \\ \bar{P}_l^{BAT}(k) &\leq P_l^{batmax} - \sqrt{2}\sigma_{P_l^{BAT}}(k) \mathrm{erf}^{-1}(1 - 2\rho_l^{Pbat}) \end{aligned} \tag{5.77}$$

$$\begin{aligned} LO + \sqrt{2}\sigma_{SOC_l}(k+1)\, \mathrm{erf}^{-1}(1 - 2\rho_l^{SOC}) &\leq \overline{SOC_l}(k+1) \\ \overline{SOC_l}(k+1) &\leq HI - \sqrt{2}\sigma_{SOC_l}(k+1)\, \mathrm{erf}^{-1}(1 - 2\rho_l^{SOC}) \end{aligned} \tag{5.78}$$

Where, erf^{-1} is the inverse error function. In this case, considering only the uncertainty in the LV loads, constraints (5.10)-(5.32) in the MPC model as well as constraints (5.68)-(5.78) form the set of constraints for the CC-SMPC model. The objective function is similar to the DMPC model (5.1)-(5.6) in Chapter 5 while the uncertain variables are replaced with their expected values.

6.3.2.2 Case 2: Uncertainty on both the HV-side and LV-side loads

In this case, in the system's normal operation mode, besides the uncertainty in LV loads mentioned in Case 1, the uncertainty of power demands of all HV loads are also considered (($\forall j \in \{1, \dots, N^{HVB}\}$, $\forall p \in \{1, \dots, N^{HVLcri}\}$, $\forall P \in \{1, \dots, N^{hVLncri}\}$). It is also assumed that the uncertain parameters follow a Gaussian PDF as shown in (6.14) and (6.15).

$$P_{jp}^{HVLcri}(k) = \mathcal{DN}(\bar{P}_{jp}^{HVLcri}(k), \sigma_{P_{jp}^{HVLcri}}(k)) \tag{5.79}$$

$$P_{jp}^{HVLncri}(k) = \mathcal{DN}(\bar{P}_{jp}^{HVLncri}(k), \sigma_{P_{jp}^{HVLncri}}(k)) \tag{5.80}$$

It should be mentioned that the uncertainty in each HV load affects only the associated HV bus and is compensated for by the generators, while the power transferred to the cells is deterministic. This assumption is reasonable as the power through the cells are maintained by some local controllers. When the system operates in a normal scenario, there is no interconnection between buses, and the APU is not used. Accordingly, the values of P_j^{AHVp}, P_j^{AHVn}, and $P_{jj'}^{HV}(k)$ are all equal to zero. Therefore, the mean value of the generator output power in (5.11) can be simplified to (6.16), with the SD value calculated in (6.17).

$$\bar{P}_j^G(k) = \sum_c^{N^C} P_{jc}^{HVC}(k) + \sum_p^{N^{HVLcri}} \bar{P}_{jp}^{HVLcri}(k) - \sum_p^{N^{HVLncri}} S_{jp}^{HVLncri}(k)\bar{P}_{jp}^{HVLncri}(k) \tag{5.81}$$

$$\sigma_{P_j^G}(k) = \sqrt{\sum_p^{N^{HVLcri}} \sigma_{P_{jp}^{HVLcri}}^2(k) + \sum_p^{N^{HVLncri}} S_{jp}^{HVLncri}(k)\sigma_{P_{jp}^{HVLncri}}^2(k)} \tag{5.82}$$

Since the generator output power is uncertain, the deterministic boundary constraints for its power limitation in (5.18) need to be replaced by the probabilistic constraint introduced in (6.18), where ρ_j^{Pg} indicates the probability for the boundary violation. The probabilistic constraint in (6.18) is linearized using (6.19) for each generator.

$$Pr(-P_j^{Gmax} \le P_j^G(k) \le P_j^{Gmax}) \ge 1 - \rho_j^{Pg} \tag{5.83}$$

$$-P_j^{Gmax} + \sqrt{2}\sigma_{P_j^G}(k)\mathrm{erf}^{-1}\left(1 - 2\rho_j^{Pg}\right) \le \bar{P}_j^G(k) \le P_j^{Gmax} - \sqrt{2}\sigma_{P_j^G}(k)\mathrm{erf}^{-1}(1 - 2\rho_j^{Pg}) \tag{5.84}$$

The complete CC-SMPC model for Case 2 contains the constraints (5.10)-(5.32) and (5.68) -(5.84) with the objectives (similar to (5.1)-(5.6) in Chapter 5), while the uncertain variables in (5.10)-(5.32) are replaced with their expected values.

6.3.2.3 Case 3: Uncertainty on loads at both the HV-side and LV-side, with component failures

In this case, the CC-SMPC model is developed taking into account the load uncertainty at both sides. Furthermore, multiple failures in generators, batteries, and transmission links from HV buses to LV buses are also considered (e.g. failures in cells). Including the failures in the system's components leads to a nonlinear and more complicated model.

To cope with the uncertainty in HV loads along with the potential generator failure, the CC-SMPC strategy is deployed. To do so, the mean value of the generator power and the interconnection power of the HV buses is calculated according to (6.20). Also, the SD of the generator output power is calculated using (6.21). According to the probabilistic constraints of the generator power in (5.83), the chance constraints in (5.84) are applicable for Case 3 with generator failure, where $\sigma^2_{P_j^G}(k)$ is calculated by (6.21).

$$\begin{aligned}&\bar{P}_j^G(k)+\left(\eta_j^{AHV}\bar{P}_j^{AHVp}(k)-\bar{P}_j^{AHVn}(k)\right)+\left(\sum_{j\neq j'}\left(\eta_{jj'}^{HV}\bar{P}_{j'j}^{HV}(k)-\bar{P}_{jj'}^{HV}(k)\right)\right)\\&=\sum_c^{N^C}P_{jc}^{HVC}(k)+\sum_p^{N^{HVLcri}}\bar{P}_{jp}^{HVLcri}(k)-\sum_p^{N^{HVLncri}}S_{jp}^{HVLncri}(k)\bar{P}_{jp}^{HVLncri}(k)\end{aligned} \tag{5.85}$$

$$\begin{aligned}&\sigma^2_{P_j^G}(k)=\gamma_j^G(k)\cdot\\&\left(\begin{array}{c}\left(\sum_p^{N^{HVLcri}}\sigma^2_{P_{jp}^{HVLcri}}(k)+\sum_p^{N^{HVLncri}}S_{jp}^{HVLncri}(k)\sigma^2_{P_{jp}^{HVLncri}}(k)\right)\\+\frac{S^{HV}(k)}{\eta^{HV^2}}\left(\sum_p^{N^{HVLcri}}\sigma^2_{P_{j'p}^{HVLcri}}(k)+\sum_p^{N^{HVLncri}}S_{j'p}^{HVLncri}(k)\sigma^2_{P_{j'p}^{HVLncri}}(k)\right)\\+\frac{1-S^{APU}(k)}{\left(\prod_j^{N^{HVB}}\eta_j^{AHV}\right)^2}\left(\sum_p^{N^{HVLcri}}\sigma^2_{P_{j'p}^{HVLcri}}(k)+\sum_p^{N^{HVLncri}}S_{j'p}^{HVLncri}(k)\sigma^2_{P_{j'p}^{HVLncri}}(k)\right)\end{array}\right)\end{aligned} \tag{5.86}$$

In generator failure cases, the APU can be activated to replace the failed generator. The mean value of the APU output power is calculated using (6.22), which is based on (5.10). According to (5.85), the APU only compensates for the HV load uncertainties when it is connected to one failed bus, hence the SD value is calculated by (6.23). Similarly, the power boundary chance constraints are modeled as (6.24).

$$\bar{P}^{APU}(k)=\sum_j^{N^{HVB}}\bar{P}_j^{AHVp}(k)-\sum_j^{N^{HVB}}\eta_j^{AHV}\bar{P}_j^{AHVn}(k) \tag{5.87}$$

$$\begin{aligned}&\sigma^2_{P^{APU}}(k)=S^{APU}\cdot\\&\left(\begin{array}{c}\frac{1-\gamma_j^G(k)}{\eta_j^{AHV^2}}\left(\sum_p^{N^{HVLcri}}\sigma^2_{P_{jp}^{HVLcri}}(k)+\sum_p^{N^{HVLncri}}S_{jp}^{HVLncri}(k)\sigma^2_{P_{jp}^{HVLncri}}(k)\right)\\+\frac{1-\gamma_{j'}^G(k)}{\eta_{j'}^{AHV^2}}\left(\sum_p^{N^{HVLcri}}\sigma^2_{P_{j'p}^{HVLcri}}(k)+\sum_p^{N^{HVLncri}}S_{j'p}^{HVLncri}(k)\sigma^2_{P_{j'p}^{HVLncri}}(k)\right)\end{array}\right)\end{aligned} \tag{5.88}$$

$$\begin{aligned}&-P_j^{Gmax}+\sqrt{2}\sigma_{P^{APU}}(k)\mathrm{erf}^{-1}\left(1-2\rho_j^{Pg}\right)\leq\bar{P}^{APU}(k)\\&\bar{P}^{APU}(k)\leq P_j^{Gmax}-\sqrt{2}\sigma_{P^{APU}}(k)\mathrm{erf}^{-1}(1-2\rho_j^{Pg})\end{aligned} \tag{5.89}$$

When one battery fails, the LV bus interconnection is required to keep the bus voltage supported, using an adjacent healthy battery. The mean value of the power from/to each available battery is similarly calculated using (5.70). The chance constraints in (5.77) are applied for fulfilling battery power boundary constraints, with the $\sigma_{P_l^{BAT}}(k)$ calculated in (6.25) including the uncertain load power propagation from the adjacent LV bus node. In addition, based on the relationship between SOC and P_l^{BAT} in (5.73) and (5.74) for calculating the mean value of SOC and its SD value, the SOC target range constraints with probability in (5.78) can also be updated by (6.25).

$$\sigma^2_{P_l^{BAT}}(k) = \gamma_j^{BAT} \cdot \left(\begin{array}{c} \left(\sum_q^{N^{LVLcri}} \sigma^2_{P_{lq}^{LVLcri}}(k) + \sum_q^{N^{LVLncri}} S_{lq}^{LVLncri}(k) \sigma^2_{P_{lq}^{LVLncri}}(k) \right) \\ + \frac{S_{l+1}^{LV}}{\eta_{l(l+1)}^{LV\ 2}} \left(\sum_q^{N^{LVLcri}} \sigma^2_{P_{(l+1)q}^{LVLcri}}(k) + \sum_q^{N^{LVLncri}} S_{(l+1)q}^{LVLncri}(k) \sigma^2_{P_{(l+1)q}^{LVLncri}}(k) \right) \\ + \frac{S_{l-1}^{LV}}{\eta_{l(l-1)}^{LV\ 2}} \left(\sum_q^{N^{LVLcri}} \sigma^2_{P_{(l-1)q}^{LVLcri}}(k) + \sum_q^{N^{LVLncri}} S_{(l-1)q}^{LVLncri}(k) \sigma^2_{P_{(l-1)q}^{LVLncri}}(k) \right) \end{array} \right) \tag{5.90}$$

The complete CC-SMPC model for case 3 contains the constraints (5.10)-(5.32) and (5.85) -(5.90) with the objectives (similar to (5.1)-(5.6) in Chapter 5), while the uncertain variables in (5.10)-(5.32) are replaced with their expected values.

6.4 Evaluation design

To compare the online DMPC and CC-SMPC performance, an evaluation framework for evaluating the system operation costs and constraint violation costs is proposed. This evaluates the system performance for N^{Scen} load scenarios over the whole flight duration T. The operation costs are calculated based on the controller objectives, which contain power losses, stored energy, load shedding, and switching activities. The details are now presented here. The overall operation cost includes all of the aforementioned operation costs.

The power loss for each single time step of each testing scenario equals the difference between the total supplied power in (6.27) and the total load power (6.28). The power loss for all test scenarios is evaluated by (6.26), calculating the average power loss weighted by the weighting factor $v_{P^{loss}}$.

$$G_{P^{loss}} = v_{P^{loss}} \left(\frac{1}{N^{Scen} T} \sum_{n=1}^{N^{Scen}} \sum_{k=0}^{T} \left(P_n^{source}(k) - P_n^{load}(k) \right) \right) \tag{5.91}$$

$$P_n^{source}(k) = \sum_j^{N^{HVB}} P_j^G(k) + P^{APU}(k) - \eta_l^{BAT} \sum_l^{N^{LVB}} P_l^{BAT}(k) \tag{5.92}$$

$$P_n^{load}(k) = \sum_p^{N^{HVLcri}} P_{jp}^{HVLcri}(k) + \sum_p^{N^{HVLncri}} S_{jp}^{HVLncri}(k) P_{jp}^{HVLncri}(k) + \sum_q^{N^{LVLcri}} P_{lq}^{LVLcri}(k) + \sum_q^{N^{LVLncri}} S_{lq}^{LVLncri}(k) P_{lq}^{LVLncri}(k)) \quad (5.93)$$

The ESS performance is evaluated by SOC level in (6.29) for all load scenarios, which indicates better performance for SOC average value which are closer to the upper bound within the target range.

$$G_{SOC} = v_{SOC}(\frac{1}{N^{Scen_T}} \sum_{n=1}^{N^{Scen}} \sum_{k=0}^{T} \sum_{l}^{N^{BAT}} |HI - SOC_{n,l}(k)|) \quad (5.94)$$

The performances for load shedding and switching activities are evaluated by similar methods, which are used in calculating the objective functions (5.4)-(5.6), considering the entire flight duration. Based on this, the load shedding and switching activity evaluations for all test scenarios are conducted by calculating the average load shedding for each scenario using (6.30) and the average switching activities using (6.31), with v_{SL}, $v_{\delta APU}$, $v_{\delta tran}$, and $v_{\delta L}$ showing the weighting factor for load shedding (J_{SL}), starting/stopping the APU ($J_{\delta APU}$), configuration changes in the transmission system ($J_{\delta tran}$), and loads on/off statuses ($J_{\delta L}$), respectively.

$$G_{SL} = v_{SL} \frac{1}{N^{Scen_T}} \sum_{n=1}^{N^{Scen}} J_{SL} \quad (5.95)$$

$$G_{\delta} = \frac{1}{N^{Scen_T}} (v_{\delta APU} \sum_{n=1}^{N^{Scen}} J_{\delta APU} + v_{\delta tran} \sum_{n=1}^{N^{Scen}} J_{\delta tran} + v_{\delta L} \sum_{n=1}^{N^{Scen}} J_{\delta L}) \quad (5.96)$$

As demonstrated in Section 6.3.2, the uncertainty leads to the potential violations of three constraints, including the violation of SOC target range, the violation of maximum power bound for battery power, and the violation of the maximum power bound for generator/APU output power. For better evaluating the violation cost, instead of using only one average value or maximum value, a new index combining four dimensions is proposed. The violation cost is calculated based on the maximum percentage of constraint violation in all scenarios over all time steps ($G'_{*\mathrm{mp}}$), the average percentage of constraint violation over all time steps with violation occurrence ($G'_{*\mathrm{ap}}$), the maximum constraint violation value ($G'_{*\mathrm{mq}}$), and the average constraint violation value among all time steps with violation occurrence and scenarios ($G'_{*\mathrm{aq}}$). For example, (6.32)-(6.35) are adopted for the SOC violation cost based on the aforementioned evaluation scheme, and the overall SOC violation cost G'_{SOC} is calculated by their combination, with weights, presented in (6.36). In this work, it is assumed that each type of violation is weighted equally, which indicates $v_{SOC\mathrm{mp}} = v_{SOC\mathrm{ap}} = v_{SOC\mathrm{mq}} = v_{SOC\mathrm{ap}} = 0.25$. Similarly, the violation cost for battery power G'_{Pbat} (including $G'_{Pbat_{mp}}$, $G'_{Pbat_{ap}}$, $G'_{Pbat_{mq}}$, $G'_{Pbat_{aq}}$) and generator/APU output power G'_{Pgen} (including $G'_{Pgen_{mp}}$, $G'_{Pgen_{ap}}$, $G'_{Pgen_{mq}}$, $G'_{Pgen_{aq}}$) can be

calculated by the same method (for the sake of brevity, detailed functions are omitted). The overall violation cost is the sum of G'_{SOC}, G'_{Pbat}, and G'_{Pgen}.

$$G'_{SOC\mathrm{mp}} = \frac{\max\{n: n \in S: \left(SOC_{n,l}(k) > HI \vee SOC_{n,l}(k) < LO\right), k \in \{1,2,\dots,T\}\}}{N^{Scen}} \tag{5.97}$$

$$G'_{SOC\mathrm{ap}} = \frac{\sum\{n \in S: (SOC_{n,l}(k) > HI \vee SOC_{n,l}(k) < LO)\}}{N^{Scen} \sum\{k \in S: (SOC_{n,l}(k) > HI \vee SOC_{n,l}(k) < LO)\}} \tag{5.98}$$

$$G'_{SOC\mathrm{mq}} = \max\{SOC_{n,l}(k): SOC_{n,l}(k) \in S: \left(SOC_{n,l}(k) > HI \vee SOC_{n,l}(k) < LO\right), k \in \{1,2,\dots,T\}\} \tag{5.99}$$

$$G'_{SOC\mathrm{aq}} = \frac{\sum_{\{SOC_{n,l}(k) \in S: (SOC_{n,l}(k) > HI \vee SOC_{n,l}(k) < LO)\}} \left(\left|SOC_{n,l}(k) - HI\right| + \left|SOC_{n,l}(k) - LO\right|\right)}{\sum\{n \in S: (SOC_{n,l}(k) > HI \vee SOC_{n,l}(k) < LO)\}} \tag{5.100}$$

$$\begin{cases} G'_{SOC} = v_{SOC\mathrm{mp}} G'_{SOC\mathrm{mp}} + v_{SOC\mathrm{ap}} G'_{SOC\mathrm{ap}} + v_{SOC\mathrm{mq}} G'_{SOC\mathrm{mq}} + v_{SOC\mathrm{ap}} G'_{SOC\mathrm{aq}} \\ v_{SOC\mathrm{mp}} + v_{SOC\mathrm{ap}} + v_{SOC\mathrm{mq}} + v_{SOC\mathrm{ap}} = 1 \end{cases} \tag{5.101}$$

Similar to Chapter 5, the total cost of the control includes both the overall operation cost and the overall violation cost.

6.5 Case studies

In this section, simulation results of system operation are evaluated and compared for all three cases discussed above, when adopting the proposed CC-SMPC and the DMPC strategies. For each case, both offline (single independent evaluations) and online (evaluation within a receding horizon approach) comparison results are presented and analyzed.

For the offline test, the CC-SMPC and DMPC strategies are applied to the system for a flight duration of T = 150 minutes, considering the forecasted loads of the system at both the HV and LV sides. Afterwards, the performance of both control strategies is evaluated under the realization of a large number of random load scenarios. The offline results provide quick verification for the CC-SMPC for power limitation violation analysis as the offline tests are quicker to execute and hundreds of load scenarios can be considered. However, offline testing is not applicable for the assessment of SOC violation and costs of system operation, because the SOC is a time accumulating variable. Offline testing leads to accumulating SOC deviations due to the lack of ability to take corrective actions when the deviations are still small. In contrast, online testing is applicable for the evaluation of all violation analyses and the real cost of system operation. However, the computational time is considerably increased to test hundreds of load scenarios. Hence, for the offline tests, 100 uncertain load profiles are tested with the maximum acceptable probability of constraint violations varying from 0.01 to 0.2, to verify the feasibility

of the model. In the second step, the online DMPC and CC-SMPC techniques are applied for 50 uncertain load profiles with a selected probability, which compares the costs of system operation and the penalty costs of constraint violations.

Table 6.1 Mean value load profile (kW) based on flight stages with indices in Figure 5.1

Load types [kW]	**Load indices**	**Ground (20min)**	**Take off (5min)**	**Climb (25min)**	**Cruise (60min)**	**Descent (10min)**	**Loiter (15min)**	**Landing (15min)**
HV Critical Loads	$HVL1^1$, $HVL2^1$	10.01	29.58	22.20	21.40	22.20	27.21	30.00
LV Critical Loads	$LVL1^1$, $LVL4^1$	1.78	1.94	2.07	3.00	2.07	2.07	1.94
	$LVL2^1$, $LVL3^1$	3.00	2.50	2.50	2.50	2.50	2.50	3.00
HV HP Loads	$HVL1^2$, $HVL2^2$	4.89	8.34	24.00	24.00	24.00	24.00	0.87
LV HP Loads	$LVL1^2$, $LVL4^2$	1.40	1.30	1.30	1.30	1.60	0.80	0.80
	$LVL2^2$, $LVL3^2$	0.50	0.50	0.50	0.50	1.50	1.00	2.20
HV MP Loads	$HVL1^3$, $HVL2^3$	15.00	3.42	14.16	14.60	14.16	14.16	3.42
LV MP Loads	$LVL1^3$, $LVL4^3$	0.50	0.35	0.35	2.00	0.35	0.35	0.35
	$LVL2^3$, $LVL3^3$	0.70	0.70	1.50	2.50	0.50	0.50	0.50
HV LP Loads	$HVL1^4$, $HVL2^4$	6.00	6.00	6.00	18.00	6.00	6.00	6.00
LV LP Loads	$LVL1^4$, $LVL4^4$	1.00	0.70	1.50	2.20	0.50	0.50	1.50
	$LVL2^4$, $LVL3^4$	2.00	1.50	2.00	3.00	2.00	2.00	2.00

The predicted load profile (mean value of load power values) is presented in Table 6.1 with indices in Figure 5.1. The SD value for each load power ($\sigma_{P_{lq}^{LVLcri}}$, $\sigma_{P_{lq}^{LVLncri}}$, $\sigma_{P_{jp}^{HVLcri}}$, $\sigma_{P_{jp}^{HVLncri}}$) is 0.05. The maximum load power is 95 kW when the aircraft enters the cruising stage, while the rated generator power is 97 kW, which is designed to cover all the MEA loads. The rated power for each DC/DC converter is 3 kW, and the battery capacity of all batteries is 4 kWh. The weighting factors for objectives and operation costs are maintained to be the same as

Chapter 5, except for the weight of J_{PG} and J_{Pbat}, which are selected as a constant values (2 and 1 respectively) to balance power losses and battery charging.

6.5.1 Simulation results for Case 1

1) Offline scenario tests

Table 6.2 presents the offline violation comparison of the battery power limitation constraints with both CC-SMPC and DMPC methods for Case 1. For the CC-SMPC approach, the test is conducted with different violation probabilities of 1%, 5%, 10%, and 20%, and for each violation probability, 100 uncertain load scenarios are applied. For the DMPC, the same uncertain load scenarios are used. As can be seen in Table 6.2, following the decrease of the violation probability, $G'_{Pbat_{\mathrm{mp}}}$ and $G'_{Pbat_{ap}}$ also decrease, which verifies the effectiveness of the proposed probabilistic approach because the maximum and average percentage of violated constraints are consistent with violation probability. In addition, $G'_{Pbat_{\mathrm{mq}}}$ and $G'_{Pbat_{\mathrm{aq}}}$ indicate the maximum and average violated values among all time steps in scenarios with violation occurrence respectively. Both of these values increase when the violation probability increases, and $G'_{Pbat_{\mathrm{mq}}}$ is approximately 5 times higher than $G'_{Pbat_{\mathrm{aq}}}$. Comparing the test with $\rho = 0.01$ to the one with $\rho = 0.2$, both $G'_{Pbat_{\mathrm{mq}}}$ and $G'_{Pbat_{\mathrm{aq}}}$ for $\rho = 0.01$ are reduced by more than 50%. Comparing the DMPC to the CC-SMPC, all of the evaluation indices have higher values for the DMPC method. Especially so when comparing the DMPC with CC-SMPC when $\rho = 0.01$, the violation indices increase by 17.8, 22.54, 3.34, and 2.29 times for the four indices, respectively. Based on these results, the offline test verifies that the CC-SMPC method achieves better battery power violation performance with respect to DMPC.

Table 6.2 Constraint violation comparisons of CC-SMPC and DMPC for Case 1 offline tests

Case	ρ	Battery power constraint violation			
		$G'_{Pbat_{\mathrm{mp}}}$ [%]	$G'_{Pbat_{ap}}$ [%]	$G'_{Pbat_{mq}}$ [kW]	$G'_{Pbat_{aq}}$ [kW]
CC-SMPC	0.01	3	1.89	0.2318	0.0540
	0.05	8	5.43	0.3908	0.0815
	0.1	14	10.7	0.4755	0.0816
	0.2	24	17.41	0.5198	0.0935
DMPC	N.A	53.5	42.61	0.7743	0.1235

2) Online scenario tests

In Figure 6.2, the operational costs and constraint violation costs for the DMPC and CC-SMPC methods are compared, based on the online testing method for 50 scenarios containing LV load uncertainty with $\rho = 0.01$. In Figure 6.2 (a), the overall operation cost, overall violation cost, and the total cost are compared for DMPC and CC-SMPC methods. Figure 6.2 (b) and Figure 6.2 (c) present the breakdown of the overall operation cost and overall violation cost in Figure 6.2 (a) respectively.

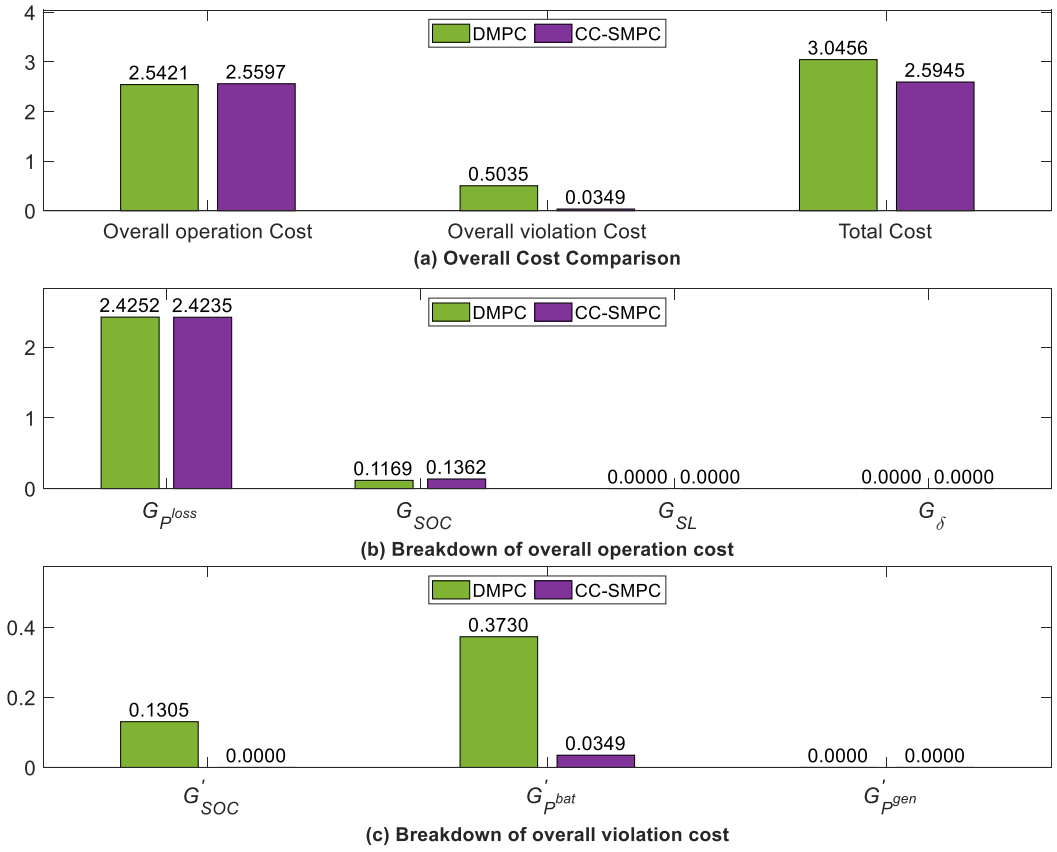
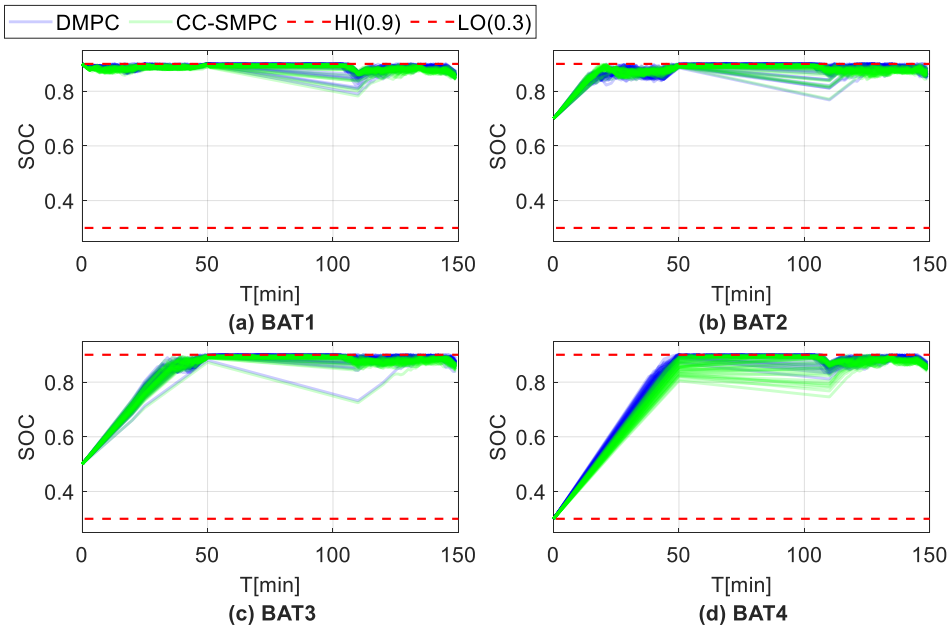


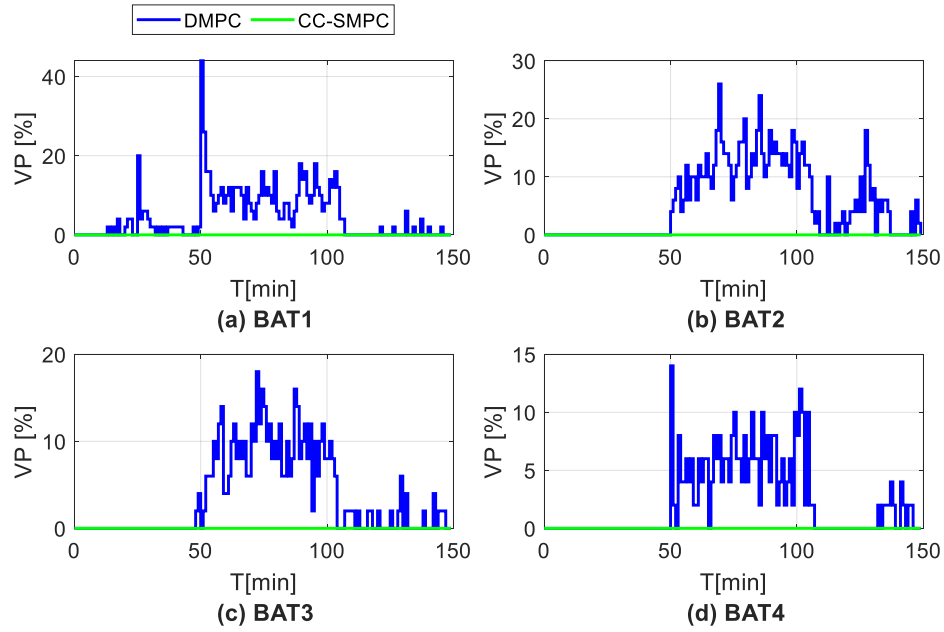
Figure 6.2 Cost comparison of online DMPC and CC-SMPC for Case 1

According to the evaluation framework, the overall operation costs for both methods is almost equal. In addition, both methods don't have costs for load shedding and switching activities, which indicates that the uncertainty in the power consumption of LV loads can be handled by adjusting the input power from the HV side with the CC-SMPC method. On the other hand, the CC-SMPC method is more conservative in charging/discharging the battery, therefore, the cost of SOC is 16.5% higher than the value when adopting the DMPC method, indicating that more of the energy in batteries is consumed by adopting the CC-SMPC method. Although the overall operation costs for both methods are approximately equal, the system controlled by the CC-SMPC method has a lower overall constraint violation cost, 93% less than the cost related to the DMPC method. As mentioned, the LV load uncertainty is compensated for by the battery and would not be propagated to the HV side. Therefore, the violation of

generator power is zero for both DMPC and CC-SMPC. However, the violation cost of the SOC target range and the battery power limits are reduced by 100% and 91%, respectively, in the CC-SMPC method compared to the DMPC method. Therefore, the total cost for the CC-SMPC method is reduced by 15% compared to the DMPC method for Case 1.

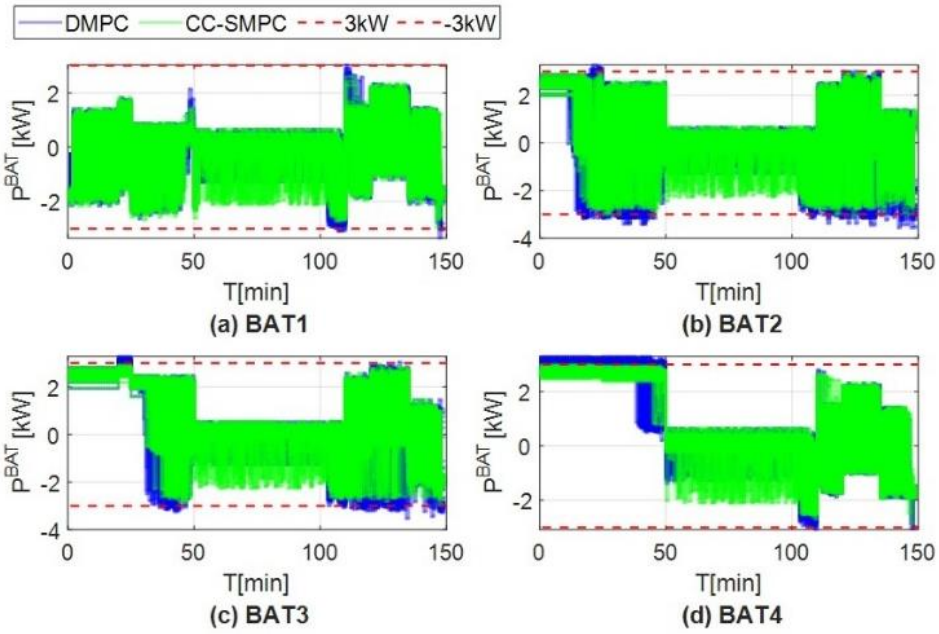


(1) SOC changes

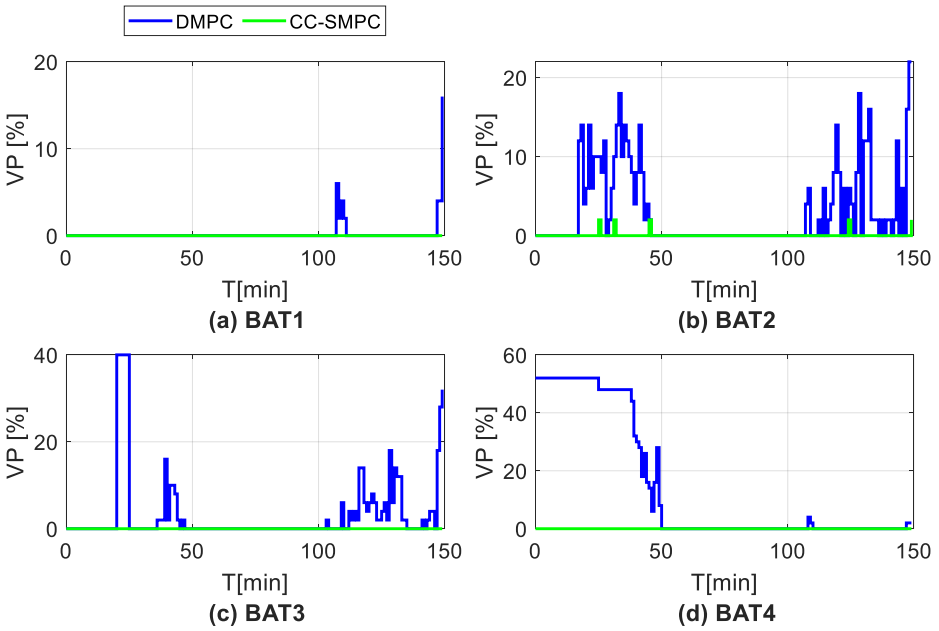


(2) Violation percentage among all uncertain scenarios

Figure 6.3 SOC results when adopting online DMPC and CC-SMPC for Case 1



(1) Battery power changes



(2) violation percentage among all uncertain scenarios

Figure 6.4 Battery power results when adopting online DMPC and CC-SMPC for Case 1

Figure 6.3 (1) and Figure 6.4 (1) present the SOC and battery power changes for Case 1 when adopting the DMPC and CC-SMPC methods for 50 uncertain LV load scenarios, and the corresponding violation percentages (VP in the figure) among all scenarios are presented in Figure 6.3 (2) and Figure 6.4 (2). The initial SOC for batteries 1-4 is set to 0.9, 0.7, 0.5, and 0.3 respectively as presented in subfigures (a) to (d) in Figure 6.3 (1). Since battery 1 starts

from an initial SOC equal to the SOC upper bound, it has more initial sensitivity to the uncertainty. Applying the DMPC strategy causes SOC to exceed the upper bound before the flight enters the cruising stage (50min), while the scenarios containing SOC violations for other batteries emerge after entering the cruising stage. In addition, up to 44% of the scenarios have violations when adopting the DMPC method for all flight stages, while there is no SOC violation for CC-SMPC. In contrast to SOC violation, the battery violations for four batteries happen before/after the cruising stage, where the CC-SMPC charges/discharges the batteries with less power compared to DMPC. For example, 50% of the scenarios result in overcharging of battery 4 before entering the cruising stage when adopting DMPC, which is completely avoided when adopting CC-SMPC.

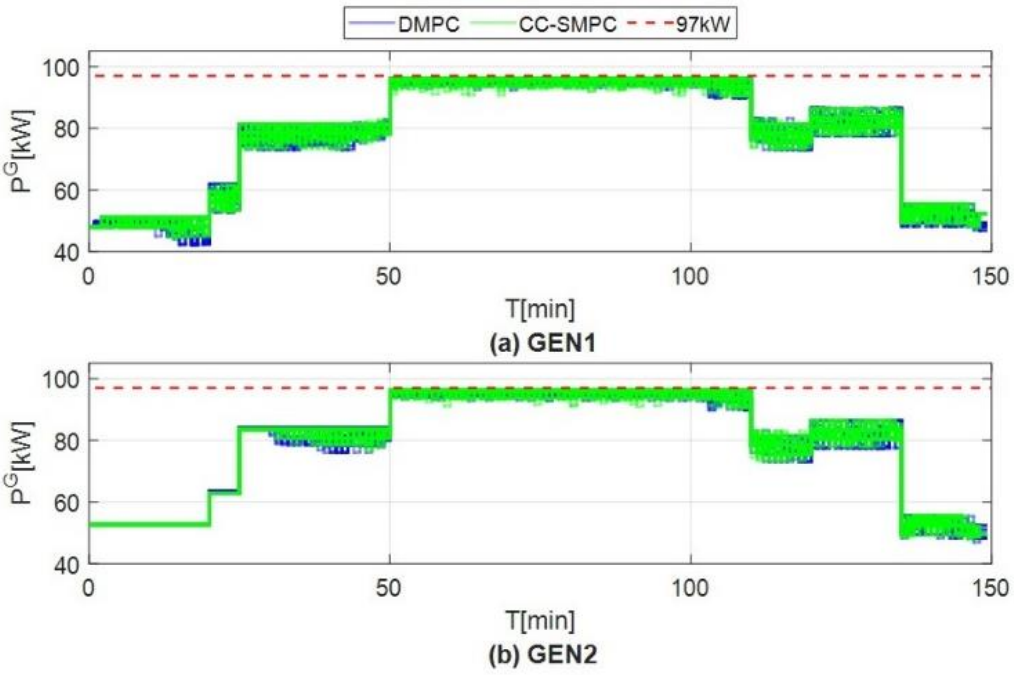


Figure 6.5 Generator power when adopting online DMPC and CC-SMPC for Case 1

6.5.2 Simulation results for Case 2

1) Offline scenario tests

Table 6.3 presents the offline simulation results for constraint violation comparisons of battery and generator power with both CC-SMPC and DMPC methods for Case 2. According to the table, when ρ increases, the constraint violation indices for the battery and generator power increase by approximately the same percentage, which verifies the effectiveness of the proposed probabilistic approach for Case 2. Comparing the results in Case 1, when $\rho = 0.01$, $G'_{P^{bat}\mathrm{mp}}$ and $G'_{P^{bat}\mathrm{mq}}$ for Case 2 remain the same values, while the other two battery violation indices show that the average constraint violation values increase by 2.6% and 43.7% respectively. The violation of generator power is maintained at 0. When ρ increases, compared

to Case 1, the average indices for battery power constraint violation $G'_{P^{bat}_{\mathrm{ap}}}$ and $G'_{P^{bat}_{\mathrm{aq}}}$ are reduced by 1.2% - 16.4%, while the violation indices for the generator power constraint increase. When the uncertainty on the HV side is taken into account, the power transferred from generators to the LV side is reduced to cope with the load uncertainty on the HV side, which results in less power for charging the battery and consequently reduces overcharging accounted for in battery power violation. In general, when summing up all violation indices for batteries and generators, Case 2 has higher total violation compared to Case 1 as the uncertainty is added to both sides. In addition, compared to offline DMPC, all offline CC-SMPC with the selected ρ reduce the power constraint violations for batteries and generators.

Table 6.3 Constraint violation comparisons of CC-SMPC and DMPC for Case 2 offline tests

Case	ρ	Battery power constraint violation				Generator power constraint violation			
		$G'_{P^{bat}_{\mathrm{mp}}}$ [%]	$G'_{P^{bat}_{ap}}$ [%]	$G'_{P^{bat}_{mq}}$ [kW]	$G'_{P^{bat}_{aq}}$ [kW]	$G'_{P^{gen}_{\mathrm{mp}}}$ [%]	$G'_{P^{gen}_{\mathrm{ap}}}$ [%]	$G'_{P^{gen}_{mq}}$ [kW]	$G'_{P^{gen}_{aq}}$ [kW]
CC-SMPC	0.01	3	1.94	0.2318	0.0776	0	0	0	0
	0.05	8	4.69	0.2940	0.0739	5	4.41	1.3088	0.7068
	0.1	14	8.95	0.4262	0.0745	12	11.6	2.0288	0.7457
	0.2	24	17.23	0.4821	0.0921	22	20.21	2.9007	1.0991
DMPC	N.A	56	42.61	0.7743	0.1235	35	27.34	3.6729	1.2533

2) Online scenario tests

Comparing Case 2 to Case 1, the HV load uncertainty is now also considered. Since generators are the only power supplies to the HV loads, to avoid generator overload situations due to the uncertain behavior of loads (unexpected peak power demands) at the HV side, the CC-SMPC-based controller allocates less power to be transferred from the HV side to the LV side. This means that more energy from batteries will be used for supplying LV loads during peak intervals. In the worst scenarios, such as low SOC conditions and high load power demand, load shedding can also be triggered. These actions lead to a higher operation cost due to low SOC levels and the additional cost imposed by load shedding and switching activities. The performance of the DMPC and CC-SMPC methods is evaluated using 50 uncertain load scenarios.

Figure 6.6 demonstrates the operation cost and the violation cost for both control strategies. In Figure 6.6 (a), the overall operation cost, overall violation cost, and the total cost are compared for DMPC and CC-SMPC methods. Figure 6.6 (b) and Figure 6.6 (c) present the breakdown of the overall operation cost and overall violation cost in Figure 6.2 (a) respectively.

In general, the CC-SMPC method leads to a higher operation cost, 12% more than the cost of the DMPC method. According to the breakdown of the operation cost represented in Figure 6.6 (b), the CC-SMPC strategy has an almost 3 times higher SOC cost compared to the DMPC method and a small amount of cost due to the load shedding and switching activities. However, compared to the DMPC method, the CC-SMPC reduces the total violation cost by 93%, which consists of a 92% reduction of SOC violation, 72% reduction of battery power violation, and 100% reduction of generator power violation cost. This indicates that the DMPC method requires corrective control actions to cope with the constraint violation situations, which will lead to additional operating costs. However, this is less likely to be an optimal solution compared to the CC-SMPC method, which explicitly accounts for the violation probability of uncertain parameters when providing the solutions. According to the results, CC-SMPC reduces the total cost by 31.4% compared to the DMPC method. Figure 6.7 to Figure 6.9 present the simulation results of both control techniques in all scenarios during the different flight stages.

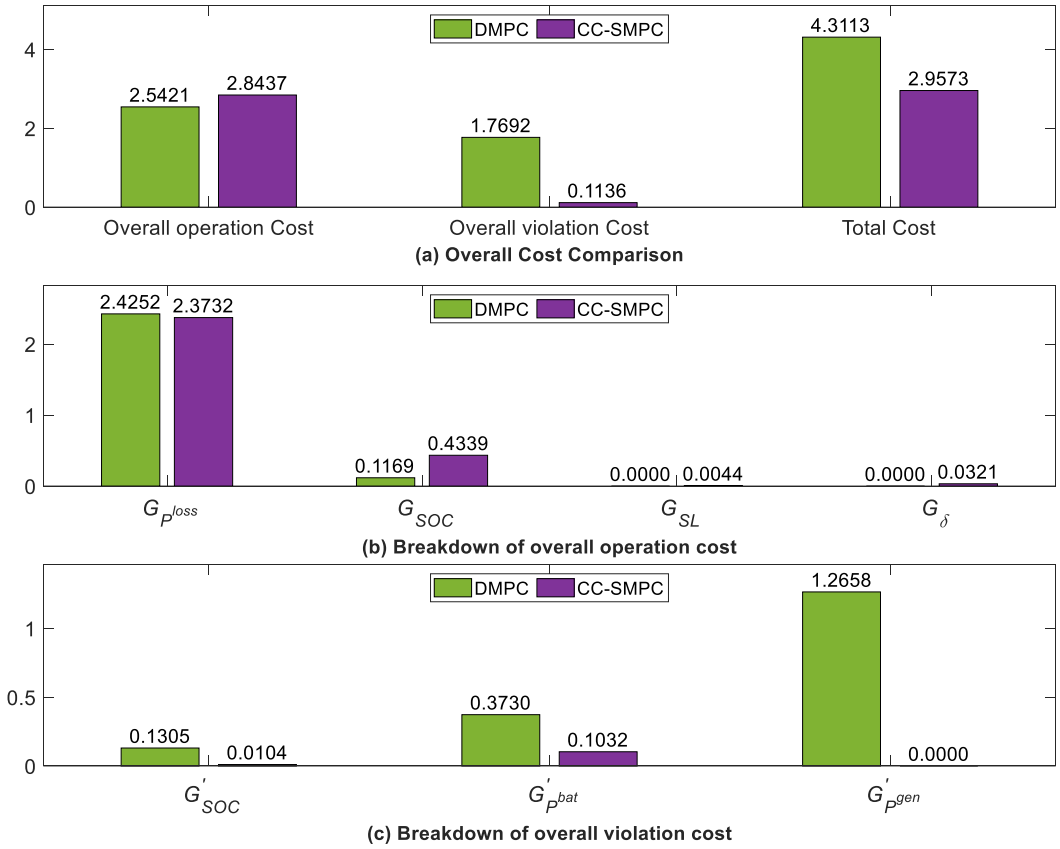
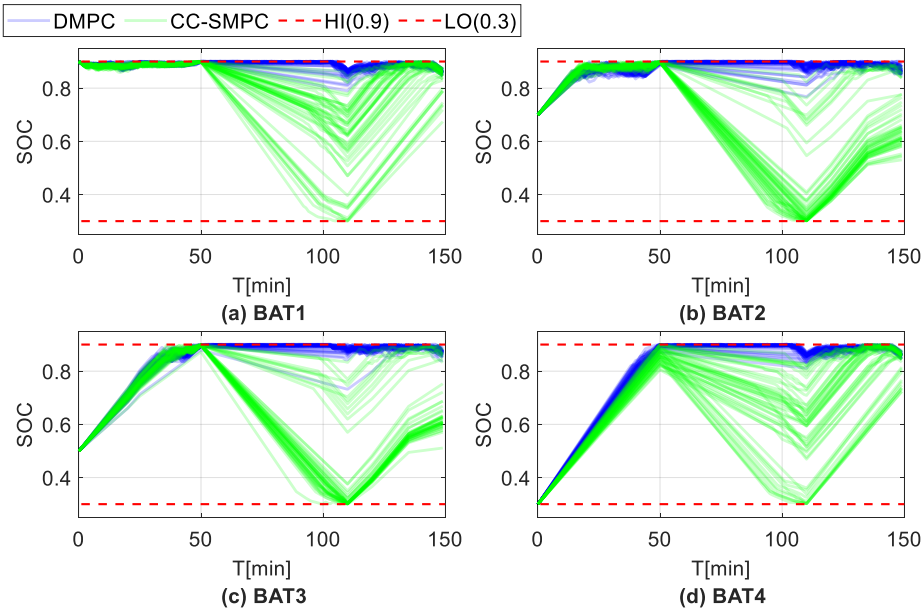


Figure 6.6 Cost comparison of online DMPC and CC-SMPC for Case 2

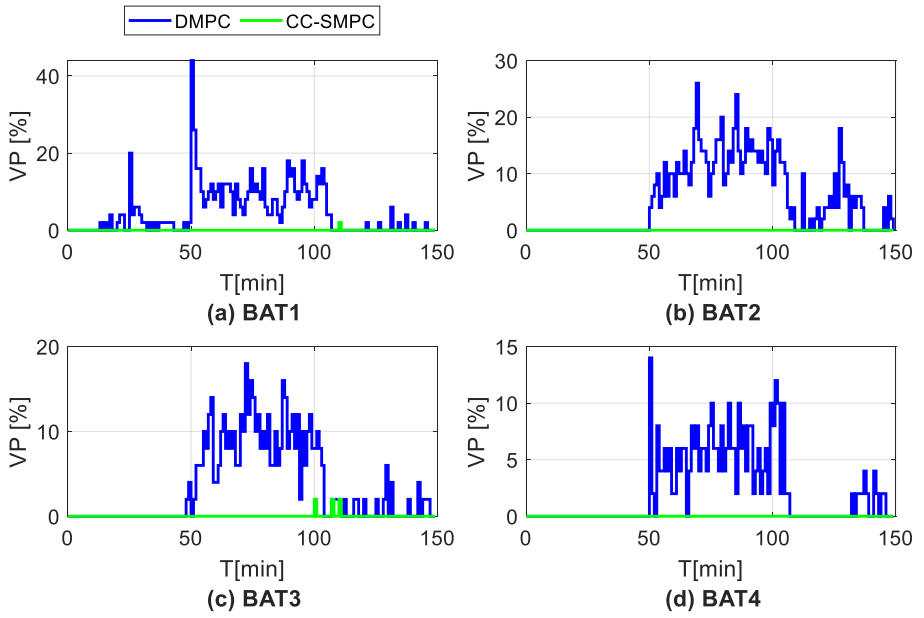
Figure 6.7 presents the SOC changes with the violation percentage for both DMPC and CC-SMPC strategies when each controller is applied for 50 uncertain scenarios, while Figure 6.8 shows the corresponding battery power. The SOC value for batteries 1 to 4 start from high

to low levels, 0.9, 0.7, 0.5, and 0.3, respectively. As can be seen in both figures, before t = 50 min, when the system loads are not in their peak interval, batteries 2-4 can be charged using generator power, while battery 1 is not charged as its initial value has been set to the maximum SOC. However, compared to the CC-SMPC method, during the charging period, the DMPC method is more likely to charge the battery with higher power values exceeding the charging power limitation (3 kW in this study). For example, battery 4 is charged with a maximum power of around 3.3kW by the DMPC method in 52% of scenarios before t = 45 min. Likewise, for batteries 2 and 3, during t = 20 to t = 25 min, the charging power reaches 3.3kW in 14% and 40% of scenarios, respectively. In addition, when the SOC becomes close to the upper bound, the battery is discharged in some time steps to keep SOC value within the target range. Compared to CC-SMPC, the DMPC method tends to discharge the battery with discharging power exceeding its maximum possible power limit, which indicates the need for a fast-acting local controller in real situations to avoid the constraint violation. For example, batteries 2 and 3 have around 20% over-discharge scenarios with a maximum power of 3.6 kW after t = 100 min. Compared to the battery power violation, although DMPC causes SOC violation in 10%-40% of scenarios from t = 50 min to t = 100 min, the exceeding level is low (approximately 0.902) with respect to the upper bound (HI = 0.9) which is due to the MPC online feedback strategy. Both DMPC and CC-SMPC online methods will correct the SOC violation once it has occurred, however, predicting and avoiding the violation before it occurs would be far preferable.

Figure 6.9 presents the output power of both generators and the violation percentage in the aforementioned 50 scenarios when adopting the DMPC and CC-SMPC methods. The figure shows that the power of the generators reaches its peak value from t = 50 to t = 110min. Compared to the DMPC method, the CC-SMPC strategy controls generator operation without exceeding their maximum power limitations, discharging the batteries when necessary during this period. Although the DMPC strategy relies less on the batteries' power to avoid costs imposed by low SOC levels, it violates the generators' power limitation in 30% of scenarios, with a maximum power of around 100.3kW for each generator. This indicates two potential drawbacks of the application of the DMPC method. One solution is to add another layer of control, such as a rule-based control layer, to work out how to compensate for satisfying the operation costs. This is likely to result in sub-optimal solutions. Another solution would be to design larger generators, with more power redundancy, leading to an increase in the generators' weight, which is not desirable in aircraft applications. Therefore, the CC-SMPC method can be considered to show its superiority compared to the DMPC method for Case 1 by avoiding both drawbacks.

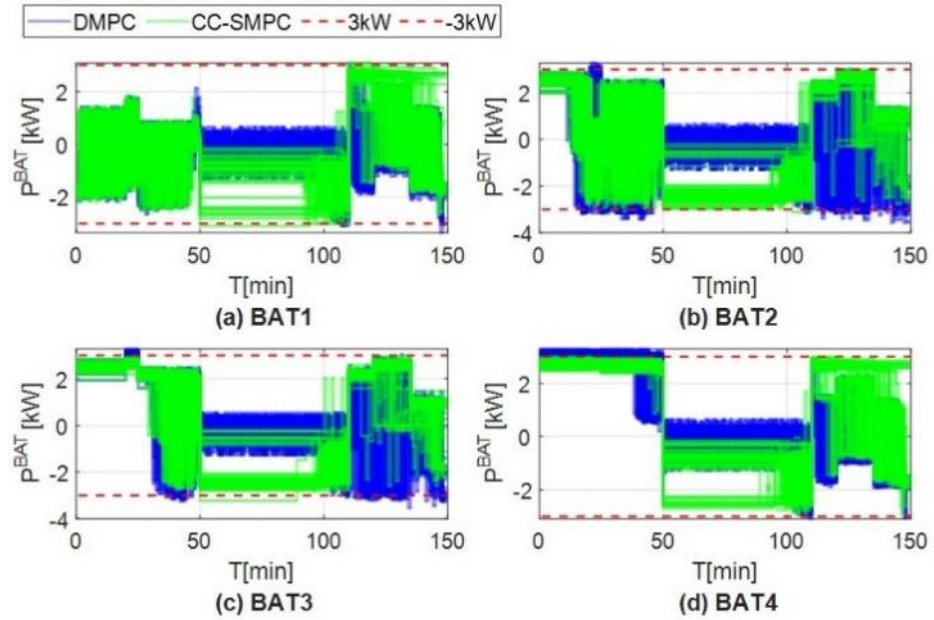


(1) SOC changes

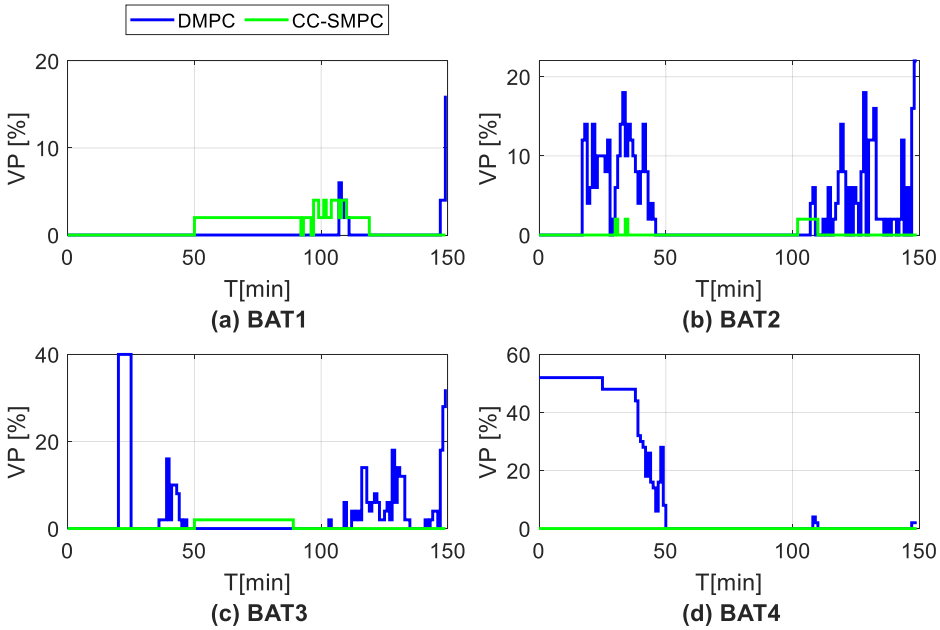


(2) Violation percentage among all uncertain scenarios

Figure 6.7 SOC results when adopting online DMPC and CC-SMPC for Case 2

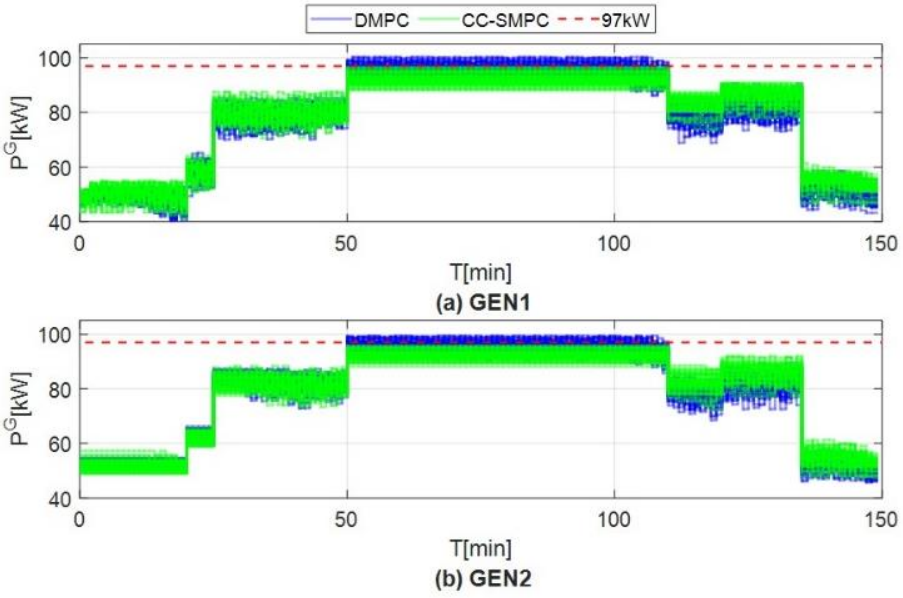


(1) Battery power changes

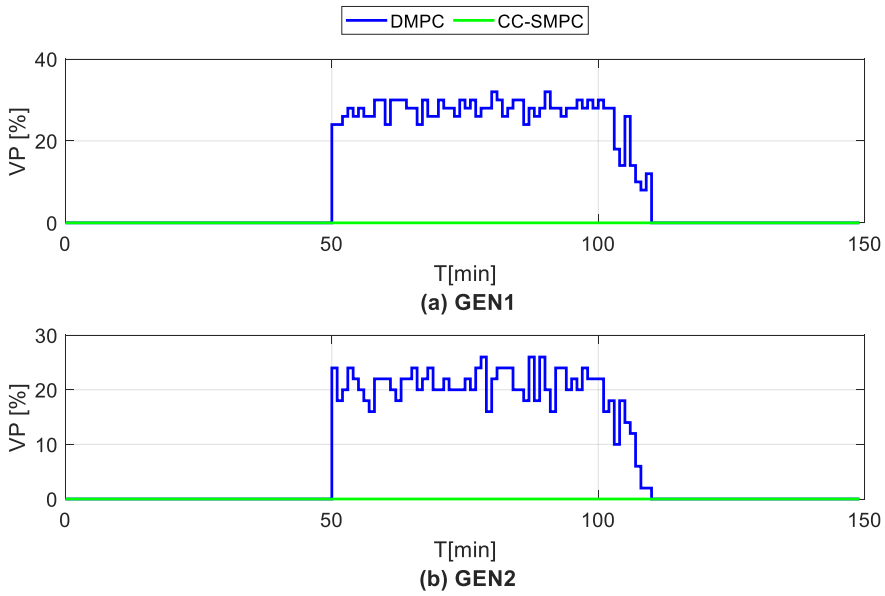


(2) Violation percentage among all uncertain scenarios

Figure 6.8 Battery power results when adopting online DMPC and CC-SMPC for Case 2



(1) Generator power changes



(2) Violation percentage among all uncertain scenarios

Figure 6.9 Generator power results when adopting online DMPC and CC-SMPC for Case 2

6.5.3 Simulation results for Case 3

In Case 3, in addition to considering the load uncertainty at both HV and LV sides, the following failure scenarios are also assumed during different flight stages: failure events for Generator 1, Cell 10, Cell 3, and Battery 2. In this case, in contrast to the previous cases which studied only normal system operation, the DMPC and CC-SMPC strategies are required to provide feasible solutions to cope with the components' failures. The failures listed in Table 6.4

are included in both offline and online testing and are assumed to occur at the specified time instances.

Table 6.4 Failure events during the flight

Time of fault occurrence	19min	49min	79min	109min
Failed Component	Generator 1	Cell 10	Cell 3	Battery 2

1) Offline scenario tests

Table 6.5 presents the offline simulation results for constraint violation comparison of battery and generator power with both CC-SMPC and DMPC methods for Case 3. In the failure scenarios, the APU is started in all tests with both the CC-SMPC and DMPC methods to avoid the load shedding caused by generator failure (which is further presented in the online results). The CC-SMPC and DMPC methods provide different configurations and load shedding results when cell and battery failures occur. The load shedding leads to less load demand in the system, which leads to reducing the sum of average constraint violations $G'_{P^{bat}{}_{\mathrm{ap}}}$ and $G'_{P^{gen}{}_{\mathrm{ap}}}$ with each ρ value, compared to Case 2 for both CC-SMPC and DMPC methods. According to Table 6.5, the values are consistent with the change of probability, which presents fewer violations when the probability decreases. Similar to the other cases, the DMPC method leads to higher violations compared to the CC-SMPC technique with different ρ values.

Table 6.5 Constraint violation comparisons of CC-SMPC and DMPC for Case 3 offline tests

Case	ρ	Battery power constraint violation				Generator/APU power constraint violation			
		$G'_{P^{bat}{}_{\mathrm{mp}}}$ Max %	$G'_{P^{bat}{}_{\mathrm{ap}}}$ Mean %	$G'_{P^{bat}{}_{mq}}$ [kW]	$G'_{P^{bat}{}_{aq}}$ [kW]	$G'_{P^{gen}{}_{\mathrm{mp}}}$ Max %	$G'_{P^{gen}{}_{\mathrm{ap}}}$ Mean %	$G'_{P^{gen}{}_{mq}}$ [kW]	$G'_{P^{gen}{}_{aq}}$ [kW]
CC-SMPC	0.01	3	1.86	0.2283	0.0627	0	0	0	0
	0.05	8	4.92	0.2684	0.0927	5	3.52	1.2834	0.7009
	0.1	14	11.23	0.5197	0.0887	12	5.51	2.0106	0.7237
	0.2	24	15.46	0.4942	0.0889	21	7.84	2.8913	0.9843
DMPC	N.A	57	31.38	0.7473	0.1110	47	12.97	4.5762	1.4077

2) Online scenario tests

Figure 6.10 illustrates both operating costs and constraint violation costs for the DMPC and CC-SMPC strategies evaluated by the framework introduced in Section 6.4. In Figure 6.10 (a), the overall operation cost, overall violation cost, and the total cost are compared for DMPC and CC-SMPC methods. Figure 6.10 (b) and Figure 6.10 (c) present the breakdown of the overall operation cost and overall violation cost in Figure 6.10 (a) respectively. Each control

method is applied to 50 uncertain load scenarios considering the components' failure events while the failures occur following the aforementioned sequence. Based on the chosen evaluation weighting coefficients, the CC-SMPC approach has a 41% higher overall operation cost compared to the DMPC method, as the CC-SMPC–based solution strategy involves load shedding and switching activities for disconnection/reconnection of the loads, which is associated with higher weighting factors than the transmission switches in this study. However, compared to the DMPC method, the CC-SMPC total cost for constraint violation is reduced by 96%, with each type of violation cost being reduced by at least 80%. Moreover, the violation of the generator output power has been avoided 100% of the time. In summary, by adopting the CC-SMPC method the total cost has been reduced by 4.37%. The detailed simulation results of both DMPC and CC-SPMC strategies for all 50 testing scenarios are now presented and discussed.

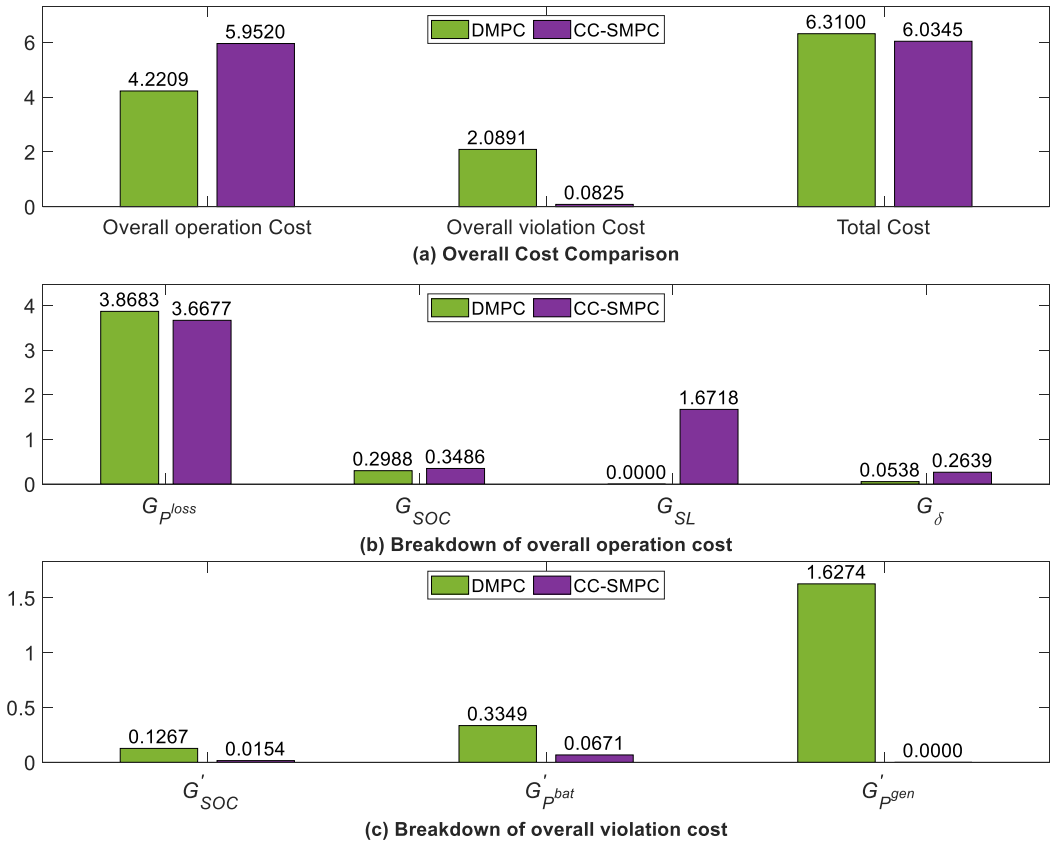
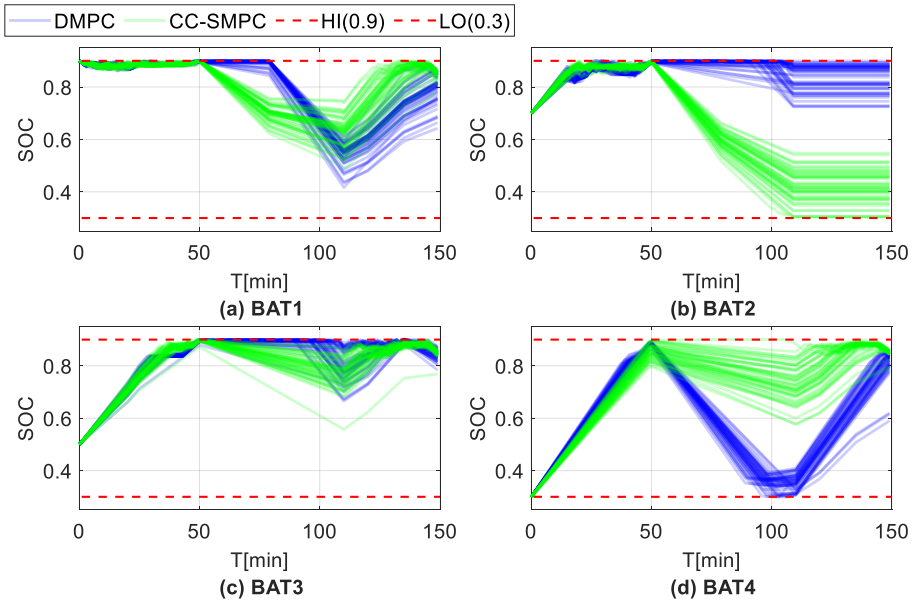
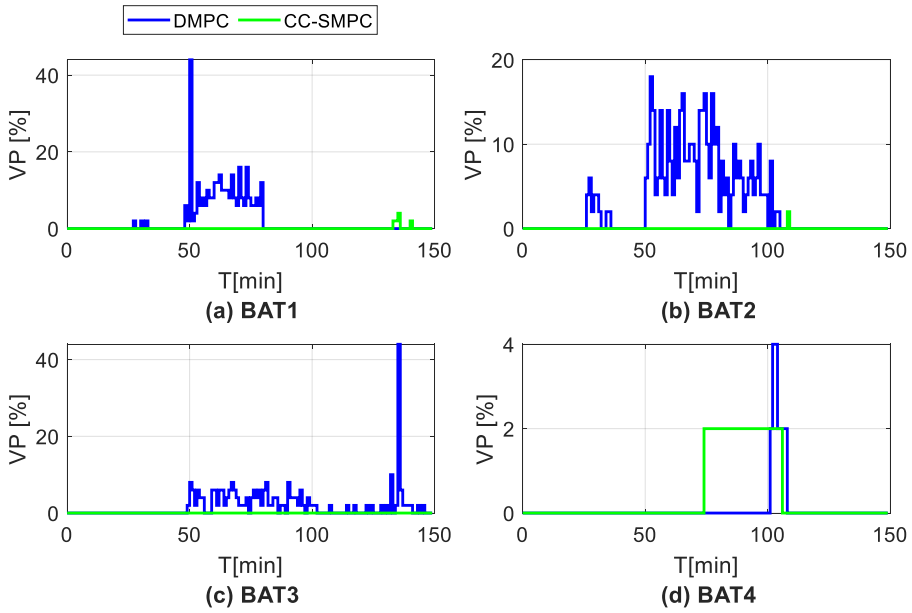


Figure 6.10 Cost comparison of online DMPC and CC-SMPC for Case 3



(1) SOC changes

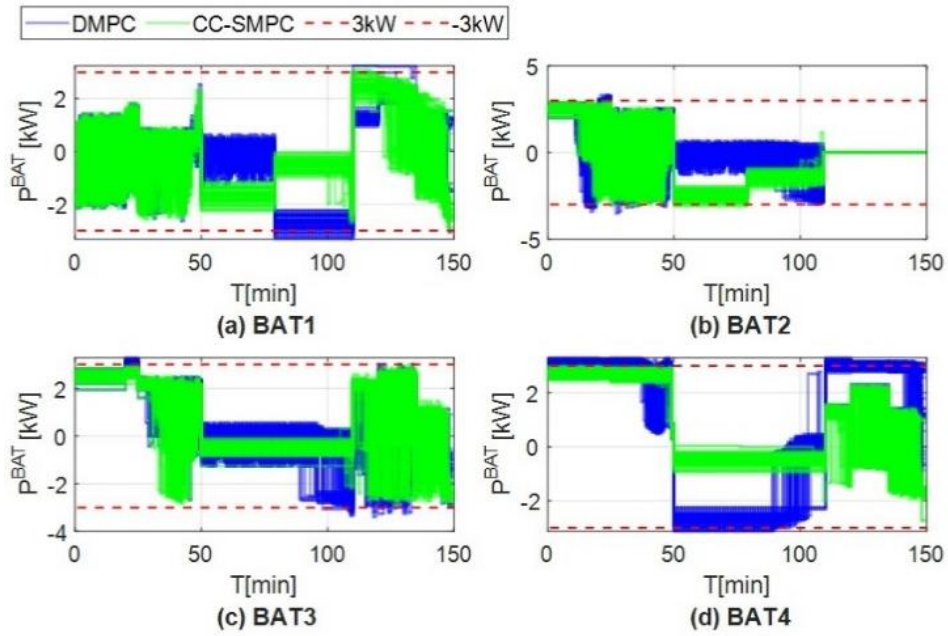


(2) Violation percentage among all uncertain scenarios

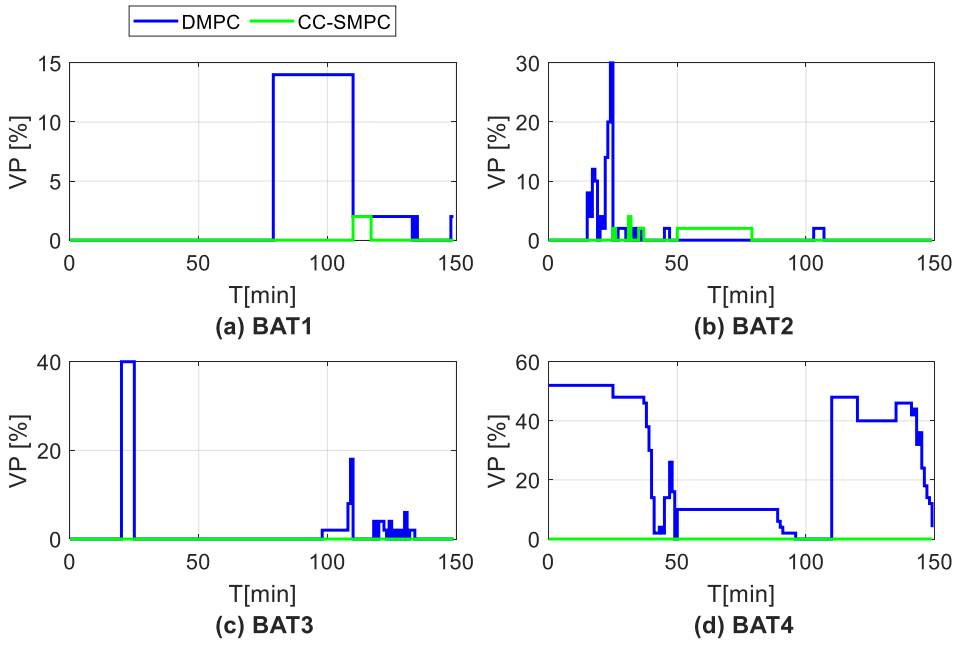
Figure 6.11 SOC results when adopting online DMPC and CC-SMPC for Case 3

Figure 6.11 to Figure 6.13 illustrate the SOC levels of the four batteries, the batteries' power, and generators/APU power, respectively. Before the generator failure occurs (at t = 19min), the system operates in normal mode, which shows the same results as Case 2. According to Figure 6.13, after the failure of generator 1, the APU is started to replace the failed generator to continue supplying the system by closing the switches at the link between the HV bus and APU bus. This has a few impacts on battery power and SOC changes before other failures occur, although the power loss slightly increases due to the bus interconnection. Before

t = 49min, similarly to Case 2 with the same configuration and load connection, the CC-SMPC performs better than DMPC by avoiding the violations of SOC and batteries' power which occurs up to 50% of the scenarios with DMPC.

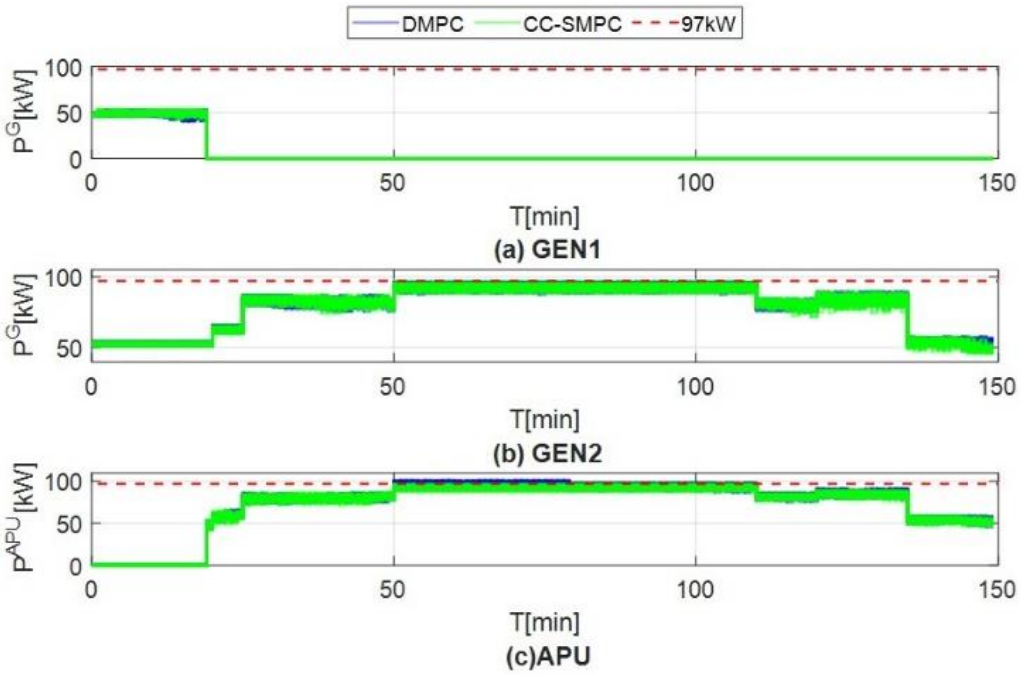


(1) Battery power changes

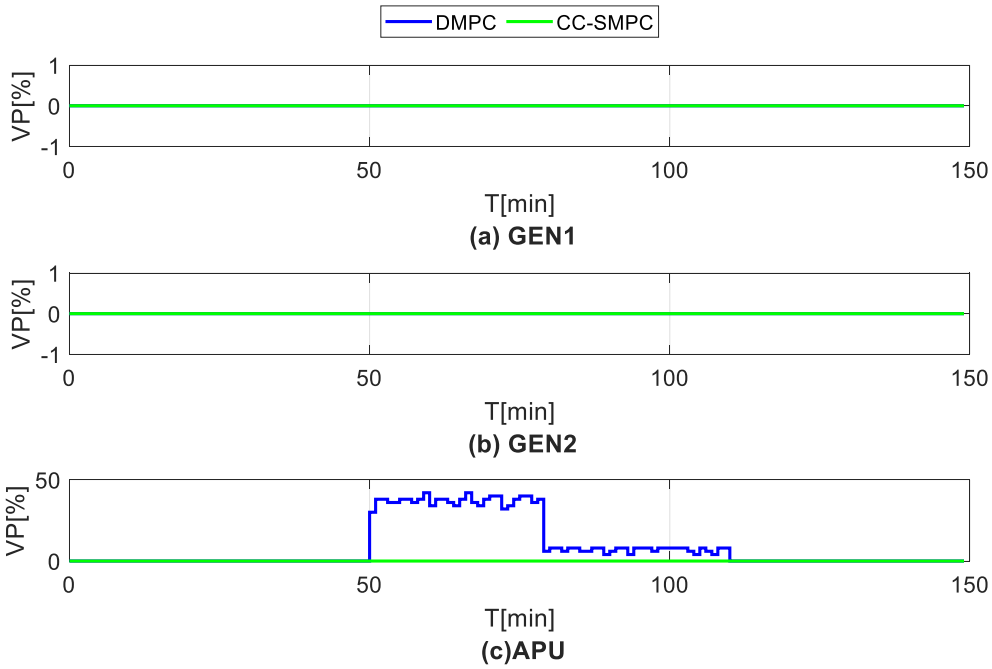


(2) Violation percentage among all uncertain scenarios

Figure 6.12 Battery power results when adopting online DMPC and CC-SMPC for Case 3



(1) Generator power changes



(2) Violation percentage among all uncertain scenarios

Figure 6.13 Generator power results when adopting online DMPC and CC-SMPC for Case 3

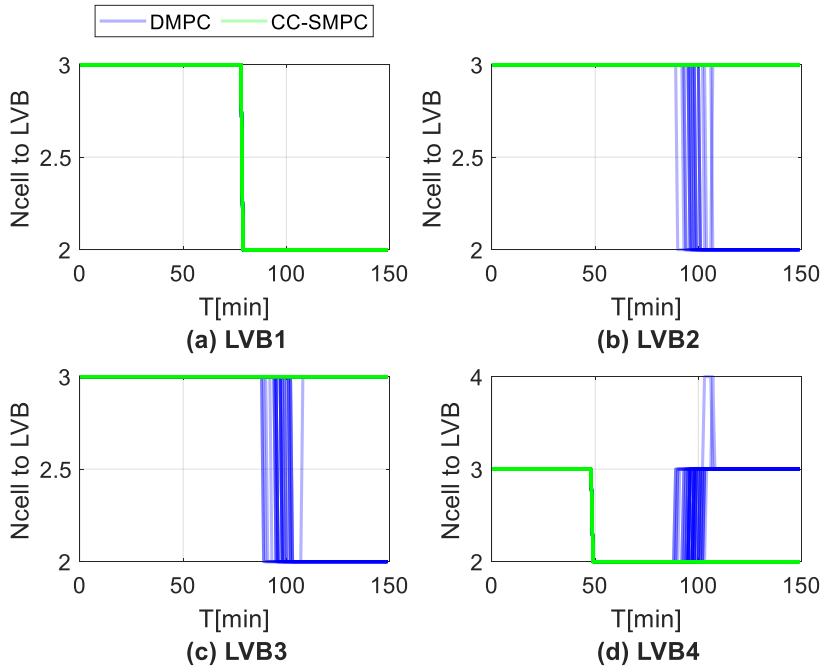
At t = 49 min, cell number 10 fails, which leads to a power shortage from the HV side, particularly on LV bus 4, while the system enters the high-power demand interval. During this period, the DMPC and CC-SMPC strategies provide different solutions for supplying the loads at LV bus 4. The DMPC-based solution strategy tries to discharge battery number 4 with a

discharging power that exceeds the maximum allowable discharging power in 10% of scenarios, with a maximum value of 3.2kW. This results in decreasing the battery SOC level but avoids loads shedding. In contrast, the CC-SMPC-based solution strategy involves shedding the load with the lowest priority on the LV bus to avoid the battery power violation and keep the battery SOC at higher levels, as presented in Figure 6.15. Compared to the CC-SMPC-based control in Case 2 during the same time interval, shedding the load at LV bus 4 also saves spare power for charging battery 3, which is also supplied by generator 2. Since the switching activities should be avoided, the load shedding remains for 60 min and the connection status of cells to LV buses is not changed before the occurrence of the next failure. In addition, from t = 50min to t = 79min, the DMPC strategy relies on the APU to supply LV bus 1 and 2, while APU maximum power violation occurs in approximately 40% of scenarios, with the maximum violation power being 4.5kW. In contrast, as shown in Figure 6.13 (c) the CC-SMPC method avoids all of this violation.

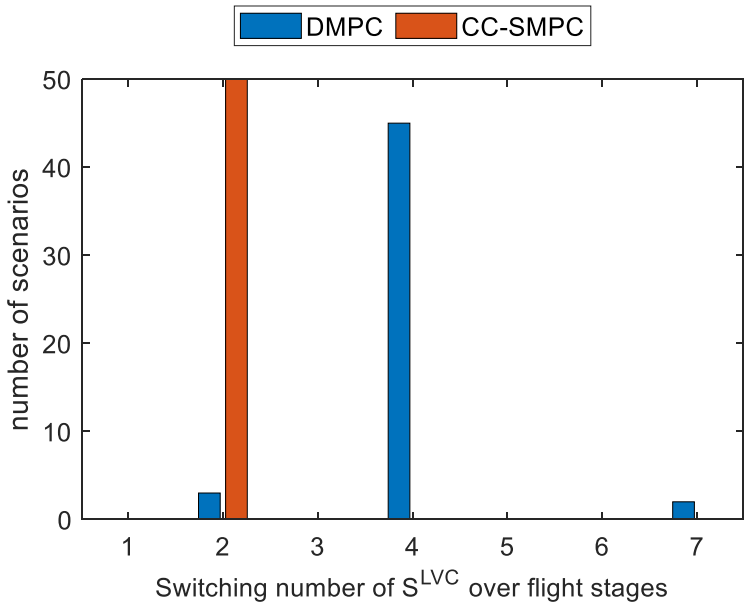
At t = 79 min, cell number 3 fails, which leads to a further power shortage in the LV side, and LV bus 1, connected to this cell, is impacted directly by this failure. According to Figure 6.14, after the occurrence of this failure, the number of cells connected to bus 1 is reduced from 3 to 2 in both DMPC and CC-SMPC methods. However, when adopting the DMPC strategy, the LV loads on LV bus 1 don't experience any load shedding as the connected battery is over-discharged in 14% of scenarios with the maximum power of 3.3kW, and the APU is overloaded in 8% of scenarios with the maximum power of 98.3kW. The CC-SMPC strategy also sheds the lowest priority load at this LV bus, which avoids all of the excessive power situations and keeps the SOC level 10% higher than the SOC in the DMPC method. This is presented in the subfigures (a)-(c) of Figure 6.15 (1). In addition, comparing the SOC changes for this period in Figure 6.11, with the DMPC method, battery 4 has been discharged to close to the lower bound during all cruising stages, and additional transmission switching activities are conducted to avoid the SOC dropping below the lower bound. In contrast, the CC-SMPC method avoids these switching activities because the lowest priority load for battery 4 remains shed.

When Battery 2 fails at t = 109 min, both DMPC and CC-SMPC methods disconnect this battery. When adopting the DMPC method, LV bus 2 and LV bus 3 are connected to supply the load at LV bus 2, while the CC-SMPC method connects LV bus 2 with LV bus 1, as presented in Figure 6.16. This difference is mainly caused by the average SOC level, which accumulates differently in the previous steps. At this stage, all loads shed by the CC-SMPC method are re-connected to the system, which causes additional switching activities. Figure 6.15 (2) shows that among 50 scenarios, the CC-SMPC leads to 48 scenarios with 4 LV load-switching activities, and 2 scenarios with 6 LV load-switching activities. However, the DMPC

method leads to battery power limit violations in 48% of scenarios as well as the violation of the SOC upper bound in 44% of scenarios, which is reduced to 2% with the CC-SMPC method.

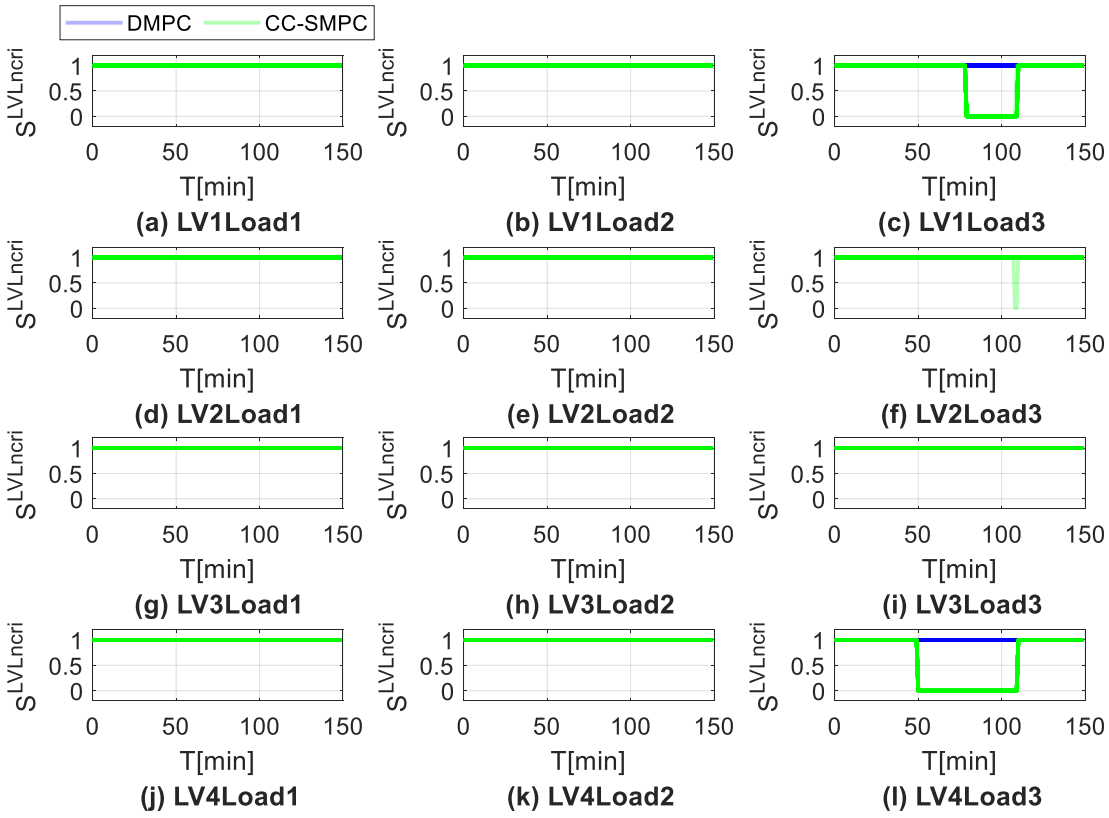


(1) Number of cells connected to each LV bus in all flight stages

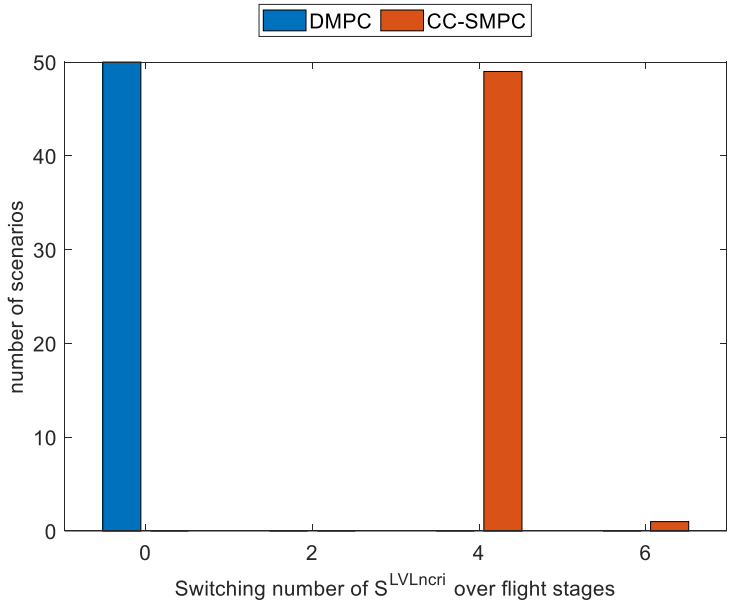


(2) Number of switching activities related to the connections of cells to LV bus

Figure 6.14 Connections of cells to LV buses when adopting online DMPC and CC-SMPC for Case 3



(1) Load shedding in all flight stages



(2) Number of switching activities of all LV noncritical loads

Figure 6.15 Connection of LV noncritical loads with online DMPC and CC-SMPC for Case 3

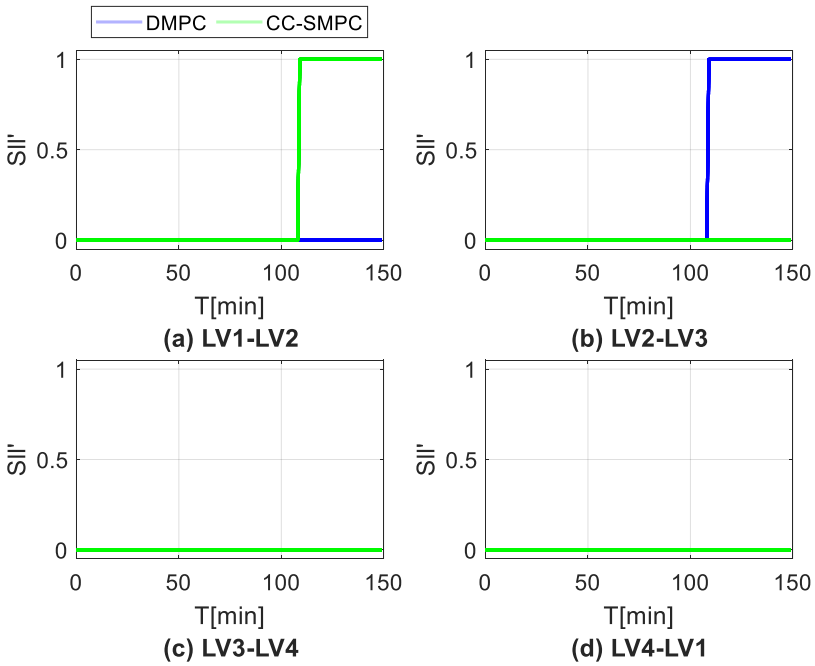


Figure 6.16 Connections of LV bus interconnections with online DMPC and CC-SMPC for Case 3

As a conclusion for Case 3, the proposed SMPC method is capable of coping with multiple failure scenarios. Compared to the DMPC method, when power shortages happen in the system because of failures, the SMPC method results in more conservative operating strategies, such as more load shedding, but less SOC reduction compared to the DMPC method. In addition, similarly to Case 1 and Case 2, the SMPC method performs better in controlling the system with fewer constraint violations.

6.6 Chapter summary

Based on the DMPC model proposed in Chapter 5, this chapter studied the optimal operational control of the MEA EPS in both normal and faulty situations, targeting the improvement of the performance of the system in terms of power losses, energy storage, and load shedding as well as reducing the number of switching activities. For dealing with the uncertainty of load power demand on both HV and LV buses, the operation management problem was formulated in the framework of CC-SMPC. Three cases have been studied to analyze the uncertainty impacts on the system, including the uncertainty of load power demand on LVBs in normal operating cases, and the uncertainty of load power demand on both LVBs and HVBs in normal operation as well as faulty operation cases. Based on the uncertainty propagation in each case, different probabilistic constraints were proposed for each case. Moreover, a comprehensive Monte-Carlo-based offline and online simulation study was

conducted for both DMPC and SMPC methods, and the results were evaluated with the proposed multi-dimensional evaluation framework. Based on the comparison of the operation costs and the violation costs in each case, the proposed CC-SMPC provides conservative strategies with uncertainty considerations, resulting in higher operation costs compared to DMPC. However, CC-SMPC improves the violation costs and the total costs compared to the DMPC technique in all cases.

This study benefits researchers in various aspects when developing optimization-based control methods considering multiple uncertainty sources in EPSs. In addition to the uncertainty on the demand side, the proposed chance-constrained model is also applicable to other subsystems considering uncertainty, such as the volatility and the forecast inaccuracy of energy output. Moreover, the uncertainty propagation analysis and its modelling in this study inspire other research coping with uncertainty sources located distributedly with/without reconfiguration considerations. Furthermore, the results and findings in this work imply the balance between EPS redundancy and model complexity in controller design. For instance, when the generators/ESSs are oversizing, CC-SMPC provides the same non-conservative strategies as DMPC; otherwise, CC-SMPC is required to avoid constraint violations though the control strategies are more conservative than DMPC. Therefore, when an EPS is highly redundant, deterministic optimization-based controllers are applicable to improve the model feasibility and reduce design complexity. In contrast, stochastic optimization-based controllers effectively ensure EPS safety when reducing system redundancy.

Chapter 7 Conclusion and Future Work

This chapter briefly reviews the most important findings of this thesis and then suggests potential future topics to be studied in this area of research.

With an expected growth in air travel over the next few decades and increasingly stringent regulations for carbon emissions, the aerospace industry is facing the challenges of greener aviation. Flight electrification is a significant way to improve fuel efficiency and reduce the aircraft environmental impact. This trend leads to increasing electrical power demands; hence, complex EPS architectures are investigated with different subsystems/components to generate/distribute power, and store energy. Consequently, to coordinate the power/energy among different subsystems/components, system-level operational control is essential to ensure the flight mission success and reduce the operational costs while guarantee the operational and safety requirements. In this thesis, an operational control design was studied for a novel modular converter-based EPS architecture, which provides an efficient and reliable operational strategy for the EPS in both normal and faulty conditions. The strategy achieves four critical functions, including intelligent load shedding, power allocation and scheduling (PAS), EPS (re)configuration, and energy storage management (ESM), which are formulated by a MILP model. In addition, operational control is improved in the following three aspects, for flight safety and better performance: 1) avoiding future worst-case scenarios by considering the future EPS status within an MPC framework; 2) quick responses to EPS real-time changes with multi-time scales by hierarchical control; 3) robust decisions considering load demand uncertainty using CC-SMPC.

This thesis first introduced the background and motivations of this study in Chapter 1. After the introduction of the development of MEA and the operational control functions, the studied modular converter-based EPS architecture was demonstrated. By reviewing the studies in the target area, the key issues, and four target functions, were identified: load shedding; PAS; EPS (re)configuration; and ESM. These were discussed for the operational control for the studied EPS.

To achieve the desired targets of the operational control problems, a number of published studies have proposed control design techniques with the consideration of the benefits in different aspects. Chapter 2 systematically reviewed these techniques for mathematical formulations and solution calculation, acting according to future predictions, responding to EPS

dynamics in different time scales, and uncertainty considerations. Based on the comparison of the advantages and drawbacks of different techniques, this chapter presented the reasons and applications for adopting different techniques in this thesis, including deterministic rule-based methods, MILP/MINLP, MPC, hierarchical control, and SMPC.

Before the entire EPS is studied with the integration of all functions, subsystems were firstly studied in Chapter 3 and Chapter 4, to provide fundamental verification of the proposed methods with just a few targets. In Chapter 3, optimized PAS, integrated with EPS reconfiguration, was modelled using MILP for the modular converter-based power distribution system. This chapter demonstrated the modelling techniques for formulating operational constraints, including power balancing, the power limits, the connection logic, the transmission losses in the cables and the nonlinear converter efficiency characteristics. The optimization model was firstly proposed to work out the most efficient paths to transfer the power with minimum total power losses. Three cases were conducted, verifying the proposed PAS strategy, allocating power appropriately, and keeping the modular converters operating at high efficiency. For considering a different objective, such as reducing each generator sizing, the MILP model was modified by including further constraints. With the modified constraints and objective function, the maximum generator output power was achieved in all three scenarios during all flight stages. Hence, the study in Chapter 3 indicates that the proposed MILP modelling method is applicable for optimized PAS integrated with EPS reconfiguration problems with different objectives. The studied modeling techniques can be modified to efficiently develop a feasible MILP model for problems relating to PAS and reconfiguration in various EPS architectures. Furthermore, this study inspires the EPS design issues, such as generator sizing, from the operational control perspective. On the one hand, the optimization-based control strategy enables reducing power consumption for a designed EPS architecture. On the other hand, the reduced power consumption indicates the potential reduction of the power rating of power sources.

In Chapter 4, the MPC-based optimal ESM and load management was studied for a main source-energy storage-load subsystem on one bus, aiming to maintain ES and prolong the battery life cycle, while minimizing load shedding, with fewer switching activities to improve device lifetimes and avoid unnecessary transients. Based on the study in Chapter 3, a MILP formulation was adopted in this study, integrated with a MPC framework based on future predictions. Following the control targets, three different objective functions were presented, and the importance of the different objective functions and prediction horizons were identified by analyzing the simulation/experimental results with the proposed evaluation framework including different performance indices. By assessing the impacts of different objectives, the chapter provided a reference for selecting the most applicable objective function combination,

as well as its potential impacts on deciding prediction horizons. The findings can be widely used when investigating energy storage and load management issues for EPSs containing battery-based ESSs. This study helps save time for trial and error when selecting objective functions and prediction horizons for MPC controller design.

Building upon the studies in Chapter 3 and 4, an intelligent two-level hierarchical supervisory control method for the entire EPS was proposed in Chapter 5. The HL controller was based on the optimization scheme of MILP-MPC to improve the long-term EPS performance with future predictions. Then, a rule-based LL controller with a faster clock was designed to provide quick responses to load changes and fault occurrences over a short time period during the HL sample intervals. Four modes were designed in the LL, to allow it to both cooperate with the online MPC in the HL and operate independently in both EPS normal and faulty conditions. Moreover, the LL independent modes were designed with BR-based and FSM-based methods for different performance. Three cases were simulated, considering the performance of the hierarchical control in different modes in each case. Based on the evaluation results, the hierarchical control in collaboration mode achieved the best performance, while maintaining the quick response to EPS changes. In contrast, when the online MPC was unavailable, the LL controller still managed the EPS operation following the real-time limitations. These case studies verified the effectiveness of the proposed hierarchical control. This study provides researchers with an innovative controller design method to improve optimization flexibility while ensuring strict safety requirements by combining deterministic rules, which is essential for aircraft EPSs. The proposed hierarchical control design allows the HL controller to flexibly provide various optimized strategies. In the meantime, all predefined rules are applied in the LL controller coordinating with the HL controller to ensure all control strategies are deterministic. Hence, both aircraft EPS safety and operating performance are improved.

In Chapter 3 to Chapter 5, the uncertainty in the EPS was not considered. In Chapter 6, a CC-SMPC method was proposed, based the MPC model formulated in Chapter 5, to improve the ability to cope with uncertainties due to fluctuating load demands. The system's operational requirements were formulated as a set of deterministic and probabilistic constraints in the CC-SMPC model. Three uncertainty/failure cases were simulated for both offline and online control strategies while the Monte-Carlo algorithm was used for scenario generation. The results, when adopting the DMPC and CC-SMPC methods, were evaluated with the proposed multi-dimension evaluation framework. Based on the comparison of the operational costs and the violation costs in each case, the proposed CC-SMPC improves the violation costs and the overall costs compared to the DMPC technique in all cases. This study inspires research in developing optimization-based control methods considering multiple distributed uncertainty

sources in EPSs, including uncertainty in power demand- and generation-side, as well as the EPS reconfiguration considerations. The results and findings indicate that, by integrating uncertainty models, stochastic optimization-based controllers provide optimized operational strategies with low constraint violation probability to ensure EPS safety. However, if an EPS is highly redundant, without resorting to complex stochastic optimization models, deterministic optimization-based controllers are beneficial in improving the model feasibility and reduce design complexity. The findings provide researchers with insight when balancing between EPS redundancy and model complexity in controller design.

Based on above, all the aims and objectives of this study formulated in Section 1.2 are fully achieved. During the conduct of this research, several aspects have been identified as follow-on studies to enhance the topic:

1) Accurate EPS models

In this thesis, some of the component dynamics were not modelled with as high an accuracy as possible, such as dealing with nonlinear power losses in cables, the relationship between charging/discharging rate of ESSs and their operating condition, the effects of operating temperature and capacity fading in ESSs, device degradation, and so on. These were not the focus of this research and would have greatly, and unnecessarily, increased the problem complexity and the required computational time using these models. However, with more accurate EPS models, more characteristics and component dynamics can be optimized in the operational control. With regard to this, proposing accurate onboard EPS models and maintaining their feasibility in controller design requires further future studies.

2) Advanced forecasting techniques

The proposed MPC control relies on the EPS status forecasting, in either a long-term or short-term manner, based on the control targets. The application of accurate forecasting techniques along with improved models might considerably reduce the power and energy estimation error of the energy sources and load demand prediction. In this thesis, load prediction is assumed to be obtained by sampling the historical load profile. However, in the application of an onboard EPS, there are only a few studies proposing forecasting methods following real flight stages. In addition, the study of forecasting techniques is limited to keeping accuracy for long-term predictions. Therefore, challenges still exist in effective accurate forecasting techniques in future EPS operational control studies.

3) More experimental validation

For large-scale operational control problems, the validation is commonly based on traditional simulation platforms or real-time experimental tests, such as hardware-in-loop,

because of inaccurate EPS models, assumptions of balance conditions or absence of harmonics, etc. In this thesis, the verification is also based on the aforementioned techniques, however, it would be beneficial to conduct further verification with more hardware to increase confidence in expected outcomes when building on this work.

Appendix A : Load profiles in Section 3.3.2

Table 7.1 Load profile (kW) for flight stages in Section 3.3.2.1

Load types [kW]	Load indices	Stage 1	Stage 2	Stage 3	Stage 4	Stage 5	Stage 6	Stage 7
HV loads	HVL1	10	30	20	50	40	35	35
	HVL2	10	30	20	50	40	35	35
LV Load	LVL1	1	1	2	2	5	1	7
	LVL2	1	1	5	5	5	9	3
	LVL3	5	3	4	6	8	2	1
	LVL4	10	10	8	5	2	2	4

Table 7.2 Load profile (kW) for flight stages in Section 3.3.2.2

Load types [kW]	Load indices	Stage 1	Stage 2	Stage 3	Stage 4	Stage 5	Stage 6	Stage 7
HV loads	HVL1	5	20	25	40	60	30	40
	HVL2	15	40	12	60	20	40	30
LV Load	LVL1	3	1	2	4	5	5	4
	LVL2	3	1	2	4	5	5	4
	LVL3	3	1	2	4	5	5	4
	LVL4	3	1	2	4	5	5	4

Table 7.3 Load profile (kW) for flight stages in Section 3.3.2.3

Load types [kW]	Load indices	Stage 1	Stage 2	Stage 3	Stage 4	Stage 5	Stage 6	Stage 7
HV loads	HVL1	5	20	25	40	60	30	40
	HVL2	15	40	12	60	20	40	30
LV Load	LVL1	1	1	2	2	5	1	7
	LVL2	1	1	5	5	5	9	3
	LVL3	5	3	4	6	8	2	1
	LVL4	10	10	8	5	2	2	4

Appendix B : Algorithms in the LL Mode 2 in Chapter 5

B.1 Algorithm II-A in Algorithm II in the LL Mode 2

The Algorithm II-A is presented in detail in this section.

Algorithm II-A Rules for generator status in Mode 2

1) Set initial HV side configurations based on the online MPC recommendations as follows, where $\forall j \in \{1, \dots, N^{HVB}\}$:
$S_j^G(k^{LL}) = S_j^G(k^{HL})$,
$s_{jj'}^{HV}(k^{LL}) = s_{jj'}^{HV}(k^{LL})$, $S_j^{AHV}(k^{LL}) = S_j^{AHV}(k^{LL})$,
$ST^{APU}(k^{LL}) = S^{APU}(k^{HL})$, $S^{APU}(k^{LL}) = S^{APU}(k^{HL})$.
2) Set initial load shedding caused by generator failure based on the online MPC recommendations as follows:
$\boldsymbol{S^{shed_g}}(k^{LL}) = \boldsymbol{S^{shed}}(k^{HL})$, where $\boldsymbol{S^{shed_g}}$ includes both HV and LV noncritical loads $S_{jp}^{HVLncri}$ and $S_{lq}^{LVLncri}$, $\forall j \in \{1, \dots, N^{HVB}\}, \forall l \in \{1, \dots, N^{LVB}\}, \forall p \in \{1, \dots, N^{HVLncri}\}, \forall q \in \{1, \dots, N^{LVLncri}\}$
3) Decide the HV side configurations, based on the generator failure status and the APU starting status

If

$\gamma_j^G(k^{LL}) = 1$ and $S_j^G(k^{HL}) \le \gamma_j^G(k^{LL})$, , $\forall j \in \{1, \dots, N^{HVB}\}$: All generators are in normal condition, and the recommended connection of the generators are applicable in this condition.

Then

The LL controller keeps the initial settings for the HV configurations and load shedding.

If

$\gamma_j^G(k^{LL}) = 0$ and $S_j^G(k^{HL}) > \gamma_j^G(k^{LL})$, $\exists j \in \{1, \dots, N^{HVB}\}$: The generator *j* is in faulty condition, while the recommendation of its connection to the HV bus *j* is inapplicable in this condition because of the violation of the health status constraint for generator *j*.

Then

(1) $S_j^G(k^{LL}) = 0$: The faulty generator *j* is disconnected by the LL controller;

(2) If the remaining generator *j'* cannot supply all critical, high-priority and mid-priority loads, then the LL controller starts the APU to maintain its operation: $ST^{APU}(k^{LL}) = 1$, otherwise, the APU is not started by the LL controller: $ST^{APU}(k^{LL}) = 0$;

(3) If $R^{APU}(k^{LL}) = 0$, the LL controller connects HV bus *j* to its neighbor bus *j'* because the APU is not fully started for connection, i.e. $s_{jj'}^{HV}(k^{LL}) = 1$, $S^{APU}(k^{LL}) = 0$, $S_j^{ahv}(k^{LL}) = 0$. In addition, because only one generator supplies the EPS, if it cannot supply the connected loads, i.e. $P_{j'}^{Gmax} < P^{criL}(k^{LL}) + P^{ncriL}(k^{LL})$, where $P^{criL}(k^{LL})$ and $P^{ncriL}(k^{LL})$ are calculated in (8.1) and (8.2), the LL controller sheds sufficient loads according to the load priorities to avoid overload by conducting Algorithm II-A-shed.

(4) If $R^{APU}(k^{LL}) = 1$, HV bus *j* is connected to the APU bus with APU connected to it, i.e. $S^{APU}(k^{LL}) = 1$, $S_j^{ahv}(k^{LL}) = 1$, $s_{jj'}^{HV}(k) = 0$

If

$\gamma_j^G(k^{LL}) = 0$ and $S_j^G(k^{HL}) \le \gamma_j^G(k^{LL})$ and $S^{APU}(k^{HL}) > R^{APU}(k^{LL})$, $\exists j \in \{1, \dots, N^{HVB}\}$: Online MPC disconnects the faulty generator *j* and recommends to connect the APU for power supply. Because of the starting time, the APU is not ready for connection at k^{LL}.

Then

(1)$S_j^G(k^{LL}) = S_j^G(k^{HL})$, $s_{jj'}^{HV}(k^{LL}) = 1$, $ST^{APU}(k^{LL}) = 1$, $S_j^{ahv}(k^{LL}) = 0$, $S^{APU}(k^{LL}) = 0$: The faulty generator *j* is disconnected following the online MPC recommendation, while the HV interconnection is adopted while starting the APU.

(2) While starting the APU, the generator *j'* supplies the EPS, if $P_{j'}^{Gmax} < P^{criL}(k^{LL}) + P^{ncriL}(k^{LL})$, the LL controller sheds sufficient loads according to the load priorities to avoid overload by conducting Algorithm II-A-shed.

If

$\gamma_j^G(k^{LL}) = 0$ and $S_j^G(k^{HL}) \le \gamma_j^G(k^{LL})$, and $S^{APU}(k^{HL}) \le R^{APU}(k^{LL})$, $\exists j \in \{1, \dots, N^{HVB}\}$: The online MPC disconnects the faulty generator *j* and recommends to connect APU for power supply, which is ready for connection. Hence, the recommendations are applicable.

Then

The LL controller keeps the initial settings for the HV configurations and the load shedding.

Load shedding is conducted when $PMAX^G < P^{criL}\left(k^{LL}\right) + P^{ncriL}(k^{LL})$ as mentioned in Algorithm II-A step 3) in the second 'If-Then' rule, where $P^{criL}(k^{LL})$ represents the power demands of all critical loads as presented in (8.1), and the $P^{ncriL}(k^{LL})$ in (8.2) represents the power demands of all noncritical loads. The load shedding is conducted from low-priority loads to the high-priority ones, as presented in Algorithm II-A-shed.

$$P^{criL}(k^{LL}) = \sum_j^{N^{HVB}} \sum_p^{N^{HVLcri}} P_{jp}^{HVLcri}(k^{LL}) + \sum_l^{N^{LVB}} \sum_p^{N^{LVLncri}} P_{jp}^{LVLcri}(k^{LL}) \quad (7.1)$$

$$P^{ncriL}(k^{LL}) = \sum_j^{N^{HVB}} \sum_p^{N^{HVLncri}} \left(S_{jp}^{HVLncri}(k^{LL}) P_{jp}^{HVLncri}(k^{LL})\right) + \sum_l^{N^{LVB}} \sum_q^{N^{LVLncri}} \left(S_{lq}^{LVLncri}(k^{LL}) S_{lq}^{LVLncri}(k^{LL})\right) \quad (7.2)$$

Algorithm II-A-shed Load shedding for HV and LV bus *l*

Start from low priority HV/LV load $p = N^{HVLncri}, q = N^{LVLncri}$

While $p, q \ge 1$, Do the following calculation for HV and LV buses:

$S_{jp}^{HVLncri}(k^{LL}) = 0, \forall j \in \{1, \dots, N^{HVB}\}$

$S_{lq}^{LVLncri}(k^{LL}) = 0, \quad \forall l \in \{1, \dots, N^{LVB}\}$

IF $PMAX^G > P^{criL}(k^{LL}) + P^{ncriL}(k^{LL})$, Break **While**;

Else $p = p - 1, q = q - 1$;

End While

B.2 Algorithm II-B in Algorithm II in the LL Mode 2

The Algorithm II-B is presented in detail in this section.

Algorithm II-B Rules for battery status in Mode 2
1) Set initial LV side configurations based on the online MPC recommendations as follows, where $\forall l \in \{1, \dots, N^{LVB}\}$: $S_l^{BAT}(k^{LL}) = S_l^{BAT}(k^{HL})$, $s_{ll'}^{LV}(k^{LL}) = s_{ll'}^{LV}(k^{LL})$,
2) Decide LV side configurations based on the battery failure status **If** $\gamma_l^{BAT}(k^{LL}) = 1$ and $S_l^{BAT}(k^{HL}) \leq \gamma_l^{BAT}(k^{LL})$, $\forall l \in \{1, \dots, N^{LVB}\}$: All batteries are in normal condition, and the connection recommendations of the batteries are applicable. **Then** Keep the initial settings for the LV side configurations **If** $\gamma_l^{BAT}(k^{LL}) = 0$ and $S_l^{BAT}(k^{HL}) > \gamma_l^{BAT}(k^{LL})$, $\exists l \in \{1, \dots, N^{LVB}\}$: The battery *l* is in faulty condition, and the recommendation of its connection to the LV bus *l* is inapplicable because of the violation of the health status constraint for battery *l*. **Then** $S_l^{BAT}(k^{LL}) = 0$, $s_{l(l+1)}^{LV}(k^{LL}) = 1$: Disconnect the faulty battery *l* from the LV bus *l*; Connect neighbor LV bus *l*+1 with the bus *l* to supply its voltage and power. **If** $\gamma_l^{BAT}(k^{LL}) = 0 \wedge S_l^{BAT}(k^{HL}) < \gamma_l^{BAT}(k^{LL}), \exists l \in \{1, \dots, N^{LVB}\}$: The online MPC disconnects the faulty battery *l* and the recommendations are applicable. **Then** Keep the initial settings for the LV configurations

B.3 Algorithm II-C in Algorithm II in the LL Mode 2

The Algorithm II-C is presented in detail in this section.

Algorithm II-C Rules for connections between the HV buses and cells in Mode 2

1) Set initial connections between the HV buses and cells based on the online MPC recommendations as follows, where $\forall j \in \{1, \dots, N^{HVB}\}$, $\forall c \in \{1, \dots, N^{C}\}$, $S_{jc}^{HVC}(k^{LL}) = S_{jc}^{HVC}(k^{HL})$

2) Decide upon the configurations between HV buses and cells based on the link failure status

If

$\gamma_c^C(k^{LL}) = 1$ and $\gamma_{jc}^{HVC}(k^{LL}) = 1$ and $S_{jc}^{HVC}(k^{HL}) \leq \gamma_{jc}^{HVC}(k^{LL})$, $\forall j \in \{1, \dots, N^{HVB}\}$, $\forall c \in \{1, \dots, N^{C}\}$: All cells and the links between the HV buses and cells are in normal condition, and the connection recommendations are applicable in this condition.

Then

Keep the initial settings for the configurations between HV buses and cells.

If

$\gamma_c^C(k^{LL}) = 0, \exists c \in \{1, \dots, N^{C}\}$: The cell *c* is in faulty condition.

Then

$S_{jc}^{HVC}(k^{LL}) = 0, \forall j \in \{1, \dots, N^{HVB}\}$: All links from HV buses to this cell *c* are disconnected.

If

$\gamma_c^C(k^{LL}) = 1$ and $\gamma_{jc}^{HVC}(k^{LL}) = 0$ and $S_{jc}^{HVC}(k^{HL}) > \gamma_{jc}^{HVC}(k^{LL})$, $\exists j \in \{1, \dots, N^{HVB}\}$, $\exists c \in \{1, \dots, N^{C}\}$: The link between HV bus *j* and cell *c* is in faulty condition, while the cell *c* is in normal condition. In addition, the recommendation of this connection is inapplicable because of the violation of health status constraint for this faulty link.

Then

(1) $S_{jc}^{HVC}(k^{LL}) = 0$: Disconnect the link between HV bus *j* and cell *c*,

(2) HV bus *j'* and cell *c'* are symmetric to HV bus *j* and cell *c* respectively. The switching of the connections is represented as follows, which is explained in 5.5.2.3 a)-c).

When $\gamma_{c'}^C(k^{LL}) = 1$ and $\gamma_{j'c}^{HVC}(k^{LL}) = 1$ and $\gamma_{jc'}^{HVC}(k^{LL}) = 1$, conduct $S_{j'c}^{HVC}(k^{LL}) = S_{jc}^{HVC}(k^{HL})$, $S_{jc'}^{HVC}(k^{LL}) = S_{j'c'}^{HVC}(k^{HL})$, $S_{j'c'}^{HVC}(k^{LL}) = 0$.

When $\gamma_{c'}^C(k^{LL}) = 0$ and $\gamma_{j'c}^{HVC}(k^{LL}) = 1$, conduct $S_{j'c}^{HVC}(k^{LL}) = S_{jc}^{HVC}(k^{HL})$, $S_{jc'}^{HVC}(k^{LL}) = 0$, $S_{j'c'}^{HVC}(k^{LL}) = 0$.

If

$\gamma_c^C(k^{LL}) = 1$ and $\gamma_{jc}^{HVC}(k^{LL}) = 0$ and $S_{jc}^{HVC}(k^{HL}) \leq \gamma_{jc}^{HVC}(k^{LL})$, $\exists j \in \{1, \dots, N^{HVB}\}$, $\exists c \in \{1, \dots, N^{C}\}$: The link between HV bus *j* and cell *c* is in faulty condition, and the recommendation of this connection is applicable and the cell *c* is in normal condition.

Then

Keep the initial settings for the configurations between HV buses and cells

B.4 Algorithm II-D in Algorithm II in the LL Mode 2

The Algorithm II-D is presented in detail in this section.

Algorithm II-D Rules for connections between the LV buses and cells in Mode 2

3) Set initial connections between the LV buses and cells based on the online MPC recommendations as follows, where $\forall c \in \{1, \dots, N^C\}$, $\forall l \in \{1, \dots, N^{LVB}\}$, $S_{cl}^{LVC}(k^{LL}) = S_{cl}^{LVC}(k^{HL})$

4) Decide upon the configurations between LV buses and cells based on the link failure status

If

$\gamma_c^C(k^{LL}) = 1$ and $\gamma_{cl}^{LVC}(k^{LL}) = 1$ and $S_{cl}^{LVC}(k^{HL}) \leq \gamma_{cl}^{LVC}(k^{LL})$, $\forall j \in \{1, \dots, N^{HVB}\}$, $\forall c \in \{1, \dots, N^C\}$: All cells and the links between the LV buses and cells are in normal condition, and the connection recommendations are applicable in this condition.

Then

Keep the initial settings for the configurations between LV buses and cells.

If

$\gamma_c^C(k^{LL}) = 0, \exists c \in \{1, \dots, N^C\}$: The cell *c* is in faulty condition.

Then

$S_{cl}^{LVC}(k^{LL}) = 0, \forall l \in \{1, \dots, N^{LVB}\}$: All links from LV buses to this cell *c* are disconnected.

If

$\gamma_c^C(k^{LL}) = 1$ and $\gamma_{cl}^{LVC}(k^{LL}) = 0$ and $S_{cl}^{LVC}(k^{HL}) > \gamma_{cl}^{LVC}(k^{LL})$, $\exists c \in \{1, \dots, N^C\}$, $\exists l \in \{1, \dots, N^{LVB}\}$: The link between LV bus *l* and cell *c* is in faulty condition, while the cell *c* is in normal condition. In addition, the recommendation of this connection is inapplicable because of the violation of health status constraint for this faulty link.

Then

(1) $S_{cl}^{LVC}(k^{LL}) = 0$: Disconnect the link between LV bus *l* and cell *c*,

(2) LV bus *l*' and cell *c*' are symmetric to LV bus *l* and cell *c* respectively. The switching of the connections is represented as follows, which is explained in 5.5.2.3 a)-c).

When $\gamma_{c'}^C(k^{LL}) = 1$ and $\gamma_{cl'}^{LVC}(k^{LL}) = 1$ and $\gamma_{c'l}^{LVC}(k^{LL}) = 1$, conduct $S_{cl'}^{LVC}(k^{LL}) = S_{c'l'}^{lVC}(k^{HL})$, $S_{c'l}^{LVC}(k^{LL}) = S_{cl}^{LVC}(k^{HL})$, $S_{c'l'}^{LVC}(k^{LL}) = 0$.

When $\gamma_{c'}^C(k^{LL}) = 0$ and $\gamma_{cl'}^{LVC}(k^{LL}) = 1$, conduct $S_{cl'}^{LVC}(k^{LL}) = S_{c'l'}^{LVC}(k^{HL})$, $S_{c'l}^{LVC}(k^{LL}) = 0$, $S_{c'l'}^{LVC}(k^{LL}) = 0$.

If

$\gamma_c^C(k^{LL}) = 1$ and $\gamma_{cl}^{LVC}(k^{LL}) = 0$ and $S_{cl}^{LVC}(k^{HL}) \leq \gamma_{cl}^{LVC}(k^{LL})$, $\exists c \in \{1, \dots, N^C\}$, $\exists l \in \{1, \dots, N^{LVB}\}$: The link between LV bus *l* and cell *c* is in faulty condition, and the recommendation of this connection is applicable and the cell *c* is in normal condition.

Then

Keep the initial settings for the configurations between LV buses and cells

References

[1] FAA, “Office of Environment and Energy January 2015,” no. January, 2015.

[2] Airbus, “Environment matters for the future of aerospace,” *Airbus Environ.*, pp. 1–26, 2019.

[3] A. Abdel-Hafez, “Power Generation and Distribution System for a More Electric Aircraft-A Review,” *Recent Adv. Aircr. Technol.*, pp. 289–308, 2012.

[4] P. Wheeler and S. Bozhko, “The more electric aircraft: Technology and challenges,” *IEEE Electrif. Mag.*, vol. 2, no. 4, pp. 6–12, 2014.

[5] P. Wheeler and S. Bozhko, “The More Electric Aircraft,” *IEEE Electrif. Mag.*, no. December, pp. 1–7, 2014.

[6] J. Chen, C. Wang, and J. Chen, “Investigation on the selection of electric power system architecture for future more electric aircraft,” *IEEE Trans. Transp. Electrif.*, vol. 4, no. 2, pp. 563–576, 2018.

[7] A. Boglietti, A. Cavagnino, A. Tenconi, “The safety critical electric ma- chines and drives in the more electric aircraft: A survey,” in *Proc. IEEE 35th Annu. Conf. Ind. Electron.*, 2009, pp. 3–5.

[8] X. Roboam, B. Sareni, and A. De Andrade, “More Electricity in the Air,” *Ind. Electron. Mag. IEEE*, vol. 6, no. 4, pp. 6–17, 2012.

[9] E. Alcorta-Garcia, A. Zolghadri, “A Nonlinear Observer-Based Strategy for Aircraft Oscillatory Failure Detection: A380 Case Study,” *IEEE Trans. Aerosp. Electron. Syst.*, vol. 47, no. 4, pp. 2792–2806.

[10] A. Ghodbane, M. Saad, C. Hobeika, J.-F. Boland, “Design of a Tolerant Flight Control System in Response to Multiple Actuator Control Signal Faults Induced by Cosmic Rays,” *IEEE Trans. Aerosp. Electron. Syst.*, vol. 52, no. 2, pp. 681–697, 2016.

[11] D. A. Molligoda, P. Chatterjee, C. J. Gajanayake, A. K. Gupta, and K. J. Tseng, “Review of design and challenges of DC SSPC in more electric aircraft,” *2016 IEEE 2nd Annu. South. Power Electron. Conf. SPEC 2016*, pp. 1–5, 2016.

[12] M. Tariq, A. I. Maswood, C. J. Gajanayake, and A. K. Gupta, “Aircraft batteries: Current trend towards more electric aircraft,” *IET Electr. Syst. Transp.*, vol. 7, no. 2, pp. 93–103, 2017.

[13] Xin Zhao, J. M. Guerrero, and Xiaohua Wu, “Review of aircraft electric power systems and architectures,” *2014 IEEE Int. Energy Conf.*, pp. 949–953, 2014.

[14] H. Zhang, F. Mollet, C. Saudemont, and B. Robyns, “Experimental validation of energy storage system management strategies for a local DC distribution system of more electric aircraft,” *IEEE Trans. Ind. Electron.*, vol. 57, no. 12, pp. 3905–3916, 2010.

[15] A. Eid, H. El-Kishky, M. Abdel-Salam, and T. El-Mohandes, “Constant frequency aircraft electric power systems with harmonic reduction,” *IECON Proc. (Industrial Electron. Conf.*, pp. 623–628, 2008.

[16] A. Eid, H. El-Kishky, M. Abdel-Salam, and M. T. El-Mohandes, “On power quality of variable-speed constant-frequency aircraft electric power systems,” *IEEE Trans. Power Deliv.*, vol. 25, no. 1, pp. 55–65, 2010.

[17] A. Lücken, J. Brombach, and D. Schulz, “Design and protection of a high voltage DC onboard grid with integrated fuel cell system on more electric aircraft,” *Int. Conf. Electr. Syst. Aircraft, Railw. Sh. Propulsion, ESARS 2010*, pp. 1–6, 2010.

[18] B. H. Nya, J. Brombach, and D. Schulz, “Benefits of higher voltage levels in aircraft electrical power systems,” *Electr. Syst. Aircraft, Railw. Sh. Propulsion, ESARS*, 2012.

[19] S. Sumsurooah *et al.*, “ENIGMA-A centralised supervisory controller for enhanced onboard electrical energy management with model in the loop demonstration,” *Energies*,

vol. 14, no. 17, 2021.
[20] S. Bozhko, M. Liserre, K. Al-Haddad, G. Buticchi, and P. Wheeler, “On-board Microgrids for the More Electric Aircraft - Technology Review,” *IEEE Trans. Ind. Electron.*, vol. 66, no. 7, pp. 1–1, 2018.
[21] Y. Zhang, J. Chen, and Y. Yu, “Distributed power management with adaptive scheduling horizons for more electric aircraft,” *Int. J. Electr. Power Energy Syst.*, vol. 126, no. PA, p. 106581, 2021.
[22] G. Benetti, D. Caprino, M. L. Della, and T. Facchinetti, “Electric load management approaches for peak load reduction : A systematic literature review and state of the art,” *Sustain. Cities Soc.*, vol. 20, pp. 124–141, 2015.
[23] J. Zhu, “Optimal load shedding,” in *Optimization of Power System Operation*, 2009, pp. 455–502.
[24] M. T. E. Heinrich, F. Kelch, P. Magne, and A. Emadi, “Regenerative braking capability analysis of an electric taxiing system for a single aisle midsize aircraft,” *IEEE Trans. Transp. Electrif.*, vol. 1, no. 3, pp. 298–307, 2015.
[25] A. Y. Abdelaziz, F. M. Mohamed, S. F. Mekhamer, and M. A. L. Badr, “Distribution system reconfiguration using a modified Tabu Search algorithm,” *Electr. Power Syst. Res.*, vol. 80, no. 8, pp. 943–953, 2010.
[26] K. Ma, T. Yao, J. Yang, and X. Guan, “Residential power scheduling for demand response in smart grid,” *Int. J. Electr. Power Energy Syst.*, vol. 78, pp. 320–325, 2016.
[27] J. Zhang, X. Wang, and L. Ma, “An optimal power allocation scheme of microgrid using grey wolf optimizer,” *IEEE Access*, vol. 7, pp. 137608–137619, 2019.
[28] J. Chen and Q. Song, “A decentralized energy management strategy for a fuel cell/supercapacitor-based auxiliary power unit of a more electric aircraft,” *IEEE Trans. Ind. Electron.*, vol. 66, no. 7, pp. 5736–5747, 2019.
[29] T. Azib, C. Larouci, A. Chaibet, and M. Boukhnifer, “Online energy management strategy of a hybrid fuel cell/battery/ultracapacitor vehicular power system,” *IEEJ Trans. Electr. Electron. Eng.*, vol. 9, no. 5, pp. 548–554, 2014.
[30] M. Maasoumy, P. Nuzzo, F. Iandola, M. Kamgarpour, A. Sangiovanni-Vincentelli, and C. J. Tomlin, “Optimal load management system for Aircraft Electric Power distribution,” *IEEE Conf. Decis. Control*, pp. 2939–2945, 2013.
[31] K. Ni *et al.*, “Electrical and Electronic Technologies in More-Electric Aircraft: A Review,” *IEEE Access*, vol. 7, no. June, pp. 76145–76166, 2019.
[32] P. Wheeler, A. Trentin, S. Bozhko, and J. Clare, “Regeneration of energy onto an aircraft electrical power system from an electro-mechanical actuator,” *Electr. Syst. Aircraft, Railw. Sh. Propulsion, ESARS*, 2012.
[33] B. Nya and D. Schulz, “Approach to Implementation of Power Management with Load Prioritizations in Modern Civil Aircraft,” *Int. J. Electr. Comput. Eng.*, vol. 6, no. 7, pp. 703–707, 2012.
[34] C. Spagnolo, V. Madonna, S. Sumsurooah, C. I. Hill, and S. Bozhko, “Optimised low voltage loads allocation for mea electrical power systems,” *AIAA Propuls. Energy Forum Expo. 2019*, no. August, pp. 1–8, 2019.
[35] X. Wang, J. Atkin, N. Bazmohammadi, S. Bozhko, and J. M. Guerrero, “Optimal Load and Energy Management of Aircraft Microgrids Using Multi-Objective Model Predictive Control,” *Sustainability* , vol. 13, no. 24. 2021.
[36] M. J. Salehpour, H. Radmanesh, S. M. H. Rostami, J. Wang, and H. J. Kim, “Effect of load priority modeling on the size of fuel cell as an emergency power unit in a more-electric aircraft,” *Appl. Sci.*, vol. 9, no. 16, 2019.
[37] Y. Ge, B. Song, Y. Pei, Y. Mollet, and J. Gyselinck, “A fuzzy logic based method for fault tolerant hierarchical load management of more electric aircraft,” *Proc. Inst. Mech. Eng. Part G J. Aerosp. Eng.*, vol. 233, no. 10, pp. 3846–3856, Nov. 2018.
[38] D. Schlabe, J. Lienig, “Energy Management of Aircraft Electrical Systems State of the Art and Further Directions,” no. October, pp. 1–6, 2012.
[39] A. Parisio, E. Rikos, G. Tzamalis, and L. Glielmo, “Use of model predictive control for experimental microgrid optimization,” *Appl. Energy*, vol. 115, pp. 37–46, 2014.

[40] J. Zhu, “Optimal reconfiguration of electrical distribution network,” *Optim. power Syst. Oper.*, vol. 62, pp. 503–543, 2002.
[41] K. W. Hedman, A. S. Korad, M. Zhang, G. Thompson, A. Dominguez-Garcia, and X. Jiang, “The Application of Robust Optimization in Power Systems,” 2014.
[42] K. Sathish Kumar, T. Jayabarathi, S. Prabhakar Karthikeyan, I. Jacob Raglend, and D. P. Kothari, “Power system restoration, reconfiguration and optimization using Field Programmable Gate Array,” in *2011 International Conference on Emerging Trends in Electrical and Computer Technology, ICETECT 2011*, 2011, pp. 57–62.
[43] D. Rehage, U. B. Carl, and A. Vahl, “Redundancy management of fault tolerant aircraft system architectures - Reliability synthesis and analysis of degraded system states,” *Aerosp. Sci. Technol.*, vol. 9, no. 4, pp. 337–347, 2005.
[44] A. Barzegar, R. Su, C. Wen, L. Rajabpour, Y. Zhang, and M. Y. Lee, “Intelligent Power Allocation and Load Management of More Electric Aircraft,” *Ieee Peds*, no. June, pp. 533–538, 2015.
[45] M. Elsied, A. Oukaour, T. Youssef, H. Gualous, and O. Mohammed, “An advanced real time energy management system for microgrids,” *Energy*, vol. 114, pp. 742–752, 2016.
[46] S. Paran, T. V. Vu, T. El Mezyani, and C. S. Edrington, “MPC-based power management in the shipboard power system,” *2015 IEEE Electr. Sh. Technol. Symp. ESTS 2015*, pp. 14–18, 2015.
[47] R. Chai, B. Zhang, J. Dou, Z. Hao, and T. Zheng, “Unified Power Flow Algorithm Based on the NR Method for Hybrid AC/DC Grids Incorporating VSCs,” *IEEE Trans. Power Syst.*, vol. 31, no. 6, pp. 4310–4318, 2016.
[48] J. Ma, L. Yuan, Z. Zhao, and F. He, “Transmission Loss Optimization-Based Optimal Power Flow Strategy by Hierarchical Control for DC Microgrids,” *IEEE Trans. Power Electron.*, vol. 32, no. 3, pp. 1952–1963, 2017.
[49] Y. Zhang, Y. Yu, R. Su, and J. Chen, “Power Scheduling in More Electric Aircraft based on An Optimal Adaptive Control Strategy,” *IEEE Trans. Ind. Electron.*, vol. PP, no. December 2019, pp. 1–1, 2019.
[50] J. Dong, S. Nie, H. Huang, P. Yang, A. Fu, and J. Lin, “Research on economic operation strategy of CHP microgrid considering renewable energy sources and integrated energy demand response,” *Sustain.*, vol. 11, no. 18, 2019.
[51] F. Garcia-Torres and C. Bordons, “Optimal Economical Schedule of Hydrogen-Based Microgrids With Hybrid Storage Using Model Predictive Control,” *IEEE Trans. Ind. Electron.*, vol. 62, no. 8, pp. 5195–5207, 2015.
[52] B. V. Solanki, K. Bhattacharya, and C. A. Canizares, “A Sustainable Energy Management System for Isolated Microgrids,” *IEEE Trans. Sustain. Energy*, vol. 8, no. 4, pp. 1507–1517, 2017.
[53] M. Alowaifeer and A. P. S. Meliopoulos, “Centralized Microgrid Energy Management System Based on Successive Linearization,” *2018 North Am. Power Symp. NAPS 2018*, 2019.
[54] H. Çınar, “Active Energy Management Based on Meta-Heuristic Algorithms of Fuel Cell / Battery / Supercapacitor Energy Storage System for Aircraft,” 2021.
[55] T. LEI, Z. YANG, Z. LIN, and X. ZHANG, “State of art on energy management strategy for hybrid-powered unmanned aerial vehicle,” *Chinese J. Aeronaut.*, vol. 32, no. 6, pp. 1488–1503, 2019.
[56] M. A. Mosa, A. A. Ali, H. M. E. Zoghpy, A. A. E. Samahy, and A. M. A. Ghany, “Energy Management System of Autonomous Low Voltage DC Microgrid Consists of Energy Storage System,” *2018 20th Int. Middle East Power Syst. Conf. MEPCON 2018 - Proc.*, no. Dc, pp. 582–588, 2019.
[57] Z. Jiang and S. A. Raziei, “Hierarchical model predictive control for real-time energy-optimized operation of aerospace systems,” *AIAA Propuls. Energy Forum Expo. 2019*, no. August, pp. 1–16, 2019.
[58] M. Elkazaz, M. Sumner, E. Naghiyev, S. Pholboon, R. Davies, and D. Thomas, “A hierarchical two-stage energy management for a home microgrid using model predictive and real-time controllers,” *Appl. Energy*, vol. 269, no. April, p. 115118, 2020.

[59] J. Shen and A. Khaligh, “A supervisory energy management control strategy in a battery/ultracapacitor hybrid energy storage system,” *IEEE Trans. Transp. Electrif.*, vol. 1, no. 3, pp. 223–231, 2015.
[60] N. Noura, L. Boulon, and S. Jemeï, “A review of battery state of health estimation methods: Hybrid electric vehicle challenges,” *World Electr. Veh. J.*, vol. 11, no. 4, pp. 1–20, 2020.
[61] BioLogic, “Battery states: State of charge (SoC), State of Health (SoH). Electrochemistry basics series,” 2022. [Online]. Available: https://www.biologic.net/topics/battery-states-state-of-charge-soc-state-of-health-soh/#:~:text=The state-of-health (,charge to its rated capacity.
[62] B. Tarhan, O. Yetik, and T. H. Karakoc, “Hybrid battery management system design for electric aircraft,” *Energy*, vol. 234, p. 121227, 2021.
[63] Q. Xue, X. Zhang, T. Teng, J. Zhang, Z. Feng, and Q. Lv, “A Comprehensive Review on Classification, Energy Management Strategy, and Control Algorithm for Hybrid Electric Vehicles,” *Energies*, vol. 13, no. 20, p. 5355, 2020.
[64] S. G. Wirasingha, S. Member, A. Emadi, and S. Member, “Classification and Review of Control Strategies for Plug-In Hybrid Electric Vehicles,” *IEEE Trans. Veh. Technol.*, vol. 60, no. 1, pp. 111–122, 2011.
[65] Y. Wang, Z. Sun, and Z. Chen, “Development of energy management system based on a rule-based power distribution strategy for hybrid power sources,” *Energy*, vol. 175, pp. 1055–1066, 2019.
[66] X. Giraud, H. Piquet, M. Budinger, X. Roboam, M. Sartor, and S. Vial, “Knowledge-based system for aircraft electrical power system reconfiguration,” *Electr. Syst. Aircraft, Railw. Sh. Propulsion, ESARS*, vol. 2048, pp. 1–6, 2012.
[67] C. Spagnolo, S. Sumsurooah, C. I. Hill, and S. Bozhko, “Finite state machine control for aircraft electrical distribution system,” *J. Eng.*, vol. 2018, no. 13, pp. 506–511, 2018.
[68] C. Spagnolo, S. Sumsurooah, C. I. Hill, and S. Bozhko, “Smart controller design for safety operation ofthe MEA electrical distribution system,” in *IECON 2018 - 44th Annual Conference of the IEEE Industrial Electronics Society*, vol. 1, pp. 5778–5785.
[69] C. Spagnolo, S. Sumsurooah, and S. Bozkho, “Advanced smart grid power distribution system for more electric aircraft application,” *Proc. - ICOECS 2019 2019 Int. Conf. Electrotech. Complexes Syst.*, 2019.
[70] Y. Wang, Z. Sun, and Z. Chen, “Energy management strategy for battery/supercapacitor/fuel cell hybrid source vehicles based on finite state machine,” *Appl. Energy*, vol. 254, no. December 2018, p. 113707, 2019.
[71] J. M. Mendel, “Introduction to Rule-Based Fuzzy Logic Systems,” in *Uncertain Rule-Based Fuzzy Systems*, 2017, pp. 1–99.
[72] N. Patcharaprakiti and S. Premrudeepreechacharn, “Maximum power point tracking using adaptive fuzzy logic control for grid-connected photovoltaic system,” in *Proceedings of the IEEE Power Engineering Society Transmission and Distribution Conference*, 2002, vol. 1, no. February, pp. 372–377.
[73] N. Vijeh, “Self Organizing Fuzzy Logic Control of a Level Control Rig,” in *Second IEEE International Conference on Fuzzy Systems*, 1993, pp. 303–308.
[74] S. Njoya Motapon, L. A. Dessaint, and K. Al-Haddad, “A comparative study of energy management schemes for a fuel-cell hybrid emergency power system of more-electric aircraft,” *IEEE Trans. Ind. Electron.*, vol. 61, no. 3, pp. 1320–1334, 2014.
[75] J. C. Swierczek, F. Mollet, C. Saudemont, R. Meuret, and B. Robyns, “Power management of a regenerative local HVDC aircraft network using supercapacitors,” *15th Int. Power Electron. Motion Control Conf. Expo. EPE-PEMC 2012 ECCE Eur.*, pp. 1–8, 2012.
[76] M. B. Kamal, J. Wei, and G. J. Mendis, “Data-driven energy management architecture for more-electric aircrafts,” *2017 19th Int. Conf. Intell. Syst. Appl. to Power Syst. ISAP 2017*, pp. 1–6, 2017.
[77] M. B. Kamal and J. Wei, “Attack-resilient energy management architecture of hybrid emergency power system for more-electric aircrafts,” *2017 IEEE Power Energy Soc.*

Innov. Smart Grid Technol. Conf. ISGT 2017, 2017.
[78] P. Xie *et al.*, "Optimization-Based Power and Energy Management System in Shipboard Microgrid: A Review," *IEEE Syst. J.*, pp. 1–13, 2021.
[79] L. M. Hvattum, A. Løkketangen, and F. Glover, "Comparisons of Commercial MIP Solvers and an Adaptive Memory (Tabu Search) Procedure for a Class of 0-1 Integer Programming Problems," *Algorithmic Oper. Res.*, vol. 7, no. 1, pp. 13–20, 2012.
[80] A. Viswanath, L. Goel, and P. Wang, "Mixed integer programming formulation techniques and applications to Unit Commitment problem," *10th Int. Power Energy Conf. IPEC 2012*, pp. 25–30, 2012.
[81] J. Zhu, *Optimization of Power System Operation, 2nd Edition*. 2015.
[82] J. Lin, F. Magnago, and J. M. Alemany, "Chapter 1 - Optimization Methods Applied to Power Systems: Current Practices and Challenges," in *Classical and Recent Aspects of Power System Optimization*, A. F. Zobaa, S. H. E. Abdel Aleem, and A. Y. B. T.-C. and R. A. of P. S. O. Abdelaziz, Eds. Academic Press, 2018, pp. 1–18.
[83] C. Wang, K. Ren, and J. Wang, "Secure Optimization Computation Outsourcing in Cloud Computing: A Case Study of Linear Programming," *IEEE Trans. Comput.*, vol. 65, no. 1, pp. 216–229, 2016.
[84] M. K. Mangoli, K. Y. Lee, and Y. Moon Park, "Optimal real and reactive power control using linear programming," *Electr. Power Syst. Res.*, vol. 26, no. 1, pp. 1–10, 1993.
[85] S. Chakraborty, M. D. Weiss, and M. G. Simões, "Distributed intelligent energy management system for a single-phase high-frequency AC microgrid," *IEEE Trans. Ind. Electron.*, vol. 54, no. 1, pp. 97–109, 2007.
[86] L. Rubino and G. Rubino, "Design of a Power System Supervisory Control with Linear Optimization for Electrical Load Management in an Aircraft On-Board DC Microgrid," *Sustain.*, vol. 13, no. 15, p. 8580, 2021.
[87] H. Wattar, J. Koch, J. Lemke, and M. Terorde, "Smart load balancing for large civil aircraft," in *2013 4th IEEE/PES Innovative Smart Grid Technologies Europe, ISGT Europe 2013*, 2013, pp. 1–5.
[88] E. Skjong, T. A. Johansen, M. Molinas, and A. J. Sorensen, "Approaches to Economic Energy Management in Diesel-Electric Marine Vessels," *IEEE Trans. Transp. Electrif.*, vol. 3, no. 1, pp. 22–35, 2017.
[89] N. Robuschi, M. Salazar, N. Viscera, F. Braghin, and C. H. Onder, "Minimum-Fuel Energy Management of a Hybrid Electric Vehicle via Iterative Linear Programming," *IEEE Trans. Veh. Technol.*, vol. 69, no. 12, pp. 14575–14587, 2020.
[90] V. K. Tumuluru, Z. Huang, and D. H. K. Tsang, "Unit commitment problem: A new formulation and solution method," *Int. J. Electr. Power Energy Syst.*, vol. 57, pp. 222–231, 2014.
[91] A. Yoza, K. Uchida, A. Yona, and T. Senju, "Optimal operation method of smart house by controllable loads based on smart grid topology," *Int. J. Emerg. Electr. Power Syst.*, vol. 14, no. 5, pp. 411–420, 2013.
[92] C. Shao, X. Wang, M. Shahidehpour, X. Wang, and B. Wang, "An MILP-Based Optimal Power Flow in Multicarrier Energy Systems," *IEEE Trans. Sustain. Energy*, vol. 8, no. 1, pp. 239–248, 2017.
[93] R. Bourbon, S. U. Ngueveu, X. Roboam, B. Sareni, C. Turpin, and D. Hernandez-Torres, "Energy management optimization of a smart wind power plant comparing heuristic and linear programming methods," *Math. Comput. Simul.*, vol. 158, pp. 418–431, 2019.
[94] T. Bradley, B. Moffitt, D. Parekh, T. Fuller, and D. Mavris, "Energy Management for Fuel Cell Powered Hybrid-Electric Aircraft," in *7th International Energy Conversion Engineering Conference*, 2009, p. 4590.
[95] M. Doff-Sotta, M. Cannon, and M. Bacic, "Optimal energy management for hybrid electric aircraft," *IFAC-PapersOnLine*, vol. 53, no. 2, pp. 6043–6049, 2020.
[96] Y. Zhang, R. Su, C. Wen, M. Y. Lee, and C. Gajanayake, "Distributed power allocation and scheduling for electrical power system in more electric aircraft," *IECON 2016 - 42nd Annu. Conf. IEEE Ind. Electron. Soc.*, pp. 102–107, 2016.
[97] W. J. Ma, J. Wang, X. Lu, and V. Gupta, "Optimal Operation Mode Selection for a DC

Microgrid," *IEEE Trans. Smart Grid*, vol. 7, no. 6, pp. 2624–2632, 2016.
[98] E. Burke and G. Kendall, *Search Methodologies*. 2005.
[99] A. Ghasemi-Marzbali, "A novel nature-inspired meta-heuristic algorithm for optimization: bear smell search algorithm," *Soft Comput.*, vol. 24, no. 17, pp. 13003–13035, 2020.
[100] Y. Zhang *et al.*, "An Energy Efficient Power Management Solution for a Fault-tolerant More Electric Engine/Aircraft," *IEEE Trans. Ind. Electron.*, vol. PP, no. c, pp. 1–1, 2018.
[101] Y. Zhang, G. O. Heo Peng, S. Dasgupta, M. Husband, R. Su, and C. Wen, "Design of the Power Management System for Electrical Power Systems in More Electric Engine / Aircraft," in *ESARS-ITEC 2018*, 2019, no. 3, pp. 0–5.
[102] J. Zhao, H. S. Ramadan, and M. Becherif, "Metaheuristic-based energy management strategies for fuel cell emergency power unit in electrical aircraft," *Int. J. Hydrogen Energy*, vol. 44, no. 4, pp. 2390–2406, 2019.
[103] Y. Mishima, K. Nara, T. Satoh, T. Ito, and H. Kaneda, "Method for Loss Minimum Re-configuration Problem of Distribution System by Tabu Search," *IEEJ Trans. Power Energy*, vol. 123, no. 10, pp. 1149–1155, 2003.
[104] N. Rugthaicharoencheep and S. Sirisumrannukul, "Feeder reconfiguration with dispatchable distributed generators in distribution system by tabu search," *Proc. Univ. Power Eng. Conf.*, pp. 1–7, 2009.
[105] Y. Zong, D. Kullmann, A. Thavlov, O. Gehrke, and H. W. Bindner, "Application of model predictive control for active load management in a distributed power system with high wind penetration," *IEEE Trans. Smart Grid*, vol. 3, no. 2, pp. 1055–1062, 2012.
[106] B. Shahsavari, M. Maasoumy, A. Sangiovanni-Vincentelli, and R. Horowitz, "Stochastic model predictive control design for load management system of aircraft electrical power distribution," *2015 Am. Control Conf.*, pp. 3649–3655, 2015.
[107] A. Barzegar, R. Su, C. Wen, L. Rajabpour, Y. Zhang, and M. Y. Lee, "Intelligent Power Allocation and Load Management of More Electric Aircraft," *Ieee Peds*, no. June, pp. 533–538, 2015.
[108] M. Doff-Sotta, M. Cannon, M. Bacic, "Optimal energy management for hybrid-electric aircraft," *Aircr. Eng. Aerosp. Technol.*, vol. 92, no. 6, pp. 851–861, 2020.
[109] W. Dunham, B. Hencey, A. R. Girard, and I. Kolmanovsky, "Distributed Model Predictive Control for More Electric Aircraft Subsystems Operating at Multiple Time Scales," *IEEE Trans. Control Syst. Technol.*, vol. 28, no. 6, pp. 2177–2190, 2020.
[110] N. Sockeel, M. Shahverdi, and M. Mazzola, "Impact of the State of Charge Estimation on Model Predictive Control Performance in a Plug-In Hybrid Electric Vehicle Accounting for Equivalent Fuel Consumption and Battery Capacity Fade," *ITEC 2019 - 2019 IEEE Transp. Electrif. Conf. Expo*, 2019.
[111] N. Sockeel, J. Shi, M. Shahverdi, and M. Mazzola, "Pareto Front Analysis of the Objective Function in Model Predictive Control Based Power Management System of a Plug-in Hybrid Electric Vehicle," *2018 IEEE Transp. Electrif. Conf. Expo, ITEC 2018*, pp. 173–177, 2018.
[112] Z. Fu, Z. Li, and F. Tao, "Adaptive energy management strategy for hybrid batteries/supercapacitors electrical vehicle based on model prediction control," *Asian J. Control*, pp. 2463–2468, 2019.
[113] O. Gomozov, J. P. F. Trovao, X. Kestelyn, and M. R. Dubois, "Adaptive Energy Management System Based on a Real-Time Model Predictive Control with Nonuniform Sampling Time for Multiple Energy Storage Electric Vehicle," *IEEE Trans. Veh. Technol.*, vol. 66, no. 7, pp. 5520–5530, 2017.
[114] A. Parisio, E. Rikos, and L. Glielmo, "A Model Predictive Control Approach to Microgrid Operation Optimization," *IEEE Trans. Control Syst. Technol.*, vol. 22, no. 99, p. 1, 2014.
[115] A. Parisio, C. Wiezorek, T. Kyntäjä, J. Elo, K. Strunz, and K. H. Johansson, "Cooperative MPC-Based Energy Management for Networked Microgrids," *IEEE Trans. Smart Grid*, vol. 8, no. 6, pp. 3066–3074, 2017.
[116] J. M. Guerrero, M. Chandorkar, T. L. Lee, and P. C. Loh, "Advanced control

architectures for intelligent microgridspart i: Decentralized and hierarchical control," *IEEE Trans. Ind. Electron.*, vol. 60, no. 4, pp. 1254–1262, 2013.
[117] S. Breban, C. Saudemont, S. Vieillard, and B. Robyns, "Experimental design and genetic algorithm optimization of a fuzzy-logic supervisor for embedded electrical power systems," *Math. Comput. Simul.*, vol. 91, pp. 91–107, 2013.
[118] H. Zhang, C. Saudemont, B. Robyns, and R. Meuret, "Comparison of different DC voltage supervision strategies in a local Power Distribution System of More Electric Aircraft," *Math. Comput. Simul.*, vol. 81, no. 2, pp. 263–276, 2010.
[119] S. Uebel, N. Murgovski, B. Bäker, and J. Sjöberg, "A Two-Level MPC for Energy Management Including Velocity Control of Hybrid Electric Vehicles," *IEEE Trans. Veh. Technol.*, vol. 68, no. 6, pp. 5494–5505, 2019.
[120] M. Restrepo, C. A. Cañizares, J. W. Simpson-porco, P. Su, and J. Taruc, "Optimization- and Rule-based Energy Management Systems at the Canadian Renewable Energy Laboratory microgrid facility," *Appl. Energy*, vol. 290, no. October 2020, p. 116760, 2021.
[121] J. D. Lara, D. E. Olivares, and C. A. Cañizares, "Robust energy management of isolated microgrids," *IEEE Syst. J.*, vol. 13, no. 1, pp. 680–691, 2019.
[122] A. R. Jordehi, "How to deal with uncertainties in electric power systems? A review," *Renew. Sustain. Energy Rev.*, vol. 96, no. June 2017, pp. 145–155, 2018.
[123] A. Soroudi, M. Aien, and M. Ehsan, "A probabilistic modeling of photo voltaic modules and wind power generation impact on distribution networks," *IEEE Syst. J.*, vol. 6, no. 2, pp. 254–259, 2012.
[124] K. Bae and J. S. Thorp, "A stochastic study of hidden failures in power system protection," *Decis. Support Syst.*, vol. 24, no. 3–4, pp. 259–268, 1999.
[125] B. Shahsavari, M. Maasoumy, A. Sangiovanni-Vincentelli, and R. Horowitz, "Stochastic model predictive control design for load management system of aircraft electrical power distribution," *2015 Am. Control Conf.*, pp. 3649–3655, 2015.
[126] A. Dos Santos and M. T. C. De Barros, "Stochastic modeling of power system faults," *Electr. Power Syst. Res.*, vol. 126, pp. 29–37, 2015.
[127] P. D. Couchman, M. Cannon, and B. Kouvaritakis, "Stochastic MPC with inequality stability constraints," *Automatica*, vol. 42, no. 12, pp. 2169–2174, 2006.
[128] M. Hemmati, B. Mohammadi-Ivatloo, M. Abapour, and A. Anvari-Moghaddam, "Optimal Chance-Constrained Scheduling of Reconfigurable Microgrids Considering Islanding Operation Constraints," *IEEE Syst. J.*, vol. 14, no. 4, pp. 5340–5349, 2020.
[129] F. H. Aghdam, N. T. Kalantari, and B. Mohammadi-Ivatloo, "A chance-constrained energy management in multi-microgrid systems considering degradation cost of energy storage elements," *J. Energy Storage*, vol. 29, no. February, p. 101416, 2020.
[130] Y. Zhang, J. Wang, B. Zeng, and Z. Hu, "Chance-Constrained Two-Stage Unit Commitment under Uncertain Load and Wind Power Output Using Bilinear Benders Decomposition," *IEEE Trans. Power Syst.*, vol. 32, no. 5, pp. 3637–3647, 2017.
[131] P. Kou, D. Liang, and L. Gao, "Distributed EMPC of multiple microgrids for coordinated stochastic energy management," *Appl. Energy*, vol. 185, pp. 939–952, 2017.
[132] N. Bazmohammadi, A. Tahsiri, A. Anvari-Moghaddam, and J. M. Guerrero, "Stochastic Predictive Control of Multi-Microgrid Systems," *IEEE Trans. Ind. Appl.*, vol. 55, no. 5, pp. 5311–5319, 2019.
[133] Z. Wang, B. Chen, J. Wang, and J. Kim, "Decentralized Energy Management System for Networked Microgrids in Grid-Connected and Islanded Modes," *IEEE Trans. Smart Grid*, vol. 7, no. 2, pp. 1097–1105, 2016.
[134] S. Esmaeili, A. Anvari-Moghaddam, S. Jadid, and J. M. Guerrero, "A stochastic model predictive control approach for joint operational scheduling and hourly reconfiguration of distribution systems," *Energies*, vol. 11, no. 7, 2018.
[135] D. van der Meer, G. C. Wang, and J. Munkhammar, "An alternative optimal strategy for stochastic model predictive control of a residential battery energy management system with solar photovoltaic," *Appl. Energy*, vol. 283, no. October 2020, p. 116289, 2021.

[136] Y. Zhang, F. Meng, R. Wang, W. Zhu, and X. J. Zeng, "A stochastic MPC based approach to integrated energy management in microgrids," *Sustain. Cities Soc.*, vol. 41, no. May, pp. 349–362, 2018.
[137] N. Bazmohammadi, A. Anvari-Moghaddam, A. Tahsiri, A. Madary, J. C. Vasquez, and J. M. Guerrero, "Stochastic predictive energy management of multi-microgrid systems," *Appl. Sci.*, vol. 10, no. 14, 2020.
[138] W. Dunham, B. Hencey, I. Kolmanovsky, and A. Girard, "Scenario based stochastic MPC for more electric aircraft coordinated engine and power management," *Proc. Am. Control Conf.*, vol. 2019-July, pp. 4223–4228, 2019.
[139] S. N. Motapon, L. A. Dessaint, and K. Al-Haddad, "A robust H2-consumption-minimization-based energy management strategy for a fuel cell hybrid emergency power system of more electric aircraft," *IEEE Trans. Ind. Electron.*, vol. 61, no. 11, pp. 6148–6156, 2014.
[140] A. Fathy, H. Rezk, and A. M. Nassef, "Robust hydrogen-consumption-minimization strategy based salp swarm algorithm for energy management of fuel cell/supercapacitor/batteries in highly fluctuated load condition," *Renew. Energy*, vol. 139, pp. 147–160, 2019.
[141] D. J. Garcia, J. Gong, and F. You, *Multi-Stage Adaptive Robust Optimization over Bioconversion Product and Process Networks with Uncertain Feedstock Price and Biofuel Demand*, vol. 38. Elsevier Masson SAS, 2016.
[142] R. Koubaa, S. Bacha, M. Smaoui, and L. krichen, "Robust optimization based energy management of a fuel cell/ultra-capacitor hybrid electric vehicle under uncertainty," *Energy*, vol. 200, 2020.
[143] H. Gao, J. Liu, L. Wang, and Z. Wei, "Decentralized Energy Management for Networked Microgrids in Future Distribution Systems," *IEEE Trans. Power Syst.*, vol. 33, no. 4, pp. 3599–3610, 2018.
[144] M. H. Moradi and M. Abedini, "Electrical Power and Energy Systems A combination of genetic algorithm and particle swarm optimization for optimal DG location and sizing in distribution systems," *Int. J. Electr. Power Energy Syst.*, vol. 34, no. 1, pp. 66–74, 2012.
[145] P. Thota and M. Venkata Kirthiga, "Optimal siting & sizing of distributed generators in micro-grids," *2012 Annu. IEEE India Conf. INDICON 2012*, pp. 730–735, 2012.
[146] R. Seresinhe and C. Lawson, "Electrical load-sizing methodology to aid conceptual and preliminary design of large commercial aircraft," *Proc. Inst. Mech. Eng. Part G J. Aerosp. Eng.*, vol. 229, no. 3, pp. 445–466, 2015.
[147] D. Alfonso *et al.*, "Batteries for Aerospace: a Brief Review," in *2018 AEIT International Annual Conference*, 2018, vol. 217.
[148] P. Fortenbacher, J. L. Mathieu, and G. Andersson, "Modeling, identification, and optimal control of batteries for power system applications," *Proc. - 2014 Power Syst. Comput. Conf. PSCC 2014*, 2014.
[149] Y. Zhang *et al.*, "An Energy Efficient Power Management Solution for a Fault-tolerant More Electric Engine/Aircraft," *IEEE Trans. Ind. Electron.*, vol. PP, no. c, pp. 1–1, 2018.
[150] W. Wang and J. P.Koeln, "Hierarchical Multi-Timescale Energy Management for Hybrid-Electric Aircraft," in *Dynamic Systems and Control Conference*, 2020, pp. 1–10.
[151] C. T. Aksland and A. G. Alleyne, "Hierarchical model-based predictive controller for a hybrid UAV powertrain," *Control Eng. Pract.*, vol. 115, no. June, p. 104883, 2021.
[152] X. Wang, J. Atkin, C. Hill, and S. Bozhko, "Power Allocation and Generator Sizing Optimisation of More-Electric Aircraft On-board Electrical Power during Different Flight Stages," in *AIAA 2019-4485 Session: Topic Area 3: System Optimization*, pp. 1–10.
[153] A. C. Luna, L. Meng, N. L. Diaz, M. Graells, J. C. Vasquez, and J. M. Guerrero, "Online Energy Management Systems for Microgrids: Experimental Validation and Assessment Framework," *IEEE Trans. Power Electron.*, vol. 33, no. 3, pp. 2201–2215, 2018.
[154] M. Madani, "OPL CPLEX tutorial : How to solve an optimization problem in IBM

ILOG CPLEX Optimization studio."
[155] G. Serale, M. Fiorentini, A. Capozzoli, D. Bernardini, and A. Bemporad, "Model Predictive Control (MPC) for enhancing building and HVAC system energy efficiency: Problem formulation, applications and opportunities," *Energies*, vol. 11, no. 3, 2018.
[156] J. Garche and A. Jossen, "Battery management systems (BMS) for increasing battery life time," *TELESCON 2000 - 3rd Int. Telecommun. Energy Spec. Conf. Proc.*, pp. 85–88, 2000.
[157] X. Wang, Y. Gao, J. Atkin, and S. Bozhko, "Neural Network based Weighting Factor Selection of MPC for Optimal Battery and Load Management in MEA," *23rd Int. Conf. Electr. Mach. Syst. ICEMS 2020*, pp. 1763–1768, 2020.
[158] Australian Government Civil Aviation Safety Authority, "Aircraft Electrical Load Analysis and Power Source Capacity," 2017.
[159] M. Elkazaz, M. Sumner, and D. Thomas, "Real-time energy management for a small scale PV-battery microgrid: Modeling, design, and experimental verification," *Energies*, vol. 12, no. 14, 2019.
[160] A. Carolina Luna *et al.*, "Online Energy Management Systems for Microgrids: Experimental Validation and Assessment Framework," *IEEE Trans. Power Electron.*, vol. 8993, no. c, pp. 1–15, 2017.
[161] R. R. Appino, J. Á. González Ordiano, R. Mikut, T. Faulwasser, and V. Hagenmeyer, "On the use of probabilistic forecasts in scheduling of renewable energy sources coupled to storages," *Appl. Energy*, vol. 210, no. October 2017, pp. 1207–1218, 2018.
[162] X. Wang, Y. Liu, L. Xu, J. Liu, and H. Sun, "A chance-constrained stochastic model predictive control for building integrated with renewable resources," *Electr. Power Syst. Res.*, vol. 184, no. February, p. 106348, 2020.
[163] F. Oldewurtel, L. Roald, G. Andersson, and C. Tomlin, "Adaptively constrained stochastic model predictive control applied to security constrained optimal power flow," *Proc. Am. Control Conf.*, vol. 2015-July, no. c, pp. 931–936, 2015.